PERFORMANCE EVALUATION OF RAMAN AMPLIFIERS IN FIBRE OPTIC COMMUNICATION SYSTEMS

PRATIM HAZARIKA

Doctor of Philosophy

ASTON UNIVERSITY

January 2023

Summary

This thesis presents an overview of Raman amplifiers in fibre optic transmission systems. Detailed analysis of the nonlinear accumulated noise and relative intensity noise (RIN) induced penalties are evaluated in discrete and distributed Raman amplifiers. In addition to these the thesis also includes different architectures of Raman amplifiers enabling multiband transmission.

The parametric dependency of fibre chromatic dispersion (CD) on the accumulated nonlinear noise in discrete Raman amplifiers (DRAs) was studied both theoretically and experimentally. Analytical modelling was performed over different fibre types that are widely used as a gain medium in DRAs. It was found that systems using Raman gain fibres with a positive value of CD induce lower accumulated nonlinear noise in comparison to systems using Raman gain fibres with a negative value of CD. The results obtained from the analytical model were then validated experimentally over a long-haul transmission system with DRAs as an inline amplifier using a recirculation loop.

RIN-induced penalties in distributed Raman amplifiers (DiRAs) were experimentally studied in two standard single-mode fibre (SSMF) G.654.E©TXF and G.652.D with different pumping schemes. Signal RIN for G.654.E© TXF was found to be lower in comparison to its counterpart G.652.D. The impact of RIN on the short-haul system was validated using both the test fibres pumped in a forward-pumped distributed Raman. Similarly, backward and bidirectional pumping was performed over a long-haul transmission system using a recirculation loop. It was experimentally observed that RIN-induced transmission penalties for G.654.E are lower in comparison to G.652.D making it a better choice of SSMF type for distributed amplification.

Experiments on novel architectures such as cascaded dual-stage and dual-band designs were demonstrated over a coherent transmission system with S-, C- and L-band signals. It was observed that the dual-stage design requires a guard band of ~10 nm to prevent overlapping of the pumps and signal, reducing the overall transmission capacity. In contrast, for dual-band design, no such guard band was required, but this benefit comes at a cost of the additional pump requirement increasing the overall amplifier power consumption. The performances of novel multistage Raman amplifier structures were also evaluated over the E-, S-, C- and L-band. Experimental studies were performed independently using DRAs only, hybrid bismuth-DRA and hybrid distributed-DRA. The E- and S-band signals were seen to have higher performance penalties in comparison to C- and L-band signals in the case of DRAs only and hybrid bismuth-DRA. In contrast, for the hybrid distributed-discrete design, the E-band signals were seen to have a similar penalty as C- and L-band signals.

Keywords: Raman amplification, coherent transmission, multiband transmission, ultra-wideband amplifiers.

Acknowledgements

Venturing on this PhD journey has been transformative from both a professional standpoint as well as personal growth and this journey would not have been possible without the support and guidance of several people. First and foremost, I am extremely grateful to my supervisor Prof. Wladek Forysiak for being a guiding light and source of encouragement during my work. I could not have asked for a nicer supervisor, who has always been calm and positive despite all my silly errors. I also would like to express my gratitude towards my associate supervisor Prof. Sergei Turitsyn for his guidance and support. This PhD work would not have been fruitful without the immense support from my mentor Dr Mingming Tan whose technical expertise paved a smoother journey for me during the experimental build-ups and analysis. Special thanks to Dr Md Asif Iqbal and Dr Lukasz Krzanowicz whose support and technical guidance during the initial days of PhD motivated me to embark on this journey.

I would also like to thank all the members of my research group especially Dr Paul Harper, Dr Ian D Phillips, Dr Aleksandr Donodin and Dr Shabnam Noor for their critical comments and support during experimental planning and brainstorming technical sessions. I express my deepest gratitude to the EU H2020 Marie Sklodowska Curie actions for giving me this opportunity to pursue my PhD as an early-stage researcher in the wideband optical network (WON) consortium. I take this opportunity to thank all my fellow early-stage researchers and fellow collaborators for being an important part of my PhD journey. Special thanks to Ms Tatiana Kilina, WON project manager for handling all administrative procedures and organizing various technical and soft-skills workshops for both professional and personal development. I extend my heartful gratitude to Dr Johannes Karl Fischer and his team at Fraunhofer HHI Berlin for hosting me as visiting researcher as part of my secondment.

I am also extremely thankful to Mrs Swaroopa Mucheli Sudhakar (AiPT lab technician) and Mr Mohammad Umar Patel (Research assistant) for being an immense helping hand throughout my time in the laboratory. I cannot thank enough all my friends in AiPT, India, England and Northern Ireland who have been a constant source of motivation throughout this PhD journey, thanks for all the wonderful memories that I will cherish throughout my life.

Most importantly, I am greatly indebted towards my father Mr Ganesh Hazarika, my late mother Mrs Banti Hazarika and my brother Mr Raktim Hazarika who have been my pillars of strength throughout my life and for all the sacrifices they made for my well-being and happiness.

Table of Contents

Chapter 1: Introduction 17

1.1 Background 17

1.2 Motivation 20

1.3 Aims and objectives 21

1.4 Thesis outline 22

1.5 Publication list 24

Chapter 2: Fibre optics communication systems 26

2.1 Optical transmitter 26

2.2 Mach-Zehnder modulator 27

2.2.1 Optical IQ Modulator 30

2.3 Optical fibre 31

2.3.1 Working principle of optical fibre 32

2.3.2 Classification of optical fibre 32

2.4 Transmission impairments in optical fibre 34

2.4.1 Attenuation in optical fibre 35

2.4.2 Chromatic dispersion in optical fibre 36

2.4.3 Polarization mode dispersion in optical fibre 38

2.4.4 Kerr-induced nonlinear effects in optical fibre 39

2.5 Optical amplifiers 42

2.5.1 Erbium-doped fibre amplifier 43

2.5.2 Other rare earth doped fibre amplifiers 46

2.5.3 Semiconductor optical amplifier 48

2.5.4 Fibre optic parametric amplifier 50

2.5.5 Raman amplifier 53

2.6 Optical receivers 53

2.6.1 Direct detection 55

2.6.2 Coherent detection 55

2.7 Performance metrics in optical communication 58
2.8 Recirculation fibre loop 61
Chapter 3: Raman amplifiers 64
3.1 Raman amplification 64
3.1.1 Raman gain spectrum 65
3.2 Types of Raman amplifier 66
3.2.1 Distributed Raman amplifier 66
3.2.2 Discrete Raman amplifier 73
3.3 Performance limiting factors in Raman amplifier 77
3.3.1 Amplified spontaneous emission 77
3.3.2 Relative intensity noise 80
3.3.3 Rayleigh backscattering 83
3.3.4 Polarization mode dispersion 84
3.3.5 Polarization dependent gain 85
3.3.6 Kerr nonlinearities 86
3.4 Recent developments in Raman amplifier 86
Chapter 4: Nonlinear penalties in discrete Raman amplifier for coherent transmission systems 88
4.1 Introduction 88
4.2 Analytical model 90
4.2.1 Parameter optimization with the analytical model for optimal performance 92
4.2.2 Raman amplifier parametric analysis using the analytical model 94
4.3 Experimental validation with single-channel transmission 96
4.3.1 Recirculation loop experimental setup 96
4.3.2 Results and discussions 97
4.4 Experimental validation with WDM transmission 100
4.4.1 Recirculation loop experimental setup 100
4.4.2 WDM transmission results and discussion 102

4.5 Conclusion 105
Chapter 5: RIN-induced penalties in distributed Raman amplifiers 107
5.1 Fibre parameters analysis 108
5.2 Relative intensity noise in forward pump distributed Raman amplifier 109
5.2.1 Experimental setup 109
5.2.2 RIN results and discussions 111
5.3 Single-span transmission with forward pump DiRA 112
5.3.1 Experimental setup 113
5.3.2 Results and discussions 114
5.4 Long haul transmission with backward and bidirectional pumped DiRA 114
5.4.1 Experimental setup 115
5.4.2 Results and discussion 117
5.5 Conclusion 119
Chapter 6: Ultrawideband Raman amplifiers for coherent transmission systems 121
6.1 Ultrawideband Raman amplifiers performance evaluation for S-, C- and L-band signal amplification 121
6.1.1 Amplifier characterization 121
6.1.2 Coherent transmission setup 128
6.1.3 Transmission results and discussions 129
6.2 Multistage discrete Raman amplifier for ultrawideband signal amplification 130
6.2.1 Multistage discrete Raman amplifier setup 131
6.2.2 Multistage Raman amplifier characterization 132
6.2.3 10G NRZ transmission with the multistage discrete Raman amplifier 134
6.2.4 E-, S-, C- and L-band coherent transmission with multistage discrete Raman amplifier 137
6.3 Hybrid Bismuth Raman amplifier for ultrawideband signal amplification 140
6.3.1 Hybrid Bi-DRA amplifier setup and characterization 140
6.3.2 Coherent transmission with hybrid Bi-DRA 143

6.4 Hybrid distributed-discrete Raman amplifier for ultrawideband signal amplification 145

6.4.1 Hybrid distributed-discrete Raman amplifier setup and characterization 145

6.4.2 Coherent transmission with hybrid Raman amplifier 147

6.5 Conclusion 149

Chapter 7: Conclusion and future works 150

7.1 Conclusion 150

7.2 Future Works 152

List of abbreviations

ADC	Analog to digital converter
AOM	Acousto-optic modulator
ASE	Amplified spontaneous emission
AWGN	Additive white gaussian noise
BDFA	Bismuth-doped fibre amplifier
BER	Bit error rate
CD	Chromatic dispersion
CRF	Corning Raman fibre
CUT	Channel under text
DAC	Digital to analog converter
dB	Decibels
DCF	Dispersion compensation fibre
DDG	Digital delay generator
DDRA	Distributed-discrete Raman amplifier
DGD	Differential group delay
DiRA	Distributed Raman amplifier
DRA	Discrete Raman amplifier
DRS	Double Rayleigh backscattering
DSF	Dispersion shifted fibre
DSP	Digital signal processing
DWDM	Dense wavelength division multiplexing
DYFA	Dysprosium-doped fibre amplifier
EDFA	Erbium-doped fibre amplifiers
EVM	Error vector magnitude
FOPA	Fibre optic parametric amplifier

FWM	Four wave mixing
GFF	Gain flattening filter
GMI	Generalized mutual information
GN	Gaussian noise
HD-FEC	Hard decision forward error correction
HNLF	Highly nonlinear fibre
IDF	Inverse dispersion fibre
IQ	In-phase and Quadrature
ISRS	Inter-channel stimulated Raman scattering
LO	Local oscillator
MBT	Multiband transmission
MZM	Mach-Zehnder modulator
NDFA	Neodymium-doped fibre amplifier
NF	Noise figure
NZDSF	Non-zero dispersion shifted fibre
OBPF	Optical bandpass filter
OSNR	Optical signal-to-noise ratio
PBC	Polarization beam combiner
PBS	Polarization beam splitter
PDFA	Praseodymium-doped fibre amplifier
PM	Polarization multiplexed
PRBS	Pseudo-random bit sequence
PS	Probabilistic shaping
QAM	Quadrature amplitude modulation
QPSK	Quadrature phase shift keying
RIN	Relative intensity noise

SNR	Signal-to-noise ratio
SPM	Self-phase modulation
SSMF	Standard single-mode fibre
TDFA	Thulium-doped fibre amplifier
TIA	Transimpedance amplifier
UWB	Ultrawideband
WDM	Wavelength division multiplexing
WSS	Wavelength selective switch
XPM	Cross-phase modulation
ZDW	Zero dispersion wavelength

List of figures

Figure 2.1 Constellation diagram for a) PM-QPSK and b) PM-16QAM signal. 27

Figure 2.2 Schematic of Mach-Zehnder modulator. 28

Figure 2.3 MZM field and power transfer function with a minimum, quadrature, and maximum transmission point. 30

Figure 2.4 Simple schematic of IQ modulator with in-parallel MZM and phase modulator. 30

Figure 2.5 Schematic of optical fibre; a) three-dimensional and, b) two-dimensional view 32

Figure 2.6 Light propagation from a higher to lower refractive index medium a) total internal reflection principle b) total internal reflection in optical fibre. 32

Figure 2.7 Refractive index profile of a) step index fibre b) graded index fibre 33

Figure 2.8 Concatenated section of random birefringent in fibres with different DGD [66]. 38

Figure 2.9 DGD distribution in a randomly birefringent optical fibre [66]. 39

Figure 2.10 Optical amplifiers for different bands of optical communication window [76]. 43

Figure 2.11 Transition of $Er3+$ ions when pumped at 980 and 1480 nm in an erbium-doped fibre. 44

Figure 2.12 Schematic of single-stage forward pumped EDFA with pump wavelength at 980 nm 45

Figure 2.13 Schematic of parallel amplification with forward-pumped EDFA for C- and L- band amplification (pump wavelength @980 nm) 46

Figure 2.14 FOPA output spectra for the pump, signal, and idler with a) single pump system; b) two-pump system [124]. 51

Figure 2.15 Schematic of optical receiver for direct detection 55

Figure 2.16 Schematic diagram of a polarization-diverse coherent optical receiver. LO: local oscillator; PBS: polarization beam splitter; TIA: trans-impedance amplifier. 56

Figure 2.17 Schematic of a 90° optical hybrid 57

Figure 2.18 Error vector between the ideal symbol and received symbol in a complex I-Q plane [144] 60

Figure 2.19 Schematic of a recirculation loop (GFF: gain flattening filter, WSS: waveshaper) (dashed blue lines: optical signal; dashed black lines: electrical signal) 62

Figure 3.1 Energy level diagram of Raman Stokes scattering 64

Figure 3.2 Raman gain spectrum measurement a) schematic diagram; b) gain spectrum 65

Figure 3.3 ASE amplification with Raman amplifier 66

Figure 3.4 Schematic representation of FW-pumped DiRA. 68

Figure 3.5 Schematic representation of BW pumped DiRA. 69

Figure 3.6 Schematic representation of Bidirectional pumped DiRA 69

Figure 3.7 Signal power profile with distributed amplification over 70 km SSMF a) forward b) backward pumping c) bidirectional pumping 70

Figure 3.8 Signal and noise power profile with Bidirectionally pumped distributed Raman amplifier 73

Figure 3.9 Schematic diagram of DRA with single pump and signal configuration. 73

Figure 3.10 Raman gain coefficient measurement using broadband ASE a) experimental setup schematic b) Measured Raman gain coefficient gr of IDF, DCF and CRF fibre 75

Figure 3.11 Multiple pump configuration with DRA for WDM signal amplification a) schematic b) pump combiner 76

Figure 3.12 Signal power profile in a backward pumped DRA with IDF as the gain fibre 76

Figure 3.13 RIN transfer function for forward (Co-pumped) and backward (Counter) pumping in distributed Raman amplifier 81

Figure 3.14 Schematic of Rayleigh scattering and double Rayleigh scattering in Raman amplifier. 84

Figure 4.1 Experimentally measured a) Raman gain coefficient b) Attenuation coefficient of IDF, DCF and CRF. 90

Figure 4.2 Schematic of a) single-span transmission with backward pumped discrete Raman amplifier b) amplified links with log signal power profile 90

Figure 4.3 Q^2 factor vs launch power per channel (@1550nm) for 1800 km with varying SSMF span length amplified using DRA 93

Figure 4.4 Q^2 Factor vs Launch power channel for the different number of 30GBaud transmitted channels at 30x63 km of transmission distance. 93

Figure 4.5 Peak SNR vs maximum transmission distance within an HD-FEC of 8.5 dB for a) 1 channel b) 96 channel 94

Figure 4.6 SNR vs Launch power per channel to SSMF (single channel @1550 nm) for 30x63 km of transmission with varying a) chromatic dispersion b) nonlinear coefficient 96

Figure 4.7 Recirculation loop experimental setup for a single channel 23 GBaud PM-QPSK transmission 97

Figure 4.8 Q^2 Factor vs Launch power per channel for 23 GBaud PM-QPSK single channel transmission with CRF and DCF as gain fibre for a) 20x63 km b) 30x63 km transmission distance 98

Figure 4.9 Q^2 Factor vs Launch power per channel for 23 GBaud PM-QPSK single channel transmission with CRF and IDF as gain fibre for a) 20x63 km b) 30x63 km transmission distance 99

Figure 4.10 Recirculation loop experimental setup for a WDM transmission with a 30 GBaud PM-QPSK modulating signal coupled with 9 ASE channels 100

Figure 4.11 Optical spectrum of 10 WDM channels a) Input spectrum; 10 span transmission with DRA stage comprising of b) DCF c) CRF d) IDF fibres 102

Figure 4.12 Optical spectrum of 10 WDM channels a) Input spectrum; 20 span transmission with DRA stage comprising of b) DCF c) CRF d) IDF fibres 102

Figure 4.13 Q^2 Factor vs launch power per channel, experimental and analytical modelling results with CRF and DCF fibre for a) 20x63 km b) 30x63 km transmission..... 103

Figure 4.14 Q^2 Factor vs launch power per channel, experimental and analytical modelling results with CRF and IDF fibre for a) 20x63 km b) 30x63 km transmission. 104

Figure 4.15 10 Channel 30 GBaud PM-QPSK transmission a) Q^2 Factor vs Distance b) Q^2 penalty (CRF-DCF and CRF-IDF) vs Distance..... 105

Figure 5.1 G.G52.D and G.654.E a) wavelength vs attenuation coefficient b) wavelength shift vs Raman gain coefficient. 109

Figure 5.2 Schematic for RIN measurement with forward pumped distributed Raman amplifier 110

Figure 5.3 Measured RIN of the 1455 nm pump used in the calculation 112

Figure 5.4 Signal RIN for PM-QPSK and PM-8QAM with G.652.D and G.654.E fibre at a) 34 GBaud and b) 69 GBaud..... 112

Figure 5.5 Schematic for single channel coherent transmission @1550 nm with FW pumped DiRA..... 113

Figure 5.6 Single channel transmission at 1550 nm Q^2 Factor vs Launch power per channel a) 34 GBaud PM-QPSK; b) 34 GBaud PM-8QAM; c) 69 GBaud PM-QPSK and e) 69 GBaud PM-8QAM 114

Figure 5.7 28 GBaud PM-QPSK transmission with recirculation loop 117

Figure 5.8 Output optical spectrum of 1550 nm signal with BW pumped DiRA 117

Figure 5.9 28 GBaud PM-QPSK, Q^2 Factor vs Launch power per channel for a) 10 b) 20 recirculation 118

Figure 5.10 FW and BW pumped DiRA distance vs a) Q^2 Factor b) Q^2 penalty 119

Figure 6.1 S-, C- and L-band grid generation a) setup b) output spectrum 122

Figure 6.2 Experimental setup for amplifier characterization a) cascaded dual-stage DRA b) in-parallel dual band DRA with reflection c) in-parallel dual band DRA without reflection 124

Figure 6.3 Optical spectrum a) input spectrum to 70 km SSMF; b) output spectrum after 70 km transmission; c) output spectra after dual-stage DRA; d) output spectrum after the dual-band DRA with unstable random lasing; e) output spectrum after dual-band DRA, reducing the pump power to avoid unstable lasing; f) out spectrum after dual-band DRA without back-reflection and unstable lasing..... 125

Figure 6.4 Net gain and noise figure for a) cascaded dual-stage DRA (Scheme 1); b) dual-band DRA with back-reflection (Scheme 2); c) dual-band DRA without back-reflection (Scheme 3) 127

Figure 6.5 Experimental setup for S-, C- and L-band coherent transmission with dual-band and dual-stage DRA as an inline amplifier 128

Figure 6.6 Q^2 factor vs wavelength for B2B and 70 km transmission with 30 GBaud PM-16QAM signals a) cascaded dual-stage (scheme 1); b) in-parallel dual band with (scheme 2) and without (scheme 3) back-reflection..... 129

Figure 6.7 Q^2 penalty vs wavelength for 30 GBaud PM-16QAM signals 130

Figure 6.8 Schematic for characterization of the multistage discrete Raman amplifier 131

Figure 6.9 E-, S-, C- and L-band WDM generation..... 131

Figure 6.10 Optical spectrum of the E-, S- C- and L-band WDM grid a) input spectrum to 70 km SSMF; b) output spectrum from 70 km SSMF; c) amplified output spectrum after the multistage DRA; zoomed Rayleigh backscattered spectrum of the; d) 1485; e) 1508 nm pumps. 133

Figure 6.11 E-, S-, C- and L-band multistage discrete Raman amplifier characterization, wavelength vs a) Gain /Noise figure; b) Output OSNR..... 134

Figure 6.12 10 Gb/s NRZ transmission a) experimental setup b) SSMF input spectrum c) amplified output spectrum 135

Figure 6.13 BER vs received power per channel for B2B and after 70 km transmission with channels at; a) 1430 nm; b) 1500 nm; c) 1550 nm and d) 1600 nm..... 136

Figure 6.14 Power penalty at BER of 10^{-4} between B2B and 70 km transmission..... 137

Figure 6.15 30 GBaud PM-16QAM transmission over 70 km SSMF experimental setup..... 138

Figure 6.16 Constellation diagrams for B2B and 70 km transmission performance for 1430, 1500, 1550, and 1605 nm 30 GBaud PM-16 QAM signals..... 138

Figure 6.17 30 GBaud PM-16QAM WDM transmission wavelength vs a) Q^2 factor b) Q^2 penalty 139

Figure 6.18 Performance penalty (Q^2 Penalty) of X and Y polarization with B2B transmission 140

Figure 6.19 Schematic of hybrid Bi-Raman amplifier for E-, S-, C- and L-band signal amplifier 141

Figure 6.20 E-, S-, C- and L-band (1410-1605) nm spectrums a) input spectrum to SSMF; b) spectrum after 70 km SSMF; c) amplified spectrum after hybrid bi-DRA amplifier..... 141

Figure 6.21 Hybrid Bi-Raman amplifier net gain and noise figure 142

Figure 6.22 Schematic of E-, S-, C- and L-band 30 GBaud PM-16QAM transmission with BDFA and DRA as an inline amplifier..... 143

Figure 6.23 30 GBaud PM-16 QAM transmission with Hybrid Bi-DRA as an inline amplifier; wavelength a) Q^2 factor for B2B and 70 km transmission b) Q^2penalty 144

Figure 6.24 Schematic of hybrid distributed discrete Raman amplifier for E-, S-, C- and L-band signal amplification..... 145

Figure 6.25 Optical WDM spectrum, wavelength vs output power; at a) SSMF input b) output from SSMF c) amplified output spectrum. 146

Figure 6.26 Ultrawideband hybrid distribute-discrete Raman amplifier a) net gain and noise figure b) amplified output OSNR..... 146

Figure 6.27 Experimental setup for 30 GBaud PM-16QAM transmission with hybrid Bi-DRA as an inline amplifier. 147

Figure 6.28 30 GBaud PM-16QAM transmission performance wavelength vs a) Q^2 penalty for B2B and 70 km transmission b) Q^2 penalty c) XY Q^2 penalty. 148

List of tables

Table 3.1 Parameters used in the numerical modelling of the bidirectionally pumped distributed Raman amplifier..... 72

Table 4.1 Summary of IDF, DCF, and CRF fibre parameters used for the analytical modelling89

Table 5.1 Fibre parameter at 1550 nm [244] 109

Table 5.2 Pump powers for the BW/BI pumped DiRA 116

Table 6.1 Pump power and wavelengths for scheme 1, scheme 2 and scheme 3 DRAs 126

Chapter 1: Introduction

1.1 Background

The history of fibre optics communication began around 1966 when Charles K Kao and GA Hockham published their paper on the propagation of optical waveguides in a dielectric medium [1]. The idea of propagating optical waveguides through a silica-based glass was seen as revolutionary where light waves could be guided inside a fibre similar to the way an electron is confined to copper cables [2]. However, propagation of light pulses through a fibre medium was extremely difficult due to the high intrinsic loss of the fibre. In 1970, researchers from Corning reduced this loss to 20 dB/km and in 1979 a group of Japanese researchers managed to reduce the fibre loss down to 0.2 dB /km in the infrared region near 1.5 μm [3,4]. With this began the era of optical communication and the first-generation optical system was implemented in 1980 using multi-mode fibres [5]. This system operated at a wavelength of 850 nm with a gallium-arsenide (GaAs) semiconductor laser at a bit rate of 45 Mbit/s. The loss in this region of operation was ~3 dB/km, hence regenerative repeaters were placed after every 10 km of optical fibres [2].

Although the optical fibre has a low-loss window near 1550 nm, the first-generation systems were operating at 850 nm as the commercially available light source was based on GaAs, which have an emission spectrum near 850 nm. However, with the introduction of heterojunction-based semiconductor lasers, such as InGaAsP with spectral emission near the low-loss window of optical fibre, the second-generation optical systems began in 1985. The second-generation optical systems were developed to operate at 1.3 μm, near the zero-dispersion wavelengths. Repeater spacing was increased from 10 to 50 km and the bit rate improved from 100 Mbit/s in 1981 to 1.7 Gbit/s in 1987 [2].

The second-generation optical systems were still costly as the repeater spacing was at 50 km due to the high fibre loss at 1.3 μm. There was an ongoing interest in the telecom community to shift the transmission window from 1.3 μm to the low loss window near 1.5 μm, and the third-generation systems were developed to operate near 1.5 μm. However, deployment of these systems was delayed due to the large chromatic dispersion (CD) near 1.5 μm. Two approaches were finally taken to mitigate this issue. The first was the development of single-mode lasers and the second was the development of dispersion-shifted fibres (DSFs) with zero dispersion near 1.5 μm. Both, these researches were conducted, and by the mid-80s experimental demonstrations showed an achievable bit rate of up to 4 Gbit/s over a distance of 100 km [2]. With this came the era of third-generation systems in 1990 operating near 1.5 μm with a conjunction of single-mode laser and DSF. The developed systems were initially operating at a bit rate of 2.5 Gbit/s which was later extended to 10 Gbit/s.

Till the third generation, signal amplification was performed using repetitive regenerators in the electrical domain where the optical signals were converted to electrical signals, followed by amplification and back conversion. This process was expensive and also introduced latency. Meanwhile, in the early 90s, optical amplifiers were developed by a group of researchers in Bell labs and the University of Southampton that revolutionized the field of optical communication [6,7]. In addition to this, the wavelength division multiplexing (WDM) technique was introduced in 1992 which increased the network capacity to multifold [2]. Thus came the era of fourth-generation optical communication which included WDM with optical amplification using erbium-doped fibre amplifiers (EDFA). In 1996 transmission systems were operating at a bit rate of 80 Gbit/s with EDFA placed at an interval of 60-80 km. The introduction of EDFA that can amplify in the low-loss window of standard single-mode fibre (SSMF) in conjunction with WDM was a breakthrough in optical communication history and by early 2000, Tb/s of data were transmitted using dense WDM (DWDM) techniques with multiple fibres over the transatlantic and transpacific networks [2].

One of the issues that were present during transmission in the low-loss window of SSMF was the fibre CD which is ~17 ps/nm/km, needing the use of regenerators at a distance of about 800-1000 km for 2.5 Gb/s per channel data rate [8]. The dispersion-induced effects were more severe with higher symbol rates, and with the internet booming in early 2000, the need for the support of capacity was growing every day. To overcome this problem, dispersion-shifted fibres (DSF) with zero dispersion near 1.5 μm were introduced. However, they suffered from nonlinear effects such as four-wave mixing, which in particular was very adverse in DWDM systems. In the later stage, dispersion-managed (DM) links were developed with non-zero dispersion shifted fibre (NZDSF) and then with dispersion compensation fibre (DCF). A combination of fibres with opposite dispersions, such that the overall CD in the link is zero was initially seen as the best solution, and dispersion mapping was introduced to manage such links [9]. However, these mappings became quite complex and aggressive with time as the data rate per channel was increasing incessantly. The problem was finally resolved with the introduction of coherent optics around mid-2000 [8,10] Digital signal processing (DSP) in coherent optics, managed to compensate for the CD in the digital domain without the need for any special fibres [11].

The fifth and the current generation optical communication is based on coherent WDM technology. While most of the existing links operate over the C- band (1530-1565 nm), with the increase in data demand some telecom operators have even started utilizing the L-band (1570-1620 nm) [12]. These two bands have been well explored and XR-optics-based point-to-point and point-to-multipoint pluggable have been demonstrated over the years by multiple telecom operators. Today transport network includes solutions such as 400G and 800G for metro networks and long-haul networks [13].

Advanced modulation formats such as 1024 QAM [14] or 4096 QAM [15] and even 16384 QAM [16] with probabilistic-shaped (PS) constellation has also been experimentally demonstrated by different research groups. However, scaling the data with advanced modulation formats also puts a limit on the maximum transmission distance, due to signal-to-noise ratio (SNR) limitations in high modulation format data [17]. Today state-of-the-art DWDM technology has achieved several milestones with DSP integration over complementary metal oxide semiconductor (CMOS) technology enabling reconfigurable baud rates up to 96 and 140 GBaud [18,19]. Modern-day pluggable transceivers such as QSFP-DD (quad small form factor double density) and OSFP (octal small form factor) line cards have reached a capacity of 1.2 Tbit/s per channel data rate. Some of the most advanced coherent DWDM pluggable optics commercially available are [18–21]:

- Infinera ICE6 (2021): 2x96 GBaud, 2x800G, PS-64QAM
- Acacia CIM 8 (2022): 140 GBaud up to 1.2 Tbit/s per channel
- Ciena Wavelogic 5 extreme (2020): 2x95 GBaud, 2x800G, PS-64QAM
- Acacia AC12000-SC2 (2020): 2x64 GBaud, 1.2T, DP-64 QAM

Although, increasing the capacity per channel with advanced modulation formats and high baud rates is the most cost-effective method, it is not a long-term solution as we are limited by the nonlinear Shannon limit for an additive white Gaussian noise (AWGN) channel [22].

$$C = B\ log_2(1 + SNR) \tag{1.1}$$

Where C is the channel capacity, B is the bandwidth of the channel and SNR is the signal-to-noise ratio. From equation (1.1) we can see that SNR and the maximum channel capacity are directly proportional to each other. Transmission with an advanced modulation format and higher baud rate will require a larger SNR in the receiver end putting a limit on the maximum transmissible distance. Hence, meeting the future demands in data by scaling the channel capacity is highly questionable as we are near the borderline of approaching the Shannon limit. In addition to this pluggable optics requires complex integration of CMOS, and for high-capacity transmission, DSP on ASIC requires lots of processing power and small-scale packaging of billions of transistors on a single silicon chip. Today 800G modules include CMOS nodes on silicon of 7 nm [23], and further increment in the channel capacity will require a more complex integration of transistors in silicon chips where we are countered by Moore's law [24].

However, where we are limited by the maximum channel capacity, the average consumption of data has been exponentially incrementing each year. Over the past decade with the evolution of technologies such as driverless vehicles, internet of things (IoT), streaming platforms, and 5G networks etc., a capacity crunch in internet traffic can be predictable in the coming years [25].

According to CISCO annual report, nearly two-thirds of the global population will have access to the internet by 2023, making it a total of approximately 5.3 billion internet users with data consumption exceeding 100s of exabytes per month [26].

1.2 Motivation

To sustain this ever-increasing demand for data, there is a requirement for new advancements in optical communication technology.

Two of the novel technologies that are highly potential to overcome this capacity crunch in future fibre-optics communication systems are.

1. Space division multiplexing (SDM)
2. Multiband transmission (MBT)

SDM is based on the utilization of the spatial domain for data transmission. The concept of SDM began in the same era as the development of fibre optics communication. However, it soon faded due to design challenges and other performance limitations such as crosstalks [27]. Recently, renewed interest in SDM has been seen among different research communities as this technology can increase the overall network capacity by multifold in comparison to the existing SSMF technology [28]. Transmission through SDM can be either through the excitation of higher spatial modes using fibres such as multimode and few-mode fibres or by parallel transmission through multiple single-mode cores using multicore fibres (MCF) [29]. An alternate possibility that includes a combination of few-mode and multicore also exists that can enable signal transmission in multiple spatial domains over different cores of fibre [30]. The first transmission capacity over 1 Pbit/s was demonstrated in 2012 using 12-core fibre over 52 km [31]. After this, the petabit barrier was crossed multiple times with the data rate reaching a record of 10.66 Pbit/s using 38 core three-mode fibre [32]. SDM has also been demonstrated over unrepeated systems, and a record distance of 213 km was achieved with a net throughput of 372 Tb/s using 4-core MCF [33]. In addition to this, SDM has also been shown over long-haul systems, where transmission over S-, C- and L-band was performed using 4-core MCF reaching a record transmission distance of 8027 km [34]. With all the above-mentioned milestones achieved using SDM, it seems SDM is the best solution for next-generation communication systems. However, the fundamental issue that lies with the utilization of SDM is power consumption and expenditure. Implementation of SDM would require the full-scale establishment of new fibre networks at both the node and operator levels, which would require a heavy investment in capital expenditure (CAPEX), and operational expenditure (OPEX). In addition to new fibre deployment, commercial-grade optical equipment such as amplifiers, reconfigurable add-drop multiplexers (ROADMS) etc, needs to be developed that can operate in the different spatial domains. The overall system power consumption required for amplification and DSP will also increase significantly. Hence, it is still

unclear whether the implementation of SDM for future optical networks is a viable solution or not.

This brings us to the next solution, MBT which is one of the major studies in this thesis. While SDM is based on signal transmission over different spatial domains, MBT involves signal transmission in the unused spectrum of the SSMF optical window [35]. Although in terms of net throughput MBT cannot replace SDM however, MBT can increase the existing network capacity by 10 times with minimal infrastructural changes [35]. Today, optical communication systems operate over the C- and L-band (1530-1620 nm) of the optical window leaving four unutilized O-, E-, S- and U- bands. Enabling data transmission over all the bands extending from O- to U-band can support us with a bandwidth of ~400 nm. However, the inclusion of these bands also will require different commercial-grade equipment such as amplifiers, ROADMS, transceivers, etc.

Speaking solely of optical amplifiers, the existing erbium-doped fibre amplifier can operate only in the C- and L-band of the optical window, extension beyond these bands requires other amplification technologies. This can be done via doped amplifiers with rare-earth materials or by using other amplifiers based on semiconductor materials, four-wave mixing (FWM), and Raman effect in optical fibres.

1.3 Aims and objectives

In this thesis, we focus on optical amplification using Raman amplifiers with both distributed and discrete modes of operation. The gain dynamics of this amplifier are flexible to provide arbitrary gain across large bandwidths making it a suitable candidate for ultrawideband (UWB) signal amplification. However, it is necessary to study the different parameters that can limit the performance of distributed and discrete Raman amplifiers before they can be utilized for UWB signal amplification.

In discrete Raman amplifiers (DRAs), the amplification medium includes nonlinear fibres with a high nonlinear coefficient (γ) and varying values of fibre chromatic dispersion (CD). The typical length of Raman gain fibre used for discrete amplification is in few kilometres which can add to a significant distance in long-haul transmission. Hence, performance evaluation of DRA was conducted with different Raman gain fibre types, to study the accumulated nonlinear noise in long-haul WDM systems.

Similarly, in distributed Raman amplifiers (DiRA) the overall transmission performance varies with different pumping schemes due to the addition of nonlinearity and relative intensity noise (RIN). To understand the accumulated RIN in different SSMFs, we conducted an experimental study over long-haul coherent systems with different pumping schemes using two SSMFs, G.652.D and G.654.E$^{@TXF}$. This study is important as many recent experimental demonstrations have shown the use of DiRA for compensation of the inter-channel stimulated Raman scattering

(ISRS) from the shorter wavelength channel to the longer wavelength channels in UWB transmission [36,37].

Finally, with the proper choice of Raman gain fibre type, we studied the performance of DRA. hybrid combinations of distributed-discrete Raman amplifiers (DDRA) and hybrid bismuth-DRA in UWB systems. It is important to evaluate the performance of different UWB Raman architectures to understand the benefits and limitations of each design. In addition to this, UWB Raman amplifiers require multiple pumping configurations operating at different wavelengths. Hence, it is crucial to arrange the pumps systematically such that the overall noise figure is low with minimal pump-to-pump and pump-to-signal overlapping. In-line amplification with DRA and DDRA has been previously reported over S-, C- and L-band with 100G coherent transmission [38]. However, the inclusion of the E-band with S-, C-, and L- using DRA and DDRA has not been reported so far. In this thesis, we have proposed a novel multistage DRA and DDRA based on the split-combine approach of spectral bands that can amplify the signal from 1410-1605 nm. A detailed study on these amplifiers was performed and their performance penalty as an inline amplifier was validated over a 200G coherent WDM transmission system. The transmission performance of the UWB Raman amplifier throughout the thesis was validated after 70 km and 50 km of SSMF without hydroxyl ion (OH) absorption peak in the E-band. The performance of the UWB Raman amplifier in G.652.D with OH ions is not explored in this thesis as most of the newly deployed fibre links are absent of the OH water peak also known as dry fibres.

In this thesis, the experimental validations of different Raman amplifiers and their parametric study of performance limiting factors provides a deeper understanding regarding the implementation of Raman amplifiers for future MBT systems.

1.4 Thesis outline

The thesis has been organized into seven chapters.

Chapter 1 presents an overview of the progression of fibre optics communication and the current state-of-the-art coherent technology. The chapter presents two novel ideas SDM and MBT that have the potential to be a part of the next-generation optical networks. The primary focus was on MBT systems and in particular optical amplifiers that can enable UWB amplification.

Chapter 2 presents a detailed discussion on fibre optics communication systems. The chapter explains the working principle of different optical communication devices such as transmitters, receivers, Mach-Zehnder modulators, optical fibres, and optical amplifiers. In addition to this, the impact of transmission limiting factors such as fibre attenuation, fibre CD, fibre nonlinearity etc. is discussed in detail. The latter half of the chapter includes an explanation of different performance metric quantities such as bit-error-rate, signal-to-noise ratio, optical signal-to-noise ratio, error vector magnitude (EVM) and generalized mutual information (GMI). In the end, we

present a cost-effective long-haul transmission setup known as a recirculation loop, its working principle and its limitations.

Chapter 3 focuses on a particular type of optical amplifier known as the Raman amplifier. The initial part of the chapter included the history and the working principle of Raman amplification. This is followed by a detailed overview of distributed and discrete Raman amplifiers, with basic simulation results. In the next section, different performance limiting factors in Raman amplifiers are discussed such as amplifier noise figure (NF), relative intensity noise (RIN), and Rayleigh backscattering that can impair the transmission performance. Finally, we present an overview of the latest progression with Raman amplifiers.

Chapter 4 deals with the nonlinear accumulated impairments in a long-haul coherent transmission system with DRA as an inline amplifier. An analytical model reported in [39,40] was used to study the impact of nonlinear noise accumulation with different Raman gain fibre types of varying values of CD. The observations made from the analytical model are then experimentally evaluated over a recirculation loop with different Raman gain fibre types as an inline amplifier gain medium.

Chapter 5 evaluates the penalties induced by RIN in DiRA using two commercial SSMFs G.652.D and G.654.E $^{@TXF}$. In the first section, RIN is measured in both the proposed SSMF using forward-pumped (FW) DiRA, and their impact on coherent transmission systems is validated with 30 and 60 GBaud single-span transmission. In the next section, long-haul transmission is performed using a recirculation loop with two different pumping schemes backward (BW) and bidirectional (BI) pumping. The accumulated RIN penalties are experimentally validated and the maximum transmissible distance using both the test fibres is observed.

Chapter 6 discusses MBT systems validation with different UWB Raman amplifiers. In the first section, we present two different architectures of UWB DRAs (cascaded dual-stage and dual-band) capable of signal amplification in the S-, C-, and L-band. Their proposed amplifiers are characterized, and their performance is validated with a 200G coherent system. WDM transmission is performed using over 70 km of SSMF with DRA as an inline amplifier. In the next section, we proposed three different combinations of Raman amplifiers that can cover the E-, S-, C-, and L-band of the optical window. These three amplifiers were multistage DRAs, hybrid BI-DRA, and DDRA based on a split-combine approach of spectral bands. The characteristics of these amplifiers are studied and their performance over is validated with a 200G WDM transmission system.

Chapter 7 concludes the thesis, presenting an overview of the main contributions and possible future works.

1.5 Publication list

1. **Pratim Hazarika**, Mingming Tan, Md Asif Iqbal, Lukasz Krzczanowicz, Abdallah A. i. Ali, Ian Phillips, Paul Harper, and Wladek Forysiak, "RIN induced penalties in G.654.E and G.652.D based distributed Raman amplifiers for coherent transmission systems," Opt. Express 29, 32081-32088 (2021).
2. **Pratim Hazarika,** Mingming Tan, Md Asif Iqbal, Ian Phillips, Paul Harper, Jeffery S. Stone, Ming Jun Li, and Wladek Forysiak, "Performance evaluation of discrete Raman amplifiers in coherent transmission systems," Opt. Express 30, 43053-43061 (2022).
3. **Pratim Hazarika**, Mingming Tan, Aleksandr Donodin, Shabnam Noor, Ian Phillips, Paul Harper, Jeffery S. Stone, Ming Jun Li, and Wladek Forysiak, "E-, S-, C- and L-band coherent transmission with a multistage discrete Raman amplifier," Opt. Express 30, 43118-43126 (2022). (Editors pick)
4. **Pratim Hazarika**, Mingming Tan, Aleksandr Donodin, Mohammad Patel, Ian Phillips, Paul Harper, Wladek Forysiak, "Ultra-wideband discrete Raman amplifier optimisation for single-span S-C-L-band coherent transmission systems," Opt. Lett. 47, 6472-6475 (2022).
5. Aleksandr Donodin, Mingming Tan, **Pratim Hazarika**, Vladislav Dvoyrin, Ian Phillips, Paul Harper, Sergei K. Turitsyn, and Wladek Forysiak, "30-GBaud DP 16-QAM transmission in the E-band enabled by bismuth-doped fiber amplifiers," Opt. Lett. 47, 5152-5155 (2022).
6. Matheus Sena, **Pratim Hazarika**, Caio Santos, Bruno Correia, Robert Emmerich, Behnam Shariati, Antonio Napoli, Vittorio Curri, Wladek Forysiak, Colja Schubert, Johannes K. Fischer, and Ronald Freund, "Advanced DSP-based Monitoring for Spatially resolved and Wavelength-dependent Amplifier Gain Estimation and Fault Location in C+L-band Systems," J. Lightwave Technol, doi:10.1109/JLT.2022.3208209 (Top-scored paper).
7. **Pratim Hazarika,** Md Asif Iqbal, Lukasz Krzczanowicz and Wladek Forysiak, "RIN Penalty Analysis in G.654.E and G.652.D Fibres with Forward Pumped Distributed Raman Amplification," *2021 Conference on Lasers and Electro-Optics (CLEO)*, 2021, pp. 1-2.
8. **Pratim Hazarika**, M. Abu-Romoh, Mingming Tan, Lukasz Krzczanowicz, T. T. Nguyen, Md Asif Iqbal, Ian Phillips, Paul Harper, Ming Jun Li, and Wladek Forysiak, "Impact of Chromatic Dispersion in Discrete Raman Amplifiers on Coherent Transmission Systems," *Optical Fiber Communication Conference (OFC) 2021*, OSA Technical Digest (Optica Publishing Group, 2021), paper Th1A.14.

9. **Pratim Hazarika**, Mingming Tan, Aleksandr Donodin, Ian Phillips, Paul Harper, Ming Jun Li, and Wladek Forysiak, "210 nm E, S, C and L Band Multistage Discrete Raman Amplifier," *Optical Fiber Communication Conference (OFC) 2022*, Technical Digest Series (Optica Publishing Group, 2022), paper Tu3E.2.
10. **Pratim Hazarika**, Mingming Tan and Wladek Forysiak, "Hybrid Raman Amplifier for E, S, C and L band Signal Amplification," *IEEE Photonics Society Summer Topicals Meeting Series (SUM),* 2022, pp. 1-2, doi: 10.1109/SUM53465.2022.9858223.
11. **Pratim Hazarika**, Aleksandr Donodin, Mingming Tan, Ian Phillips, Paul Harper, and Wladek Forysiak, "30-GBaud PM-16-QAM transmission over E-, S-, C- and L-band with hybrid Raman amplifier," *Optical Fiber Communication Conference (OFC) 2023,* Technical Digest Series (Optica Publishing Group, 2023), paper Th1B.7.
12. **Pratim Hazarika**, Mingming Tan and Wladek Forysiak, "Recent advances in wideband Raman amplifier", *Proc. SPIE 12429, Next-Generation Optical Communication: Components, Sub-Systems, and Systems XII, 124290R (15 March 2023);* https://doi.org/10.1117/12.2662867
13. Chandra B. Gaur, Vladimir Gordienko, **Pratim Hazarika**, and Nick J. Doran, "Polarization Insensitive Fiber Optic Parametric Amplifier with a Gain Bandwidth of 22 nm in S-Band," *Optical Fiber Communication Conference (OFC) 2022*, Technical Digest Series (Optica Publishing Group, 2022), paper W4J.1.
14. Chandra B. Gaur, Vladimir Gordienko, Abdullah A. I Ali, **Pratim Hazarika**, Andrew Ellis, and Nick J Doran, "Polarization- insensitive fibre optic parametric amplifier with gain bandwidth of 35 nm in L-band," *2021 European Conference on Optical Communication (ECOC)*, 2021, pp. 1-4, doi: 10.1109/ECOC52684.2021.9605891.
15. Aleksandr Donodin, Mingming Tan, Ian Phillips, Abdullah AI Ali, **Pratim Hazarika**, Mohammad Patel, Paul Harper, Vladislav Dvoyrin, Wladek Forysiak, and Sergei Turitsyn, "50 GBaud QPSK E-band Transmission Using Bismuth Doped Fiber Amplifiers," *Optical Fiber Communication Conference (OFC) 2022*, Technical Digest Series (Optica Publishing Group, 2022), paper W3J.5.
16. Aleksandr Donodin, **Pratim Hazarika**, Mingming Tan, Ian Phillips, Vladislav Dvoyrin, Mohammad Patel, Ian Phillips, Paul Harper, Sergei Turitsyn, and Wladek Forysiak, "195-nm Multi-Band Amplifier Enabled by Bismuth-doped Fibre and Discrete Raman Amplification", European conference on optical communication (ECOC) 2022, Th2A.1, pp. 1-4.

Chapter 2: Fibre optics communication systems

In this chapter, we will discuss in detail fibre optics communication systems. The main takeaway from this chapter will be an understanding of optical components, the working principle of different optical components, limiting factors in optical communication, and performance metrics to quantify the quality of transmission (QOT) in optical communication. The chapter starts with descriptions of transmission components such as optical transmitters, optical amplifiers, optical fibres and optical receivers with a detailed explanation of all the parameters associated with these components. The second section will include discussions on transmission impairments such as fibre attenuation, fibre chromatic dispersion, polarization mode dispersion and Kerr-induced nonlinearities in optical fibre. In the next part, we will talk briefly about various performance-determining factors such as bit-error-rate (BER), signal-to-noise ratio (SNR), error-vector-magnitude (EVM), etc. We will then end the chapter with a cost-effective laboratory-based setup known as a recirculation loop for conducting long-haul transmission experiments.

2.1 Optical transmitter

An optical transmitter is a device that converts the electrical input into an optical signal, that gets launched into a fibre for transmission. The transmitter usually comprises of digital to analog converter (DAC) and a semiconductor optical diode laser [41]. This field distribution of this optical laser source acts as a carrier for the transmission of the baseband signals. The electric field distribution of the optical carrier of amplitude (A_c) at frequency (ω_c) and phase $(\emptyset_c)$ can be represented in the time domain as:

$$X_c(t) = A_c \sin(\omega_c t + \emptyset_c) \tag{2.1}$$

The baseband or the information-carrying signal can be modulated in amplitude, known as amplitude modulation (AM), in the phase known as phase modulation (PM), or in both amplitude and phase domains. Modern-day coherent communication modulation of the baseband signal is performed in both amplitude and phase to increase the information rate. This technique is known as quadrature amplitude modulation (QAM), and we will focus on this particular modulation format throughout the thesis.

If the signal is bandlimited to a bandwidth of (B) Hz. Then the digitized samples X_k sampled at a Nyquist rate of $2B$ can be constructed to an analog time domain signal $X(t)$ by multiplying these samples with a Sinc function [42].

$$X(t) = \sum_k X_k sinc(2Bt - k) \tag{2.2}$$

Equation (2.2) in the frequency domain satisfies the condition $X(-\omega) = X^*(\omega)$, where * is the complex conjugate. The negative frequency components are redundant to the positive components. Thus, we can represent $X(t)$ in frequency domain by only considering the positive frequency components. This is known as the single sideband (SSB). Similarly, a passband signal can be represented as:

$$X(t) = X_1 \sin(\omega_c t + \varphi) + X_2 Cos(\omega_c t + \varphi) \tag{2.3}$$

Where, X_1 and X_2 are the two sidebands and ω_c is the carrier frequency and φ is the carrier phase. We can rewrite equation (2.3) by representing X_1 and X_2 as a complex baseband signal ($X_b(t)$) such that $X_b(t) = X_1(t) + iX_2(t)$. Considering the real components only, equation (2.3) can be rewritten as:

$$X(t) = Re\left(X_b(t)e^{i(\omega_c t+\varphi)}\right) \tag{2.4}$$

Where, $X_1(t)$and $X_2(t)$ are the in-phase (I) and quadrature component (Q) of the baseband signal and the signal $X_b(t)$ is known as the complex envelope of $X(t)$ [42]. The modulated signal $X(t)$ lies within the bandwidth of $\left(\omega_C - \frac{B}{2} < \omega < \omega_c + \frac{B}{2}\right)$ and can be represented as a constellation in a complex plane as shown below in Figure 2.1 (a-b).

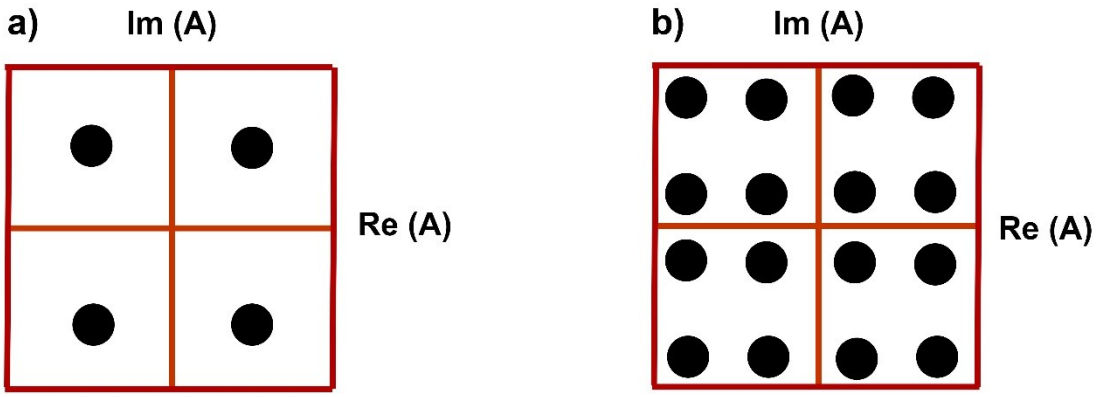

Figure 2.1 Constellation diagram for a) PM-QPSK and b) PM-16QAM signal.

2.2 Mach-Zehnder modulator

A Mach-Zehnder modulator (MZM) is an interferometric device that modulates the oncoming data stream using a high-frequency carrier signal. This interferometric device is made of heterogeneous materials such as lithium niobate ($LiNbO_3$), indium phosphide (InP), and gallium arsenide (GaAs) [43].

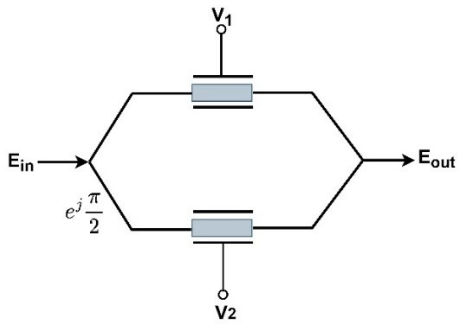

Figure 2.2 Schematic of Mach-Zehnder modulator.

Figure 2.2 illustrates the simple schematic of a dual-drive MZM which is a combination of two phase-modulators. The input optical field E_{in} is divided into two paths using a 50/50 coupler, where a phase shift of $\frac{\pi}{2}$ is added in one of the paths [44]. A phase shift is generated by applying voltages V_1 and V_2 between both the arms, changing the optical path length. The output from the two arms interferes constructively or destructively depending upon the phase of the modulated field. The output power is maximum when the difference in the phase of the two fields is 0 degrees and is minimum when the phase difference is π degree. The optical field (E_{out}) can be defined as a transfer function of the input optical field (E_{in}) [43] .

$$E_{out} = H(V_1, V_2)E_{in} \tag{2.5}$$

$$E_{out} = \frac{E_{in}}{2}\left\{\left(e^{j\emptyset_1(V_1)} + e^{j\emptyset_2(V_2)}\right)\right\} \tag{2.6}$$

$$H(V_1, V_2) = \frac{1}{2}\left(e^{j\emptyset_1(V_1)} + e^{j\emptyset_2(V_2)}\right) \tag{2.7}$$

Where, $H(V_1, V_2)$ is the MZM transfer function and is dependent on the phase of the two optical fields, E_{in} the input optical field to the MZM can be represented as E_{in}=$\sqrt{P_{in}}e^{j2\pi f_c t}$, where, P_{in} is the power of the input optical field and f_c is the central frequency of the carrier. $\emptyset_1$ and $\emptyset_2$ are the optical phase of both the field, which is dependent on the drive voltage V_1 and V_2. These optical phases can be represented as:

$$\emptyset_1(V_1) = \frac{\pi}{V_{1\pi}}V_1, \quad \emptyset_2(V_2) = \frac{\pi}{V_{2\pi}}V_2, \tag{2.8}$$

Here, $V_{1\pi}$ and $V_{2\pi}$ are the voltage required for a π phase shift in the upper and lower arm of an MZM. Now putting the values of $\emptyset_1(V_1)$ and $\emptyset_1(V_2)$ in equation (2.7) the transfer function can be rewritten as:

$$H(V_1, V_2) = \frac{1}{2}\left(e^{j\frac{\pi}{V_{\pi 1}}V_1} + e^{j\frac{\pi}{V_{\pi 2}}V_2}\right) \tag{2.9}$$

The drive voltage V_1 and V_2 can be defined using the following equations [45]:

$$V_1 = V_{dc1} + \frac{V_{Pk1-Pk1}}{2}\sin(2\pi ft) \tag{2.10}$$

$$V_2 = V_{dc2} + \frac{V_{Pk2-Pk2}}{2}\sin(2\pi ft) \tag{2.11}$$

Where, V_{dc1} and V_{dc2} are the dc voltages applied to the two arms of the MZM that induces a phase shift in one of the MZM arm, $V_{Pk1-Pk1}$ and $V_{Pk2-Pk2}$ are the peak-to-peak voltages in the two arms of MZM and f is the frequency of the RF signals. Pure phase modulation is achieved when the conditions are $V_{\pi 1} = V_{\pi 2} = V_{\pi}$ and $V_1 = V_2 = V$. In such a case equation (2.9) reduces to

$$H(V_1, V_2) = exp\left(j\frac{\pi}{V_{\pi}}V\right) \tag{2.12}$$

This transfer function now represents a phase modulator mode, and the output optical field is given by:

$$E_{out} = \frac{E_{in}}{2}\left(e^{j\frac{\pi}{V_{\pi}}V}\right) \tag{2.13}$$

Similarly, when opposite voltages are applied to both arms such that $V_1 = -V_2 = \frac{V}{2}$, then equation (2.9) reduces to:

$$H(V_1, V_2) = cos\left(\frac{\pi}{2V_{\pi}}V\right) \tag{2.14}$$

This condition is known as pure amplitude modulation with no frequency chirp and the output optical field becomes:

$$E_{out} = \frac{E_{in}}{2}\, cos\left(\frac{\pi}{2V_{\pi}}V\right) \tag{2.15}$$

An MZM operates in an asymmetric mode when $V_1 = -\delta V_2 = V$, in such a condition the transfer function and the output electric field can be represented as

$$H(V_1, V_2) = \frac{1}{2}\left(e^{j\frac{\pi}{V_{\pi}}V} + e^{-j\frac{\pi V}{V_{\pi}\delta}}\right), \qquad E_{out} = \frac{E_{in}}{2}\left(e^{j\frac{\pi}{V_{\pi}}V} + e^{-j\frac{\pi V}{V_{\pi}\delta}}\right) \tag{2.16}$$

Where δ is the in an integral multiple. The power transfer function (H_P) in a chirp-free condition can be obtained by squaring equation (2.14) and applying general trigonometry.

$$H_P(V_1, V_2) = \frac{1}{2} + \frac{1}{2} cos\left(\frac{\pi}{V_\pi} V\right) \tag{2.17}$$

Figure 2.3 show the optical field and power transfer function with a minimum, quadrature, and maximum operating point.

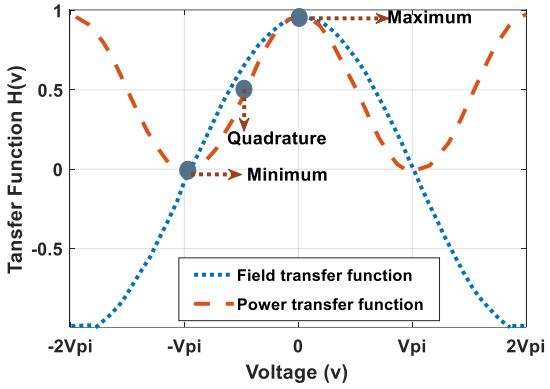

Figure 2.3 MZM field and power transfer function with a minimum, quadrature, and maximum transmission point.

2.2.1 Optical IQ Modulator

An IQ modulator is a parallel combination of two MZM with a phase shift of $\frac{\pi}{2}$ in one of the arms [44]. The simple schematic of the IQ modulator is illustrated in Figure 2.4.

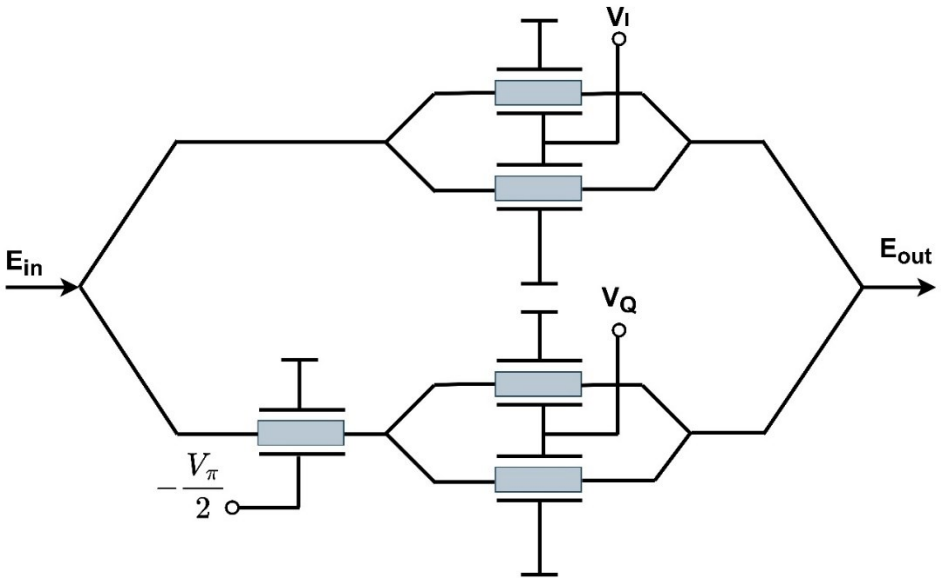

Figure 2.4 Simple schematic of IQ modulator with in-parallel MZM and phase modulator.

From the above schematic, we can see that the IQ modulator consists of two MZM in-parallel driven with a push-pull condition ($V_1 = -V_2$) and an additional phase modulator with a phase shift of $\frac{\pi}{2}$ [44]. The incoming optical signal is split into two paths, where a phase shift of $\frac{\pi}{2}$ is applied in the lower arm, this is known as the quadrature component of the signal. In the upper

arm, where no phase shifter is added is known as the in-phase component of the signal. Amplitude modulation is generated in each arm of the MZM under push-pull conditions by applying equal voltages (V_I) and (V_Q). The field transfer function of an MZM can be expressed as [46]:

$$H(V_I, V_Q) = \frac{1}{2}\cos\left(\frac{\Delta\theta_I}{2}\right) + \frac{1}{2}\sin\left(\frac{\Delta\theta_Q}{2}\right) \tag{2.18}$$

Where, $\Delta\theta_I$ and $\Delta\theta_Q$ represents the in-phase and quadrature-phase difference in the MZM and is equivalent to, $\Delta\theta_I = \frac{V_I\pi}{V_\pi}$ and $\Delta\theta_Q = \frac{V_Q\pi}{V_\pi}$ respectively.

The amplitude and phase of the signal after IQ modulation can be obtained from the transfer function and the modulated signal after an IQ modulator can be represented as a function of amplitude (A_{IQ}) and phase $(\Delta\theta)$ in a complex plane as [47].

$$A_{IQ} = \frac{1}{2}\sqrt{\cos^2(\Delta\theta_I) + \sin^2(\Delta\theta_Q)} \tag{2.19}$$

$$A_{IQ} = \frac{1}{2}\sqrt{\cos^2\left(\frac{V_I\pi}{V_\pi}\right) + \sin^2\left(\frac{V_Q\pi}{V_\pi}\right)}$$

$$\Delta\theta = arg\left(cos\left(\frac{V_I\pi}{V_\pi}\right), sin\left(\frac{V_Q\pi}{V_\pi}\right)\right) \tag{2.20}$$

2.3 Optical fibre

Optical fibres are the medium of transmission for information-carrying signals, these are thin wires of glass, of the order of hundreds of microns in size that are bundled together to transmit optical signals over a long distance. The central section of the optical fibre is known as the core and is the medium that propagates information in the form of light pulses. The core is surrounded by another glass layer called the cladding, whose refractive index is slightly lower in comparison to the refractive index of the core. The cladding is surrounded by an additional coating layer, acting as a protective layer from physical damage and this layer is further covered with a jacket layer for recognization of the fibre type [48]. The standard design of an optical fibre is illustrated in Figure 2.5 (a-b)

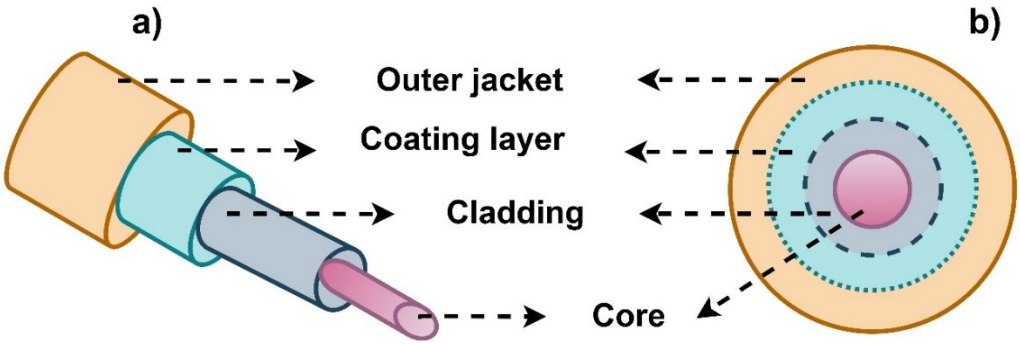

Figure 2.5 Schematic of optical fibre; a) three-dimensional and, b) two-dimensional view

2.3.1 Working principle of optical fibre

Optical fibre works on the principle of total internal reflection of light (TIR), a light-guiding phenomenon that occurs at the interface between the core and fibre cladding. Due to the high refractive index of the core the light propagating through the fibre confines within the core under the condition of a fibre critical angle (θ_c).

When light propagates from a high refractive index medium to a low refractive index medium it undergoes both reflections as well as refractions. The critical angle is the angle between two interfaces where the reflected light traverses at an angle of 90° to the incident medium. If the incident angle (θ_i) is greater than (θ_c) then the light pulses will confine within the medium with no refraction. The phenomenon of the confinement of light within a medium of high refractive index is known as TIR and is the guiding principle behind the propagation of optical waveguides in a fibre. The working phenomenon of an optical waveguide in fibre under TIR is illustrated in Figure 2.6 (a-b).

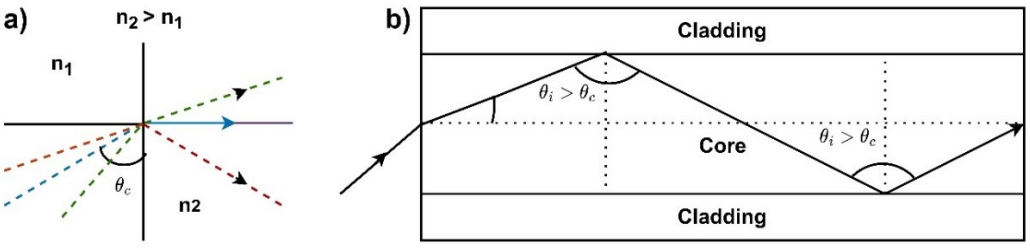

Figure 2.6 Light propagation from a higher to lower refractive index medium a) total internal reflection principle b) total internal reflection in optical fibre.

2.3.2 Classification of optical fibre

Optical fibres are primarily classified based on two different characteristics.

- Based on the number of propagating modes.
- Based on the refractive index profile.

2.3.2.1 Classification based on the number of modes

The number of modes propagating through a fibre is determined by a parameter known as the normalized frequency (V). An optical fibre can propagate only a single electromagnetic field known as modes through the core if the V number is < 2.405. This type of fibre is known as standard single-mode fibre (SSMF). Correspondingly if the V number is > 2.405, then fibre can propagate more than one mode and these categories of fibres are known as multimode fibres. The general expression of normalized frequency (V) can be represented as.

$$V = \frac{2\pi a}{\lambda}(n_1^2 - n_2^2)^{\frac{1}{2}} \tag{2.21}$$

Where a is the core radius, λ is the wavelength of the light and n_1, n_2 are the refractive index of the core and the cladding.

2.3.2.2 Classification based on refractive index profile

Optical fibres can be further categorized into two types based on the refractive index variation of the fibre core. These two types are,

- Step Index fibres
- Graded index fibres

In step-index fibres, the refractive index remains constant across the core of the fibre and then drops down rapidly at the core-cladding interface. However, in a graded-index fibre, the refractive index varies as a function of the core diameter. The refractive index is maximum at the centre of the core, then gradually falls off with an increase in radial distance and gets minimum at the interface between the core and cladding.

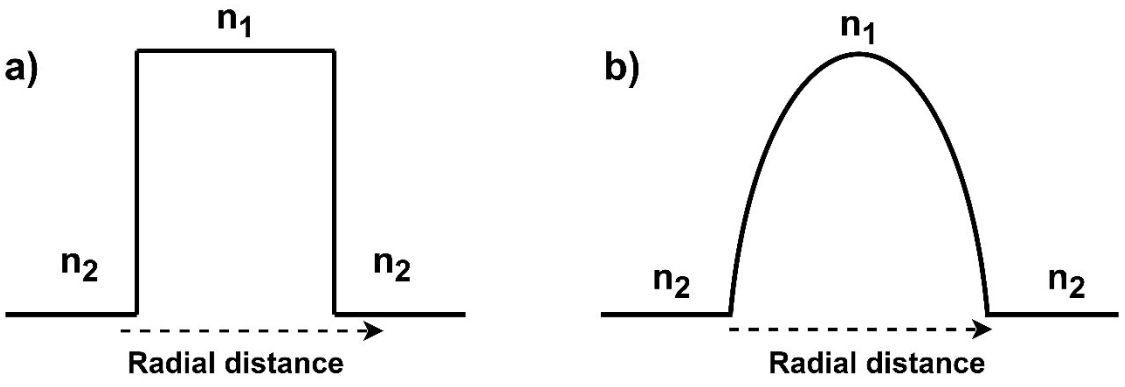

Figure 2.7 Refractive index profile of a) step index fibre b) graded index fibre

Figure 2.7 (a-b) illustrates the refractive index profile of a step and graded-index fibre. Here, n_1 and n_2 are the refractive indexes of the fibre core and cladding.

2.4 Transmission impairments in optical fibre

When signals propagate through an optical fibre, they are subjugated to various linear and nonlinear impairments. Impairments such as attenuation, chromatic dispersion, and polarization mode dispersion (PMD) fall under the category of linear impairments that dominate when the signal power is relatively lower. On the other hand, Kerr-induced nonlinear effects such as self-phase modulation (SPM), cross-phase modulation (XPM), and four-wave mixing (FWM), also degrade the performance of the signals at high power. In addition to these effects, nonlinear Raman scattering also known as inter-channel stimulated Raman scattering (ISRS) contributes to performance degradation in an ultra-wideband WDM transmission.

The generalized signal propagation over an optical fibre can be represented by the nonlinear Schrodinger equation (NLSE) which can be written down mathematically as: [49].

$$\frac{\partial A}{\partial z} + \frac{\alpha}{2}A + j\frac{\beta_2}{2}\frac{\partial^2 A}{\partial t^2} = j\gamma|A|^2 A \tag{2.22}$$

Equation (2.22) represents a slowly varying envelope of a complex optical field $A(z,t)$ along an optical fibre, t is the time in a moving frame of reference along the pulse with a group velocity of $\left(T = t - \frac{z}{V_g}\right)$, α is the fibre attenuation coefficient for an optical field, β_2 is the group velocity dispersion (GVD) and γ is the Kerr nonlinear coefficient defined as:

$$\gamma = \frac{n_2\omega_0}{cA_{eff}} \tag{2.23}$$

Where, n_2 is the nonlinear refractive index, ω_0 is the frequency of the optical field, c is the speed of light and A_{eff} is the fibre core effective area.

However, the generalized NLSE doesn't take into consideration polarization-dependent effects such as PMD. Considering the polarization effects, the NLSE can be expressed as a vectorial representation of X and Y polarization [50,51].

$$\frac{dA_X}{dz} + \frac{\alpha}{2}A_X + j\frac{\beta_2}{2}\frac{\partial^2 A_X}{\partial t^2} = j\gamma\left(A_X^2 + \frac{2}{3}A_Y^2\right)A_X + j\frac{\gamma}{3}A_Y^2 A_X^* \exp(-2j\delta\beta z) \tag{2.24}$$

$$\frac{dA_Y}{dz} + \frac{\alpha}{2}A_Y + j\frac{\beta_2}{2}\frac{\partial^2 A_Y}{\partial t^2} = j\gamma\left(A_Y^2 + \frac{2}{3}A_X^2\right)A_Y + j\frac{\gamma}{3}A_X^2 A_Y^* \exp(-2j\delta\beta z) \tag{2.25}$$

Where, A_X and A_Y are the amplitude of X and Y polarization, $\delta\beta$ represents the wave-vector mismatch due to linear or modal fibre birefringence [49].

Due to the presence of fibre birefringence between both the polarization. The vectorized NLSE can be represented by Manakov equations by averaging the nonlinear mixing between two states of polarization [52,53].

$$\frac{dA_X}{dz} + \frac{\alpha}{2}A_X + j\frac{\beta_2}{2}\frac{\partial^2 A_X}{\partial t^2} = j\frac{8}{9}\gamma(A_X^2 + A_Y^2)A_X \tag{2.26}$$

$$\frac{dA_Y}{dz} + \frac{\alpha}{2}A_Y + j\frac{\beta_2}{2}\frac{\partial^2 A_Y}{\partial t^2} = j\frac{8}{9}\gamma(A_X^2 + A_Y^2)A_Y \tag{2.27}$$

2.4.1 Attenuation in optical fibre

When a signal propagates through an optical fibre it undergoes decay in power with an increase in the propagation distance. The extent of this power degradation depends on the wavelength of a given signal. The variation of power in an optical fibre in the axial direction Z can be expressed as follows:

$$\frac{dP}{dz} = -\alpha P \tag{2.28}$$

Where α is the attenuation coefficient of the fibre at a given wavelength. The power at any given distance Z =L can be obtained by solving the differential equation (2.28):

$$P\,(L) = P_{in}e^{-\alpha L} \tag{2.29}$$

Where, P_{in} is the power at the input section of the fibre. The attenuation coefficient (α) can be obtained by taking the difference between the input and output power of a signal when propagated through a fibre of length L. The unit of attenuation coefficient is dB/km and its logarithmic value can be expressed as.

$$\alpha\left(\frac{dB}{km}\right) = -\frac{10}{L}\log\left(\frac{P_{inp}}{P_{out}}\right) \tag{2.30}$$

Where, P_{inp} and P_{out} are the power at the input and output of a fibre of distance L. The attenuation coefficient of an optical fibre depends on the intrinsic and extrinsic factors of the fibre. The intrinsic factor mainly includes Rayleigh scattering and infrared absorption (IR) respectively. Whereas the extrinsic factor includes hydroxyl ion (OH^{-1}) ions and metallic impurities. The OH^- ions also known as water peaks, are the remnants in the manufacturing process of silica fibres, which contribute to absorption near 950, 1240, and 1390 nm. However, in modern-day silica fibres, this OH absorption is reduced by the isotopic exchange of OH^- with deuterium (D_2) [54]. These types of fibres are known as dry fibres or zero water peak fibres.

Absorption by a material at a certain wavelength corresponds to the vibrational and electronic resonances associated with the specific molecule. In fused silica molecules the vibrational resonance occurs in the infrared (IR) region (~780 nm-1mm) and the electronic resonance occurs in the ultraviolet region (~100-400 nm). In optical communication, the wavelength of operation is in the IR region and the intrinsic absorption is due to the vibrational resonance, where the absorption loss contribution is ~0.03 dB/km in the wavelength range of 1300-1600 nm [55]. The intrinsic loss due to infrared absorption is expressed as [56].

$$\alpha_{IR} = Ce^{D\lambda} \tag{2.31}$$

Where C and D are the fitting coefficients and are equal to 4.6 x 10^{-14} and 1.72 x 10^{7} [57].

Rayleigh scattering is another factor that contributes to the intrinsic loss in optical fibres. Rayleigh scattering occurs due to the microscopic fluctuation in the density of silica molecules. In the molten state the silica molecule vibrates randomly however, during the fabrication process the silica molecules are frozen into a solid form. This causes a density fluctuation leading to a small variation in the refractive index of the fibre on a scale smaller than the optical wavelength (λ). The scattered light due to this variation of refractive index is known as Rayleigh scattering and the intrinsic loss due to Rayleigh scattering can be expressed as:

$$\alpha_R = \frac{A_R}{\lambda^4} \tag{2.32}$$

Where, A_R is the Rayleigh scattering coefficient which varies from ~0.7-0.9 dB in silica fibres [58,59].

2.4.2 Chromatic dispersion in optical fibre

When an optical signal propagates through a fibre, different spectral components travel at different group velocities. This effect is known as group velocity dispersion (GVD) causing a temporal broadening of pulse and the different spectral components reach their destination at different time intervals. This effect of GVD causes signal distortion through inter-symbol interference (ISI) degrading the overall transmission performance over a longer distance.

If ω is the frequency of a spectral component with a group velocity of V_g, then the total time required to propagate through an optical fibre of length L can be calculated as $T = \frac{L}{V_g}$, where,

$$V_g = \left(\frac{d\beta}{d\omega}\right)^{-1} \tag{2.33}$$

β is the frequency-dependent propagation constant and can be represented as $\beta = \frac{n_g \omega_s}{c}$ where, n_g is the group index and is related to the fibre refractive index [49].

$$n_g = n + \omega \frac{dn}{d\omega} \tag{2.34}$$

This variation of refractive index with different frequencies causes pulse broadening as different spectral components in the pulse will travel at different velocities causing a delay in the output of the fibre. The extent of pulse broadening (ΔT) at a given frequency (ω) after propagation through a fibre of length L can be expressed as [55]:

$$\Delta T = \frac{dT}{d\omega}\Delta\omega = \frac{d}{d\omega}\left(\frac{L}{V_g}\right)\Delta\omega \tag{2.35}$$

$$\Delta T = L\frac{d^2\beta}{d\omega^2}\Delta\omega = L\beta_2\Delta\omega \tag{2.36}$$

Here, $\Delta\omega$ is the width of the pulse and β_2 is known as the GVD parameter and determines the extent of pulse broadening. In terms of wavelength λ the pulse width can be expressed as:

$$\Delta\omega = \left(-\frac{2\pi c}{\lambda^2}\right)\Delta\lambda \tag{2.37}$$

Now, replacing the $\Delta\omega$ and $\omega = \frac{2\pi c}{\lambda}$ in equation (2.35) where c is the speed of light in a vacuum, the pulse broadening can be rewritten as

$$\Delta T = \frac{d}{d\lambda}\left(\frac{L}{V_g}\right)\Delta\lambda = DL\Delta\lambda \tag{2.38}$$

Where D is known as the chromatic dispersion (CD) parameter and is equivalent to $\left(D = \frac{d}{d\lambda}\left(\frac{1}{V_g}\right) = \left(-\frac{2\pi c}{\lambda^2}\right)\beta_2\right)$. D is expressed in the units of ps/nm/km and varies with different wavelengths during propagation through an optical fibre. The wavelength at which D equals zero is known as the zero dispersion wavelength (ZDW) and for an SSMF this lies at around 1300 nm [60].

As mentioned previously distortion can cause ISI if the pulse broadening is larger than the time slot for data recovery. The effects of D are more dominant with an increase in transmission distance where the pulse broadens to large extent degrading the overall transmission performance. Hence, to mitigate the effect of dispersion different techniques were developed over time. The transmission window in an optical communication lies within the C- band (1530-1565 nm) and the value of D is ~17 ps/nm/km at 1550 nm for SSMF fibre. To minimize the effects of D in

transmission, the development of dispersion-shifted fibre (DSF) fibre was realized initially where the fibre refractive index profile was tailored to shift the ZDW from 1300 to 1550 nm [61]. However, in a WDM system with multiple carriers, DSF was not suitable due to the large accumulation of nonlinear effects such as four-wave mixing (FWM). A different approach of dispersion management was developed where accumulated dispersion in SSMF was compensated using a negative dispersion fibre at the reception. Dispersion mapping was introduced to calculate the overall accumulated dispersion for different fibre links [62]. However, these mappings were complicated to manage. Later the introduction of digital signal processing (DSP) in coherent optics paved the way to compensate for the overall accumulated dispersion in the receiver end without the addition of any special fibres [63].

2.4.3 Polarization mode dispersion in optical fibre

Polarization mode dispersion is a performance-limiting factor that is related to differential group delay (DGD) due to optical fibre birefringence. Birefringence is an optical property of a material in which the refractive index depends on the state of polarization (SOP) of the light. A single-mode fibre can support two orthogonally polarized modes simultaneously. In an ideal fibre these two modes will travel at the group velocity. However, the cylindrical asymmetry of the fibre core leads to birefringence causing these two modes to propagate at slightly group velocities [64]. In addition, external factors such as bend, twist, external stress and ambient conditions such as temperature variation also will produce birefringence in fibre. This birefringence rotates the orthogonally polarized modes in a random fashion causing output SOP to fluctuate with time [65].

Hence, a signal launched at the fibre due to the fibre random birefringence will cause both the polarization of an optical field in the X- and Y-direction to propagate at a different group velocity. This overall effect of birefringence causes a delay between the two polarization states and this delay is known as differential group delay (DGD). This delay is not constant along the length of the fibre. If the fibre is segmented into different small independent segments of equal lengths, then the birefringence across all the segments will also vary due to external factors and the ambient conditions. This will cause the DGD to change over different segments of the fibre, randomly with time as shown below in Figure 2.8 [66].

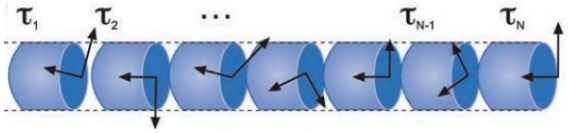

Figure 2.8 Concatenated section of random birefringent in fibres with different DGD [66].

If the instantaneous DGD is measured at the output of fibre the DGD will vary randomly. This variation in DGD can be represented by histograms showing the 'Maxwellian' probability distribution as shown below in Figure 2.9 [66].

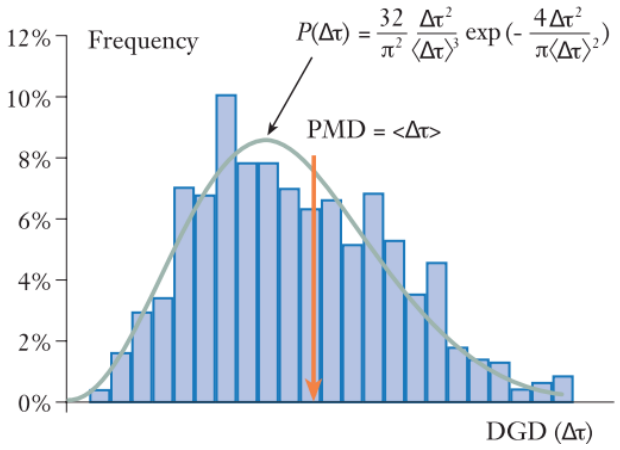

Figure 2.9 DGD distribution in a randomly birefringent optical fibre [66].

Figure 2.9 shows the frequency of occurrence of a given distribution at a different location and time instances of an optical fibre, experimentally demonstrated over a field trial by Corning Incorporated [66]. One can observe from Figure 2.9 that the distribution is governed by only one parameter i.e average DGD $(\Delta\tau)$. This average value of DGD probability distribution is known as polarization mode dispersion (PMD) of an optical fibre [66].

Experimental demonstrations with different fibre lengths have shown that the PMD of a fibre is directly proportional to the square root of fibre length (L) multiplied by a proportionality coefficient. This coefficient is known as the PMD coefficient (PMD_c) and its unit is picoseconds/square root kilometres [65].

2.4.4 Kerr-induced nonlinear effects in optical fibre

Kerr-induced nonlinearities arise in optical fibre when an intense electromagnetic wave propagates through a nonlinear medium. The confinement of high-intensity optical waves in the core of the fibre modifies the refractive index of the fibre core. This variation is due to the anharmonic response to the optical field resulting in a nonlinear susceptibility [55,67], where the refractive index changes as [49]

$$n_{i\prime} = n_i + n_2\left(\frac{P}{A_{eff}}\right) \tag{2.39}$$

Where, $n_{i\prime}$ is the modified refractive index of the core, n_2 is the nonlinear index and for silica fibre, this value is about $2.6\text{x}10^{-20}$ m^2/W, P is the optical power of a given signal and A_{eff} is the

effective core area. This variation of the refractive index gives rise to nonlinear phenomena such as self-phase modulation (SPM), cross-phase modulation (XPM), and four-wave mixing (FWM).

2.4.4.1 Self-phase modulation

This is the very modulation that can impair the transmission performance in the presence of a single channel. As explained previously power level of a signal can modify the refractive index, which can cause spectral broadening of the optical pulse during the propagation through an optical fibre [49]. This variation in the refractive index doesn't change the shape of an optical mode but rather changes the propagation constant in a nonlinear fashion and this variation can be expressed as:

$$\beta' = \beta + \gamma P \tag{2.40}$$

From equation (2.40) we can quantify that variation of the nonlinear refractive index differs for different wavelengths and the effective area of the fibre core. For SSMF the value of γ is ~1 W^{-1} km^{-1}. The new propagation constant (β') will result in a nonlinear phase shift (NPS) which can be represented as:

$$\varphi_{NL} = \int_0^L (\beta' - \beta) dz = \int_0^L \gamma P(z) dz = \gamma P_{in} L_{eff} \tag{2.41}$$

Where, $P(z) = P_{in}\exp(-\alpha z)$, and L_{eff} is the effective length of the fibre at which φ_{NL}=1 [49]. Since this NPS is self-induced within the signal itself, this phenomenon is known as self-phase modulation (SPM).

2.4.4.2 Cross-phase modulation

The variation in the nonlinear refractive index due to signal intensity generates another phase effect known as cross-phase modulation (XPM). This occurs in a WDM system when two or more channels are transmitted simultaneously [68]. The neighbouring channels interact with the channel under test causing NPS which can be given as [55].

$$\varphi_{NL} = \gamma L_{eff} \left(P_{CUT} + 2 \sum_{K \neq CUT} P_K \right) \tag{2.42}$$

Where, P_{CUT} is the power of the channel under test, P_K are the powers of any neighbouring channels and factor 2 comes from nonlinear susceptibility [49]. Equation (2.42) indicates that NPS is twice as effective as SPM from the same launch power per channel.

2.4.4.3 Four-wave mixing

The third-order nonlinear susceptibility (χ^3) in optical fibre induces a power-dependent variation in refractive index [69]. This variation gives rise to another nonlinear effect known as four-wave mixing (FWM) [67]. This effect is dominant in WDM systems when three propagating waves at frequencies ω_i, ω_j and ω_k interacts in a nonlinear medium to give rise to the fourth frequency ω_F. This new frequency is related to the three frequencies by the relation $(\omega_F = \omega_i \pm \omega_j \pm \omega_k)$. Different combination of new frequencies is possible with the addition and subtraction of the three frequency components. However, these combinations can build up only under the condition of phase matching [49]. Among all the possible combinations the most significant combination is of the form $(\omega_i + \omega_j - \omega_k)$. This combination can get nearly phase-matched and the newly generated frequency at ω_F can interact with the CUT causing serious degradation if the CUT is operating near zero dispersion wavelength (ZDW). If $\omega_i \neq \omega_j \neq \omega_k$ then the process of FWM is known as non-degenerate FWM, and for combinations such as $\omega_i = \omega_j$ is known as degenerate FWM [55].

At a fundamental level, FWM can be defined as a scattering process of two photons of energy $h\omega_i$ and $h\omega_j$ whose energy is transferred to two new photons of energy $h\omega_k$ and $h\omega_F$. Using conservation of momentum, the phase matching condition can be written as $\Delta\beta = \beta_F + \beta_k - \beta_i - \beta_j$ where β is the propagation constant of the optical field. In the degenerate condition $\omega_i = \omega_j$, ω_k and ω_F can be rewritten as $\omega_k = \omega_i + \Delta\omega$ and $\omega_F = \omega_i - \Delta\omega$, where $\Delta\omega$ is the channel spacing. Using the Taylor expansion of propagation equation upto second order the propagation constant of an optical field can be approximated using the equation (2.43) [55]

$$\beta(\omega) \approx \beta_0 + \beta_1(\Delta\omega) + \frac{\beta_2}{2}(\Delta\omega)^2 \tag{2.43}$$

Where, β_0 is the propagation constant of the optical field at z=0, $\beta_1 = \frac{1}{V_g}$ is the group velocity, β_2 is the group velocity dispersion coefficient (GVD) and is related to fibre CD by the relation $\left(CD = \frac{-2\pi C}{\lambda^2}\right)$. In a nonlinear medium β_0 and β_1 cancels each other and the phase mismatch can be rewritten as an equation (2.44) [55].

$$\Delta\beta = \beta_2(\Delta\omega)^2 \tag{2.44}$$

From equation (2.44) we can see that FWM can be phase matched when $\beta_2 = 0$, hence, FWM will be significant for signal wavelengths near zero-dispersion wavelength. In addition to this when channel spacing $(\Delta\omega)$ is smaller the phase matching condition is satisfied. Hence, a lower

value of β_2 and $(\Delta\omega)$ will lead to transfer of power from neighbouring channels inducing crosstalk in the form of FWM deterring the channel performance significantly.

2.4.4.4 Nonlinearity mitigation

Several methods to reduce fibre nonlinearities have been reported over time. One of the popular methods is digital backpropagation (DBP) using inverse NLSE however, in a broadband WDM system nonlinear mitigation using DBP is not an efficient method due to carrier aliasing and computation complexity [70]. An optical way of spectral inversion is another novel technique for mitigating the nonlinear effects. This technique is known as optical phase conjugation (OPC). OPC uses the nonlinear property of fibre to create a conjugated copy of the transmitted channel [71]. The conjugated copy is created by using high-power pumps and a highly nonlinear fibre (HNLF). The optical field of a signal (E_{sig}) and the pumps (E_{pump1}, E_{pump2}) creates a new field known as idler (E_{idler}) in the HNLF fibre, with has an inverse value of fibre dispersion and negative nonlinear fibre factor [72]. By adding a OPC module after each transmission link one can compensate the accumulated nonlinearity in each fibre link. However, the efficiency of OPC depends on the symmetry of the signal power profile before and after the link [72].

2.5 Optical amplifiers

The propagation of signals through an optical fibre introduces power degradation of the signals due to the intrinsic loss of the fibre. This loss is directly proportional to the length of the transmission fibre. Hence, it is necessary to amplify the signals after a particular distance before they can be detected by a receiver. In the initial transmission system, amplification was performed using optoelectronic regenerators, where the signals were first converted to the electrical domain and were back converted to optical signals. However, these regenerators were expensive and introduces latency for WDM systems [55]. Later on, optical amplifiers were developed that could amplify the signals in the optical domain without conversion. These amplifiers were transparent to WDM signals and were independent of modulation formats. The high conversion efficiency of optical amplifiers led many scientific communities to develop optical amplifiers in the 80s and 90s and by the mid-90s optical amplifiers was deployed over transatlantic and transpacific cables [73].

The implementation of optical amplifiers has been one of the significant technologies behind high-speed fibre-optics communication systems. This technology has enabled, the transmission of data in petabits over hundreds of kilometres. The major parameters that govern the performance of optical amplifiers are the amplifier gain and the noise figure (NF). In addition to gain and NF, amplification bandwidth is another important characteristic that can determine the number of WDM channels it can amplify.

Optical amplifiers are designed to provide a dynamic range of gain for different input power levels. However, there is a limitation in the amount of gain with the amount of input power. For a very low input power, the intrinsic noise added by an amplifier can be quite large whereas, for a high input power, the gain can get saturated. The maximum output power that can be obtained from an amplifier is also known as saturated output power.

Over the period, different optical amplifiers were developed based on various dopants, semiconductor optical properties, and fibre nonlinearities. The most famous among them is the Erbium-doped fibre amplifier (EDFA) which is widely used in the current WDM systems over the C-band of the communication window. However, the booming of internet technology worldwide has led to an exhaust in the C-band, and data rate per channel as we approach the nonlinear Shannon limit [74]. Hence, different scientific communities are looking for novel data transmission technologies such as space-division multiplexing (SDM) [75] and multiband transmission (MBT) [35]. Speaking particularly on MBT the existing EDFA cannot support beyond the C- and L- bands of the optical window thereby, renewed interest in different amplification technologies has been looked forward for enabling signal amplification in the remaining bands [76].

In this section, we will present different amplifiers such as EDFA, other doped fibre amplifiers, semiconductor optical amplifiers, Fibre optic parametric amplifiers, and Raman amplifiers shown in Figure 2.10 [76]. We will discuss their working principles, design challenges, performance, bandwidth limitations, and recent progress with these amplifiers.

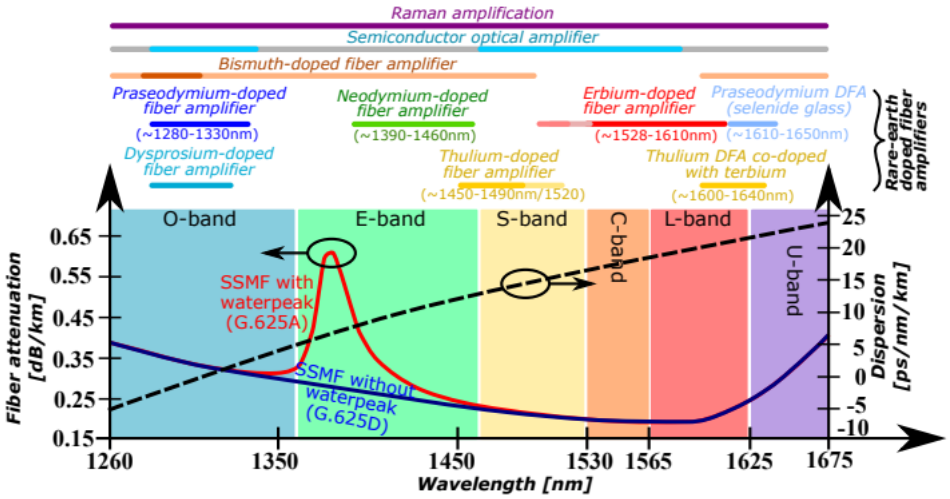

Figure 2.10 Optical amplifiers for different bands of optical communication window [76].

2.5.1 Erbium-doped fibre amplifier

Erbium-doped fibre amplifiers (EDFAs) are the most widely used amplifiers that are been implemented in current optical communication systems. This amplifier uses a specially doped

fibre with erbium ions (Er^{3+}) acting as an excitation medium. In germanium-doped silica fibres, this emission spectrum lies with the C-band (~1525-1565 nm) enabling optical amplification in the low-loss window of the optical fibre [55].

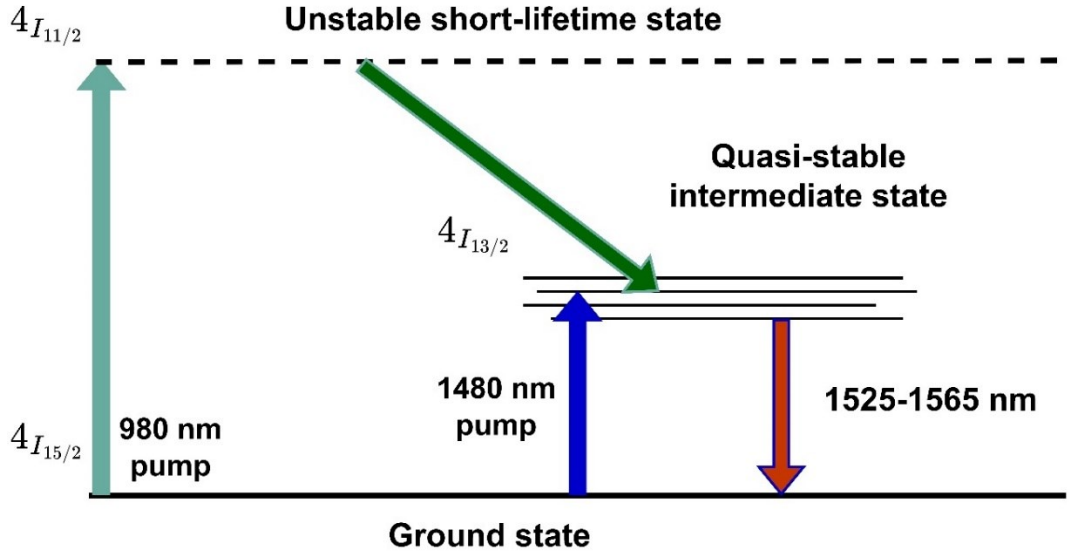

Figure 2.11 Transition of (Er^{3+}) ions when pumped at 980 and 1480 nm in an erbium-doped fibre.

Amplification using EDFA is performed by illuminating the (Er^{3+}) using a pump either at 980 or 1480 nm. A semiconductor laser diode is usually used as a pump source for the excitation of erbium ions. When the Erbium-doped fibre is pumped using a 980 nm pump the Er^{3+} ions are excited from the ground state to an unstable energy state $\left(4_{I_{15/2}} \rightarrow 4_{I_{11/2}}\right)$for a short time of a few microseconds. It then decays down to a quasi-stable state $\left(4_{I_{11/2}} \rightarrow 4_{I_{13/2}}\right)$ with a lifetime of ~8-10 milliseconds. On the other hand, when pumped using a 1480 nm laser source the Er^{3+} ions are excited from the ground state directly to a quasi-stable state $\left(4_{I_{15/2}} \rightarrow 4_{I_{13/2}}\right)$. Stimulated amplification occurs in this state due to population inversion, where the decay from the quasi-state to the ground state is slower than decay from the excitation state to the quasi-state. After a period of a few milliseconds at the quasi-state level, the (Er^{3+}) decays to the ground state radiating light in the wavelength region of ~1525-1565 nm [77].

The extent of gain that can be obtained from an EDFA depends on multiple parameters such as the erbium-doped fibre (EDF) length, core diameter, pump power and concentration of Er^{3+} ions in the doped fibre [78]. Typically, a shorter length of fibre with a high concentration of doping is desirable because for a given length of fibre the gain increases exponentially and reaches a maximum value at a particular distance followed by a sharp drop in the gain. This is because the remaining length of the EDF remains unpumped and absorbs the amplified signals causing an overall decay in gain [55].

Similarly, an EDFA efficiency depends on erbium concentration. Usually, the output power of an EDFA should increase with an increase in the doping concentration. However, the doping can be increased only to a certain amount beyond this the efficiency of an EDFA degrades significantly [79,80]. This is due to the upconversion process that gets activated in the presence of high concentration of Er^{3+} ions. This causes a non-radiative energy transfer between the erbium ions reducing the overall efficiency of the amplifier [81].

EDFAs can be configured using three different pumping schemes with respect to the direction of the signals. These configurations are forward (FW) pumping, backward (BW) pumping, and bidirectional (BI) pumping. Both FW and BW pumping configuration has similar performance in the unsaturation regime when the signal power is small. When the signal power goes too high in the saturation regime, BW pumping is a better choice due to its improved conversion efficiency [78], but it suffers from higher amplified spontaneous noise (ASE). In BI configuration, the erbium-doped fibre (EDF) is pumped using two laser diodes in both directions simultaneously. This configuration is beneficial in providing uniform small signal gain across the entire amplifier length. In practice, the most commonly used configuration for EDFA is the FW pump configuration using a 980 nm pump the general setup of which is shown below in Figure 2.12 [82].

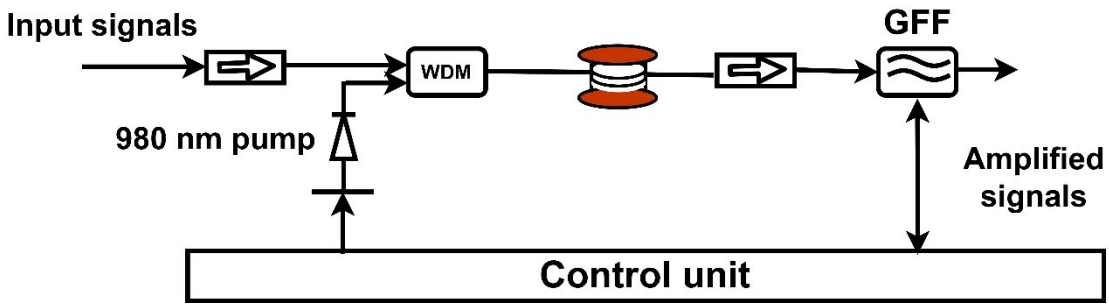

Figure 2.12 Schematic of single-stage forward pumped EDFA with pump wavelength at 980 nm

The single pump configuration includes a WDM coupler to couple the pump and the transmitted signals, which were then amplified using an EDF. A gain-flattening filter (GFF) is added to the output to flatten the gain or the power of the signals depending on the mode of operation. The GFF applies an attenuation profile to the signals which is an inverse replica of the EDF amplified spectrum to obtain an equal optical power per channel.

Investigation on combined pumping of 980 and 1480 nm has also been carried out at different inversion levels. The combination of 980 nm and 1480 nm at a low inversion level provides lower noise and the best pump power efficiency [47,83]. In addition, improvement in gain flatness, power conversion efficiency, and NF can be achieved, using cascaded multistage EDFA with intermediate optical components such as GFF and filters [84,85].

Amplification using EDFA is possible also in the L-band (~1570-1620 nm). An EDFA operating in the L-band however, requires a longer length of fibre >100 m so that the inversion level remains relatively low. Using a combination of FW pumping with a 980 nm pump and BI pumping with a 1480 nm pump broadband amplification of 50 nm (1530-1570 nm) was reported in [86]. In addition to this numerous works on the optimization of fibre length with different pumping schemes for L-band amplification have been reported [87,88].

Parallel configuration for simultaneous amplification of C- and L-band has also been developed [89,90]. In such a design both the C- and L-bands are separated using a WDM splitter and are amplified separately using EDF of appropriate length for each band. The amplified signals of the two bands are then combined using a WDM coupler. A general schematic of C+L-band parallel amplification using EDF is illustrated in Figure 2.13.

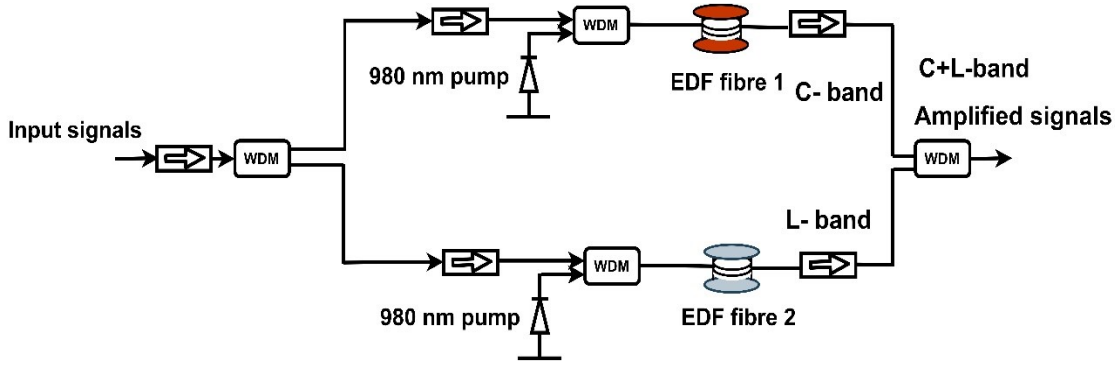

Figure 2.13 Schematic of parallel amplification with forward-pumped EDFA for C- and L- band amplification (pump wavelength @980 nm)

Broadband amplification has been realized with erbium dopants over different host materials such as tellurite, fluoride, aluminosilicate, and lithium niobate glass [91,92]. These host materials can provide varying gains over different bandwidths. However, due to the non-silica nature of the glass material, they suffer from splicing difficulties.

2.5.2 Other rare earth doped fibre amplifiers

As explained previously EDFAs can support only the C- and L-band of the optical communication window. However, with the ever-increasing demand for data inclusion of bands other than the C- and L-band of SSMF is a new strategy to meet up these demands. Amplification in these bands requires different co-dopants over silica or other host materials with emission bands beyond Er^{3+}. The emission spectra of some of the rare earth materials such as bismuth (Bi), thulium (Th), praseodymium (Pd), neodymium (Nd), and dysprosium (Dy) open up new emission bands other than the C- and L-band of the optical window [76]. However, some major challenges lie ahead in the design and manufacturing of such amplifiers in addition to their performances.

2.5.2.1 Bismuth-doped fibre amplifier

Bi-doped fibre amplifier (BDFA) is one of the interesting doped amplifiers for ultrawideband (UWB) signal amplification. Bi-doping over different host materials such as germanosilicate, aluminosilicate, and phosposilicate enables a large emission spectrum extending from 1150-1500 nm [93,94]. Numerous experimental demonstrations of the performance of BDFAs over O-, E- and S- bands have been reported. Experimental demonstrations have shown an amplification bandwidth of 115 nm over the O- and E-band with Bi-doped over phosphosilicate fibre [95]. In addition to this coherent transmission with 200G signals using all BDFA over E-band has been reported in [96]. A record gain of 40 dB with an NF of 5 dB has also been reported over the O-band using Bi over phosphosilicate fibre [96]. The performance of BDFA over O-, E- and S-band makes it a very promising candidate to merge with EDFAs for enabling UWB transmission extending from O- to L-band. However, the nature of Bi- active centres over phosphosilicate and aluminosilicate fibre are still not very clear, and also the dependency of BDFAs on temperature during fabrication causes unknown infrared radiation leading to absorption in the excited states [97,98].

2.5.2.2 Neodymium-doped fibre amplifier

Neodymium-doped fibre amplifier (NDFA) is another doped amplifier potential of generation amplification in the E- band. This amplifier can produce a gain in the larger part of the E-band with an experimental demonstration showing an amplification bandwidth of ~100 nm from 1350-1450 nm [99]. The absorption spectrum of this amplifier lies near 800 nm with a strong emission spectrum near 920, 1060, and 1350 nm [76]. The power conversion efficiency (PCE) is lower in the E-band due to the strong ASE emission near 920 and 1060 nm. However, with techniques such as wavelength selective filter and scalable waveguide design using microstructured cavity, the ASE near 920 and 1060 nm can be suppressed improving the performance in the E- band [100,101].

2.5.2.3 Thulium-doped fibre amplifier

Thulium-doped fibre amplifier is another interesting amplifier that can amplify signals in the S-band of the communication window (~1470-1520 nm). Amplification with TDFA using a four-level system provides better noise performance. However, with a standard single pumping scheme, the excitation is directly from the ground state to the metastable state. This is because the lifetime of the second energy state is greater by nine times in comparison to that of the metastable state [76]. Hence, an auxiliary pump is added for up-conversion in addition to the main pump causing absorption to occur from both the ground and the second energy state [102]. With the use of auxiliary pumps, PCE of 48% has been reported [103].

Also with different host materials such as tellurite, fluoride, silicate, etc the gain bandwidth of TDFA can be varied over the S-band (1480-1530 nm) and S^+-band (1450-1480) [104].

2.5.2.4 Praseodymium-doped fibre amplifier

Praseodymium-doped fibre amplifier (PDFA) can be used for the amplification of O-band signals. In this amplifier signal amplification occurs due to the transition from metastable state to the second energy state [76]. Only a single wavelength band around 1030 nm is available to provide an emission spectrum near O-band (1260-1360 nm) [105]. Since the absorption spectrum of the pump is ten times smaller than that of the emission spectrum, the fraction of pump power absorbed by the dopant is much smaller in comparison to other doped amplifiers [105]. Due to the low pump power absorption, amplification using PDFAs requires very high pump powers decreasing the overall lifespan of the amplifier.

2.5.2.5 Dysprosium-doped fibre amplifier

Dysprosium-doped fibre amplifier (DYFA) like PDFA is another optical amplifier that can amplify optical signals in the O-band. Unlike PDFA with has a single absorption band near 1030 nm, DYFA has eight narrow and intense absorption bands [106]. Also, DYFA requires shorter fibre length in comparison to PDFA for the same concentration of doping [76]. However, the PCE of this amplifier is smaller in comparison to PDFA due to its short lifetime of the metastable state making it still a challenge for implementation in coherent WDM systems.

Many of the above-mentioned doped-fibre amplifiers are not commercially available and many are not tested over real-time optical networks. However, experimental and theoretical studies have shown their potential to be part of the next-generation communication system. There are still many challenges in the design and development of these rare-earth doped amplifiers before they can be launched in the telecom market. Nevertheless, the limitations of these amplifiers also motivate the scientific community to conduct further research for improving their performance before they can be implemented for future optical communication systems.

2.5.3 Semiconductor optical amplifier

A semiconductor optical amplifier (SOA) is another category of optical amplifier that differs from other fibre-based amplifiers in terms of size, compactness, and operating principle. The working principle of SOA is similar to that of a semiconductor laser diode without any optical feedback. The operation of SOAs is based on electron transition from the conduction band to the valance band, where signals are amplified due to electron-hole recombination in the P-N junction of the semiconductor material [107]. The gain medium of SOA is usually a bulk composition of heterogeneous materials such as Gallium arsenide (GaAs), Indium phosphide (InP), or an alloy of both compounds [108]. Unlike other optical amplifiers, where energy for exciting electrons is

provided using a laser source, in SOAs this energy is provided electrically. Population in the conduction band is achieved using current injection to the active medium, and maximum gain occurs when the energy exceeds the energy band gap between the conduction and valence bands [76]. SOAs are compact when compared to other optical amplifiers making them very handy and flexible for implementation in integrated photonics.

Confinement of the optical wave in SOAs is achieved by sandwiching the active medium between two cladding layers of low refractive index. To prevent end-reflections SOAs are usually coated with anti-reflection coatings [109]. In SOA the amount of gain depends on the carrier density in the conduction band and the amount of injected current. However, the gain can be optimized using carrier-confining nanostructures such as quantum wells and quantum dash/dot [108]. With appropriate design and composition of the active material, SOAs can be operated over a wide range of wavelengths with a gain bandwidth of ~100 nm [110].

However, there are certain limitations with SOAs which prevents their widespread operation in WDM transmission system.

2.5.3.1 SOA limitations and progress

The coupling of light into SOAs active medium is very challenging as it is not a fibre-based amplifier. This introduces a high coupling loss and limits the overall gain of the signals. SOAs also have higher NF in comparison to other doped amplifiers and exhibit nonlinear responses to WDM signals [108]. These nonlinear distortions can have adverse effects on pluggable transceivers.

Another important characteristic of SOAs is the short lifetime of the injected carriers in the order of nanosecond to picosecond. Hence, the response time of SOAs is very fast and the gain fluctuates with varying input power at such a short time scale [108]. This gain fluctuation leads to phase distortion, inducing crosstalk between the neighbouring WDM signals [111]. SOAs operating in the saturation regime are affected by the dynamic behaviour of the transmitted bits. This phenomenon is known as the bit-pattern effect [112], causing the SOA output power to fluctuate with different bit patterns [113].

The NF of SOAs is larger than EDFAs by ~3 dB with typical values lying in the range of 6-8 dB. This is due to the larger contribution from the spontaneous emission factor (n_{sp}) [55].

$$n_{sp} = \frac{N_2}{N_2 - N_1} \tag{2.45}$$

Where, N_2 and N_1 are the population of the ground and excited state respectively. For ideal amplifier n_{sp} is equal to 1 but for most practical amplifiers this value is >1. In addition to the spontaneous emission, additional contributions due to internal losses such as free carrier

absorption and scattering losses also degrade the NF. Different methodologies such as alteration of confinement factor [114], vertical cavity SOAs [115], and the use of lateral lasing to shape the carrier density profile have been proposed to minimize the NF [116]. However, the implementation of such techniques in SOAs adds other disadvantages such as reductions in optical gain and bandwidth [117].

SOAs are also polarization sensitive, causing the gain to differ by an amplitude of 5-8 dB between the transverse electric (TE) and transverse magnetic (TM) modes [55]. This makes the amplifier sensitive to the state of polarization (SOP) which is undesirable in modern coherent transmission systems. However, in current SOAs the gain difference has been reduced to <1 dB by tailoring the optical cavity structure [118,119]. In addition to optical amplification, SOAs can also be used for other optical applications such as wavelength conversion using cross-gain and cross-phase modulation, fast optical switching, optical phase conjugation (OPC), gating, and optical detection [108,120]

Even with these limitations, the compact size and flexibility of SOAs to cover wide bandwidth make them very attractive for ultrawideband communication. Experimental demonstration with SOAs for ultrawideband transmission has shown an amplification bandwidth of over 100 nm, with an achieved data rate of 115 Tb/s, up to 100 km [121]. Recently experiments with hybrid combination of SOA and Raman amplifier have also been demonstrated over an unrepeated transmission system, where a net throughput of 80.2 Tb/s and 99.35 Tb/s was reported over a transmission distance of 257.5 km [122,123].

2.5.4 Fibre optic parametric amplifier

Fibre optic parametric amplifier (FOPA) is another interesting amplifier that is based on the third-order Kerr nonlinearity in optical fibre. The working principle of FOPA is based on four-wave mixing, over a short length of highly nonlinear fibre (HNLF) with a nonlinear coefficient (γ) of ~$10W^{-1}km^{-1}$. This HNLF is pumped using one or two high-power laser sources at frequencies of ω_{P1} and ω_{P2} near ZDW of the HNLF. When a weak signal at a frequency ω_s is injected into the HNLF, the co-propagating pump generates a new wave known as idler at a frequency ω_i which grows along with it. The idler spectrum is a mirror image and complex conjugate of the signal whose position to the centre frequency ω_c is equal to $(\omega_{P1} + \omega_{P2})/2$ [124]. The spectral representation of signal and idler with one and two pumps is illustrated in Figure 2.14 (a-b).

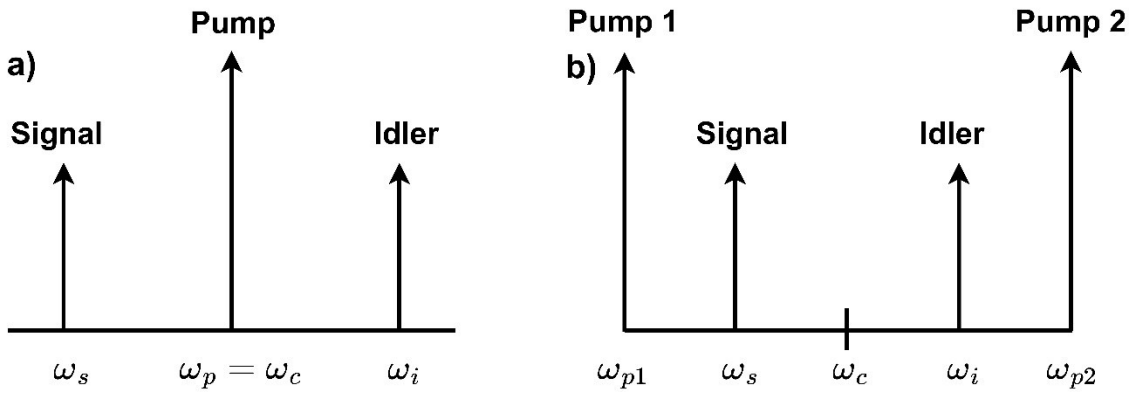

Figure 2.14 FOPA output spectra for the pump, signal, and idler with a) single pump system; b) two-pump system [124].

The gain bandwidth and the amount of gain in FOPA depend on the zero-dispersion wavelength of the HNLF used for the parametric process. It is necessary to operate the pumps in the region such that ω_c is close to ZDW, where the chromatic dispersion (CD) vanishes i.e. $\beta^2(\omega_c) = 0$. The fourth-order dispersion $\beta^4(\omega_c)$ determines the gain bandwidth of the FOPA and scales as $\left(\frac{\gamma P_{pump}}{\beta^4(\omega_c)}\right)^{1/4}$ where, P_{pump} is the pump power [124]. Hence, fibre with a higher value of non-linear coefficient and lower value of fourth-order dispersion $\beta^4(\omega_c)$ are desirable for increasing the gain bandwidth of FOPA. In addition to this higher value of pump, powers can also increase the gain bandwidth of FOPA.

FOPA can be operated in two different modes

- Phase insensitive parametric amplifier (PIA)
- Phase sensitive parametric amplifier (PSA)

2.5.4.1 Phase insensitive parametric amplifier

In this mode of operation, the only waves inserted into HNLF are the pumps and the signal. In this case, the FOPA gain is independent of the relative phase of the signal to the pumps. The gain of PIA can be represented as $G_{PIA} = \cosh^2\theta$ where $\theta = \gamma P_{pump} L$ (L: length of the gain fibre) [125]. In this mode, the performance of FOPA is very similar to that of EDFA. Experimental demonstrations have shown a record gain of 70 dB with one pump using PIA [124].

2.5.4.2 Phase sensitive parametric amplifier (PSA)

In this configuration, in addition to the signal and pumps, an additional idler beam is injected into the gain fibre. In PSA the signals and the idler waves are added coherently in a similar way as the local oscillator and a modulating signal adds up in a coherent receiver. The in-phase components between the signal and idler add up constructively while the out-of-phase components add up destructively. Similarly, the noise components add up constructively in half while the other half

cancels out destructively. Due to the cancellation of the noise components, a very low NF can be obtained using PSAs. Reports have shown NF of 1.1 dB with 26 dB gain i.e. a number well below the 3 dB quantum limit of high power amplifier [126].

Since the gain in PS-FOPA depends on the relative phase of the waves, appropriate phase-matching conditions need to be generated. Techniques such as phase-locked loop (PLL) and phase modulation are generally implemented to maintain optimal phase conditions [125]. In a single pump configuration, the signal and idler are located symmetrically around the pump. Similarly, multiple pairs of signal-idler can interact with the pump enabling WDM signal amplification [127].

2.5.4.3 FOPA limitations and progress

FOPA presents several interesting features such as high gain, low NF, high output power, and high bandwidth that are very suitable for coherent WDM systems. However, certain limitations halt the implementation of FOPA in commercial-grade WDM systems.

One of the serious performance limiting factors in FOPA is stimulated Brillouin scattering (SBS). Due to the requirement of the high pump of powers for operating FOPAs, the pump powers can easily exceed the Brillouin threshold of silica fibre. In such a scenario all the pump power will be reflected without any signal amplification. Hence it is necessary to reduce the effectiveness of SBS by a large amount [124]. Techniques such as phase modulation (PM) of the pump are used to broaden the pump spectrum [128]. However, PM also modulates the phase-matching condition as the pump frequency gets modulated. This indirectly modulates the signal gain and induces noise to the signal [124].

The shape of the gain spectrum in FOPA also varies from one spool to another even with identical fibre types. This is due to the lack of longitudinal uniformity in different fibre spools, which leads to a spatial modulation of the dispersion parameter altering the gain profile. Hence, it is essential to tailor novel fibre designs with minimal sensitivity of dispersion to diameter fluctuations [129].

The gain of FOPAs also depends on the SOP of the modulated signals. Hence, if the modulated signals are polarization multiplexed or if the SOP of the signals fluctuates during transmission, then the gain of FOPA for both polarizations is not equal. This effect can be significant in PDM higher-order modulated signals, which will eventually degrade the overall transmission performance. Numerous methodologies have been proposed to mitigate the polarization diverse gain. One of the proposed techniques for 1-pump FOPA is, splitting of the X- and Y- polarization using a polarization beamsplitter (PBS), followed by amplification of two polarization independently with identical FOPAs using a single fibre loop [130]. Although this method is economical, it can induce some nonlinear cross-talk at higher gain due to XPM and SBS.

The same technique can also be applied for a 2-pump FOPA, this will result in a flatter gain profile in comparison to a 1-pump FOPA. However, the pump power required using this method is three times more in comparison to 1-pump FOPA, if the pumps are co-polarized, making SBS suppression more complicated.

Despite of above-mentioned limitation, numerous experimental demonstrations has shown the potential of FOPA for wideband and access networks. In addition to the commercial C- band, transmission using polarization-insensitive FOPAs has been demonstrated over the S- and L-band with a gain bandwidth of 22 and 35 nm [131,132]. Due to the fast response time in the order of femtoseconds (fs), FOPAs are very attractive for burst modes in access networks [133]. In terms of gain bandwidth, a flat gain of 23.5 +/- 1 dB over 100 nm using 2-pump FOPA has been reported in [134]. Nevertheless, the progress of FOPA in both PIA and PSA configurations, makes it also a potential candidate, like other doped and undoped amplifiers for future optical communication systems.

2.5.5 Raman amplifier

Raman amplifiers work on the principle of stimulated Raman scattering (SRS), which is an inelastic scattering that occurs between the pump photon and the molecules of silica fibre. A new photon is generated near the signal frequencies, that are downshifted from the pump frequency. This process is known as stimulated Raman scattering (SRS) and in silica-based fibre, this phenomenon can be used to amplify the propagating signals. The peak Raman gain spectrum occurs at approximately 13 THz (~100 nm) downshifted from the pump frequency. The dynamics of this amplifier can provide arbitrary gain across a large bandwidth of the optical communication window. However, there are a few design challenges, as well as performance-limiting factors that can degrade the overall transmission performance in a Raman, amplified coherent system. To study this amplifier in detail we have a dedicated chapter (Chapter 3) specifically for this amplifier, explaining in detail its working principle, design challenges, limitations and recent progression with this amplifier.

2.6 Optical receivers

An optical receiver is a device that converts an optical signal into an electrical signal for data processing. It is an essential component in optical communication as it determines the performance of a transmitted signal. Optical to electrical conversion is performed using either a homogeneous or heterogeneous P-N junction material under reverse biasing. Initially homogenous germanium (Ge) based photodetectors were employed for direct detection, however, they deter in performance due to large dark currents. Later heterojunction-based semiconductors with materials such as Indium-gallium-arsenide (InGaAs) and Gallium-arsenide (GaAs) with tailored bandgaps were developed to improve the conversion efficiency. The critical parameters

that are desirable for the optimal performance of detectors are fast responsivity, high quantum efficiency to convert photons into electrical current, and large operating bandwidth.

When an incident photon of energy $h\upsilon$ exceeds the energy band gap of the material an electron-hole pair is generated in the semiconductor material after absorption. The electrons and holes flow through the material due to the applied bias voltage generating an electric current. This generated current is known as photocurrent I_P and can be represented as [55]:

$$I_P = RP_{in} \tag{2.46}$$

Where, P_{in} is the incident power to the photodetector and R is known as the responsivity of the photodetector.

The quantum efficiency of a photodetector in terms of responsivity can be represented as:

$$\eta = \frac{I_P/q}{P_{in}/h\upsilon} = \frac{h\upsilon}{q}R \tag{2.47}$$

Using equation (2.47) the responsivity R can be rewritten as:

$$R = \frac{\eta q}{h\upsilon} \sim \frac{\eta\lambda}{1.24} \tag{2.48}$$

The quantum efficiency η depends on the absorption coefficient (α) of the semiconductor material and the power absorbed by the semiconductor material of width W. The absorbed power can be written as:

$$P_{abs} = P_{in} - P_{tr} \tag{2.49}$$

Where, P_{tr} is the power transmitted through the semiconductor material and equal to $P_{abs} = P_{in}\exp(-\alpha W)$. The electron-hole pairs are generated in the depletion region due to the power absorbed, thus the quantum efficiency can be written as

$$\eta = \frac{P_{abs}}{P_{in}} = 1 - \exp(-\alpha W) \tag{2.50}$$

Another important parameter that governs the performance of an optical detector is the rise time T_R and the electrical bandwidth. Rise time is the total time required by the optical detector to convert the incident photon into electrical current. In an RC circuit, it is the time required for the current to rise from 10 to 90 %. In photodetector, this corresponds to the time of the photocurrent and can be written as [55].

$$T_R = \ln(9)(\tau_{tr} + \tau_{RC}) \tag{2.51}$$

Where, τ_{tr} is the transit time and τ_{RC} is the time constant for an equivalent RC circuit. Similarly, the bandwidth Δf of a photodetector, related to the transit and time constant is given as [55].

$$\Delta f = \frac{1}{[2\pi(\tau_{tr} + \tau_{RC})]} \tag{2.52}$$

2.6.1 Direct detection

This detection procedure is used for binary intensity modulated signals of low data rates. The receiver front comprises a photodiode that converts the input bit stream into a time-varying electrical signal. The electrical signals are then amplified using a preamplifier, which is mostly a trans-impedance amplifier (TIAs).

The signals are then linearly channelized using a high-gain amplifier and a low-pass filter for filtering the unwanted noise without introducing inter-symbol interference (ISI). The signals are then passed through a decision circuit and a clock recovery circuit for data synchronization and recovery. The schematic for direct detection of an intensity-modulated signal is illustrated in Figure 2.15.

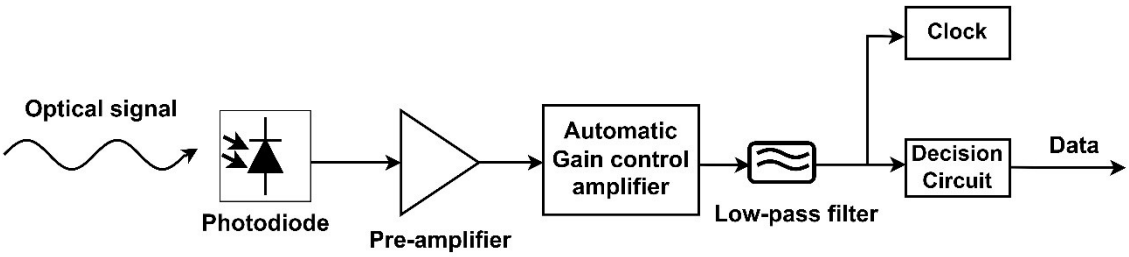

Figure 2.15 Schematic of optical receiver for direct detection

2.6.2 Coherent detection

Coherent receivers are the main building block of coherent fibre optics communication systems [135]. While conventional optical receivers with photodiodes can only extract the amplitude of a signal. Coherent receivers can extract both the phase and amplitude of a modulated signal. In addition to this, polarization information of the signal can also be extracted by splitting the signal and local oscillator (LO) power using a polarization beam splitter (PBS) [136].

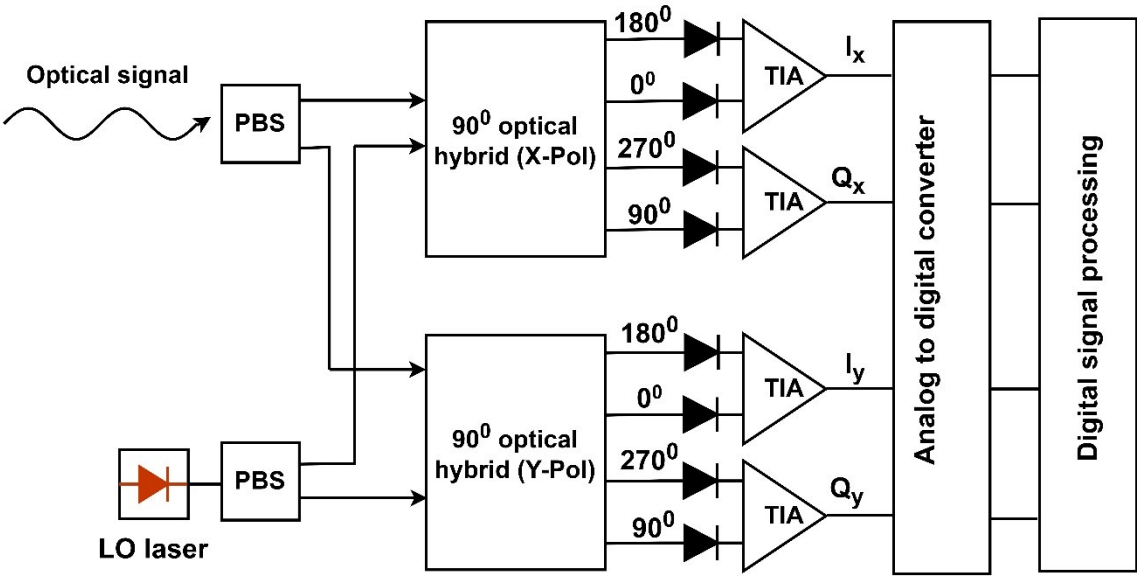

Figure 2.16 Schematic diagram of a polarization-diverse coherent optical receiver. LO: local oscillator; PBS: polarization beam splitter; TIA: trans-impedance amplifier.

Figure 2.16 shows the schematic of a polarization-diverse optical coherent receiver. The polarization multiplexed optical signal is split into two orthogonal polarizations (X and Y) using a polarization beam splitter (PBS). A narrow linewidth external cavity laser (ECL) is used as a local oscillator (LO) which also gets split using a PBS and couples with the optical signal using a 90° optical hybrid. The electric field distribution of the signal and LO oscillator can be expressed using the below equations [55].

$$E_s = A_s \exp\left[-i(\omega_s t) + \emptyset_s\right] \tag{2.53}$$

$$E_{LO} = A_{LO} \exp\left[-i(\omega_{LO} t) + \emptyset_{LO}\right] \tag{2.54}$$

Where, A_s, ω_s, and $\emptyset_s$ are the amplitude, frequency, and phase of the signal and A_{LO}, ω_{LO}, and $\emptyset_{LO}$ are the amplitude, frequency, and phase of the local oscillator. Correspondingly, the optical power incident to the photodetector is a combination of the signal and the local oscillator field distribution, which can be given by [137].

$$P = |E_S + E_{Lo}|^2 \tag{2.55}$$

$$P(t) = P_s + P_{LO} + 2\sqrt{P_s P_{LO}} cos(\omega_{IF} t + \emptyset_s - \emptyset_{LO}) \tag{2.56}$$

P_s and P_{LO} are the powers of the signal and LO, ω_{IF} is the frequency difference between the signal and LO. The linear frequency difference between the signal and LO is known as an intermediate frequency (IF) and is equal to $\nu_{IF} = \omega_{IF}/2\pi$. Coherent detection can be performed in two ways homodyne detection and intradyne detection.

In homodyne detection, the frequency of the LO overlaps with the frequency of the optical carrier. In such a scenario the IF equals zero. It means the received optical power $P(t)$ will comprise only the phase term of equation (2.56). Homodyne detection improves the received signal-to-noise ratio (SNR). However, in homodyne detection, the difference in the phase between the signal and LO needs to be constant, but practically both $\emptyset_s$ and $\emptyset_{LO}$ will vary with time in random fashion. Hence, it is necessary to implement additional circuitry such as a phase-locked-loop (PLL) to maintain a constant difference between $\emptyset_s$ and $\emptyset_{LO}$. However, the implementation of PLL is complex for fast coherent detectors.

In intradyne detection, the carrier frequency is first down-converted into intermediate frequency such that the frequency difference between the LO and the signals is <1 GHz [55,138]. The SNR in intradyne detection is lower by a magnitude of 2 to 3 dB in comparison to homodyne detection. However, the receiver design is much simpler as there is no requirement for PLL in this method. Using a stable and narrow linewidth laser source for carrier and LO the phase fluctuations can be suppressed [55].

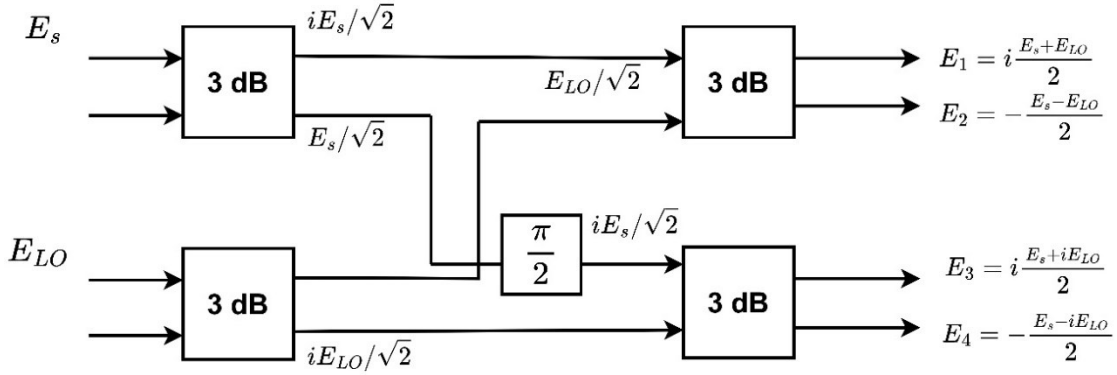

Figure 2.17 Schematic of a 90° optical hybrid

The internal schematic of the 90° optical hybrid with output field distribution is illustrated in Figure 2.17. The input signal and the LO are split using a 2x2 3 dB coupler. A 90° phase shifter is added to one of the arms of a 3 dB coupler. The output of the signals and the orthogonal outputs from the LO are combined using another pair of 3 dB couplers. The resultant photocurrent (I_1, I_2, I_3, I_4) at the four photodetectors can be obtained from the field distribution of the in-phase and quadrature components [137,139].

$$I_1 \sim \left| i\frac{E_s + E_{LO}}{2} \right|^2 = \frac{1}{4}(|E_s|^2 + |E_{LO}|^2 + 2\,Re\{E_s E_{LO}^*\}) \tag{2.57}$$

$$I_2 \sim \left| -\frac{E_s - E_{LO}}{2} \right|^2 = \frac{1}{4}(|E_s|^2 + |E_{LO}|^2 - 2\,Re\{E_s E_{LO}^*\}) \tag{2.58}$$

$$I_3 \sim \left| i\frac{E_s + iE_{LO}}{2} \right|^2 = \frac{1}{4}(|E_s|^2 + |E_{LO}|^2 + 2\, Im\{E_s E_{LO}^*\}) \tag{2.59}$$

$$I_4 \sim \left| -\frac{E_s - E_{LO}}{2} \right|^2 = \frac{1}{4}(|E_s|^2 + |E_{LO}|^2 - 2\, Im\{E_s E_{LO}^*\}) \tag{2.60}$$

After, the conversion of the optical signals into the electrical domain. The analog signals are down-converted using an analog-to-digital converter (ADC). The conversion process involves two steps, firstly the ADC samples the continuous time signal into discrete time analog signals using a sampler. In the second step, the discrete signals are quantized into finite sets of values depending on the resolution of the ADC [63]. The discrete samples are then passed through a chain of DSP algorithms for data recovery [140,141].

2.7 Performance metrics in optical communication

The performance of direct detection and digital coherent transmission can be quantified using different figures of merit. These metrics are essential to estimate the quality of transmission (QOT), although there are multiple metrics to quantify the QOT we will discuss only a few of these in this section.

Bit error rate (BER) is the most fundamental performance metric of any received channel. It is defined as the ratio of error bits to the total number of bits over a certain time frame. It can be represented using a simple formula.

$$BER = \frac{error\ bits}{Total\ number\ of\ bits} \tag{2.61}$$

If the noise sources distorting a channel are considered as an independent random variable with a Gaussian distribution, then the system performance can be characterized using another metric known as Q-factor. In systems with hard decision thresholding, the Q-factor is obtained by integrating the tail of the Gaussian noise distribution extending beyond the decision threshold. In direct detection with a binary system, the Q-factor can be represented as [142].

$$Q = \frac{\mu_1 - \mu_0}{\sigma_1 + \sigma_0} \tag{2.62}$$

Where, μ_0, μ_1 are the amplitude of the first and second levels (i.e., for 0's and 1's), and σ_0, σ_1 are the corresponding standard deviation.

For a non-binary system, it is known as an effective Q-factor (Q_{eff}), and can be correlated to BER and vice versa using the complementary error function [47].

$$Q_{eff} = \sqrt{2}[Erfcinv(2XBER)] \tag{2.63}$$

$$BER = \frac{1}{2}Erfc\left(\frac{Q_{eff}}{\sqrt{2}}\right) \tag{2.64}$$

The performance of any signal can also be quantified using the metric signal-to-noise ratio (SNR). In the optical domain, it is known as the optical-signal-to-noise ratio (OSNR). OSNR is the value of optical signal power to the noise power, over a noise bandwidth of 0.1 nm. Similarly, electrical SNR, or simply SNR is the electrical signal power to noise ratio. It can also be defined in terms of energy per bit (E_b) to noise spectral density (N_0).

$$OSNR = \frac{Optical\ signal\ power}{Noise\ power\ (0.1\ nm\ bandwidth)} \tag{2.65}$$

$$SNR = \frac{elctrical\ signal\ power}{Noise\ power\ in\ the\ same\ bandwidth} \tag{2.66}$$

$$SNR = \frac{E_b}{N_0}\frac{f_{bit}}{B} \tag{2.67}$$

Where, f_{bit} is the channel data rate in bits/s, and B is the channel bandwidth.

For high-order modulation format with m square constellation points, SNR and BER can be co-related to each other by using the following expression [17,143]

$$BER = \frac{2}{\log_2 m}\left(1 - \frac{1}{\sqrt{m}}\right)Erfc\left(\sqrt{\frac{3.SNR.\log_2(m)}{2.(m-1)}}\right) \tag{2.68}$$

Another important performance metric to estimate a channel transmission performance is error vector magnitude (EVM). EVM quantifies the root mean square deviation of a received symbol from the ideal symbol in amplitude and phase. This deviation can be represented using error vectors in the I-Q plane of the constellation point as shown in Figure 2.18. For quadrature amplitude modulated (QAM) signals with N transmitted symbol EVM can be expressed as [143].

$$EVM = \sqrt{\frac{\frac{1}{N}\sum_{i=1}^{N}\left|Sv_i^r - Sv_i^t\right|}{P_{avg}^t}} \tag{2.69}$$

Where Sv_i^r is the received signal vector for the ith symbol, Sv_i^t is the ideal signal vector for the ith symbol and P_{avg}^t is the average transmitted power for an m-QAM signal.

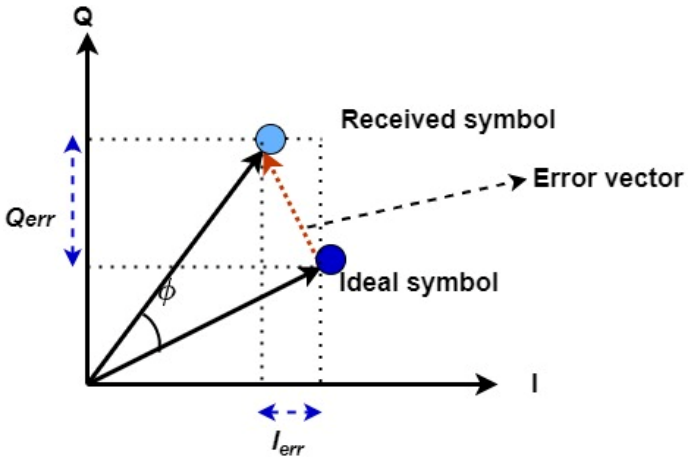

Figure 2.18 Error vector between the ideal symbol and received symbol in a complex I-Q plane [144]

For an m-QAM signal (m>2), EVM, SNR, and BER are correlated to each other as below.

$$SNR \sim \frac{1}{EVM^2} \tag{2.70}$$

$$BER \sim 2\left[\frac{1-\frac{1}{L}}{\log_2 L}\right].Erfc\left(\sqrt{\left[\frac{3\log_2 L}{L^2-1}\right]\left[\frac{1}{EVM^2(\log_2 m)}\right]}\right) \tag{2.71}$$

Where L is the number of distinct signal levels in the I-Q complex plane and m is the number of constellation points [143].

While BER, Q-factor, EVM, and SNR are the most commonly used pre-forward-error correction (FEC) metrics in optical communication. With the increasing channel capacity in modern-day communication, the optical community is changing their paradigm towards achievable information rate (AIR) i.e. identifying the number of bits per symbol that can be effectively transmitted through a channel [145]. Incorporating soft-decision (SD) thresholding after post-FEC BER is a new way forward to estimate channel performance for high-cardinality and probabilistic-shaped data [146]. Hence, metrics such as generalized mutual information (GMI), and normalized GMI have been reported in numerous literatures, that can perform robust prediction of the post-FEC BER [147].

For an additive white gaussian noise (AWGN) channel with a noise variance of σ^2, the probability distribution of a received symbol x_r for a transmitted symbol x_t can be represented as.

$$P(x_r|x_t) = \frac{1}{\sqrt{2\pi\sigma^2}}.exp(-|x_t - x_r|^2/2\sigma^2) \tag{2.72}$$

Using the probability distribution of the channel the GMI can be expressed as [146].

$$GMI \sim m + \log_2 \frac{1}{N} \sum_{k=1}^{N} \sum_{i=1}^{m} \log_2 \frac{\sum_{x \in X_{t_{b_{k,i}}}} P(x_r|x_t) P_X(x_t)}{\sum_{x \in X} P(x_r|x_t) P_X(x_t)} \tag{2.73}$$

Where, X denotes the set of m-QAM symbols, $P_X(x_t)$ is the statistics of the channel, $X_{t_{b_{k,i}}}$ is the set of m-QAM symbols, whose i^{th} bit value of the k^{th} symbol is b_{ki}, $m = \log_2 M$ (M is the number of constellation points in the I-Q complex plane) and N is the total number of transmitted symbols [146].

Normalized GMI (NGMI) denotes the number of information bits per transmitted bit and can be determined for an m-QAM signal from the GMI using the below expression [146].

$$NGMI = \frac{GMI}{m} \tag{2.74}$$

2.8 Recirculation fibre loop

A recirculation loop is an emulation of long-haul transmission with fewer amplifiers and fibre spans. In real-time long-haul communication with multiple spans, every fibre span is followed by an inline amplifier to compensate for the power loss. However, implementing such a fibre link for short-time laboratory experiments requires adequate space and expenditure. Hence, a recirculation loop is a cost-effective solution to recreate long-haul transmission with multiple propagations through a fibre span [148]. It is a time-controlled transmission where a signal enters and exits a fibre span multiple times depending on the number of desired recirculations.

The simple schematic of a recirculation loop is illustrated in Figure 2.19. The optical signal from the transmitter is fed into the recirculation loop using a controlled optical switch. Acousto-optic modulators (AOMs) with fast response time and high extinction ratio are typically used as optical switches. The AOMs-based optical switches are operated using gated pulses generated from a digital delay generator (DDG). The optical switch 1 is first closed to fetch the loop with a burst of signals for a certain time interval, known as the loop fill time. During this time interval switch 2, is open so that the signal can enter the loop but can't exit the loop. The fill time should exactly match the length of the burst signal, or else the signal will be underfilled or overfilled. If the loop is underfilled ASE noise from the loop amplifier will build up. On the other hand, if the loop is overfilled then the pulses will complete one round trip and will overlap with the next oncoming pulse causing multi-path interference (MPI) [149].

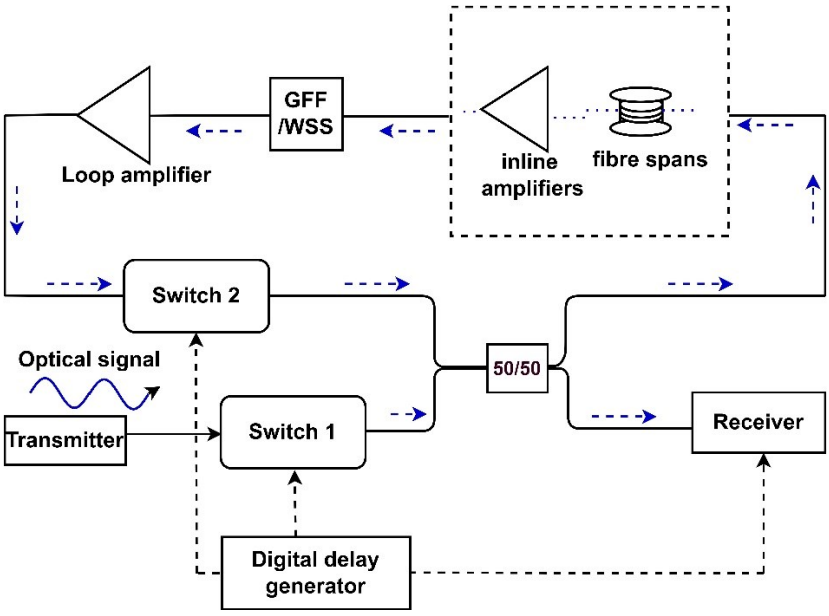

Figure 2.19 Schematic of a recirculation loop (GFF: gain flattening filter, WSS: waveshaper) (dashed blue lines: optical signal; dashed black lines: electrical signal)

The signal after passing through switch 1, is split into two paths using a 2x2 3 dB coupler. On one path the signal is fetched into the recirculation loop, while on the other path the signal is directed toward the receiver. Once the loop is filled switch 2 (loop switch) is closed using a DDG, and the signal starts circulating in the loop for a fixed time interval before getting captured by the receiver for processing.

Signals inside the recirculation loop can either go through single or several fibre spans, and inline amplifiers according to experimental necessity. For WDM transmission a gain flattening (GFF) filter or a waveshaper needs to be added inside the recirculation loop for equalizing the gain across the bandwidth The inline amplifier gain is generally adjusted to compensate for the span loss. Hence, an addition amplifier known as a loop amplifier is added to compensate for the loop losses (AOMs, 3 dB coupler, and GFF) and to maintain constant power to the input of the fibre span after each circulation. The loop amplifier can be any doped or undoped amplifier depending on the wavelengths of operation. To maintain a constant input power to the fibre span a 1% tap can be inserted at the loop output for monitoring. The output of this tap can be connected to a low-speed photodetector, with the electrical output connected to a low-speed oscilloscope triggered using a DDG [137,150].

To capture the data after several recirculations. The receiver oscilloscope is triggered using the same DDG as used for switch 1 and switch 2. The oscilloscope captures the traces at the rising or falling edge of the trigger depending on the trigger type (High Z, edge, level trigger, etc). Once the traces are captured it goes through a standard detection process for data recovery.

It is also important that the components inside the recirculation loop are polarization insensitive, which can degrade the transmission performance over multiple round trips [151]. A polarization controller or a scrambler can be added inside the loop after the loop amplifier to reduce these effects. However, the addition of these devices also adds to higher insertion loss, which can increase the noise addition from the loop amplifier, as the input power to the loop amplifier will get lower. The addition to the high insertion losses the AOMs also induce a frequency shift in a few MHz which can add to a significant phase shift if the recirculation number is very large [148]. This can be compensated using suitable DSP such as frequency offset algorithms for data recovery on captured traces [152].

Chapter 3: Raman amplifiers

This chapter will present a literature review on Raman amplifiers, factors affecting the amplification and recent developments in Raman amplifiers. In the first section, we will present an overview of discrete and distributed Raman amplifiers, different pumping schemes and the factors associated with different pumping. In the second section, we will discuss some of the performance limiting factors that affect Raman amplification such as nonlinearity, relative intensity noise and amplifier noise figure (NF), and finally, we will discuss the progress in Raman amplifiers over different time scales.

3.1 Raman amplification

Raman amplification is an inelastic scattering process caused due to the interaction between two photons propagating either in the opposite or the same direction. This effect is known as stimulated Raman scattering (SRS) and a new photon is generated at the same frequency as the signal (ϑ_s), downshifted from the pump frequency (ϑ_p) [153,154]. This process leads to a transfer of energy from the pump frequency to the signals frequency and optical fibre behaves as an amplifying medium. The difference in the energy between pump and signal photons creates an optical phonon due to absorption by the host material at different vibrational states. These vibrational states determine the spectral shape of the Raman gain profile in different fibre types. A broad Raman gain can be obtained in germanium (Ge) doped silica (Si) based optical fibre due to its amorphous nature [155]. The frequency difference between the pump and the signal photon $(\vartheta_p - \vartheta_s)$ is known as Stoke's shift and the newly generated signal photon is known as Stoke's wave [49]. This newly generated Stoke's wave in a Ge-doped-Si fibre peaks at ~13.2 THz (100 nm) downshifted from the pump photon frequency. The process of Raman scattering is illustrated in the energy state diagram of Figure 3.1.

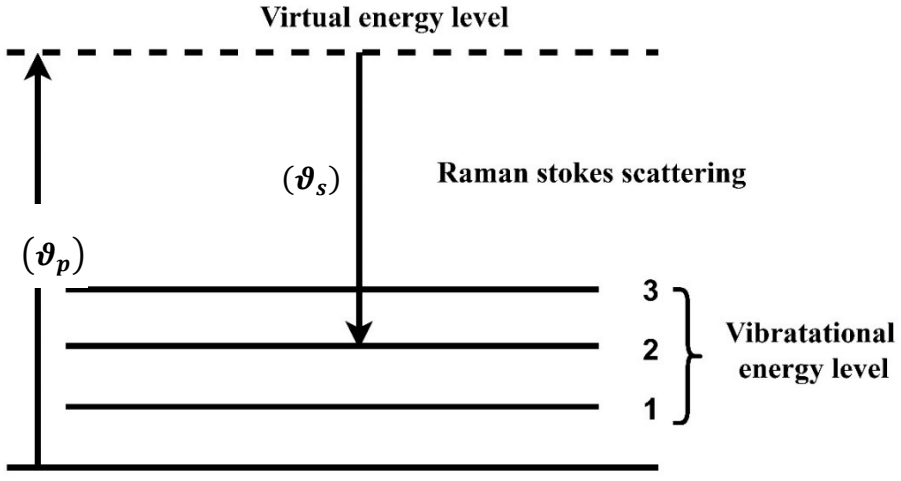

Figure 3.1 Energy level diagram of Raman Stokes scattering

From Figure 3.1 we can see Raman Stoke's scattering where a pump photon at a frequency (ϑ_p) excites a molecule to the virtual state. The molecule instantaneously decays to the lower energy state releasing a photon of frequency (ϑ_s). The entire scattering process is much faster in comparison to an erbium-doped fibre amplifier (EDFA) whose energy is stored in the upper energy bands of the erbium ions making it a slower process [156]. In the presence of enough pump power, the scattered power can grow rapidly converting the pump energy into signal energy. Unlike an EDFA it doesn't require any special doping as the process can happen in any standard Ge-doped-Si fibre. A major advantage of Raman amplification is its flexibility to provide arbitrary gain at any wavelength. With the proper choice of pump wavelength, Raman gain can cover any bandwidth in the optical window of a standard single-mode fibre (SSMF). In the case of EDFA, this bandwidth is limited to only C- band (~1530-1565 nm) [157] and L-band (1570-1620 nm) [158] due to the discrete resonant level of the erbium ions. Raman amplification is also independent of the direction of pumping as phase matching is maintained throughout the scattering process [153].

3.1.1 Raman gain spectrum

As explained previously, Raman gain occurs at any wavelength depending on the pump wavelength. Here, we demonstrated a simple schematic to explain the Raman gain profile generation using a single pump wavelength.

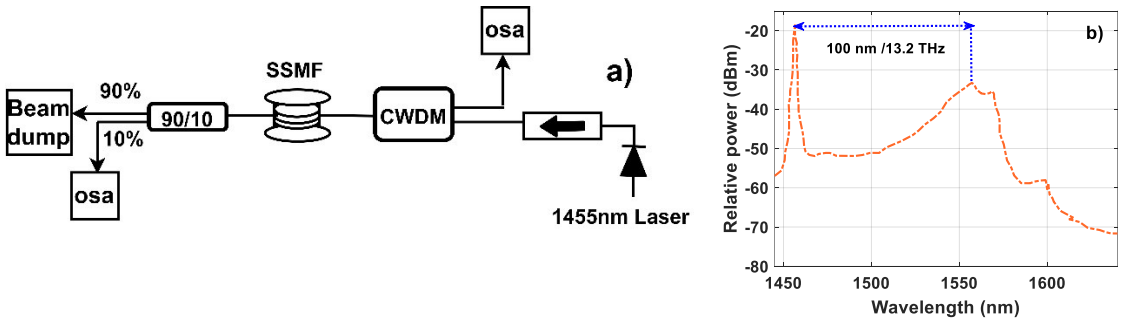

Figure 3.2 Raman gain spectrum measurement a) schematic diagram; b) gain spectrum

The effect of SRS generating a gain spectrum was performed using a simple single-pump experiment as shown in Figure 3.2 (a). In the setup, 10 km of SSMF was pumped using a 1455 nm fibre laser source. An input pump power of 1W was coupled to the fibre using a coarse wavelength division multiplexer (CWDM) centred at 1450 nm. The pump was then propagated through a 90/10 tap whose 10% arm was used to monitor the pump spectrum and the remaining 90% was discarded to a beam dump. The SRS effect in the backward direction was measured using an optical spectrum analyser (OSA) after being separated by the CWDM. Figure 3.2 (b) illustrates the gain bandwidth of the Raman spectrum due to SRS. The peak gain was observed at

a wavelength of ~1555 nm which is downshifted in frequency by 13.2 THz (100 nm) and the full-width half maximum (FWHM) of the overall profile has a bandwidth of approximately 6 THz.

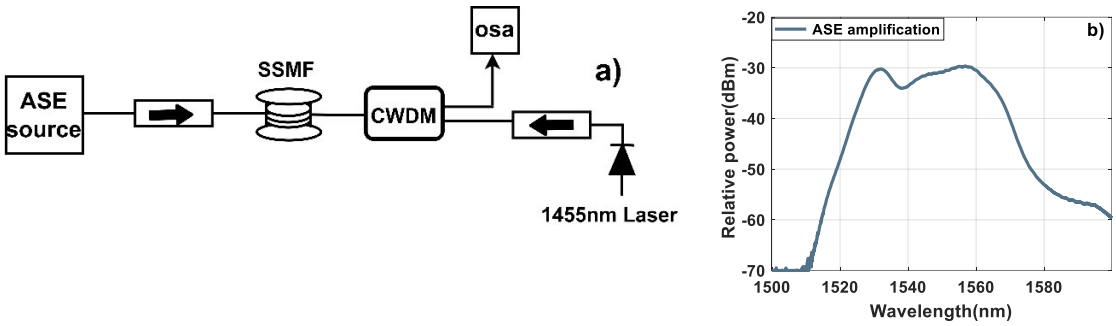

Figure 3.3 ASE amplification with Raman amplifier

The amplification of an amplified spontaneous emission (ASE) spectrum using a Raman amplifier is shown in Figure 3.3 (a-b). The experimental setup comprised an ASE source whose output was connected to an SSMF. The signal was propagated in the forward direction over 10 km of SSMF. A 1455 nm laser source was used as a pump and was coupled to SSMF using a CWDM centred at 1455 nm. Isolators were added to the fibre and the pump input section to prevent back reflections. Total power of 500 mW was pumped into the SSMF in the backward direction of the signal propagation. The amplified ASE spectrum after the CWDM separation was captured using an OSA. A flat gain of ~30 nm from 1530-1560 nm can be seen in Figure 3.3 (b), which then rolls off significantly due to the limited amplification bandwidth of the Raman amplifier with a single pump configuration.

3.2 Types of Raman amplifier

Raman amplifiers can be categorized based on two different amplification methods.

1) Distributed Raman amplifier.
2) Discrete Raman amplifier.

3.2.1 Distributed Raman amplifier

Distributed Raman amplifier (DiRA) is a special kind of amplification technique in which the transmission fibre operates as an amplifying medium. The loss of the transmission fibre (SSMF) is balanced by parallel amplification of the signals in the transmission fibre itself such that the overall fibre loss is nearly zero. As a consequence, this amplification method improves the overall optical signal-to-noise ratio (OSNR) in comparison to other lumped amplification techniques. In addition to this distributed amplification does not require any special fibre as an amplifying medium making it an attractive choice.

In the late eighties, long-haul transmission with DiRA was performed to compensate for the SSMF attenuation loss [159], but with the commercialization of EDFAs in early the early nineties experiments with Raman amplifiers got halted. However, during the mid-nineties with the availability of high-power lasers, the benefits of DiRA were realised and experiments over repeaterless subsea transmission were performed [160]. High-capacity terrestrial experiments [161,162] and shorter single-channel systems with 320 Gbit/s pseudo-nonlinear transmissions were also performed [163]. These experiments paved the way towards further research in DiRAs for long-haul transmission and increased the popularity of DiRAs among the scientific community.

The major benefit of distributed amplification is its improved SNR that can be achieved due to the amplification of a signal along the transmission fibre unlike doped fibre amplifiers (EDFAs) which are based on lumped amplification. In lumped amplification, the signals are attenuated through the transmission fibre (SSMF) and are then amplified using a specially doped fibre, where SNR goes low in the input section of the doped fibre due to the large power loss in the SSMF fibre. However, in DiRA the SNR does not drop as much as it would have in a lumped amplification as the signals are constantly amplified in the transmission fibre compensating the losses in parallel. This makes the DiRA very suitable for long-haul transmission with a higher modulation format where an improved SNR is essential for error-free detection. This benefit of DiRA led in the late nineties to perform experiments over 100 km spans with 40 channels at a data rate of 40 Gbit/s per channel [164] and 10x10 Gbit/s WDM transmission over 7200 km [165].

Raman amplifiers can be used to obtain a flat gain across large bandwidths. Although the 3 dB gain spectrum of Raman with a single pump configuration is relatively small, however, this bandwidth can be extended over hundreds of nanometers using a multiple pump configuration selected at suitable wavelengths and powers [166]. Several works of literature have shown an amplification bandwidth of 100 nm with multiple pumping configurations, with one experiment managing to achieve a gain flatness of +/- 0.5 dB with a 6.5 dB gain over a bandwidth of 100 nm with 12 semiconductor pumps [166].

Another major benefit of Raman amplifiers is their flexibility of amplification at any wavelength of the communication window. This arbitrary gain can be achieved by selecting a suitable pump at 100 nm or 13.2 THz above the frequency of the signal. This arbitrary amplification was first demonstrated in 1998 by A.K Srivastava *et al*, where amplification at 1400 nm and 1550 nm were performed simultaneously [167]. In this experiment, four channels at 10 Gbit/s near 1400 nm were transmitted and amplified simultaneously with 16 channels of 2.5 Gbit/s around 1550 nm using an all-wave fibre of 80 km whose OH peak at 1385 nm was removed.

3.2.1.1 Pumping schemes in distributed Raman amplifier

Raman amplification is independent of the direction of the pump and signal. The only necessity is the depolarization of the pump as Raman amplification is polarization dependent. Raman amplification in distributed fashion can be performed using three different pumping schemes which are categorized based on the direction of the signal and pump propagation. These three pumping schemes are.

1. Forward pumping or co-directional pumping.
2. Backward pumping or counter-directional pumping.
3. Bidirectional pumping.

3.2.1.1.1 Forward pumping

In this pumping scheme both the pump and signal propagate in the same direction. In this process, the signals undergo amplification in the initial part of the SSMF fibre followed by attenuation such that the overall loss is nearly zero. However, in this pumping scheme, amplitude fluctuations of the pump can transfer its power to the signal in the form of intensity noise commonly known as relative intensity noise (RIN) degrading the overall transmission performance. In addition to this due to amplification in the initial section of the SSMF, a higher extent of nonlinearity adds up due to the high signal power.

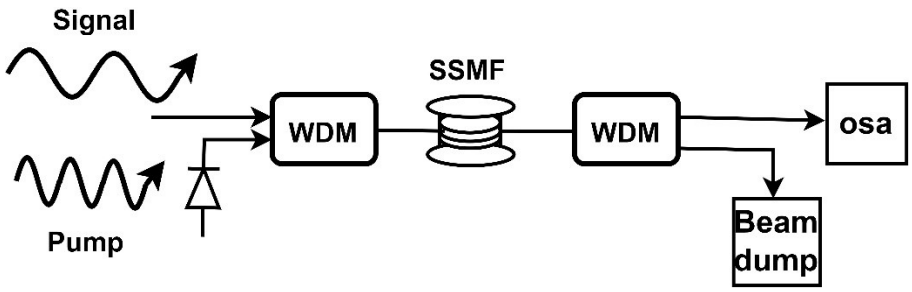

Figure 3.4 Schematic representation of FW-pumped DiRA.

Figure 3.4 illustrates the general schematic of a FW-pumped DiRA where the signal and pump co-propagate in the same direction and the SSMF behaves as both transmission and amplifying medium.

3.2.1.1.2 Backward pumping

In this pumping scheme, the pump and signal propagate in the opposite direction. In this process, the signal undergoes attenuation in the initial part of the SSMF fibre followed by amplification in the later stage such that the overall loss is nearly zero. This pumping scheme is preferred over FW pumping since the interaction between the pump and signal is less and the amplitude fluctuations get cancelled out when the pump and signal quickly pass each other. The addition of

RIN is negligible in backward (BW) configuration making it a preferable scheme for distributed amplification.

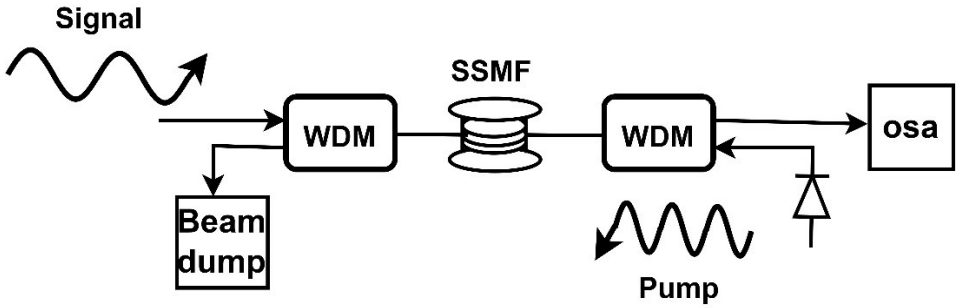

Figure 3.5 Schematic representation of BW pumped DiRA.

Figure 3.5 illustrates the schematic of a BW-pumped DiRA, here the pump and signal propagate in the opposite direction and the signal in the SSMF will undergo attenuation in the initial stages followed by amplification in the later stage.

3.2.1.1.3 Bidirectional pumping

The third pumping scheme is the bidirectional (BI) pumping scheme, where amplification occurs in both FW and BW directions by pumping the SSMF in both directions. This scheme is interesting for transmission systems that require high OSNR and longer span lengths. In this scheme, a minimal percentage of FW pumping is done to improve the OSNR. In the counter direction, BW pumping is provided to minimize the RIN penalty. Figure 3.6 illustrates the schematic for BI-pumped DiRA with a single pump in BW and FW direction over SSMF.

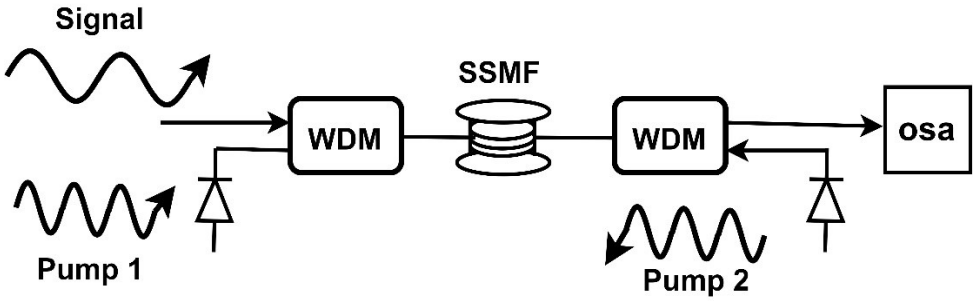

Figure 3.6 Schematic representation of Bidirectional pumped DiRA

3.2.1.2 Couple mode equation for pulse propagation with single pump system in distributed Raman amplifier

The power profile of the pump and signal propagating in a nonlinear medium with distributed amplification can be represented by equations (3.1) and (3.2). Here, the interaction is solely due to the pump and signal power transfer with attenuation being the only degrading parameter. Assuming, the evolution of the pump and signal along the fibre longitudinal axis z, the

propagation of the pump and signal can be represented by the coupled mode differential equation [153]

$$\frac{dP_p^{\pm}}{dz} = \pm\alpha_p P_p \pm \frac{\omega_p}{\omega_s} g_R P_s P_p^{\pm} \tag{3.1}$$

$$\frac{dP_s}{dz} = -\alpha_s P_s + g_R\left(P_p^{+} + P_p^{-}\right)P_s \tag{3.2}$$

Here, P_s is the signal power and $P_p^{\pm}$ are the pump power in (+) forward and (-) in backward direction along the longitudinal axis z, α_p and α_s are the attenuation coefficient of the pump and signal, g_r is the Raman gain coefficient of the fibre and ω_p and ω_s are the pump and signal operating frequencies respectively. Considering the sole effect of fibre attenuation as a degrading parameter the variation in pump powers in a FW and BW-pumped DiRA can be represented as:

$$P_p^{+}(Z) = P_p(0)\exp\left(-\alpha_p Z\right) \tag{3.3}$$

$$P_p^{-}(Z) = P_p(L)\exp\left(-\alpha_p\{L - Z\}\right) \tag{3.4}$$

Substituting the above equations in equation (3.2) over a span length L, the simplified signal power profile can be represented as

$$\frac{dP_s}{dz} = -\alpha_s P_s + g_R\left(P_p(0)\exp\left(-\alpha_p Z\right) + P_p(L)\exp\left(-\alpha_p\{L - Z\}\right)\right)P_s \tag{3.5}$$

For forward pumping, the second term of equation (3.5) goes to zero and as for backward pumping, the first term reduces to zero. Solving equation (3.5) using the boundary conditions at z=0 and z= L gives the variation of power profiles of the pump and signal over an SSMF of length L.

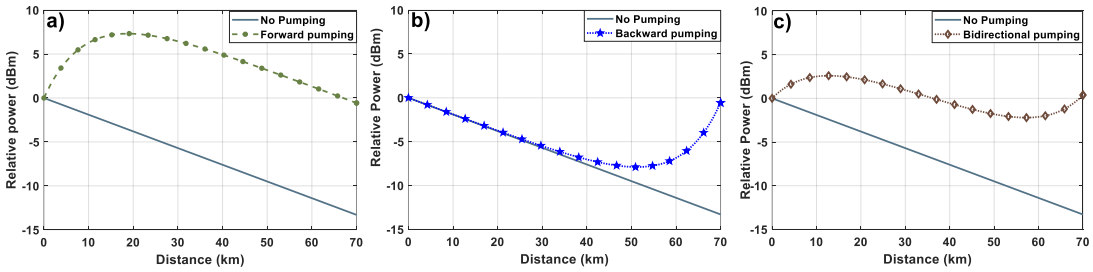

Figure 3.7 Signal power profile with distributed amplification over 70 km SSMF a) forward b) backward pumping c) bidirectional pumping

Figure 3.7(a-c) shows the corresponding signal power profiles with amplification and without amplification. The ordinary differential equations (3.1) and (3.2) were solved at a boundary condition for all three test cases.

The simulation above was performed using a single channel at 1550 nm with an input power of 0 dBm and the corresponding pump was chosen at 1450 nm with pump power values of 185 mW for FW and 200 mW for BW pumping. This numerical modelling was performed using the symbolic (SYM) toolkit of MATLAB using the ordinary differential equation (ODE) function [168].

Numerical modelling was also performed for the above differential equation in the presence of ASE and Rayleigh backscattering. In the presence of these two components, the model can be extended by introducing the two new equations for FW and BW propagating noise in a BI-pumped DiRA [47].

$$\frac{dP_P^{\pm}}{dz} = \pm \frac{\omega_p}{\omega_s} g_r \left(P_s + n_s^+ + n_s^- + 4h\omega_s \Delta\omega_s \left(1 + \frac{1}{\exp\left(\frac{h(\omega_P - \omega_s)}{K_B T}\right) - 1} \right) \right) P_P^{\pm} \tag{3.6}$$

$$\frac{dP_s}{dz} = -\alpha_s P_s + g_r (P_P^+ + P_P^-) P_s \tag{3.7}$$

$$\frac{dn_s^+}{dz} = -\alpha_s n_s^+ + g_r (P_P^+ + P_P^-) \left(n_s^+ + 2h\omega_s \Delta\omega_s \left(1 + \frac{1}{\exp\left(\frac{h(\omega_P - \omega_s)}{K_B T}\right) - 1} \right) \right) + \in n_s^- \tag{3.8}$$

$$\frac{dn_s^-}{dz} = \alpha_s n_s^- - g_r (P_P^+ + P_P^-) \left(n_s^- + 2h\omega_s \Delta\omega_s \left(1 + \frac{1}{\exp\left(\frac{h(\omega_P - \omega_s)}{K_B T}\right) - 1} \right) \right) - \epsilon (n_s^+ + P_s) \tag{3.9}$$

The above equations (3.6)-(3.9) show the signal, pump and noise propagation in a BI-pumped DiRA for a transmission distance of 100 km. Here, P_P^+ and P_P^- are FW and BW propagating pumps, n_s^+ and n_s^- are the FW and BW propagating noise, h is the Planck's constant, K_B is the Boltzmann's constant, $\Delta\omega_s$ is the signal bandwidth, T is the absolute temperature, ϵ is the Rayleigh backscattering coefficient, ω_s and ω_p are the pump and signal frequencies, g_r is the Raman gain coefficient and α_s and α_p are the attenuation coefficient for the pump and signal. The system of differential equations shown above was solved using the MATLAB 'bvp4c' solver for the boundary value problem [169]. The value of the above parameters used for solving the differential equation is shown below in Table 3.1.

Table 3.1 Parameters used in the numerical modelling of the bidirectionally pumped distributed Raman amplifier.

Input Parameters	Value	Unit
Signal frequency (ω_s)	193.1	THz
Pump frequency (ω_p)	206.7	THz
Pump powers ($P_P^+ \; and \; P_P^-$)	185 (each)	mW
Signal attenuation (α_s) at 1550 nm	0.19	dB
Signal power (P_s)	1	mW
Simulation fibre length (SSMF)	100	km
Signal bandwidth ($\Delta\omega_s$)	120	GHz
Pump attenuation at (α_p) 1450 nm	0.27	dB
Rayleigh scattering coefficient (ϵ) at 1550 nm	4.3×10^{-5}	km^{-1}
Raman gain coefficient (g_r) at 1550 nm	0.4	$W^{-1}km^{-1}$
Planck's constant (h)	6.626×10^{-34}	J-s
Boltzmann constant (K_B)	1.38×10^{-23}	J/K
Absolute temperature (T)	298	K

The simulation results for the BI-pumped DiRA embedded with ASE noise are illustrated in Figure 3.8. The noise power for the BW pumping (pink line) is higher indicating the accumulation of higher ASE noise for the configuration. The pump powers were kept at an equal value to monitor the ASE noise accumulation for both the FW and BW pumps for a fixed span length. From below Figure 3.8, we can say that by increasing the FW pump power in a BI-configured DiRA the ASE noise will get lower and will improve the total output optical signal-to-noise ratio (OSNR). However, it should be noted that this benefit of FW pumping comes at the cost of a large accumulation of relative intensity noise (RIN), consequently degrading the overall transmission performance.

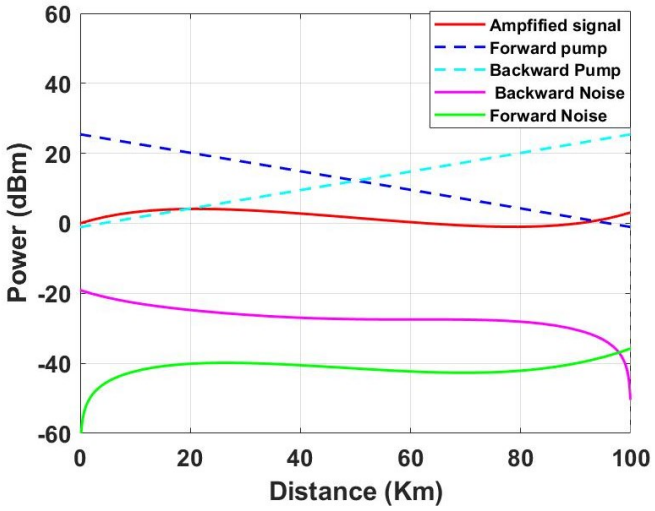

Figure 3.8 Signal and noise power profile with Bidirectionally pumped distributed Raman amplifier

3.2.2 Discrete Raman amplifier

In this section, we will discuss a separate class of amplifier based on lumped amplification known as discrete Raman amplifier (DRA). DRA is an alternate choice to DiRA for amplification of bandwidth >100 nm, minimizing the pump-to-pump and pump-to-signal overlapping. In recent years DRA has been an attractive solution for multiband transmission (MBT), as DRA can cover the entire bandwidth of the communication window with multiple pump configurations [76]. However, many limiting factors can impact the overall performance of a WDM signal with DRA and the design of DRA is an important criterion to minimize these limiting factors.

DRA uses a special nonlinear fibre with a smaller effective area as a gain medium. These fibres have a large Raman gain coefficient and are of few kilometres in length. Some of the fibre types that are commonly used as gain fibre for discrete amplification are inverse dispersion fibre (IDF) [170], dispersion compensation fibre (DCF) [171,172], dispersion shifted fibre (DSF) [173][174] and highly nonlinear fibre (HNLF) [175]. The major parameters that influence the performance of DRAs are 1) the attenuation coefficient and Raman gain coefficient of the gain fibre 2) the Rayleigh backscattering coefficient of the gain fibre 3) the nonlinear coefficient of the gain fibre and 4) the length of the gain fibre.

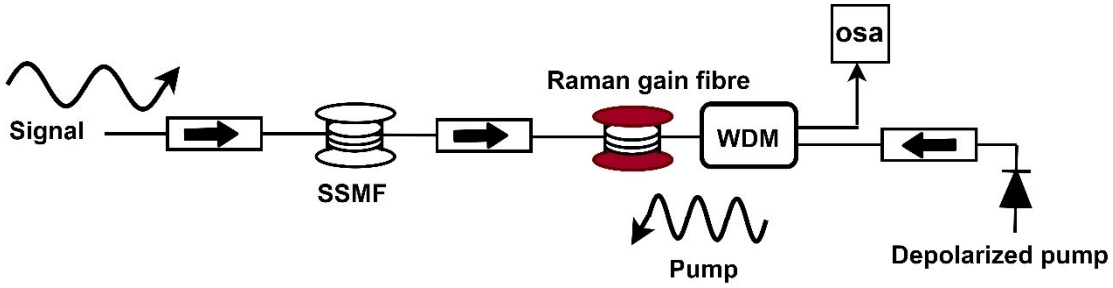

Figure 3.9 Schematic diagram of DRA with single pump and signal configuration.

A general schematic of DRA with BW pumping is illustrated in Figure 3.9 Figure 3.9 Schematic diagram of DRA with single pump and signal configuration. A signal propagating in the forward direction after attenuation through an SSMF enters the amplification stage. Fibres with a low effective area with a higher Raman gain coefficient (g_r) are typically used as an amplifying medium. As seen in the above schematic a depolarized pump at a higher frequency is counter-propagated in the direction of the signal enabling Raman amplification in the gain fibre. Higher power WDM couplers at appropriate wavelengths are required to couple and separate the pump and the signals to prevent overlapping. After amplification, the signal can be separated using the WDM coupler and the counterpropagating pump is prevented from entering the SSMF by using a high-power optical isolator.

3.2.2.1 Raman gain coefficient in discrete Raman amplifier

One of the important parameters necessary for the design of DRA is the fibre Raman gain coefficient (g_r). Figure 3.10 (a) shows the experimental setup for the measurement of the Raman gain coefficient of different fibre types. A C-band ASE source was used as an input spectrum to the Raman gain fibres. The test fibres were 7.5 km of IDF, 5 km of DCF and 8.25 km of a newly developed fibre known as Corning Raman fibre (CRF) [176]. The gain fibre was pumped using a 1455 nm laser source in a BW configuration. The required pump powers were 523 mW for IDF, 383 mW for DCF and 330 mW for CRF to provide a fixed on-off gain ($G_{on\text{-}off}$) of 12 dBm. The amplified signals were then separated using a CWDM and the corresponding traces were captured using a high-resolution OSA. The captured traces were then used to calculate the Raman gain coefficient (g_r) using the below equation (3.10)

$$g_r = \frac{G_{on-off}}{4.343 * L_{eff} * P_p} \tag{3.10}$$

Here, G_{on-off} is the Raman on-off gain, L_{eff} is the effective fibre length and P_p is the pump power used to obtain the 12 dB gain.

Figure 3.10 (b) shows the Raman gain coefficient (g_r) of the test fibres. The obtained values of the peak g_r were 1.2 $W^{-1}km^{-1}$, 1.8 $W^{-1}km^{-1}$ and 1.95 $W^{-1}km^{-1}$ for IDF, DCF and CRF fibres. The detailed parameters of these fibres are presented in Chapter 4 of this thesis.

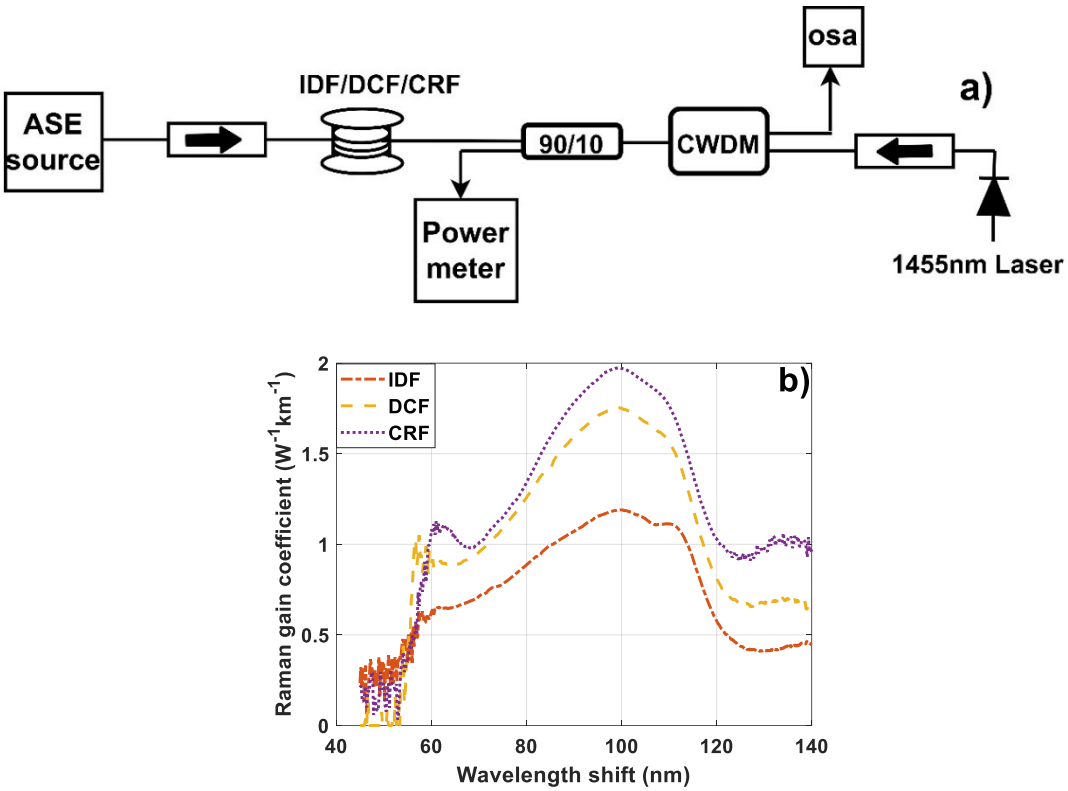

Figure 3.10 Raman gain coefficient measurement using broadband ASE a) experimental setup schematic b) Measured Raman gain coefficient (g_r) of IDF, DCF and CRF fibre

3.2.2.2 Discrete Raman amplifier with multi-pump configuration

As shown previously in Figure 3.1 (b) the gain profile of Raman amplifier with a single pump has a flat profile across a bandwidth of ~20 nm. This bandwidth is insufficient to amplify a fully loaded WDM signal over different bands. Hence, we require multiple pumps to provide variable gain across a wider bandwidth for amplifying broadband WDM signals. This can be achieved by coupling multiple pumps together such that an averaging effect takes place, enabling broadband signal amplification [154,177]. Using WDM pumping configuration Namiki and Emori *et al.*, have shown amplification of 80 nm with gain flatness of 0.1 dB [178] whereas, B Zhu *et al.,* have also demonstrated all Raman transmission over C-and L-band using multiple pumping over 100 km spans of dispersion compensating link [179].

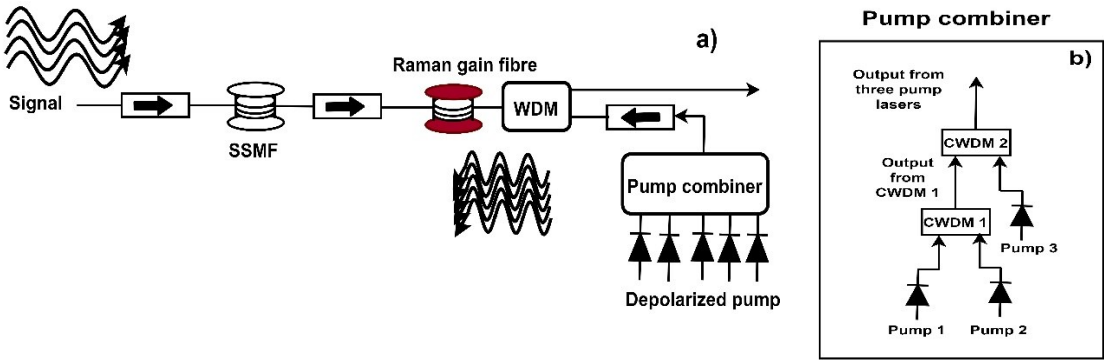

Figure 3.11 Multiple pump configuration with DRA for WDM signal amplification a) schematic b) pump combiner

The setup for a multi-pumping configuration to amplify broadband WDM signal is illustrated in Figure 3.11(a). The setup is similar to a single pump configuration apart from the use of multiple diode pumps and a pump combiner to combine all the pumps. This pump combiner is an array of CWDMs with a passband attached to one pump and the reflection band arm connected to another pump of a different wavelength. Figure 3.11(b) shows the schematic of a pump combiner to combine three pump diodes using two CWDMs.

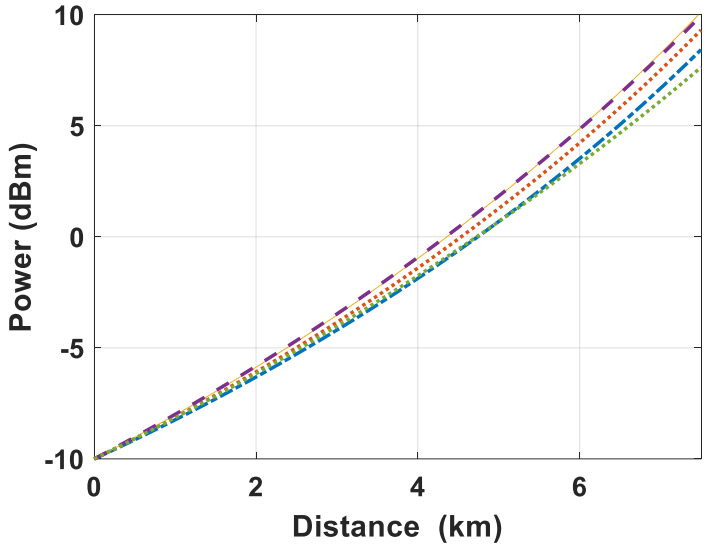

Figure 3.12 Signal power profile in a backward pumped DRA with IDF as the gain fibre

The signal power profiles in the amplification stage of a DRA are illustrated in Figure 3.12. The simulation shows the WDM signal power profiles over 7.5 km of IDF fibre undergoing Raman amplification in a BW pumping configuration. The simulation was performed using VPI simulation maker 11.0 where 4 WDM signals at a wavelength of 1531, 1540, 1545 and 1550 nm were passed through a 7.5 km of IDF. The launch power per wavelength was -10 dBm at the input of IDF and was pumped using two laser diodes at 1425 and 1450 nm with pump powers of 280 and 320 mW.

3.3 Performance limiting factors in Raman amplifier

Various factors impair the overall performance of both DRA and DiRA. In this section, we will discuss some of these factors such as amplified spontaneous emission (ASE) noise, RIN, Rayleigh backscattering, polarization mode dispersion, polarization-dependent gain and Kerr nonlinearity.

3.3.1 Amplified spontaneous emission

Spontaneous Raman scattering is an inherent effect that arises along with stimulated Raman scattering [180]. The spontaneously generated photon adds up in the form of noise because of the random phase of the photons [181]. The noise mechanism in the Raman amplifier is similar to that of EDFA. The ASE noise degrades the signal-to-noise ratio (SNR), and the extent of this degradation can be quantified through a parameter known as the amplifier noise figure (NF).

$$NF = \frac{SNR_{inp}}{SNR_{out}} \tag{3.11}$$

Here, SNR_{inp} and SNR_{out} are the electric signal-to-noise ratio at the input and output respectively, when the optical signal is converted into an electric current. In the case of an ideal detector whose performance is only limited by shot noise. The SNR at the input can be represented as [55,182]:

$$SNR_{inp} = \frac{\langle I_{inp} \rangle^2}{{\sigma_{shot}}^2} = \frac{\langle R_d P_{inp} \rangle^2}{{\sigma_{shot}}^2} \tag{3.12}$$

$$\sigma_{shot}^2 = 2q\left(R_d P_{inp}\right) B_w \tag{3.13}$$

Where, I_{inp} is the input current of the photodetector, R_d is the responsivity of the detector and is equivalent to $\frac{q}{h\vartheta}$ with 100% quantum efficiency and ${\sigma_{shot}}^2$ is the variance of shot noise over a receiver bandwidth of B_w. Hence, equation (3.12) can be represented as:

$$SNR_{inp} = \frac{R_d^2 P_{inp}^2}{2h\vartheta\left(R_d^2 P_{inp}\right) B_w} = \frac{P_{inp}}{2h\vartheta B_w} \tag{3.14}$$

The output electrical SNR of the amplified signal can be calculated by adding the contribution of the ASE to the receiver noise. Linearly adding all the contributed noise the detected current can be expressed as:

$$I_{out} = R_d \left[\left| \sqrt{G_{net}} E_{sig} + E_{COP} \right|^2 + |E_{OP}|^2 \right] + I_{shot} + I_{thermal} \tag{3.15}$$

Where, I_{out} is the detected current, G_{net} is the amplifier's net gain, E_{sig} is the electric field of the signal, E_{COP} and E_{OP} are the co-polarized and orthogonally polarized part of the electric field and I_{shot} and $I_{thermal}$ are the current fluctuations induced by the shot and thermal noises.

Since ASE noise occurs over a broader bandwidth, it can be divided onto N segments for each bandwidth $\Delta\vartheta_s$. The co-polarized and orthogonally polarized components of the signal can be represented as:

$$E_{sig} = \sqrt{P_{inp}}\exp\left(\theta_s - i\omega_s t\right) \tag{3.16}$$

$$E_{COP} = \sum_{n=1}^{N} \sqrt{S_{ASE}\Delta\vartheta_s}\exp\left(\theta_m - i\omega_m t\right) \tag{3.17}$$

$$E_{OP} = \sum_{n=1}^{N} \sqrt{S_{ASE}\Delta\vartheta_s}\exp\left(\theta_m + i\omega_m t\right) \tag{3.18}$$

Replacing equations (3.16), (3.17) and (3.18) in equation (3.15) the output current I_{out} can be represented as:

$$I_{out} = R_d G_{net} P_{inp} + I_{SIG/ASE} + I_{ASE/ASE} + I_{shot} + I_{thermal} \tag{3.19}$$

Here, S_{ASE} is the ASE spectral power density, and $I_{SIG/ASE}$, $I_{ASE/ASE}$ are the current fluctuations due to signal-ASE and ASE-ASE components. The output current variance can be written as.

$$\sigma^2 = \sigma^2_{sig/ASE} + \sigma^2_{ASE/ASE} + G_{net}\sigma^2_{sig} + \sigma^2_{thermal} \tag{3.20}$$

The contribution of thermal noise variance is relatively small and can be neglected. The ASE/ASE beat noise variance is also small in comparison to SIG/ASE noise and this component too can be discarded from the above equation (3.20). The beat noise due to SIG/ASE ($\sigma^2_{sig/ASE}$) can be reduced with the implementation of a narrow-band optical filter [153] and the variance of shot noise can be written as:

$$\sigma^2_{sig/ASE} = 4R_d^2 G_{net} P_{inp} S_{ASE} B_w \tag{3.21}$$

Where, $\sigma^2_{sig-ASE}$ is the beat noise between the signal and ASE. The ASE spectral density (S_{ASE}) can be expressed as [153]:

$$S_{ASE} = n_{sp} h\vartheta g_r G_{net} \int_0^L \frac{P_{pump}(z)}{G(z)} dz \tag{3.22}$$

Where, n_{sp} is the spontaneous-scattering factor, $h\vartheta$ is the photon energy, g_r is the Raman gain coefficient, G_{net} is the amplifier net gain and L is the amplifier span length and P_{pump} is the pump power along the amplifier span length z. Now considering an ideal optical filter with a transfer function $H_F(\vartheta)$ at the output of the amplifier, equation (3.22) reduces to:

$$P_{ASE} = 2\int_{-\infty}^{+\infty} S_{ASE} H_f(\vartheta) d\vartheta = 2S_{ASE} B_w \tag{3.23}$$

Factor 2 in the above equation (3.23) is due to the two polarization modes of the fibres. Hence, replacing S_{ASE} term, equation (3.21) can be rewritten as

$$\sigma^2_{sig/ASE} = 2R_d^2 G_{net} P_{inp} P_{ASE} \tag{3.24}$$

Now, the output electrical SNR of the amplified signal can be approximated as

$$SNR_{out} = \frac{\left(R_d G_{net} P_{inp}\right)^2}{G_{net}\sigma^2_{shot} + \sigma^2_{sig/ASE}} \tag{3.25}$$

Replacing σ^2_{shot} and $\sigma^2_{sig/ASE}$ from equations (3.21) and (3.26) in (3.25), SNR_{out} can be rewritten as:

$$SNR_{out} = \frac{\left(R_d G_{net} P_{inp}\right)^2}{2G_{net} h\vartheta R_d^2 P_{inp} B_w + 2R_d^2 G_{net} P_{inp} P_{ASE}} \tag{3.27}$$

Hence, the NF in equation (3.11) can be represented using equations (3.14) and (3.27) as

$$NF = \frac{P_{ASE}}{G_{net} h\vartheta B_w} + \frac{1}{G_{net}} \tag{3.28}$$

The noise figure shown in equation (3.28) depends on the ASE noise power (P_{ASE}) for both polarization, the amplifier net gain (G_{net}), energy of the photons $h\vartheta$ and the reference bandwidth of the noise. For Raman amplification the noise figure can be represented in terms of the pump power and Raman gain coefficient as:

$$NF = 2n_{sp} g_r \int_0^L \frac{P_{pump}}{G(z)} dz + \frac{1}{G_{net}} \tag{3.29}$$

The equation (3.29) above shows that the NF of an amplifier depends on the pumping scheme, hence the direction of pumping will add different extend of noise to the transmitted signals. In FW pumping the pump power is concentrated mostly in the input section of the fibre and hence an improved SNR and low NF will be present. Similarly in BW pumping the signals will undergo

attenuation in the starting length of the fibre and thereby, the input SNR near the amplification stage will be lower increasing the overall NF.

In the presence of multiple amplifiers cascaded together, the total NF of the amplifier chain can be expressed as [154,183]:

$$NF_{Total} = NF_1 + \frac{NF_2 - 1}{G_1} + \frac{NF_3 - 1}{G_1 G_2} + \cdots \tag{3.30}$$

Where, NF_i and G_i are the NF and the net gain of the ith amplifier in the cascaded chain. The expression in equation (3.30) shows, that in a chain of high-gain amplifiers, the overall NF is dominated by the NF of the first amplifier. Hence, many high-gain amplifiers are designed with multistage architectures having high gain and low NF in the first stage.

The amplifier NF in distributed amplification is slightly a complex expression as the transmission fibre itself is the amplifying medium. The NF in distributed amplifier is known as effective NF and is equal to $NF_{eff} = NF \exp(-\alpha L)$, where α is the fibre loss and L is the fibre length. This effective NF can be considered as an addition of the lumped pre-amplifier after the transmission span with a net gain of G_{net} and noise figure of NF. In decibel scale the effective NF can be represented as:

$$NF_{eff} = NF\ (dB) - \alpha L \tag{3.31}$$

From equation (3.31) we can see that the NF of a distributed Raman amplifier could even be negative depending on the span length making it very attractive for long-haul WDM transmission. The effective NF will also depend on the direction of pumping as shown in Figure 3.8 this ASE noise is minimum for FW pumping and so the NF will be lowest for FW DiRA and highest for BW pumped DiRA.

3.3.2 Relative intensity noise

Relative intensity noise (RIN) also known as pump noise transfer is an important parameter that can adversely affect the overall performance of DiRA. This is highly dominant in FW pumping where the interaction between the pump and signal takes place over a longer distance. Although FW pumping generates less ASE noise, however, the RIN transfer from the pump to the signal can counter-balance this benefit and degrade the system performance drastically. We will discuss in detail the effect of RIN with different pumping schemes in Chapter 5. Here, we will focus on the theoretical and mathematical expressions of RIN.

Signal gain due to stimulated Raman scattering is a dynamic process that is in the order of femtoseconds [184]. The extent of power transfer from the pump to a signal depends on the operating power of the pump. Hence, any fluctuation in the pump laser couples efficiently with

the signal causing large fluctuations in the amplified signal power. The level of power fluctuations depends on the type of laser used as a pump, for example, a semiconductor diode laser has large power fluctuations due to its large spontaneous emission [185], leading to the worst situation for Raman scattering. The extent of RIN transfer to the signals depends on parameters such as the length of the amplifying fibre, pumping direction and the chromatic dispersion of the amplifying fibre.

The intensity fluctuation in the pump is a frequency-dependent quantity known as pump RIN and can be represented as a variance of pump power to that of the average pump power [153].

$$\frac{\sigma_{pump}^2}{\langle P_{pump} \rangle^2} = \int_0^\infty RIN_{pump}(f)df \tag{3.32}$$

Where, σ_{pump}^2 is the variance of pump power, $\langle P_{pump} \rangle$ is the average pump power and $RIN_{pump}(f)$ is the RIN of the pump at a frequency (f). In the presence of pump RIN, the transferred RIN to the signal due to intensity fluctuations can be expressed as.

$$\frac{\sigma_{sig}^2}{\langle P_{sig}(L) \rangle^2} = \int_0^\infty RIN_{sig}(f)df \tag{3.33}$$

Equation (3.33) shows the signal RIN generated due to the pump intensity fluctuations. The increase in the signal noise at a specific frequency (f) due to the pump-noise transfer can be defined by the RIN transfer function.

$$H(f) = \frac{RIN_{sig}(f)}{RIN_{pump}(f)} \tag{3.34}$$

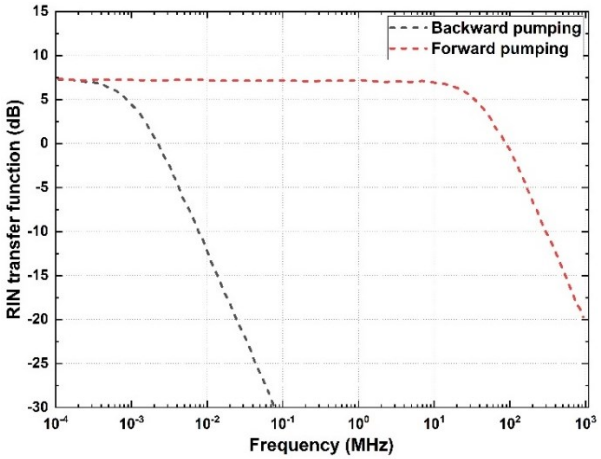

Figure 3.13 RIN transfer function for forward (Co-pumped) and backward (Counter) pumping in distributed Raman amplifier.

Figure 3.13 illustrates the RIN transfer function for FW and BW pumping with 100 km of nonzero dispersion-shifted fibre (NZDSF) taken from [154]. It can be observed that the corner frequency for FW pumping extends to ~ 40 MHz whereas, for BW pumping this is in the kHz range, clearly showing the higher induced RIN for FW pumping in comparison to its counterpart BW pumping.

For the calculation of the RIN transfer function $H(f)$, one must take into account that the signal and pump travel at different group velocities due to their different frequencies. This difference in velocity depends on the dispersion of the fibre at different frequencies. The parameter guiding the dispersion-dependent pump to signal RIN transfer is termed the pump-to-signal walk-off parameter and the larger the value of this walk-off parameter, the lower will be the overall RIN transfer.

In the worst-case scenario when there is no walk-off between pump and signal the overall RIN transfer to the signal can be expressed as [153,186]:

$$RIN_{sig}^{out} = \ln^2 G_{on-off}.RIN_{pump} + RIN_{sig}^{inp} \tag{3.35}$$

Where, RIN_{sig}^{out} is the RIN of the signal at the output of the amplifier, RIN_{pump} is the pump RIN and RIN_{sig}^{inp} is the RIN of the signal at amplifier input and G_{on-off} is the Raman on-off gain.

As mentioned previously the amount of RIN transfer from the pump to the signal also depends on the direction of the pumping. In DiRA with FW pumping, as the pump and signal propagate in the same direction with slightly different group velocities, overlapping between the pump and signal will be maximum in the temporal window. Hence, any intensity fluctuation in the pump within a temporal window will transfer efficiently to the signal in the form of noise. The RIN transfer in an FW-pumped DiRA with walk-off can be represented as [153]:

$$RIN_{sig}^{out} = RIN_{sig}^{inp} + RIN_{pump} ln^2 G_{on-off} \frac{1/L_{eff}}{\alpha_{pump}^2 + (2\pi f D \Delta\lambda)^2} \tag{3.36}$$

The term $(2\pi f D \Delta\lambda)$ in equation (3.36) is the pump-to-signal walk-off parameter, which depends on the fibre chromatic dispersion D, f is the frequencies of the noise components and $\Delta\lambda$ is the wavelength separation between pump and signal. The overall signal RIN at the output decreases with an increase in this walk-off parameter. Hence, by implementing higher-order Raman pumping the walk-off parameter can be increased, due to the increase in the wavelength separation $\Delta\lambda$ [187,188]. Similarly, this walk-off parameter can also be increased, by using a fibre with a higher value of chromatic dispersion [189]. It can also be seen from equation (3.36) that the higher frequency noise components will have a lower RIN transfer to the signal, demonstrating a low-pass noise filtering effect [153].

In the case of BW-pumped DiRA as the pump and signal propagate in opposite directions the relative velocity difference between the pump and signal is extremely large. In such a scenario the pump power fluctuations are averaged out and a minimal amount of RIN is transferred to the signal. Hence, BW-pumped DiRA is preferred over FW pumping despite its higher NF. The general expression for RIN transfer in BW-pumped DiRA is:

$$RIN_{sig}^{out} = RIN_{sig}^{inp} + RIN_{pump} ln^2 G_{on-off} \frac{1/L_{eff}^2}{\alpha_{pump}^2 + \left(4\pi f/V_g\right)^2} \tag{3.37}$$

The walk-off parameter in backward pumping is independent of the wavelength separation and fibre chromatic dispersion. The only dependent factor is the group velocity V_g which is considered to be the same for both the pump and signal [186].

3.3.3 Rayleigh backscattering

Rayleigh backscattering (RBS) is another important performance limiting factor in Raman amplifiers that occurs due to the non-uniformity in the core of optical fibre [190]. This is a fundamental scattering loss, where most of the scattered light escapes through the fibre cladding and a portion of the light gets coupled back into the core of the fibre [153]. Normally, the scattered light has a very low power however, in the presence of Raman amplification this scattered light can get amplified along with the signals.

Rayleigh's backscattered light can affect the performance of a Raman amplified transmission system in two ways. In the first scenario, backward propagating ASE can be scattered back in the direction of the signal, amplifying the overall ASE noise. In the second scenario, the backward propagating reflected light can further go through reflection again and propagate in the same direction as the signal. In this case, this double scattered light will be amplified too and will lie nearly in the same spectral range as the signal. This effect is known as double Rayleigh backscattering (DRS) and is a major source that limits the performance of a Raman amplified transmission system.

In distributed amplification where the fibre length is very long the Rayleigh backscattered light can undergo multiple reflections. The longer the span length of the fibre, the higher will be the number of reflections and simultaneous amplification. This phenomenon is known as multipath interference (MPI) noise [154,191].

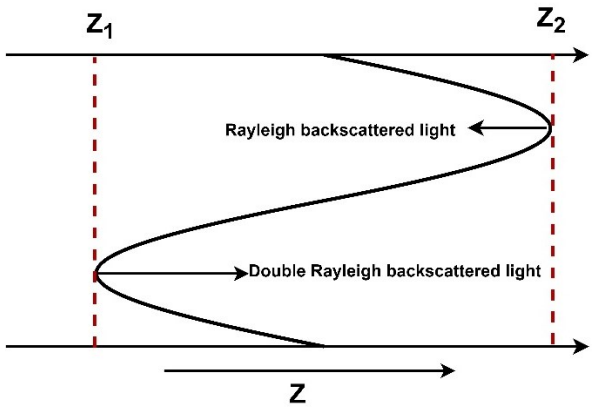

Figure 3.14 Schematic of Rayleigh scattering and double Rayleigh scattering in Raman amplifier.

Figure 3.14 shows, the general schematic of Rayleigh and double Rayleigh scattering in a Raman amplifier. Here, the ongoing signal is first reflected at a fibre location of Z_2 (Rayleigh scattering) and then is reflected again at location Z_1 (double Rayleigh scattering) [153]. The equations governing signal propagation, RBS and DRS are shown below [154].

$$\frac{dP_{sig}}{dz} = -\alpha_{sig}P_{sig} + g_r P_{sig}P_{pump} \tag{3.38}$$

$$\frac{dP_{RBS}}{dZ} = \alpha_{sig}P_{RBS} - g_R P_{RBS}P_{pump} - \kappa P_{sig} \tag{3.39}$$

$$\frac{dP_{DRS}}{dZ} = -\alpha_{sig}P_{DRS} + g_R P_{RBS}P_{pump} + \kappa P_{RBS} \tag{3.40}$$

Where, P_{sig}, P_{RBS} and P_{DRS} are the power of the signal, Rayleigh and double Rayleigh backscattered power along the longitudinal axis Z of the fibre, α_{sig} is the attenuation coefficient of the signal, g_R is the Raman gain coefficient of the fibre and κ is known as the coupling coefficient or the capture facture, having different values for different fibre types [154]. This factor is dependent on the fibre material composition and the design structure [56,192]. The typical values of κ for SSMF and DCF are 4.3~6.4 x 10^{-5} km and 6~7 x 10^{-4} km^{-1} [193,194].

3.3.4 Polarization mode dispersion

The polarization effect in a Raman amplifier can be related to the third-order nonlinear susceptibility in silica [195]. Raman amplification is a polarization-dependent effect and the gain is maximum when both the pumps and signals are co-polarized and maintain their state of polarization (SOP) during propagation [196]. However, due to the fibre birefringence, the SOP changes in a random fashion leading to an effect known as polarization mode dispersion (PMD) [197]. This causes the amplifier average gain to degrade significantly [198].

The average gain in a Raman amplifier depends on the PMD parameter (D_P) [153]. It has been experimentally demonstrated in [199] that when D_P is zero then the two polarizations maintain their SOPs, and the co-polarized signals experience maximum gain while the orthogonally polarized signals gain lowers significantly. As the PMD parameter increases, the gain difference between both the SOPs decreases and eventually disappears [153].

The level of signal power fluctuation (σ_s) for both co-polarized and orthogonally polarized also varies with D_P. The fluctuation level first increases with an increase in D_P and then reaches a peak which then eventually decays down to zero with further increase in D_P. The location of the peak where the power fluctuation is maximum depends on the direction of the pumping and the initial polarization of the pump. Using vector theory Lin and Agrawal [153,200] have shown that the fluctuations for forward pumping are larger than that of backward pumping and forward-pumped Raman amplifier will perform better with fibre of $D_P > 0.1ps\sqrt{km}$ whereas, for backward pumping the fluctuations are minimal even for fibres with $D_P < 0.01ps\sqrt{km}$.

It has also been experimentally demonstrated that with an increase in the differential group delay (DGD) the state of polarization (SOP) rotates rapidly, causing a distortion in the signal and reducing the average Raman gain [201].

3.3.5 Polarization dependent gain

The varying SOP of an optical field alters the amount of gain for both polarizations. The difference in the gain (ΔG) varies randomly because of the random birefringence in the co-polarized and orthogonally polarized signal. This variation in the gain from the polarization components is known as polarization-dependent gain (PDG). Uncontrolled variation in the SOP of the pump and signal can alter the gain flatness and can result in degradation of the overall transmission performance [202]. Models based on Vector theory [200] and random birefringence [203] have been reported previously to study the maximum PDG values in Raman amplifiers. In addition to this stochastic model based on the randomly varying birefringence that can calculate both the maximum and minimum PDG as a function of pump SOP and PMD has been reported [204]. We won't be doing the detailed derivations of the model however, the average and the root mean square (RMS) value of PDG in distributed Raman amplifier using the vector model can be represented by below equations (3.41) and (3.42)[153].

$$PDG_{avg} \sim \frac{4ag_R P_{inp}}{\sqrt{\pi} D_P |\Delta\omega|} \left[L_{eff} \left(1 - \frac{\alpha_p L_{eff}}{2}\right) \right]^2 \tag{3.41}$$

$$PDG_{RMS} \sim \left(\frac{3\pi}{8} - 1\right)^{\frac{1}{2}} . PDG_{avg} \tag{3.42}$$

Here, $a = 10/\ln(10)$, g_R is the Raman gain coefficient, P_{inp} is the input pump power, L_{eff} is the effective fibre length defined as $\left(L_{eff} = [exp(\alpha_P L) - 1]/\alpha_P\right)$, α_p is the pump attenuation coefficient, D_P is the PMD parameter defined in section 3.3.4 and $|\Delta\omega|$ is the difference between pump and signal frequency which equals to $\omega_P - \omega_s$ for forward pumping and $\omega_P + \omega_s$ for backward pumping.

3.3.6 Kerr nonlinearities

One of the other performance limitations that occur in Raman amplifiers for WDM signal amplification is Kerr nonlinearity. In distributed Raman amplifier (DiRA) this effect is dominant if the location of the pump is near zero dispersion wavelength (ZDW). This will give rise to four-wave mixing (FWM) products due to the pump-to-pump and pump-to-signal interaction. If the FWM sidebands lie near the pumps, the pump power will deplete significantly [205]. The extent of the nonlinear effects depends on the power of the highest wavelength pump and the direction of pumping [206]. Experimental demonstrations with non-zero DSF with ZDW at 1497 nm, have shown Raman gain depletion of ~2-3 dB due to pump-signal FWM with minimum phase matching [207].

In a discrete Raman amplifier (DRA), the Kerr nonlinear effect is more significant. The nonlinear noise accumulation due to self-phase modulation (SPM), cross-phase modulation (XPM) and four-wave mixing (FWM) are more dominant in DRAs due to the use of nonlinear fibre in lengths of kilometres as a gain medium. These gain fibres usually have a higher nonlinear coefficient (γ) in comparison to that of SSMF. The accumulated nonlinear noise in the DRA section of a transmission link depends also on the chromatic dispersion of the gain fibre which alters the phase-matching coefficient $(\Delta\beta)$ of the total nonlinear noise [208,209]. The total accumulated nonlinear noise in a DRA can be calculated by analytical modelling of piecewise signal power profile for each fibre and amplifier section of a link. The expression for the nonlinear noise accumulation in DRA is discussed in detail in Chapter 4 and a full derivation of the model is presented in [72,210].

3.4 Recent developments in Raman amplifier

The evolution of Raman amplification towards the late eighties was perceived as a method to compensate for the fibre loss. When Mollenauer *et al.* in the mid-eighties first demonstrated distributed amplification over long fibre length, it was thought to be the sole solution for compensating fibre loss in the optical domain [159]. However, with the invention of EDFAs by Bell Laboratory (USA) and the University of Southampton (UK) in the early nineties [6,7], research in Raman amplifiers halted for a few years. Meanwhile, EDFA was commercialized as a new optical amplifier for replacing electrical regenerative repeaters in the telecom lines. The transatlantic systems TAT-12 and TAT-13 were the first optically amplified system using EDFA

in a ring network, where a single channel at 1550 nm was amplified enabling a bidirectional data rate of 5 Gbit/s [211].

However, with the availability of high-power pump lasers renewed interest in distributed Raman amplifiers was seen. Various experiments were performed with WDM signals over the submarine and unrepeated networks [160,165]. The implementation of coherent optics in telecommunication, for high throughput, further inspired the research community to continue research in Raman amplifiers, both in distributed and discrete domains [212].

The current trend in data consumption has also led the scientific community to pursue research in Raman amplifiers for multiband transmission (MBT). Numerous experimental demonstrations with Raman amplifier as a seed and inline, in both discrete and distributed mode have been demonstrated in the past decade over different bands of the optical window. An experiment over C-and L-band with a dual-stage DRA was demonstrated by Krzczanowicz *et al.,* where a transmission distance of 3040 km was achieved with 30 GBaud DP-QPSK. In terms of maximum gain, a record gain of 27 dB with an average NF of 5.8 dB over C- and L-band with dual-stage DRA has been reported in [213]. In addition to the bandwidth total data capacity of 101.7 Tb/s and 102 Tb/s over C- and L-band, with BW pumped DiRA has been experimentally demonstrated in [214,215].

In the S-, C- and L- bands too Raman amplification over 150 nm has been achieved using dual-stage and dual-band DRA [38,170]. Ultrawideband transmission with a hybrid combination of distributed Raman and doped fibre amplifier has also been performed by different research groups. Hamaoka *et al.* in such a hybrid architecture achieved a net throughput of 150.3 Tb/s over a transmission bandwidth of 13.6 THz in the S-, C- and L- bands with varying optical launch power [216]. Similarly, experiments were also performed by Galdino *et al.* and Puttnam *et al.* where distributed Raman amplifiers were coupled with doped fibre amplifiers, achieving a net throughput of 178.8 Tb/s and 256.4 Tb/s over the S-, C- and L-band [36,37].

Recently, Raman amplifiers have also been implemented over unrepeated transmission too. A record net throughput of 99.35 Tb/s over 257.5 km of SSMF has been achieved by Ghazisaeidi *et al.* using a combination of distributed Raman and semiconductor optical amplifiers (SOAs) [123]. These recent demonstrations show the potential of Raman amplifiers to be an integral part of high-capacity fibre optics communication systems.

Chapter 4: Nonlinear penalties in discrete Raman amplifier for coherent transmission systems

In this chapter, the impact of nonlinear penalties in a discrete Raman amplified coherent transmission system is studied. The performance penalty due to Kerr nonlinearities in discrete Raman amplifier (DRA) was evaluated using the standard analytical Gaussian noise (GN) model [217,218] with a piecewise power profile approximation. The primary goal was to understand the dependency of fibre chromatic dispersion (CD) and fibre nonlinear coefficient (γ) on the total accumulated nonlinear noise. The analytical modelling was performed with three different Raman gain fibre with a varying value of fibre CD and nonlinear coefficient (γ), these test fibres were inverse dispersion fibre (IDF) [219], dispersion compensation fibre (DCF) [220], and a new development fibre known as Corning Raman fibre (CRF) [176,221] with a value of CD opposite to the other two.

The experiments were performed in AiPT optical communication laboratory, with support from Dr Mingming Tan (AiPT) who helped in conducting the recirculating loop experiment that was built by Dr Paul Harper. Dr Mahmood Abu-Ramoh (currently in Infinera) and Dr Tu T. Nyugen (Currently in Infinera) provided their DSP for processing. The author would also like to thank Dr Ming Jun Li and Jefferey S. Stones (Corning Inc.) for loaning us the Corning Raman fibre.

The fibre parameters used for the modelling were provided by Dr Md Asif Iqbal (currently with British Telecom), and Dr Lukasz Krzczanowicz (Currently with DTU Denmark). Technical feedback was provided by Dr Paul Harper, Dr Ian Phillips and Prof Wladek Forysiak.

4.1 Introduction

The performance of an optical transmission system is limited by the accumulation of amplified spontaneous emission (ASE) and nonlinear noise generated due to Kerr nonlinearities along the transmission fibre. The accumulated nonlinear noise can be theoretically calculated, solving the nonlinear Schrodinger equation (NLSE) [49] using both the analytical and numerical split-step approach. The GN model [217,218,222,223] is a well-known technique to calculate the accumulated nonlinear noise due to self-phase modulation (SPM), cross-phase modulation (XPM), and four-wave mixing (FWM) in an optical fibre [224]. This model is attractive as it reduces the computational processing time in comparison to other numerical techniques of solving the NLSE using the split-step Fourier method (SSFM) [225]. Analytical modelling of the GN model using a closed-form approximation has also been reported in [226,227], which takes into consideration the effects of inter-channel stimulated Raman scattering (ISRS) for improved accuracy of the nonlinear noise calculation when the transmission bandwidth is >100 nm.

A modified analytical GN model was used to quantify the accumulation of nonlinear noise in a DRA-based coherent WDM system. The model was initially studied to understand the effect of accumulated nonlinear noise with different Raman gain fibre types, the results of which were then evaluated experimentally. A standard fibre preferable for Raman amplification is the one with a large value of Raman gain coefficient (g_r) however, fibres with a high value of (g_r) will subsequently result in a higher value of (γ) which will add larger nonlinear noise degrading the transmission performance. Nevertheless, the total accumulated nonlinear noise depends on several other parameters that can be optimized to improve the performance. One such dependent parameter that impacts the total nonlinear accumulated noise is fibre CD. It's important to know whether a fibre with positive or negative CD is a better choice for DRA based coherent WDM system. Experiments with a positive and negative value of CD were previously demonstrated in [228][229] but any comparative study on the performance penalty in a long-haul transmission has not been verified so far. For this study, three fibres, IDF, DCF, and CRF were considered as the test fibre in the DRA section of the transmission link, the parameters of which are given in Table 4.1. The experimentally measured Raman gain coefficient (g_r) and the wavelength dependent attenuation profile of the test fibres are shown in Figure 4.1(a-b). The Raman gain coefficient (g_r) of both DCF and CRF are somewhat equal due to its similar fibre effective area (A_{eff}) whereas, for IDF this was slightly lower due to its larger effective area (A_{eff}). Similarly, the experimentally measured attenuation profile for IDF, CRF and DCF shows a lower value of loss for IDF with ~0.22 dB at 1550 nm whereas, for DCF and CRF this value is ~0.51 and ~0.44 dB at 1550 nm.

Table 4.1 Summary of IDF, DCF, and CRF fibre parameters used for the analytical modelling

Parameters @1550 nm	Unit	IDF	DCF	CRF	SSMF
Chromatic dispersion (CD)	ps/nm/km	-44	-96	11.7	16.5
Nonlinear coefficient(γ)	$W^{-1}km^{-1}$	3.53	8.43	8.87	1.3
Noise figure in DRA stage (NF)	dB	6.1	6.6	6.6	x

Fibre effective area (A_{eff}).	μm^2	31	19	17	80
Fibre length	km	10.1	8	8.25	63
Attenuation coefficient (α)	dB/km	0.23	0.51	0.44	0.2
Peak Raman gain coefficient (g_r)	$W^{-1}km^{-1}$	1.3	1.8	1.9	0.43

Parameters of the different fibre types used in the analytical model and experimental verification are given in Table 4.1 (x- not required in the calculation).

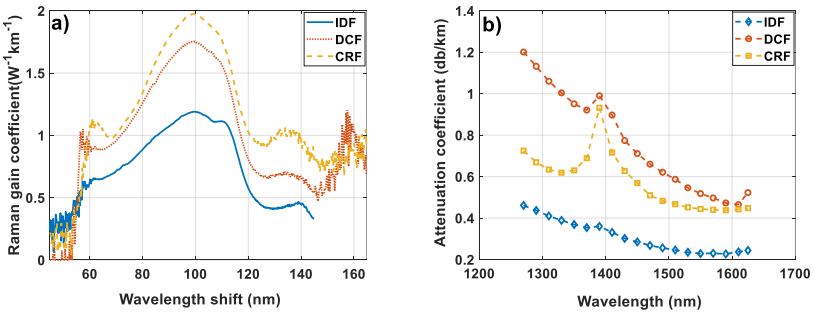

Figure 4.1 Experimentally measured a) Raman gain coefficient b) Attenuation coefficient of IDF, DCF and CRF.

4.2 Analytical model

The analytical modelling of the pulse propagation in a nonlinear medium subjected to the Kerr power products can be obtained by solving the inhomogeneous NLSE. A simplified power profile distributed in a Raman amplified transmission link (transmission fibre followed by a DRA) can be assumed as a piecewise power profile approximation where in the transmission section the signal undergoes attenuation followed by an amplification as shown in Figure 4.2(b).

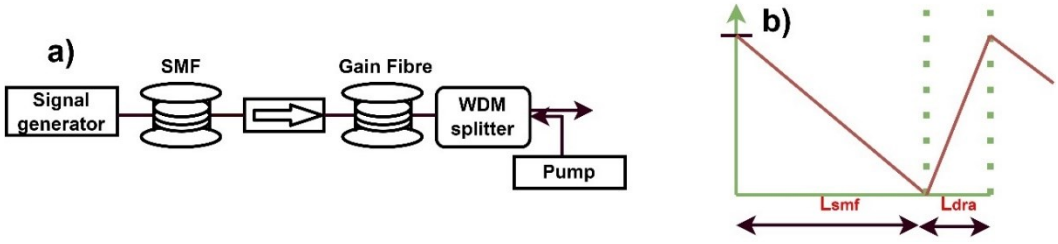

Figure 4.2 Schematic of a) single-span transmission with backward pumped discrete Raman amplifier b) amplified links with log signal power profile

The assumption used in the above link is that the loss of the SSMF is fully compensated by the gain of DRA. In such a transmission link the accumulated nonlinear noise can be calculated by an analytical representation of the piecewise signal profile approximation (SSMF loss section +DRA gain section) [40], which can be derived from the field equations of three optical waves at frequencies (ω_i, ω_j and ω_k) resulting in a Kerr total product power. The nonlinear field at frequency (ω_c) can be represented as below [230] equation (4.1) and the corresponding nonlinear power can be obtained by taking the square of the field distribution $|E_{NL}|^2$ as shown in equation (4.2)

$$E_{NL} = i\left(\frac{D}{3}\right)E_i(0)E_j(0)E_k^*\left\{\left[\gamma_{smf}\frac{e^{[-\alpha_{smf}L_{smf}+i(\Delta\beta_{smf})L_{smf}]}-1}{-\alpha_{smf}+i(\Delta\beta_{smf})}\right]\right. \\ \left. + e^{[-\alpha_{smf}L_{smf}+i(\Delta\beta_{smf})L_{smf}]}\left[\gamma_{dra}\frac{e^{[-g_{dra}L_{dra}+i(\Delta\beta_{dra})L_{dra}]}-1}{g_{dra}+i\Delta\beta_{dra}}\right]\right\} \tag{4.1}$$

$$P_{NL} = \left(\frac{D}{3}\right)^2 P_iP_jP_k\left|\gamma_{smf}\frac{e^{[(-\alpha_{smf}+i\Delta\beta_{smf})L_{smf}]}-1}{-\alpha_{smf}+i\Delta\beta_{smf}}\right. \\ \left. + \gamma_{dra}e^{\left[(-\alpha_{smf}+i\Delta\beta_{smf})\frac{L_{smf}}{2}\right]}\frac{e^{[(g_{dra}+i\Delta\beta_{dra})L_{dra}]}-1}{g_{dra}+i\Delta\beta_{dra}}\right|^2 \tag{4.2}$$

For N identical span, the nonlinear power can be deduced down to the below equation (4.3) [39].

$$P_{NL,N} = \left(\frac{D}{3}\right)^2 P_iP_jP_k\left[\frac{\sin^2(N\Delta\beta L)}{\sin^2(\Delta\beta L)}\right]\left|\gamma_{smf}\frac{e^{[(-\alpha_{smf}+i\Delta\beta_{smf})L_{smf}]}-1}{-\alpha_{smf}+i\Delta\beta_{smf}}\right. \\ \left. + \gamma_{dra}e^{\left[(-\alpha_{smf}+i\Delta\beta_{smf})\frac{L_{smf}}{2}\right]}\frac{e^{[(g_{dra}+i\Delta\beta_{dra})L_{dra}]}-1}{g_{dra}+i\Delta\beta_{dra}}\right|^2 \tag{4.3}$$

The above equation (4.3) represents the nonlinear accumulated power ($P_{NL,N}$) after N identical transmission and amplification span. Here, D is the degeneracy factor where D =1 when,($\omega_i = \omega_j = \omega_k$), D =3 when, ($\omega_i = \omega_j \neq \omega_k$) and D =6 when, ($\omega_i \neq \omega_j \neq \omega_k$). The sine term in the left hand of the equation (4.3) is an integral power addition after N periodic unit cell. P_i, P_j and P_k are the power profile of the three nonlinear components interacting the channel of interest. N is the number of periodic unit cell (SSMF+DRA) transmission spans, $\Delta\beta_{smf}$ and $\Delta\beta_{dra}$ is the phase matching coefficient of the SSMF and DRA fibre section which can be represented by the below equation (4.4)[208].

$$\Delta\beta_{smf/dra} = \frac{2\pi\lambda_c^2}{c}(\omega_i - \omega_j)(\omega_i - \omega_k)CD_{smf/dra} \tag{4.4}$$

Where, λ_c is the wavelength of the channel of interest, c is the speed of light and $CD_{smf/dra}$ is the CD of the SSMF or DRA section. $L = L_{smf} + L_{dra}$ is the sum of SSMF and DRA fibre span

length, $\Delta\beta L = \Delta\beta_{smf} L_{smf} + \Delta\beta_{dra} L_{dra}$ is the effective phase-matching coefficient for each periodic unit cell, α_{smf} is the attenuation coefficient of the SSMF at the channel wavelength, g_{dra} is the Raman gain coefficient of the DRA fibre section, γ_{smf} is the nonlinear coefficient of the SSMF section and γ_{dra} is the nonlinear coefficient of the DRA section. Using the total nonlinear and linear noise the system performance can be estimated by the below equation (4.5)

$$SNR = \frac{P_{sig}}{P_{ASE} + P_{NL/N}} \tag{4.5}$$

Here, SNR is the signal to the noise ratio, P_{sig} is the signal power spectral density, P_{ASE} is the linear amplified spontaneous emission (ASE) noise and $P_{NL/N}$ is the accumulated nonlinear noise after the N transmission span. The obtained SNR can be converted into its correspondence performance metrics (Q^2 factor) using the relation presented in [17].

As can be seen from the above equations (4.2) and (4.3) that the total nonlinear accumulated noise is a dependent function of the phase matching coefficient $\Delta\beta$ which linearly depends on the sign and value of fibre chromatic dispersion [231,232]. Hence, it is important to study different Raman gain fibre types with varying values of CD to minimize the accumulated nonlinear noise. In a Raman amplified transmission link a typical Raman gain fibre length is in few km which in the case of a long-haul system adds up to a few hundred km hence the value of fibre CD can strongly impact the overall system performance. It is to be noted that a Raman fibre with a low nonlinear coefficient (γ) too will reduce the total accumulated nonlinear noise. However, a lower value of (γ) might also result in insufficient gain due to the lower value of the Raman gain coefficient (g_{dra}) and the power requirements of the commercially available pumps.

4.2.1 Parameter optimization with the analytical model for optimal performance

Investigation with the analytical model was initially performed to understand the best possible combination of fibre links with different span lengths for 1800 km signal transmission i.e., 40x45 km, 36x50 km, 30x60 km, 20x90 km, and 15x120 km. The validation was performed using a 30 GBaud channel at 1550 nm with a gain fibre of similar characteristics as DCF as shown in Table 4.1 in the DRA stage of the transmission link.

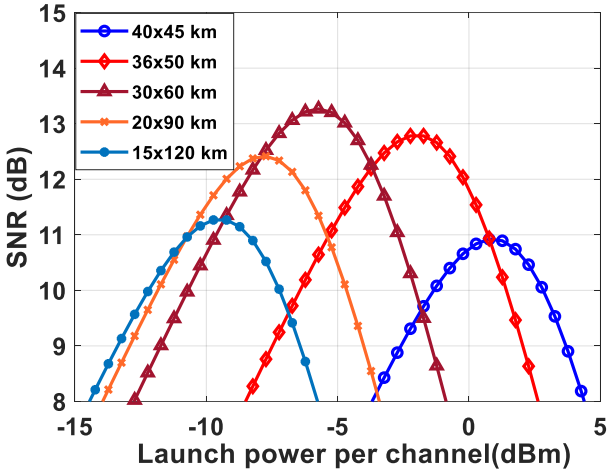

Figure 4.3 Q^2 factor vs launch power per channel (@1550nm) for 1800 km with varying SSMF span length amplified using DRA

The optimum launch power for single-channel transmission for a different combination of span lengths is shown in Figure 4.3. The simulation results indicate that the combination of 30x60 is the best choice for optimum performance. This is likely because for lower number span lengths to achieve a target distance the number of amplifiers required will be more resulting in a larger accumulation of linear ASE noise, whereas for longer span lengths the accumulated signal will undergo higher power loss resulting in a lower value of the received optical signal to noise ratio (OSNR). Hence, it is important to choose the correct span length for the optimal performance of a transmission link. However, for all the subsequent modelling and experimental validation, an SSMF span length of 63 km was chosen, as it was the available spool length in our facility and can be assumed to have a similar performance to that of a 60 km fibre length.

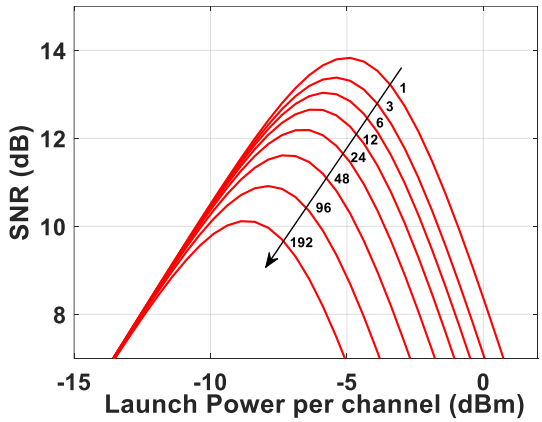

Figure 4.4 Q^2 Factor vs Launch power channel for the different number of 30GBaud transmitted channels at 30x63 km of transmission distance.

The impact of increasing the number of channels from 1 to 96 for a 30 GBaud channel bandwidth at 1550 nm after a 30x63 km transmission distance is illustrated in Figure 4.4. The SNR vs launch power per channel shows a performance penalty of ~3.8 dB with an increase in the channel

number from 1 to 192. A shift towards the lower launch power can be observed with an increase in channel number, this is likely due to the accumulation of higher nonlinear noise with an increase in channel numbers.

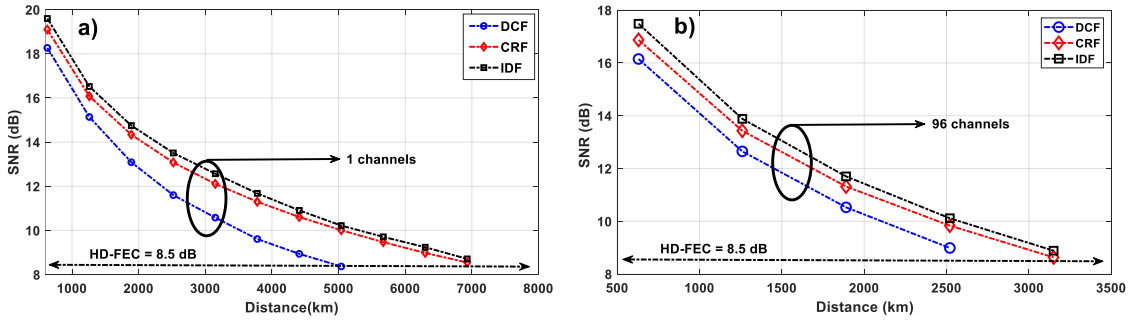

Figure 4.5 Peak SNR vs maximum transmission distance within an HD-FEC of 8.5 dB for a) 1 channel b) 96 channel

Figure 4.5(a-b) illustrates the estimated theoretical maximum SNR for 30 GBaud 96 PM-QPSK, Nyquist-WDM, and single-channel transmission. The modelling was performed with a single span length of 63 km with DCF, IDF, and CRF as the gain fibre in the DRA stage of the transmission link. The modelling parameters of all the fibres used in the simulation were taken from Table 4.1 Summary of IDF, DCF, and CRF fibre parameters used for the analytical modelling. Modelling results show an enhanced performance for IDF and CRF fibre over its counterpart DCF with maximum transmission distance reaching out to ~7000 and ~3200 km for 1 and 96 WDM channels. Whereas, in the case of DCF, this reach was ~5000 and ~2500 km for 1 and 96 WDM channels within an HD-FEC threshold of 8.5 dB.

4.2.2 Raman amplifier parametric analysis using the analytical model

This section involves studies on the performance of DRAs using the above-mentioned model, analysing the parametric dependence of fibre CD and fibre nonlinear coefficient (γ) on the performance penalty. The overall performance of a coherent transmission system depends on multiple parameters of both the transceivers and the amplifiers [233]. In the amplifier section of a transmission system, the parameters that likely impact the transmission performance are the gain and noise figure (NF) of the amplifier. However, in the Raman amplifiers, an additional impact of nonlinear noise also needs to be considered particularly for a long-haul transmission due to the finite length of the gain fibre in km.

The length of the gain fibre for achieving a target net gain can vary significantly with the different fibre types. Fibres such as highly nonlinear fibre with a typical Raman gain coefficient (g_r) of 6.3 $W^{-1}km^{-1}$ require a lower length in comparison to a fibre with a lower Raman gain coefficient (g_r) (e.g., SSMF) for achieving a target gain. However, these high nonlinear fibres do suffer from high power loss due to their large attenuation coefficient resulting in pump power

depletion and at the same time will add higher nonlinear noise. Similarly, to achieve the same net gain with IDF, the length required will be slightly longer [234] and will require increased pump powers. In wideband WDM systems, other effects such as Rayleigh scattering also play a role in limiting the performance of a DRA transmission system. This effect dominates in the regime where the pump wavelength overlaps with the signal wavelength. However, studies have shown that with the appropriate insertion of a narrow guard band between the pump and signal wavelengths, this effect can be minimized [235][236].

Another important parameter that can impair the transmission performance of a DRA-assisted fibre link is the gain fibre CD. The total accumulation of CD (SSMF+DRA) causing pulse broadening can be compensated using the standard digital signal processing (DSP) [236] procedure in the receiver chain for signal recovery. However, CD in the gain fibre of the DRA stages also varies the nonlinear accumulated noise for a given channel of interest as explained previously in section 4.2.1. Hence, to study the extent of nonlinear noise accumulation with fibre CD, a hypothetical DCF-like fibre was considered as depicted in Table 4.1 as a gain fibre in the DRA stage of the analytical model. The standard SSMF fibre length was taken at 63 km matching the parameters of Table 4.1. The CD of this hypothetical test fibre was varied from -100 ps/nm/km to 40 ps/nm/km. In terms of channel parameters, the study was performed using a Nyquist 30 GBaud channel at 1550 nm and the performance penalty with the variation in CD was observed after 30 span transmission (30x63 km). The input launch power to the SSMF was varied and the corresponding SNR was calculated using the achieved nonlinear noise and a constant linear ASE noise of the amplifier using equation (4.5). The modelling results show SNR improvement of ~2.1 dB with CD variation from -100 ps/nm/km to 40 ps/nm/km, as illustrated in Figure 4.6(a). This test case also somewhat resembles a comparison between DCF and CRF, whose parameters are nearly identical, except for the value of fibre CD whose value is positive (11.7 ps/nm/km) for CRF and negative for DCF (-96 ps/nm/km) as shown in Table 4.1. The modelling results for this test case show that a Raman gain fibre with positive CD is a better choice for a DRA-assisted transmission system, where the accumulated nonlinear noise is limited due to the positive CD of gain fibre.

The nonlinear accumulated noise will also increase due its linear dependency of the on the fibre nonlinear coefficient (γ) as shown in equation (4.3). Although it's obvious that a low value of the nonlinear coefficient is always preferable for reducing the accumulated nonlinear noise. However, a lower value of the nonlinear coefficient (γ) might also result in insufficient gain due to the lower value of the Raman gain coefficient (g_{dra}) which eventually will require higher pump powers to achieve a target gain and with the limited availability of power in commercial pumps the net gain can get reduced. Hence, to analyse the performance penalty in a fibre link with varying values of (γ), the SNR vs launch power in a 30x63 km SSMF link was calculated with

another hypothetical DCF-like gain fibre in the DRA stage. For this case, all the parameters of the hypothetical DCF were fixed along with the fibre CD (-96 ps/nm/km) and the nonlinear coefficient which varied from 2 to 9 $W^{-1}km^{-1}$. The modelling results in Figure 4.6(b) show a maximum SNR variation of ~1.3 dB over the range of nonlinear coefficient variation from 2 $W^{-1}km^{-1}$ to 9 $W^{-1}km^{-1}$. Overall, the results of Figure 4.6(a) and (b) suggest that a DRA fibre with high positive dispersion (>10 ps/nm/km) and a relative nonlinear coefficient (< 4 W^{-1} km^{-1}) would be a good choice for DRA-assisted coherent transmission systems. The values of CD and nonlinear coefficient would be more critical for higher cardinality (e.g. 64 QAM, 128 QAM) modulating signal where the received SNR is critical in determining the performance of an optical link [237].

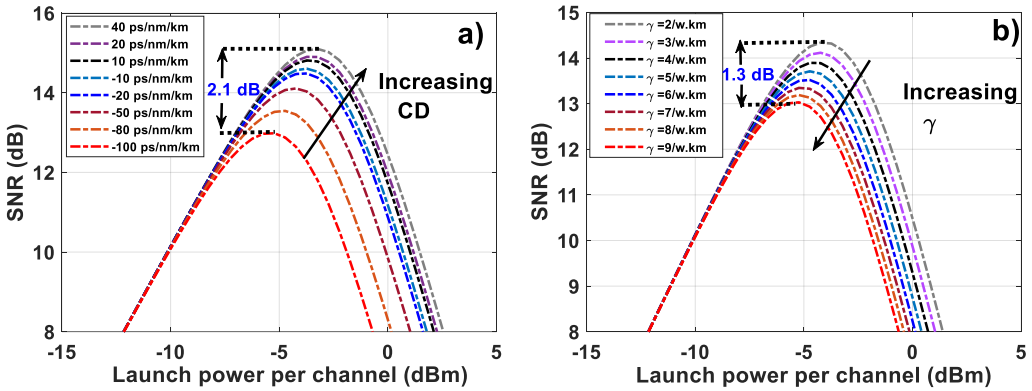

Figure 4.6 SNR vs Launch power per channel to SSMF (single channel @1550 nm) for 30x63 km of transmission with varying a) chromatic dispersion b) nonlinear coefficient

4.3 Experimental validation with single-channel transmission

To validate the assumption on the impact of CD and selection of optimized nonlinear coefficient (γ) for minimizing the accumulated nonlinear noise. A long-haul transmission experiment was performed with a 23 GBaud single-channel transmission at 1550 nm using a recirculation loop. In this experiment, the accumulation of nonlinear noise is only due to the interacting components of a single channel.

4.3.1 Recirculation loop experimental setup

The schematic for the recirculation loop transmission experiment is illustrated in Figure 4.7. The transmitter section includes a 23 GBaud PM-QPSK modulated signal at 1550 nm generated using a 120 GSa/s DAC and a standard C- Band $LiNbO_3$ DP-IQ modulator. The modulated signal was then passed through a C- band EDFA and variable optical attenuator (VOA) for input launch power sweep.

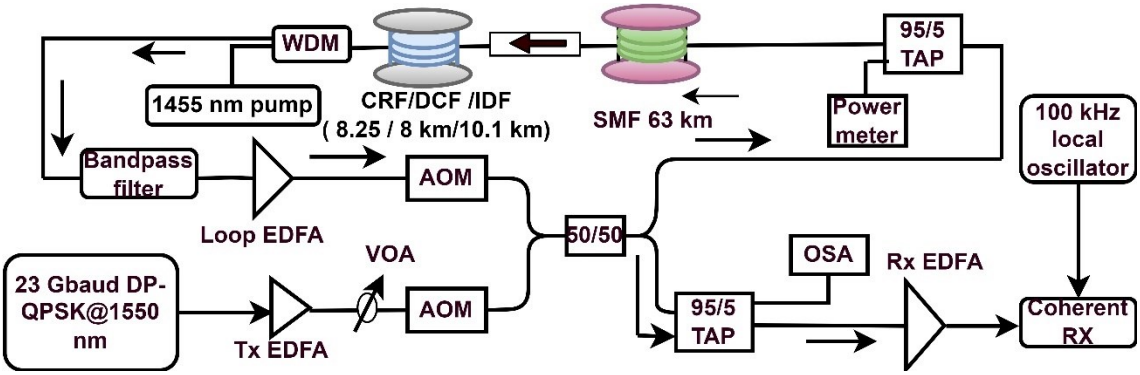

Figure 4.7 Recirculation loop experimental setup for a single channel 23 GBaud PM-QPSK transmission

The recirculation loop comprised two acousto-optic modulators (AOMs) and a 50/50 coupler for power insertion to the transmission fibre. The AOMs are practically an optical switch for filling the loop and recirculating the signals in the loop. The transmission section included a 95/5 tap for monitoring the input launch power to the test fibre followed by a 63 km SSMF with a span loss of 12.4 $\pm$ 0.2 dB. The DRA section comprises either CRF, DCF, or IDF fibre with a span length of 8.25 km, 8 km, and 10.1 km. The DRA gain fibre was pumped using a backward pumped fibre laser at 1455 nm coupled to the gain fibre using a high-power filtered WDM. The required pump powers were ~380 mW, ~448 mW, and ~521 mW for CRF, DCF, and IDF fibres. The amplified signal after the DRA section was then passed through a bandpass filter to filter out the unwanted noise. An additional EDFA (loop EDFA) was inserted in the loop section to compensate for the additional loss of ~13 dB due to the AOM, 3 dB coupler, bandpass filter and additional loss due to 95/5 tap, optical isolators and connectors.

The receiver chain included a 95/5 tap to monitor the out spectrum and the OSNR followed by an Rx-EDFA operation at an output power mode into the optical hybrid whose design is shown in Figure 2.17 followed by the photodiodes for optimal operation [238]. The transmitted signals were then mixed with a 100 kHz linewidth local oscillator and the corresponding traces were captured using a 28 GHz bandwidth real-time oscilloscope. The coherent detection was then followed by a standard offline DSP on the captured traces to recover the transmitted data. The recovered symbols together with the transmitted symbols were then used to measure the received bit error rate (BER) [141,239] which was then converted into its corresponding Q^2 factor for QPSK signals[17].

4.3.2 Results and discussions

The transmission performance with DCF and CRF as gain fibre in the recirculation loop for 20x63 and 30x63 km of transmission distance is illustrated in Figure 4.8(a-c). This test case was performed to validate the effect of fibre CD on the nonlinear accumulated noise solely due to SPM in the transmitted signal. The experimental results were validated with the results obtained

from the analytical model and a maximum difference of < 1 dB was obtained for the peak Q^2 factor difference between the modelling and experimental results.

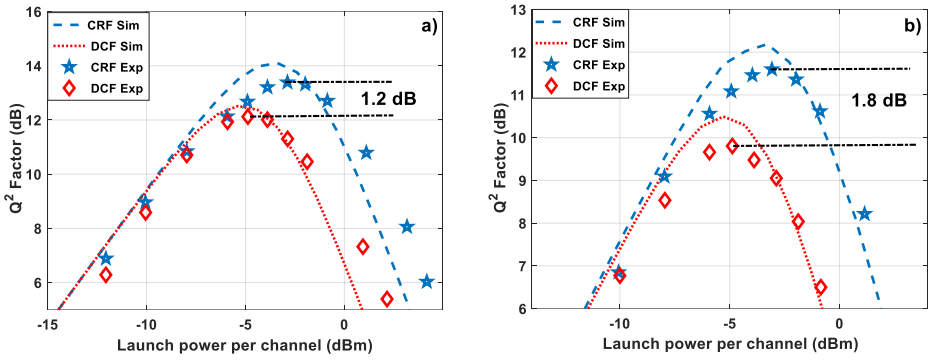

Figure 4.8 Q^2 Factor vs Launch power per channel for 23 GBaud PM-QPSK single channel transmission with CRF and DCF as gain fibre for a) 20x63 km b) 30x63 km transmission distance

The experimental and modelling results show an enhanced transmission performance with CRF (blue star markers [experimental] and blue dashed line [simulation]) as gain fibre in the DRA stage than in counterpart DCF (red diamond markers [experimental] and red dotted line [simulation]). The maximum Pk-Pk performance (Q^2 factor) difference was observed to be 1.2 dB and 1.8 dB for 20x63 and 30x63 km of transmission distance respectively. Considering the case of DCF and CRF for a 30x63 km transmission distance, a Pk-Pk difference of ~2 dB was obtained between the modelling results of Figure 4.6(a) and the experimental results of Figure 4.8 (c). This is due to the additional loss exerted by the loop EDFA in the experiment with an NF of ~6 dB. In the case of modelling results shown in Figure 4.8(a-c), the NF of the loop EDFA was considered as a linear addition of noise to the below SNR equation (4.6) which was then correspondingly converted into Q^2 factor performance metrics for PM-QPSK signals using the conversion method explained in [17].

$$SNR = \frac{P_{sig}}{P_{ASE,(Raman)} + P_{ASE,(EDFA)} + P_{NL/N}} \tag{4.6}$$

Also, the difference Q^2 factor between CRF and DCF in the nonlinear regime of Figure 4.8(a-b) increases with an increase in the span number from 20 to 30, clearly indicating that the nonlinear noise accumulation for DCF is larger due to its high negative value of fibre CD impacting the overall transmission performance. The test cases from the above results indicate that a fibre with a positive value of CD is a better choice for DRA assisted transmission system as it limits the total accumulated nonlinear noise due to a higher value of phase mismatching.

The second study was performed comparing the transmission performance of CRF and IDF as the gain fibre in the DRA section of the recirculation loop. This study was primarily performed to understand the nonlinear noise accumulation with a varying value of the nonlinear coefficient (γ).

Although IDF has a negative value of fibre CD (Table 4.1) however, a direct comparison between CRF and IDF is not ideal, because the NF of DRA with IDF and the attenuation coefficient of IDF is lower than its competitor CRF. Nevertheless, the experiments were continued with IDF in the DRA stage due to the absence of a fibre type with a similar parameter as IDF with an additional positive dispersion.

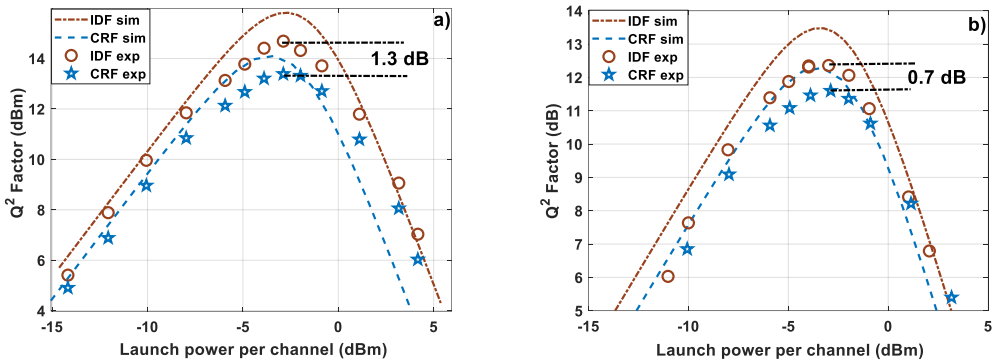

Figure 4.9 Q^2 Factor vs Launch power per channel for 23 GBaud PM-QPSK single channel transmission with CRF and IDF as gain fibre for a) 20x63 km b) 30x63 km transmission distance

The experimental and modelling results show a slightly improved performance of IDF (brown circle markers [experimental] and brown dashed-dot line [simulation]) over CRF (blue star markers [experimental] and blue dashed line [simulation]) for a transmission distance of 20x63 and 30x63 km as shown in Figure 4.9(a-c). The Pk-Pk Q^2 factor difference of the experimental results was ~ 1.3 dB and ~0.7 dB for 20x63 and 30x63 km of transmission distance. This enhanced performance of IDF over CRF despite its negative value of fibre CD can be well attributed to the lower value of linear NF of the DRA, low fibre attenuation, and the lower value of fibre nonlinear coefficient (γ) improving the overall transmission performance.

However, an interesting observation to note here is unlike the previous test case where an increment in the Pk-Pk Q^2 factor difference was observed with an increase in transmission distance, here the Pk-Pk Q^2 factor can be seen to be decreasing with an increase in the transmission distance. Apart from the increment in the Pk-Pk Q^2 factor, a decrement in the difference in the Q^2 factor in the nonlinear regime of the bell curve can be observed with an increase in the span number from 20 to 30 Figure 4.9(a-b). Whereas, for the test case with CRF and DCF the difference in the Q^2 factor value between CRF and DCF was seen to be increasing with an increase in the span number from 20 to 30.

This effect is likely due to the accumulation of positive CD in CRF with an increase in the transmission distance, but this distance is insufficient to accumulate enough positive CD for CRF to outperform IDF in terms of overall system performance. Nevertheless, the modelling and experimental results are sufficient to infer that a fibre with positive CD is a better choice for DRA

assisted transmission system in contrast to a fibre with negative CD in a DRA-assisted transmission system. Also, with the positive value of CD any developed fibre with a low attenuation profile and nonlinear coefficient (γ) similar to that of IDF would be a very suitable candidate for DRA based coherent transmission system for long-haul communication.

4.4 Experimental validation with WDM transmission

The experimental validation with single-channel transmission is not sufficient to claim the performance enhancement due to fibre type with positive CD as the nonlinear accumulated noise is dominantly due to the nonlinear noise of a single channel, inter-channel crosstalk between the channels is not dominant due to the absence of any neighbouring channels. In a standard optical link, WDM transmission is generally performed where nonlinear effects such as SPM, XPM and FWM effects significantly increases with an increase in transmission distance. To validate the analytical model in the presence of WDM signals and to observe the total impact of CD and nonlinear coefficient (γ) on the transmission performance, a recirculation loop experiment was performed using 10 WDM channels. The transmission was restricted to only 10 channels as the dominant nonlinear noise on a centre channel of interest is predominantly to be due to its neighbouring channels.

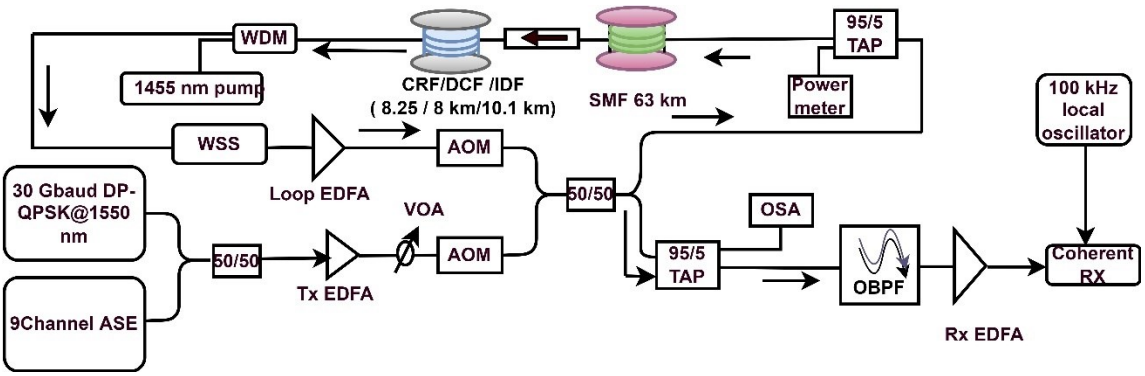

Figure 4.10 Recirculation loop experimental setup for a WDM transmission with a 30 GBaud PM-QPSK modulating signal coupled with 9 ASE channels

4.4.1 Recirculation loop experimental setup

The schematic of the recirculation loop for WDM transmission is illustrated in Figure 4.10. The experimental setup is somewhat similar to that of a single-channel recirculation loop transmission setup as shown previously in Figure 4.7. Here, for the WDM grid, nine spectrally shaped ASE signals of 50 GHz in bandwidth were generated using a commercial C- band waveshaper and C-band EDFA. The generated ASE signals were then coupled with a 30 GBaud PM-QPSK signal at 1550 nm generated using a commercial transponder to form a 10-channel WDM grid extending from (1546.05 – 1553.3 nm). The WDM signals were passed through a transmitter (Tx) C- band EDFA and a VOA for launch power sweep.

The recirculation loop setup is similar to the one previously explained in section (4.3.1). The transmission and the gain fibre length too were of the same value as taken for the single-channel transmission. The required pump powers for the DRA stage with CRF, DCF, and IDF were 380 mW, 448 mW and 521 mW. No major changes were observed in the values of pump powers due to the use of only a single pump which was sufficient to compensate for the span loss over a bandwidth of ~8 nm. A dynamic waveshaper was used for the spectral flattening after each recirculation. An additional loss of ~18 dB due to the AOMs, waveshaper 3 dB coupler, 99/1 tap and optical isolators were compensated using an EDFA with an NF of ~6 dB.

The receiver (Rx) section comprises of a 95/5 tap whose 1% was used to capture the output spectrum and the remaining 95% was passed through an optical bandpass filter tuned at a central frequency of the modulating signal. The filtered signal was then passed through an Rx-EDFA operating at a constant output power mode to provide constant output power for optimized operation of the coherent receiver. A narrow linewidth laser source of 100 kHz was tuned at the frequency of the modulating signal (@1550 nm) and was then mixed with the modulated signal using a 90° hybrid for balance detection. The detected symbols were then captured using an 80 GSa/s, 36 GHz bandwidth real-time oscilloscope. The raw traces were captured and processed using a standard offline DSP for data recovery, a procedure similar to the one explained in section (4.3)

The input and output optical spectra after 10 and 20 recirculation can be seen below in Figure 4.11(a-d) and Figure 4.12(a-d). A maximum spectral tilt of +/- 1.75 dB was observed for all the test cases. From the spectrum, one can also see a higher noise floor i.e., low OSNR in the vicinity of wavelengths < 1551 nm this can be likely due to the combined NF of all the EDFA and the DRA where a wavelength-dependent gain is practically required for minimal channel ripple in a coherent WDM system. Also from Figure 4.11(b-d) and Figure 4.12(b-d) an increase in the ASE noise floor was observed for all the channels with an increase in the recirculation number from 10 to 20.

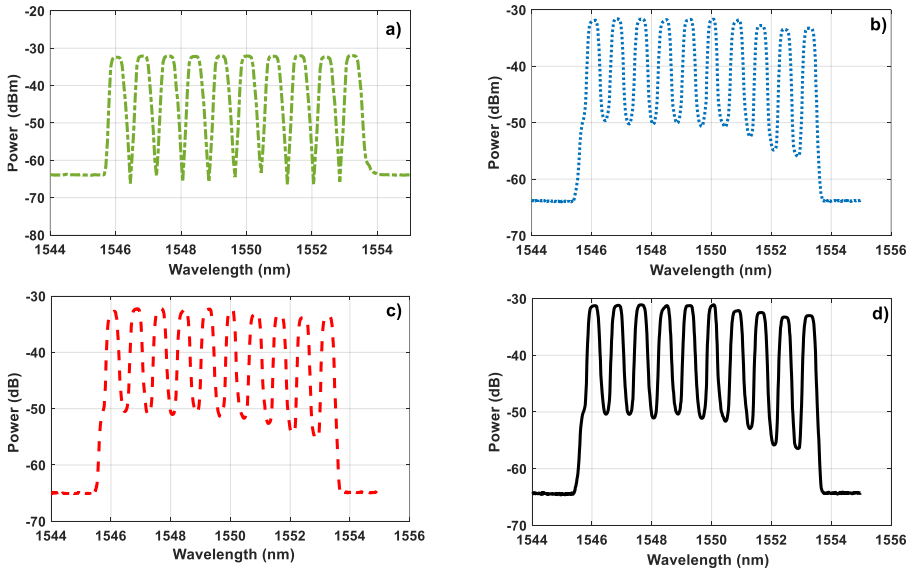

Figure 4.11 Optical spectrum of 10 WDM channels a) Input spectrum; 10 span transmission with DRA stage comprising of b) DCF c) CRF d) IDF fibres

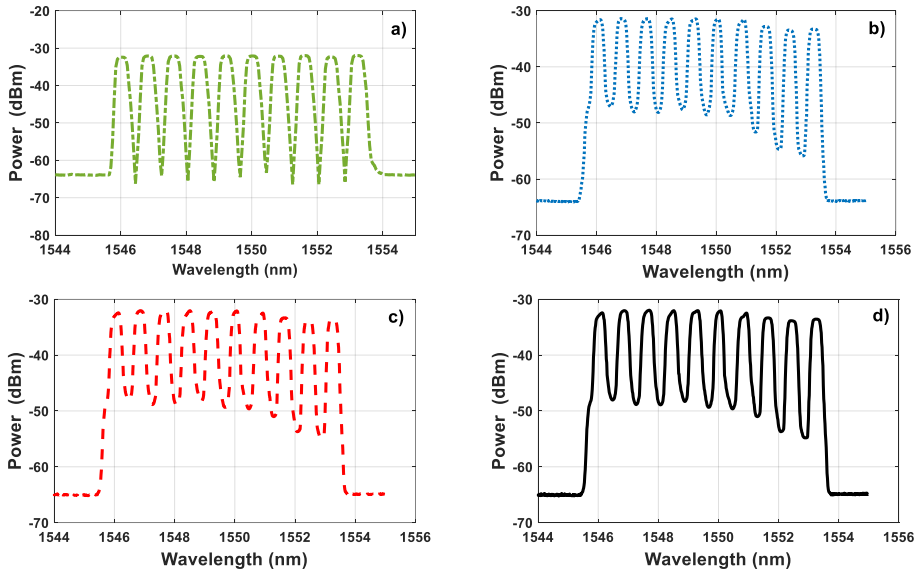

Figure 4.12 Optical spectrum of 10 WDM channels a) Input spectrum; 20 span transmission with DRA stage comprising of b) DCF c) CRF d) IDF fibres

4.4.2 WDM transmission results and discussion

Similar to the test case with a single channel, two test cases were studied for this set of experiments. Test case 1 comparison with DCF and CRF fibre to analyse the performance penalty in presence of a positive CD DRA and negative CD DRA. The modelling predictions are in good agreement with the experimental results where enhanced performance of CRF (blue star markers [experimental] and blue dashed line [simulation]) over DCF (red diamond markers [experimental] and red dotted line [simulation]) in the DRA amplification stage was obtained. The maximum peak Pk-Pk Q^2 factor difference for the experimental results was ~0.8 dB and ~1 dB for 20x63

km and 30x63 km of transmission distance, respectively. The modelling results are also in good agreement with the experimental results and a maximum discrepancy of < 0.8 dB was observed for both test cases. Similar to the previous test case a single channel NF of 6 dB for the loop EDFA was added during the analytical modelling and the corresponding performance metric was calculated. The experimental results in Figure 4.13(a-b) suggest that the addition of residual dispersion in the DRA stages impacts the overall performance of a DRA-assisted transmission system and the penalty for this accumulated nonlinear noise is larger for a negative CD fibre compared to a positive CD fibre, implying that fibre with positive CD is a better choice for DRA assisted WDM systems. Similar to the test case with a single channel, in the WDM system also an increase in the difference of the Q^2 factor was observed in the nonlinear regime of the bell curve (Figure 4.13(a-b)) indicating the lower nonlinear noise accumulation in positive CD gain fibre.

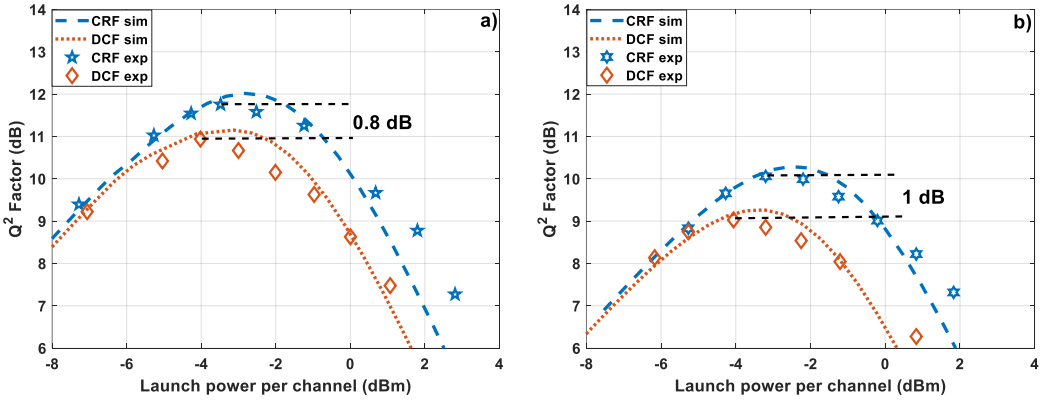

Figure 4.13 Q^2 Factor vs launch power per channel, experimental and analytical modelling results with CRF and DCF fibre for a) 20x63 km b) 30x63 km transmission.

The second test case included WDM transmission with CRF and IDF as gain fibre in the DRA stage of the transmission link. Figure 4.14(a-b) shows experimental and modelling results after 20x63 and 30x63 km of transmission. Likewise, the previous results from single channel transmission the obtained WDM experimental results show a slightly enhanced performance of IDF (brown diamond markers [experimental] and brown dashed-dot line[simulation]) over CRF (blue star markers [experimental] and blue dashed line [simulation]) with the Pk-Pk Q^2 factor variation from ~0.4 dB to ~0.35 dB after 20 and 30 recirculation. Similarly, the modelling results are in close agreement with the experimental values, with a maximum discrepancy of < 0.8 dB for both test cases. The better performance of IDF over CRF can be attributed to its lower nonlinear coefficient (γ) and lower NF in the region of operation.

Similarly, a decrement in the Pk-Pk Q^2 factor from ~0.4 dB to ~0.35 dB was observed with an increase in span number from 20 to 30, unlike the previous case with DCF and CRF where an increment in the Q^2 factor was observed with an increase in span number from 20 to 30. A slight

shift in the performance of CRF towards the nonlinear regime too can be observed making the difference between the Q^2 factor smaller between IDF and CRF in the nonlinear regime. This effect was observed in both single and WDM transmission in CRF and IDF, clearly indicating that the accumulation of positive CD can be an important parameter in lowering the total nonlinear noise, but the overall system performance depends on both the linear and nonlinear noise components. IDF benefits from its low nonlinear coefficient (γ), lower NF, and lower attenuation coefficient (α), whereas CRF has an advantage over its positive CD value, but it is insufficient to result in CRF outperforming IDF in terms of overall system performance. Nevertheless, the analytical model matches quite well with the experimental results and the predictions on the performance benefit of using Raman gain fibre with positive CD can be claimed with the experimental results obtained in sections 4.2 and 4.4. From the transmission performance with both single and WDM channels (section 4.2 and section 4.3), one can also conclude that a positive dispersion fibre with a value of nonlinear coefficient similar to that of IDF would be a better choice as a gain fibre in the DRA stage of a transmission system.

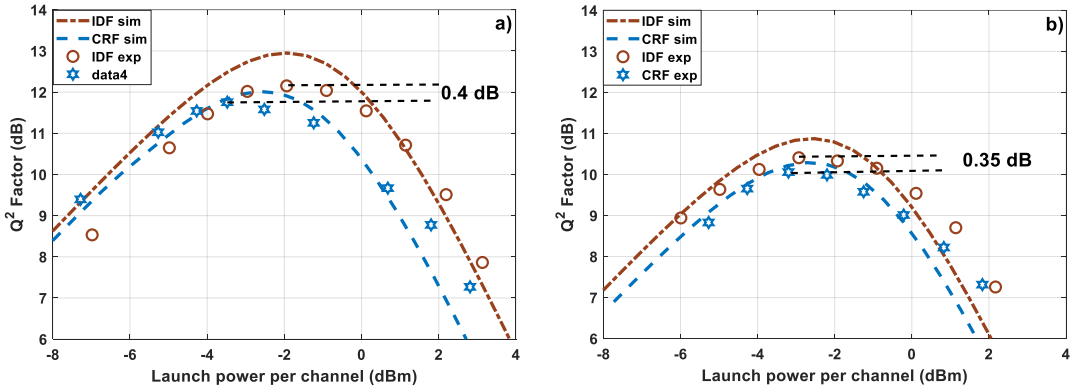

Figure 4.14 Q^2 Factor vs launch power per channel, experimental and analytical modelling results with CRF and IDF fibre for a) 20x63 km b) 30x63 km transmission.

In addition to the above results, the maximum transmission reach at the optimum launch power with each DRA gain fibre (Figure 4.15(a)) was measured assuming an HD-FEC threshold of 8.5 dB. As expected, CRF and IDF outperformed DCF in terms of the Pk-Pk Q^2 factor with a maximum transmissible distance extending out to ~ 2600 km, whereas for DCF this distance was limited to ~ 1900 km. The peak Q^2 factor for DCF in the DRA stage was found to be lower when compared to both CRF and IDF in the DRA stage for a given transmission distance, with a linear increase in the difference with an increment in transmission distance.

The Q^2 penalty shown in Figure 4.15 (b) represents the maximum Pk-Pk Q^2 factor difference between the two test cases. For the first case, the Q^2 penalty between CRF and DCF (blue dashed line circles marker) has a positive slope with an increase in transmission distance, with a maximum penalty of ~1 dB at ~1900 km. The positive slope of the penalty curve indicates that

the residual CD in positive fibre improves the overall transmission performance. Hence, a fibre with a positive value of CD is a better choice than its counterpart negative CD for a DRA-assisted system and in particular, this effect is more dominant when implemented over a long-haul coherent WDM system.

In comparison to CRF and DCF, the Q^2 penalty between IDF and CRF in Figure 4.15(b) shows a negative slope (red dashed line with diamond markers) with an increase in transmission distance. The Q^2 penalty decreased from ~ 0.7 dB at 600 km to ~0.3 dB at 2600 km. The decrement in Q^2 penalty indicates that the accumulation of positive CD in CRF reduces the accumulated nonlinear noise with an increase in distance however, due to the lower nonlinear coefficient (γ) and lower linear NF of the IDF, CRF is unable to exceed in terms of performance in comparison to IDF within the assumed range of HD-FEC limit of 8.5 dB. However, this advantage of IDF over CRF comes at a cost of higher pump power required for achieving a target gain.

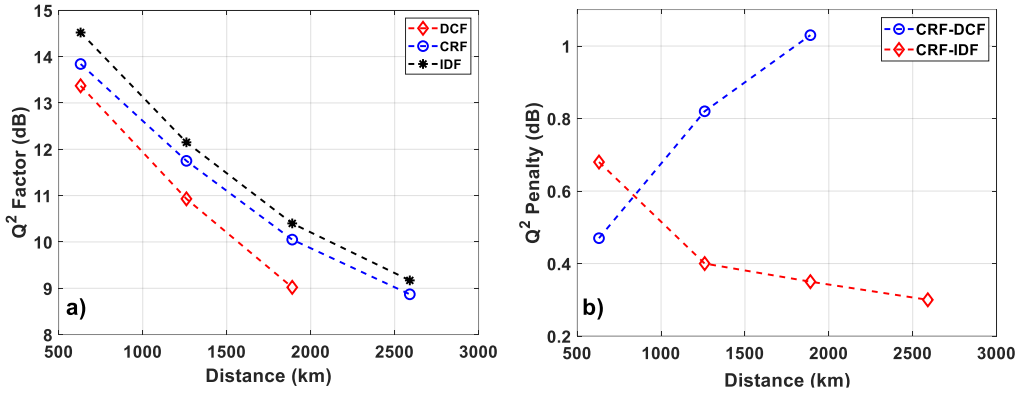

Figure 4.15 10 Channel 30 GBaud PM-QPSK transmission a) Q^2 Factor vs Distance b) Q^2 penalty (CRF-DCF and CRF-IDF) vs Distance

4.5 Conclusion

In this chapter, an analytical model has been introduced to calculate the nonlinear product power in a coherent system with DRAs as an inline amplifying medium. Together with the linear ASE noise, the model enables the evaluation of the performance penalty and optimum launch power in the region of operation. The analytical model was initially analyzed to estimate the appropriate span length for 1800 km transmission, and the results showed that a fibre length of ~60 km is a good choice for optimal performance. Further analysis was carried out to determine the impact of CD and the nonlinear coefficient on the accumulation of nonlinear noise in a DRA transmission system. The analytical modelling results showed that a positive dispersion gain fibre is a better choice than a negative dispersion fibre for a DRA-assisted transmission system.

The experimental investigation was initially performed to validate the analytical model, primarily to study the impact of CD and nonlinear coefficient variation on the total accumulated nonlinear noise. This experimental validation was performed using a 23 GBaud PM-QPSK modulated

signal at 1550 nm over a recirculation loop. The initial experimental results with CRF and IDF in the DRA stage showed an enhanced performance of CRF over DCF for 20x63 km and 30x63 km of transmission distance. The second set of test cases involved IDF and CRF as gain fibres in the DRA transmission system where a slightly improved performance of IDF over CRF was observed. For all the test cases a maximum discrepancy of <1 dB was observed between the modelling and the experimental results.

The second set of experimental investigations was performed in a WDM scenario. Similar to the previous case of single channel experimental, results with 10 channel WDM too showed an improved performance of CRF over DCF for 20x63 km and 30x63 km of transmission distance. This enhanced performance can be attributed to the accumulated residual dispersion arising due to the positive value of fibre CD in CRF. In addition to this, an increment in the Q^2 factor difference between the two test fibres was observed with an increase in the recirculation number from 20 to 30. This indicates the performance enhancement of CRF over DCF in the nonlinear regime over an incremental transmission distance.

In the second experimental validation with IDF and CRF as gain fibres, a slightly improved performance of IDF over CRF was observed. This improved performance of IDF over CRF is likely due to the lower accumulation of nonlinear noise due to its smaller nonlinear coefficient (γ) and a lower value of linear NF improving the overall system performance. However, this benefit of IDF over DCF comes with the cost of high pump power requirements which can be critical in wideband transmission scenarios due to the limited pump power availability in commercial pumps.

The maximum transmission reach with IDF and CRF in the DRA stage was ~2600 km, whereas for DCF it was ~1900 km. In addition, a positive slope for the Q^2 penalty was observed in the transmission performance of CRF and DCF, clearly indicating the improved performance of positive CD fibre versus negative CD fibre. In contrast, a negative slope for the Q^2-penalty between IDF and CRF was observed, indicating a slight performance improvement of IDF over CRF.

Overall, the experimental results support the predictions of the analytical model and conclude that a Raman gain fibre with positive CD is a better choice than a fibre with negative CD for coherent WDM transmission systems. In addition to this, the experimental and analytical model demonstrates that a fibre type of similar parameters as IDF with an additional positive CD would be an ideal choice of Raman gain fibre for long-haul communication systems.

Chapter 5: RIN-induced penalties in distributed Raman amplifiers

In this chapter, the accumulation of relative intensity noise (RIN) in two standard single mode fibre (SSMF) G.652.D and ultra-low loss (ULL) G.654.E© TXF fibre is studied experimentally. The detailed description of RIN accumulation in distributed Raman amplifiers has been discussed in section 3.3.2 of chapter 3. However, the parametric dependence of RIN on fibre chromatic dispersion (CD) resulting in a pump signal walk-off can be an interesting study to understand the nature of RIN accumulation in different fibre types with different pumping configurations. RIN is a dominant parameter in forward (FW) pumping where the gain dynamics of the Raman amplification process couples the pump RIN efficiently leading to a signal degradation impacting overall performance [240]. However, a combination of both FW and backward (BW) schemes also known as bidirectional (BI) pumping too is interesting, particularly for transmission systems that require high OSNR and systems with longer span lengths. Hence, the study of RIN-induced penalties is very relevant for systems where the demand for high OSNR per transmission distance is important.

The approval of G.654.E by ITU-T as a new fibre for the terrestrial network [241] has led the scientific community to proceed with practical investigation such as cabling, splice loss and applicability of ULL fibre for Raman amplification [242]. The large effective (A_{eff}) of this fibre can provide spectral bandwidth enabling larger channel capacity over a longer reach [243]. Long-haul transmission with ULL fibre has been shown to have a 55% longer transmission reach than the standard G.652.D with 200 Gb/s PM- 16QAM signals [244]. Unrepeated transmission with ULL fibre has been reported to have achieved a net throughput of 80.2 Tb/s over a span length of 257.5 km [122]. However, an interesting parameter of this G.654.E fibre is its cable cut-off value which is ~1530 nm unlike that of a standard G.652.D SSMF whose value is <1260 nm Table 5.1. This necessities assessment of system performance for signal transmission below its cable cut-off. Transmission below the cable cut-off results in the generation of higher order modes which can cause intermodal coupling between the corresponding modes as well as multi-path interference (MPI) due to the presence of different light paths. Experimental demonstration with an optical supervisory channel (OSC) at 1510 nm using G.654.B compliant fibre has shown to have no significant penalty due to MPI-induced RIN indicating that transmission below the cable cut-off has no adverse effect from MPI-induced RIN [245]. In terms of Raman amplifiers, MPI-Induced RIN has been studied using the analytical model presented in [246] where, the authors claimed an insignificant effect on the transmission performance due to the signal noise, induced by Raman pump MPI [247].

However, an experimental demonstration showing the impact of pump RIN in a distributed Raman amplifier with different configurations over G.654.E fibre has not been studied previously.

In this chapter, experimental investigation on pump-induced signal RIN in FW, BW and BI-pumped DiRA comparing both the SSMFs is being presented. As a test fibre for distributed amplification G.652.D and G.654.E©TXF from Corning were used as both transmission and amplification medium. Signal RIN measurements were performed with 34 and 69 GBaud PM-QPSK and PM-8QAM signals with the measurement methods explained in [248]. The performance penalties due to signal RIN were then validated in a long-haul in-house recirculation loop setup, with both G.652.D and G.654.E as the transmission and gain medium using a 28 GBaud PM-QPSK signal at ~1550 nm. Further investigation on the performance limit of both the test fibre under identical scenarios were validated, by demonstrating the maximum transmission reach with both these fibres within an assumed HD-FEC of 8.5 dB.

The experiments for RIN calculation were performed in AiPT optical communication Laboratory with support from Dr Mingming Tan and Dr Md Asif Iqbal. The single-span experiment was performed with support from Dr Lukasz Krzczanowicz using a commercial OC1200 transponder provided on loan by Lumentum. The recirculation loop was developed by Dr Paul Harper and the long-haul transmission with the loop was performed with support from Dr Mingming Tan. The author also thanks Dr Sergejs Makovejs of Corning Incorporated for the loan of G.654.E© Corning ultra-low loss fibre. Technical feedback was provided by Dr Paul Harper, Dr Ian Phillips and Prof Wladek Forysiak.

5.1 Fibre parameters analysis

The first study involved the characterization of both G.654.E ©TXF and G.G52.D SSMF. The characterization includes the experimentally measured wavelength-dependent attenuation coefficient using a standard optical time domain reflectometer (OTDR). The other characterization involved measurements of the Raman gain coefficient for the fibres using the standard procedure mentioned in section 3.1.1 of Chapter 3. The obtained results for both the test fibre can be seen in Figure 5.1 (a-b) where the peak Raman gain coefficient of G.654.E was found to be ~0.25 $W^{-1}km^{-1}$ whereas for G.652.D this value was ~0.40 $W^{-1}km^{-1}$. This is primarily due to the large effective area of G.654.E in comparison to its counterpart. However, the attenuation coefficient of G.654.E is lower than G.652.D for the entire optical window with its minimum value being ~0.16 dB at 1550 nm. The additional parameters of both the fibre can be seen in Table 5.1 obtained from [244]. These parameters are important in understanding the accumulation of RIN noise for the test fibre which will be discussed in detail in the next section.

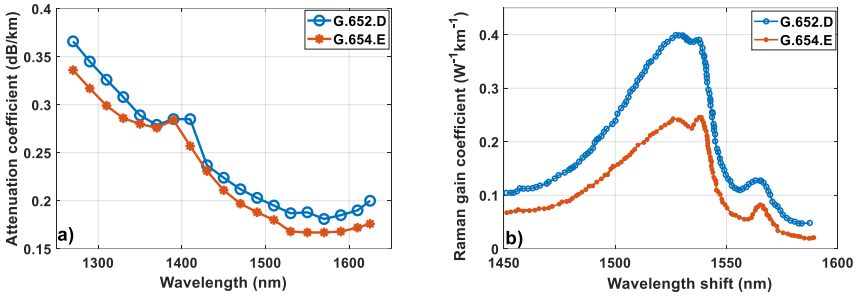

Figure 5.1 G.G52.D and G.654.E a) wavelength vs attenuation coefficient b) wavelength shift vs Raman gain coefficient.

Table 5.1 Fibre parameter at 1550 nm [244]

Parameters @1550 nm	**G.652.D (SSMF)**	**G.654.E (TXF)**
Attenuation (dB/km)	0.189	0.168
Effective area (μm^2)	82	125
NL index n_2 (m^2/W)	2.3×10^{-20}	2.2×10^{-20}
Dispersion (ps/nm/km)	16.5	21
Peak Raman gain coefficient using 1430 nm pump (1/W/km)	0.4	0.25
Splice loss to self (dB)	0.03	0.02
Splice loss to G.652 (dB)	0.03	0.15
Cable cut-off λ_{cc} (nm)	< 1260	< 1530

5.2 Relative intensity noise in forward pump distributed Raman amplifier

5.2.1 Experimental setup

The experimental setup for RIN with FW-pumped DiRA is shown in Figure 5.2. The signal RIN measurements were performed using a single channel rather than with WDM signals as RIN is independent of channel number but dependent on the laser fluctuation which then gets coupled in the transmission signal. The transmitter section includes a commercial transponder (OC-1200), to generate PM-QPSK and PM-8QAM signals at 34 and 69 GBaud baud rates (@1550 nm). The

launch power from the transponder was 3 dBm which was the optimum operating point of the transponder. The modulated signal was then coupled to the fibre under test (FUT) using a WDM coupler. A Raman fibre laser operating a wavelength of 1455 nm with a maximum output power of 5 W and RIN level shown in Figure 5.3 was pumped in an FW configuration. The FW configuration was deliberately chosen to induce maximum RIN to the FUT. To maintain a constant pump RIN, the output pump power was driven at a fixed value of 1W, and a variable optical attenuator (VOA) was tuned to maintain the power level for different test cases. The coupled pump and signal were then passed through a high-power isolator to prevent back-reflection to the transponder before passing through the FUT.

The transmission medium included either a G.652.D of 93.18 km or 98.45 km of G.654.E. The obtained total span loss for G.652.D was 19.5 dB [4*(SMF-SMF-28e splicing) + Fibre loss] whereas, for G.654.E the loss was 17.7 dB [3*(TXF-TXF splicing) + Fibre loss +2*(TXF-SMF -28e splicing). Apart from the fibre losses, an additional loss of ~ 2dB was present due to the connectors and WDM insertion losses. The total loss was measured by standard power measurement by calculating the power difference between the fibre input and fibre output section using a high-power resolution power meter tuned at 1550 nm. A fixed gain of 18 dB using a 1455 nm fibre laser was set to analyze the maximum accumulated signal RIN when targeted towards a specific net gain. The required pump powers for a target net gain were ~ 363 and 521 mW for G.652.D and G.654.E fibres.

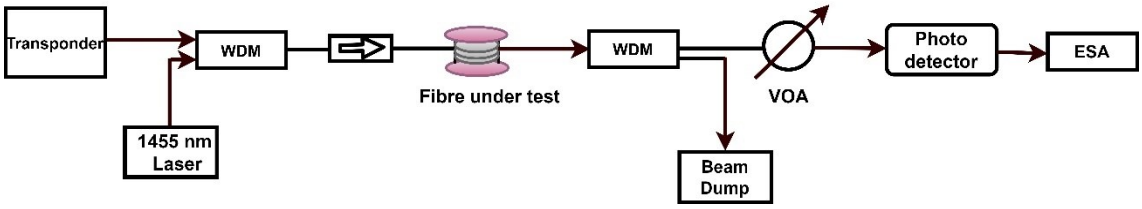

Figure 5.2 Schematic for RIN measurement with forward pumped distributed Raman amplifier

The transmitted signals were then passed through the FUT for transmission which was decoupled and used using a high-power WDM for separation of the pump from the signal. The segregated pump was passed to a beam dump and the signal was then passed through a variable optical attenuator (VOA) for power adjustment for optimal operation of the photodetector. A low-noise photoreceiver was then used to detect the signal RIN and the corresponding traces were captured using an electrical spectrum analyzer (ESA) within a frequency range of 1 to 200 MHz. The captured traces were then used to calculate the average signal RIN over a resolution bandwidth of 1KHz.

5.2.2 RIN results and discussions

As mentioned previously signal RIN arises due to the change in pump noise normalised by total intensity [249–251]. The fast gain dynamics of the Raman amplification lead to a fast pump to signal power coupling [252]. This is particularly dominant in FW pumping as both the signal and the pump co-propagates in the same direction, resulting in the efficient coupling of the pump noise to signals. However, the total accumulated RIN manifesting in the form of noise in a FW-pumped DiRA also depends on fibre parameters and can be represented by equation (5.1) [153].

$$RIN_{sig}^{out} = RIN_{sig}^{inp} + RIN_{pump} \ln^2 G_{on-off} \frac{1/L_{eff}^2}{\alpha_{pump}^2 + (2\pi f D_c \Delta\lambda)^2} \tag{5.1}$$

From the above equation (5.1) we can see that the output signal RIN is a dependent function of both the fibre and pump parameters. Here, RIN_{sig}^{inp} is the signal RIN at the input of fibre span, RIN_{pump} corresponds to the RIN of the pump, G_{on-off} is the amplifier on-off gain which was fixed at 18 dB for both test cases, L_{eff}, is the effective length of the FUT, α_p is the attenuation coefficient of the pump at the operating wavelength, f is the frequency of the noise components, D_c, is the fibre chromatic dispersion and $\Delta\lambda$ is the pump to signal wavelength separation. An interesting parameter that can alter the amount of RIN penalty is the term $(2\pi f D_c \Delta\lambda)$ in the denominator of equation (5.1), known as the pump to signal walk-off parameter. This parameter can alter the amount of RIN transfer to a given channel of interest (COI). Also, it can be seen from equation (5.1) that the walk-off parameter increases with the increase in pump signal wavelength separation $(\Delta\lambda)$, lowering the RIN transfer to a signal. Hence, technique such as higher order pumping can be used to minimize the effect of RIN [253,254]. However, an interesting observation that can be made from the above is the dependency of RIN transfer on the fibre CD. In a FW-pumped DiRA, the rate of pump oscillation increases with an increase in fibre CD [153], causing the signals to undergo an averaging effect in gain thereby reducing the RIN transfer [255]. Hence, theoretically, the signal RIN for G.654.E TXF fibre should be lower than its counterpart G.652.D in a FW-pumped DiRA as the CD for G.654.E is 21 ps/nm/km whereas, for G.652.D this value is 16 ps/nm/km @ 1550 nm as shown in Table 5.1 [244].

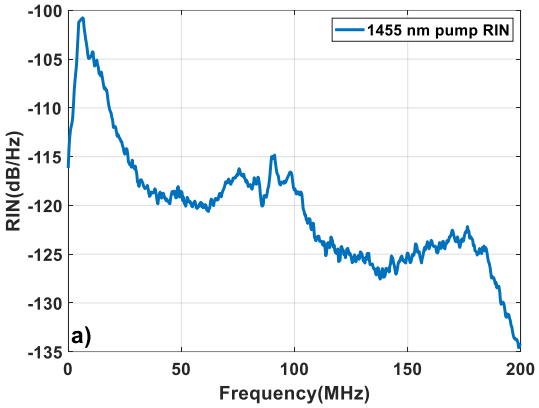

Figure 5.3 Measured RIN of the 1455 nm pump used in the calculation

Figure 5.3 shows the measured RIN of the 1455 nm pump. The measured signal RIN for PM-QPSK and PM-8QAM at 34 and 69 GBaud can be seen in Figure 5.4. The measured RIN for G.654.E was found to be approximately 3.5 dB and 2 dB lower at frequencies > 50 MHz for 34 and 69 GBaud baud rates. The experimental results of signal RIN are in good accordance with the theoretical prediction where an enhanced performance of G.654.E was expected over G.652.D. The lower value of signal RIN in G.654.E can be attributed to the dependency of signal RIN on fibre CD which correspondingly decreases the pump RIN transfer to a given signal due to the large value of the pump-to-signal walk-off parameter. From experimental results, we can conclude that despite the presence of the higher order modes in G,654.E due to the operation of the pump at 1455 nm, well below G.654.E cable cut-off (Table 5.1), the pump to signal RIN transfer is nominal due to the larger pump-to-signal walk-off parameter in G.654.E.

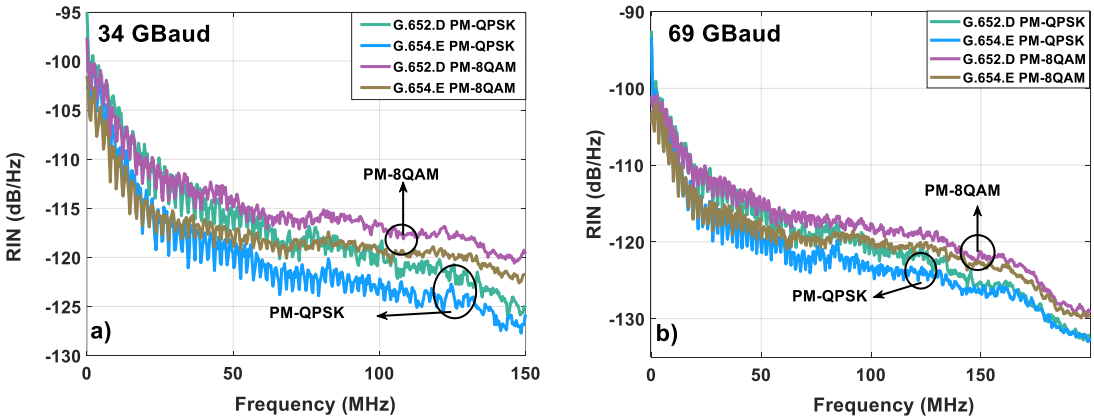

Figure 5.4 Signal RIN for PM-QPSK and PM-8QAM with G.652.D and G.654.E fibre at a) 34 GBaud and b) 69 GBaud

5.3 Single-span transmission with forward pump DiRA

To validate the performance penalty in both the fibres. A single-channel transmission was performed over a span length of 93.18 km and 98.45 km of G.652.D and G.654.E using an FW-

pumped DiRA. The FW pumping configuration was initially chosen to validate the test fibres under the worst-case scenario where the RIN transfer would be maximum. It should also be noted that the nonlinearity in such a configuration will also increase due to the distributed configuration where the signal amplification is throughout the transmission fibre [153].

5.3.1 Experimental setup

The experimental setup for performance penalty investigation with both the test fibre under FW pumping configuration can be seen from Figure 5.5. A commercial transponder (Oclaro OC-1200) was used to generate PM-QPSK and PM-8QAM modulating signals at 34 and 69 GBaud. Only a single-channel transmission at 1550 was performed to minimize the unwanted effects of channel crosstalk due to fibre nonlinearity. The output power generated by the transponder had a maximum value of 3 dB which was insufficient for a steady power sweep. Hence, the modulated signals were amplified with a Tx EDFA operating at a fixed output power mode. The amplified signal was then passed through a VOA for launch power sweep and the input power to the fibre was monitored by a calibrated 99/1 tap. A 1455 nm Raman fibre laser was coupled using a high-power WDM to form a FW-pumped DiRA. The pump power was adjusted to provide a fixed 18 dB gain for both test cases, similar to that of the measured RIN setup. The modulated signal and the pump were then co-propagated through the 93.18 km G.652.D or 98.45 km of G.654.E. After the transmission the remaining pump power was decoupled using a high-power WDM followed by a beam dump for power dissipation. The modulated signal was decoupled too to separate from the pump for the detection procedure. The receiver (Rx) chain comprises a VOA and an EDFA to provide fixed output power to the receiver. The detected traces were then followed by an inbuilt transponder DSP based on the SD-FEC threshold to calculate the real-time bit error rate (BER). The noted BER was then converted into the corresponding Q^2 factor using the technique mentioned in [17].

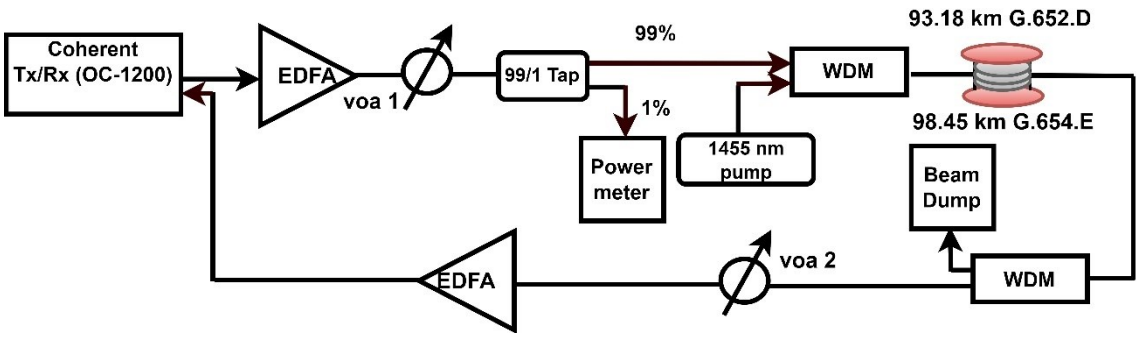

Figure 5.5 Schematic for single channel coherent transmission @1550 nm with FW pumped DiRA

5.3.2 Results and discussions

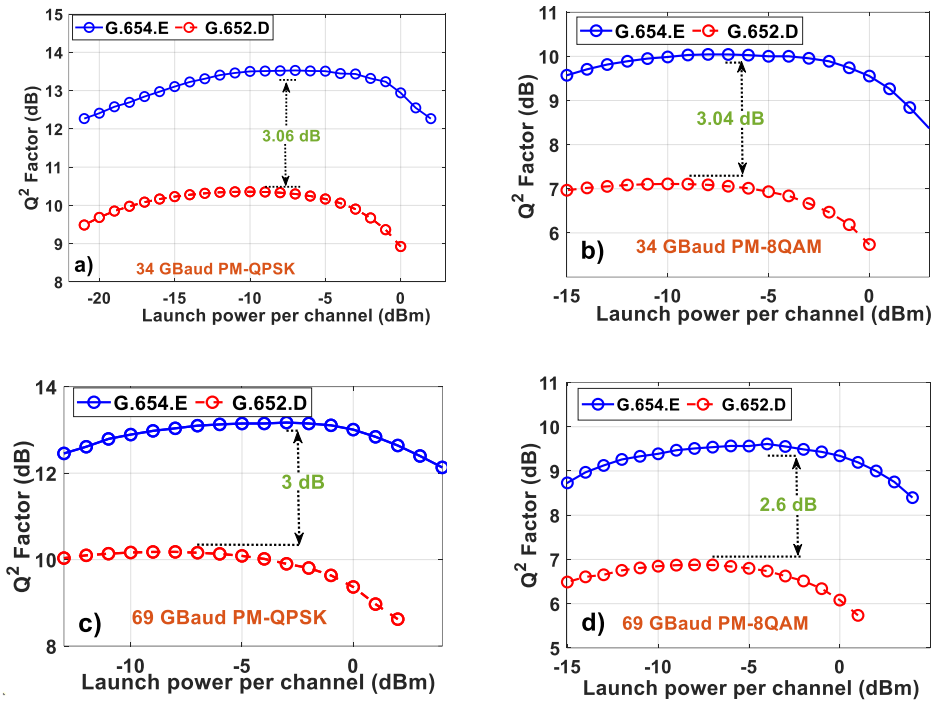

Figure 5.6 Single channel transmission at 1550 nm Q^2 Factor vs Launch power per channel a) 34 GBaud PM-QPSK; b) 34 GBaud PM-8QAM; c) 69 GBaud PM-QPSK and e) 69 GBaud PM-8QAM

The transmission performance of both the test fibres with FW-pumped DiRA can be seen from Figure 5.6 (a-d). At 34 GBaud a Q^2 factor difference of ~3 dB (peak-to-peak Q^2 factor difference) was observed between G.654.E (blue curve with circle markers) and G.652.D (red curve with circle markers) for both PM-QPSK and PM-8QAM signals. Whereas, for 69 GBaud this deviation was ~ 3 dB and ~2.6 dB for PM-QPSK and PM-QAM signals. This superior performance of G.654.E over G.652.D in the region of optimum launch power can be attributed to the high positive CD value which limits the induced RIN due to the large pump signal walk-off [153]. Apart from the low pump-induced RIN, G.654.E also has a lower value of nonlinear and attenuation coefficient (Table 5.1) which improves the overall transmission performance. Furthermore, an additional positive shift in the optimum launch power can be seen in G.654.E whereas, for G.652.D this launch power was lower. This is probably due to the low nonlinear coefficient and the large effective area (A_{eff}) of the TXF fibre [241] decreasing the overall accumulated nonlinear noise [223].

5.4 Long haul transmission with backward and bidirectional pumped DiRA

The experimental results with single-channel transmission for FW DiRA show an enhanced performance for G.654.E over G.652.D. However, FW pumping is not a suitable scheme for long-haul links as the RIN and nonlinear noise adds up significantly due to signal amplification in the

initial length of the fibre [153]. Experimental demonstrations have shown the use of distributed amplification as a seed amplifier in BI and BW configuration for long-haul and unrepeated links [36][123]. Hence, to analyse the performance of both the test fibre for long-haul links, under the effect of RIN we performed a recirculation loop experiment with BI and BW-pumped DiRA using a recirculation loop.

These two pumping schemes were chosen as previous literature has shown that the RIN in BW-pumped DiRA has a negligible effect on the transmission performances [240,256] and the performance penalty obtained is primarily due to the nonlinear effects and amplifier noise figure (NF). Similarly, for BI pumping [257] (Pumping in both FW and BW direction) a finite impact of RIN can be induced due to the presence of the FW pump in addition to the nonlinear effects and amplifier NF. Thus, a single-channel transmission was performed over a long-haul coherent system using a recirculation loop with two test cases.

I. Case 1: BW pumping in distributed configuration with G.652.D and G.654.E.
II. Case 2: BI pumping in distributed configuration with G.652.D and G.654.E.

As for case I, the RIN penalty would be negligible and for case 2 an additional penalty due to pump-induced RIN should be present. Thus, the Q^2 Factor difference between BW and BI configuration for a given recirculation number with the same fibre type should present a better analysis of the RIN impact for these test fibres. Additionally, these results would also help in understanding the better suitable SSMF fibre type with DiRA configuration for long-haul systems.

5.4.1 Experimental setup

The schematic for recirculating loop transmission for BW and BI pumped DiRAs with G.652.D and G.654.E as test fibres are illustrated in Figure 5.7. A 28 GBaud PM-QPSK signal was generated using a 120 GSa/s digital-to-analog converter (DAC) and a standard C- Band $LiNbO_3$ DP-IQ modulator. An external cavity laser (ECL) tuned at a wavelength of 1550 nm was used to emulate the carrier. The modulated signal was then passed to a transmitter (Tx) EDFA for signal amplification (booster amplifier) followed by a VOA for launch power sweeping and the input power to the FUT was monitored using a calibrated 95/5 tap.

The recirculating loop comprised a pair of acousto-optic-modulator (AOMs) triggered using a delay generator and a 3 dB coupler for signal insertion and recovery from the loop. The test fibre includes either 98.45 km of G.654.E or 93.18 km of G.652.D with a span loss of 19.5 and 17.7 dB, respectively. The Raman amplification stage included either one or two 1455 nm Raman fibre lasers configured in BW or BI scheme. The pump powers used for both configurations are shown in Table 5.2 below.

Table 5.2 Pump powers for the BW/BI pumped DiRA

Backward pumping		**Bidirectional pumping**			
G.652.D	**G.654.E**	**G.652.D**		**G.654.E**	
436 mW	624 mW	**Forward pumping**	**Backward Pumping**	**Forward pumping**	**Backward Pumping**
		86 mW	384 mW	125 mW	532 mW

In BI configuration, approximately 20% of the BW pump power (i.e., 20% of 436 mW and 624 mW) was used as a FW pump and the remaining required pump powers were provided by the BW pump to compensate for the total fibre loss. The percentage of FW pump power was chosen at 20% to induce the nominal value of RIN to the signal which would partially degrade the signal performance when transmitted over a few thousand km.

The amplifier section was followed by a narrow optical bandpass filter (OBPF) to filter out the out-of-band noise. The internal loop section also comprises an EDFA (Loop EDFA) with an NF of ~6 dB. This EDFA was installed to compensate for the additional 13 dB loss arising due to the combined insertion loss of the AOM, bandpass filter and the 3dB coupler and additional losses due to the isolator, 95/5 tap and connectors.

The receiver (Rx) chain comprises a 99/1 tap whose 1% was used to monitor the output spectrum and the remaining 99% was passed to the Rx EDFA for optimal power operation of the receiver. The transmitted signals were then mixed with a 100 kHz local oscillator (ECL) for balanced detection and the corresponding traces were captured using an 80 GSa/s, 36 GHz analog bandwidth real-time oscilloscope. The detection process was then followed by a standard offline DSP chain on the captured traces for data recovery [63,258]. The retrieved symbols along with the transmitted symbols were then used to calculate the Q^2 factor from the hard decision bit error rate (BER) [17].

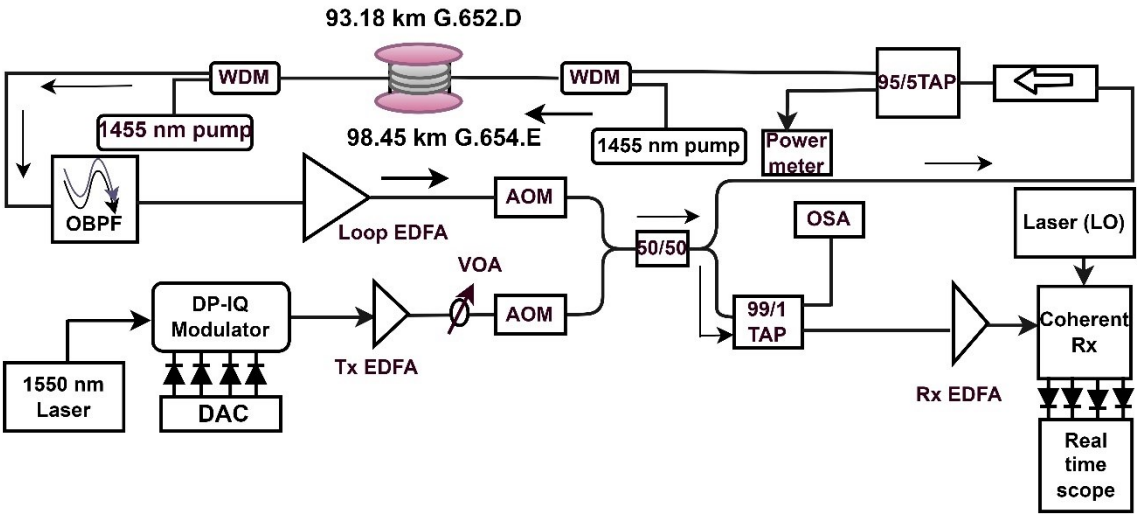

Figure 5.7 28 GBaud PM-QPSK transmission with recirculation loop

5.4.2 Results and discussion

Figure 5.8 (a-b) shows the output spectrum of the 1550 nm signal after 20 recirculation with G.652.D and G.654.E. A higher noise floor can be observed in the case of G.652.D in comparison to its counterpart G.654.E.

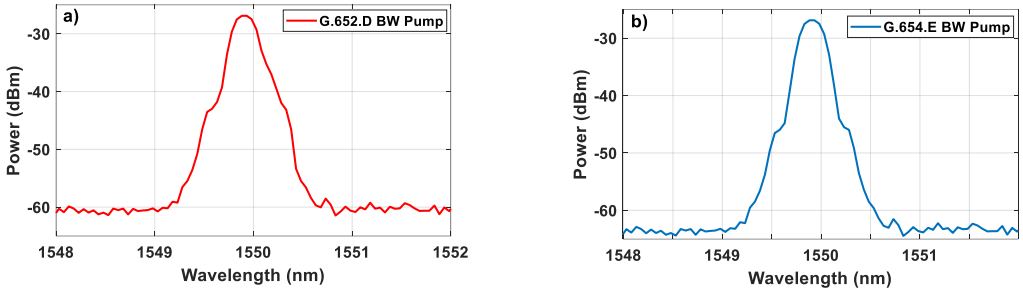

Figure 5.8 Output optical spectrum of 1550 nm signal with BW pumped DiRA

The experimental results with the long-haul recirculation loop show an enhanced performance of G.654.E over G.652.D for both BW and BI-pumped DiRA Figure 5.9 (a-b). The comparison was done by taking the Q^2 factor curve for 10 and 20-span transmission with BW and BI-pumped DiRA as this distance is sufficient to induce some finite RIN to both the fibres. A lower value of the Q^2 factor can be seen for BI pumping DiRA in comparison to BW pumping DiRA for all the test cases indicating the detrimental effect of accumulating signal RIN lowering the transmission performance of both the fibres. The Pk-Pk Q^2 factor difference between BW and BI pumping scenarios for the same fibre type demonstrates the performance penalty due to the presence of finite RIN (BI pumping) and negligible RIN (BW pumping). The Pk-Pk Q^2 factor difference after 10 recirculation was ~ 3 dB for G.652.D whereas, for G.654.E this value was only ~ 1.6 dB. Similarly, after 20 recirculation the Q^2 factor difference was ~4.1 dB for G.652.D and ~2.4 dB for G.654.E. These, larger Pk-Pk Q^2 factor differences in G.652.D after 10 and 20 recirculation

demonstrate that the RIN penalty for G.652.D is larger than G.654.E and this penalty degrades the transmission performance with an increase in transmission distance. Also, like the test case of FW pumping (Figure 5.6 (a-d)) a positive shift in the optimum launch power was too observed for G.654.E with both BW and BI pumping, indicating the lower accumulated nonlinear noise in G.654.E due to its low nonlinear coefficient.

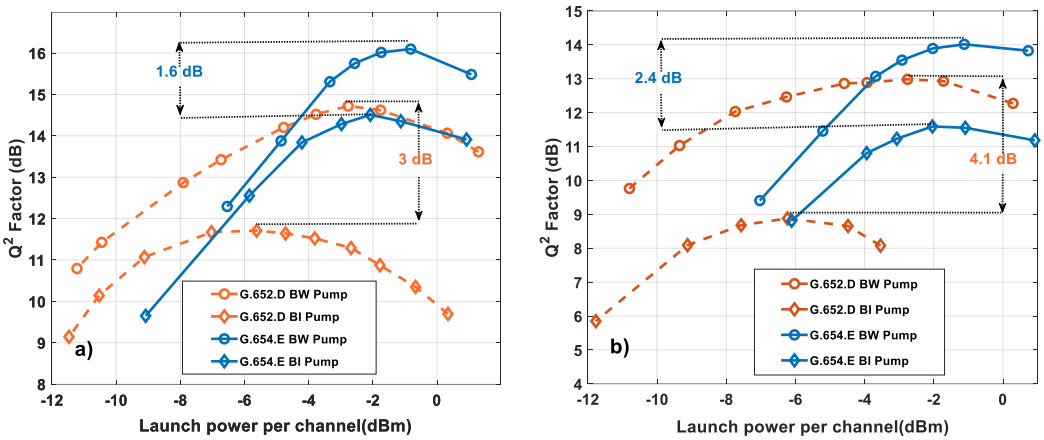

Figure 5.9 28 GBaud PM-QPSK, Q^2 Factor vs Launch power per channel for a) 10 b) 20 recirculation

The maximum transmissible distance and the Q^2 penalty within an assumed HD-FEC threshold of 8.5 dB are illustrated in Figure 5.10 (a-b). The experimental results show G.654.E outperforms G.652.D for all the test cases. For BW pumping DiRA G.654.E exceeded the transmission reach by >1000 km in comparison to G.652.D with a maximum transmission distance of ~6000 km whereas, for G.652.D this distance was ~4900 km. Similarly, for BI pumping G.654.E exceeded the transmission reach by >1000 km indicating that the RIN penalty for G.654.E is lower than its counterpart. The maximum transmission distance for G.654.E was ~3000 km whereas, for G.652.D it was around ~1800 km.

The Q^2 penalty as can be seen from Figure 5.10 (b) shows a lower performance penalty in the case of G.654.E for all the test cases. The maximum obtained penalty for G.654.E was ~3 dB for the maximum transmission distance of ~3000 km whereas for G.652.D this penalty increases to ~4 dB within a mere maximum transmission distance of ~1800 km.

These experimental results with a long-haul coherent system indicated that the RIN penalty for G.654.E is lower than G.652.D and the operation of G.654.E below its cable cut-off in DiRA-based transmission system has a negligible effect on the transmission performance. The pump-to-signal noise-induced RIN is lowered due to its large value of positive CD increasing the pump signal walk-off. These reduced effects of RIN in G.654.E make it a very suitable candidate for DiRA-based long-haul terrestrial networks.

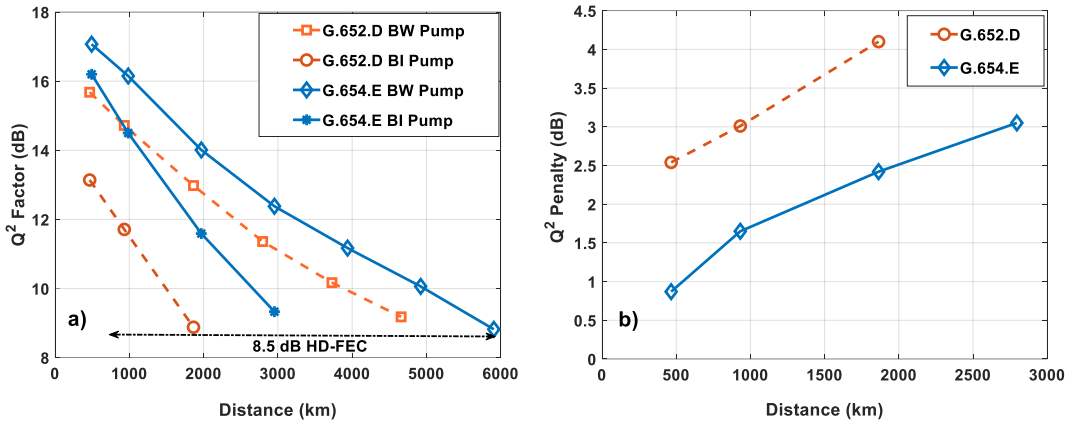

Figure 5.10 FW and BW pumped DiRA distance vs a) Q^2 Factor b) Q^2 penalty

5.5 Conclusion

In this chapter, the impact of RIN-induced penalty in distributed Raman amplifiers with G.654.E and G.652.D as test fibre was experimentally validated. Signal RIN was observed to be lower for G.654.E than G.652.D when tested for a fixed 18 dB gain. The obtained signal RIN was ~ 3.5 dB and ~2 dB lower for G.654.E than its counterpart G.652.D for 34 and 69 GBaud PM-QPSK and PM-8QAM signals. This lower signal RIN for G.654.E can be attributed to the parametric dependence of pump-to-signal RIN transfer on fibre CD, increasing the overall pump-to-signal walk-off. To experimentally investigate the performance penalty due to signal RIN in a coherent transmission system with G.652.D and G.654.E as transmission and amplifying medium. A single-channel transmission was performed at 1550 nm with FW-pumped DiRA. This FW pumping scheme was chosen to induce maximum RIN transfer to the modulated signal and to validate the performance of both the test fibre for short-haul links. The transmission results with these test fibres showed an improved performance for G.654.E with a Q^2 factor improvement of ~3 and ~2.6 dB for PM-QPSK and PM-8QAM signal at 34 and 69 GBaud baud rate. This investigation with FW-pumped DiRA indicates that a coherent transmission system for short-haul links with G.654.E lower performance penalty than its counterpart G.652.D.

Further investigation on the performance penalty due to RIN was investigated using BW and BI-pumped DiRA. For all the test cases G.654.E exhibited superior performance over G.652.D with a maximum transmission distance reaching ~6000 km and ~3000 km for BW and BI pumping whereas for G.652.D this distance was ~4900 and ~1800 km within an assumed HD-FEC threshold of 8.5 dB. The impact of RIN was also evaluated by considering the Pk-Pk Q^2 factor difference between BW and BI pumping, where this difference was observed to ~1.6 and ~2.4 dB for G.654.E with 28 GBaud PM-QPSK signals after 10 and 20 recirculation's. However, this Q^2 factor difference was observed to be around 3 and 4.1 dB for G.652.D fibre.

With all the obtained experimental results one can conclude that RIN-induced penalties in G.654.E are lower than its counterpart G.652.D despite its cable cut-off value at >1530 nm. The presence of the higher order modes due to the Raman pump operation below its cable cut-off value has a negligible effect on the performance penalty. This certainly makes G.654.E a very suitable candidate for DiRA-assisted transmission systems for both short and long-haul fibre links.

Chapter 6: Ultrawideband Raman amplifiers for coherent transmission systems

In this chapter, the experimental investigation of different Raman amplifier architectures will be discussed. The initial study involves a comparison of two key ultrawideband structures, a cascaded dual-stage and in-parallel dual-band for S-, C- and L-band signal amplification. This design was further extended by adding an E-band amplifier to form an E-, S-, C-, and L-band multistage discrete Raman amplifier (DRA). The next design was a combined architecture of Bismuth doped fibre amplifier (BDFA) developed by Dr Aleksandr Donodin for E-band coupled with a dual-stage DRA to form an E-, S-, C- and L-band Bismuth (Bi)-Raman amplifier for ultrawideband (UWB) signal amplification. The last part of the chapter proposes a hybrid design of distributed-discrete architecture (DDRA) based on a split-combine approach of spectral bands, where the E-band signals were amplified in a distributed fashion and the S-, C- and L-band signals were amplified with a dual-stage DRA.

The experiments were performed in AiPT optical communication laboratory with support from Dr Mingming Tan who provided his expertise in the experimental buildup, and Dr Aleksandr Donodin provided us with his E-band BDFAs for signal booster and pre-amplification. Dr Ian Phillips helped in setting the high-speed 128 GSa/s DAC and Dr Pavel Skvortvoc (Currently in Infinera) for providing the DSP for data processing. The author would also like to thank Dr Ming Jun Li and Jefferey S. Stones (Corning inc.) for loaning us the Corning Raman fibre which was used as a Raman gain fibre for the E-band signal amplification in hybrid and discrete Raman amplifier.

6.1 Ultrawideband Raman amplifiers performance evaluation for S-, C- and L-band signal amplification

The main aim of this study was to understand the performance of different architectures of ultrawideband Raman amplifiers when implemented over a coherent transmission system. Here, performances of two UWB DRAs, cascaded dual-stage, and in-parallel dual-band structures were experimentally demonstrated over a coherent transmission system. Previous works of literature have shown the noise performance improvement of broadband Raman amplifiers over C- and L-band [259] but this was not studied over S-, C- and L-band.

6.1.1 Amplifier characterization

The developed cascaded dual-stage and in parallel, dual-band was characterized using a 143x100 GHz channelized amplified spontaneous emission grid shown in Figure 6.1 (a-b). The WDM grid comprises signals from 1470-1605 nm covering the S-, C- and L-band of the optical window. The S-band channels from 1470-1520 were generated using an in-house supercontinuum source [260],

whose power profile was fed to a commercial S-band waveshaper for channel shaping and flattening followed by a thulium-doped fibre amplifier TDFA for amplification.

The C- and L-band were similarly generated using a dual-stage C- and L-band commercial EDFA and two waveshapers for channel shaping and equalization. The operation bandwidth of the C-bandwidth was ~1530-1565 nm and for the L-band EDFA was ~1570-1605 nm. The C- and L-band ASE were coupled with the S-band signals using a wideband S-, C- and L-band WDM coupler. A variable optical attenuator was attached to the input of the coupler to adjust the power level of the C- and L-band similar to that of S-band signals. The output power of S-band TDFA was limited to 19 dBm which after channel shaping and coupling lowers down to 17.8 dBm. The coupled S-, C- and L-band signals were then passed through a 95/5 tap whose 5% tap was passed to the optical spectrum analyzer (OSA) for spectral monitoring and the remaining 95% was used for the experimental purpose. A higher noise floor can be observed for the S-band signals (1470-1520 nm) (Figure 6.1 (b)), this is due to the high noise figure (NF) of the TDFA and the high insertion loss of the S-band waveshaper. The C- and L-band signals have a lower noise floor due to the low NF of the C- and L-band EDFAs. This higher noise floor of the S-band can put a limitation on the performance of these signals due to low OSNR when implemented over a coherent transmission system.

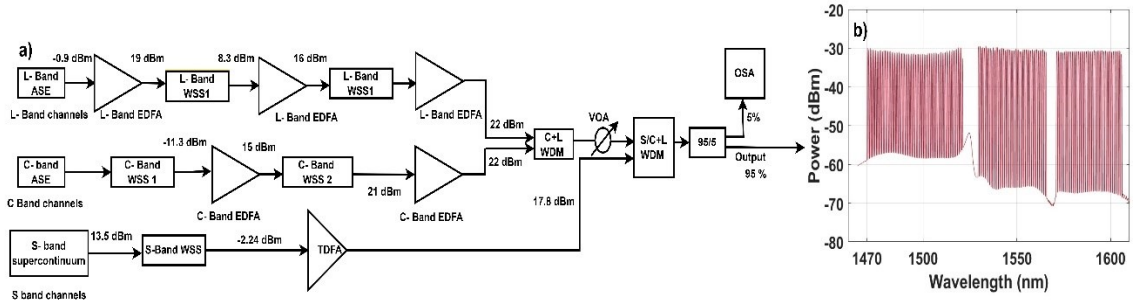

Figure 6.1 S-, C- and L-band grid generation a) setup b) output spectrum

The experimental setup for the three ultrawideband S-, C- and L-band DRA are illustrated in Figure 6.2 (a-c) where a 70 km SSMF was inserted before the amplifier stage. This was done to conduct a standalone experiment and to validate the amplifiers in a realistic UWB scenario where the effects of inter-channel stimulated Raman scattering (ISRS) and wavelength-dependent loss are dominant [227].

The first UWB DRA scheme is a cascaded dual-stage architecture (Figure 6.2 (a)) where the signals, were amplified in two stages to prevent pump-to-pump overlapping. The WDM signals after transmission through a 70 km SSMF were amplified separately for different bands where the S-band signals (1470-1520 nm) were amplified in stage 1 of the dual-stage DRA, with an inverse dispersion fibre (IDF) of 7.5 km using three pumps at 1365, 1385 and 1405 nm in a backward pumping configuration. In this stage the C- and L-band signals don't get amplified due

to the absence of suitable pumps. However, the C- and L-band signals do benefit from ISRS power transfer from the S-band signals. In stage 2 of the DRA, the C- and L-band signals undergo amplification using another 7.5 km of IDF as the gain medium, pumped with five different wavelengths at 1425, 1445, 1465, 1485, and 1508 nm. Each of the pump wavelengths was a combination of two semiconductor laser diodes of a particular wavelength which were then combined using a polarization beam combiner (PBC) for depolarization. The depolarized pumps were then combined using CWDMs whose passband was connected to a pump of one particular wavelength and the reflection band to another pump of different wavelengths to form as bank a multiple-pump configuration as illustrated previously in Figure 3.11 (b).

The other two architectures of DRAs shown in Figure 6.2 (b-c) are the same schemes that are in-parallel dual-band DRA. In this scheme, the S-band and the C- and L-band are separated into two paths using a wideband filtered wavelength division multiplexer (FWDM). Path 1 includes the S-band signals from 1470-1520 nm which were then amplified using a 7.5 km IDF pumped backwards using 1365, 1385, 1405, and 1425 nm. To note an additional 1425 nm pump was required for amplification of the longer S-band signals typically in the range of 1510-1520 nm. This additional pump was not required in stage 1 of the cascaded dual-stage design as the 1425 nm was present in stage 2 of the DRA which was sufficient to provide partial gain to the longer S-band and the shorter C-band signals. Path 2 comprises C- and L-band signals extending from 1530-1605 nm, which was then amplified similarly as dual-stage using five different pumps at 1425, 1445, 1465, 1485, and 1508 nm, with 7.5 km of IDF as a gain medium.

The key difference between scheme 2 and scheme 3 is the minimization of the back-reflection from the output connector of the FWDM in the S-band signal path. In scheme 2 there is no isolation between the IDF WDM output and the input of the FWDM in the S-band amplification path, as a result, a half-open random fibre laser cavity was formed [261–263]. One side of the cavity was open due to the distributed Rayleigh scattering of the 7.5 km IDF fibre with no isolation and the other side was a closed cavity, due to 4% Fresnel reflection from the FC/UPC connector at the output of FWDM. This half-open random fibre laser cavity [264] resulted in an unstable lasing as illustrated in Figure 6.3 (d), however, the pump powers were insufficient in exceeding the threshold to achieve a stable random lasing. This random lasing is not preferable in discrete Raman, even if the lasing is stable this is not necessary as the proposed amplification is of the first order. Such random lasing is specifically preferred in higher-order pumping for distributed and discrete amplification [264]. Hence, to avoid this unstable lasing the pump power was reduced which resulted in lower output power for the S-band signals (Figure 6.3 (e)).

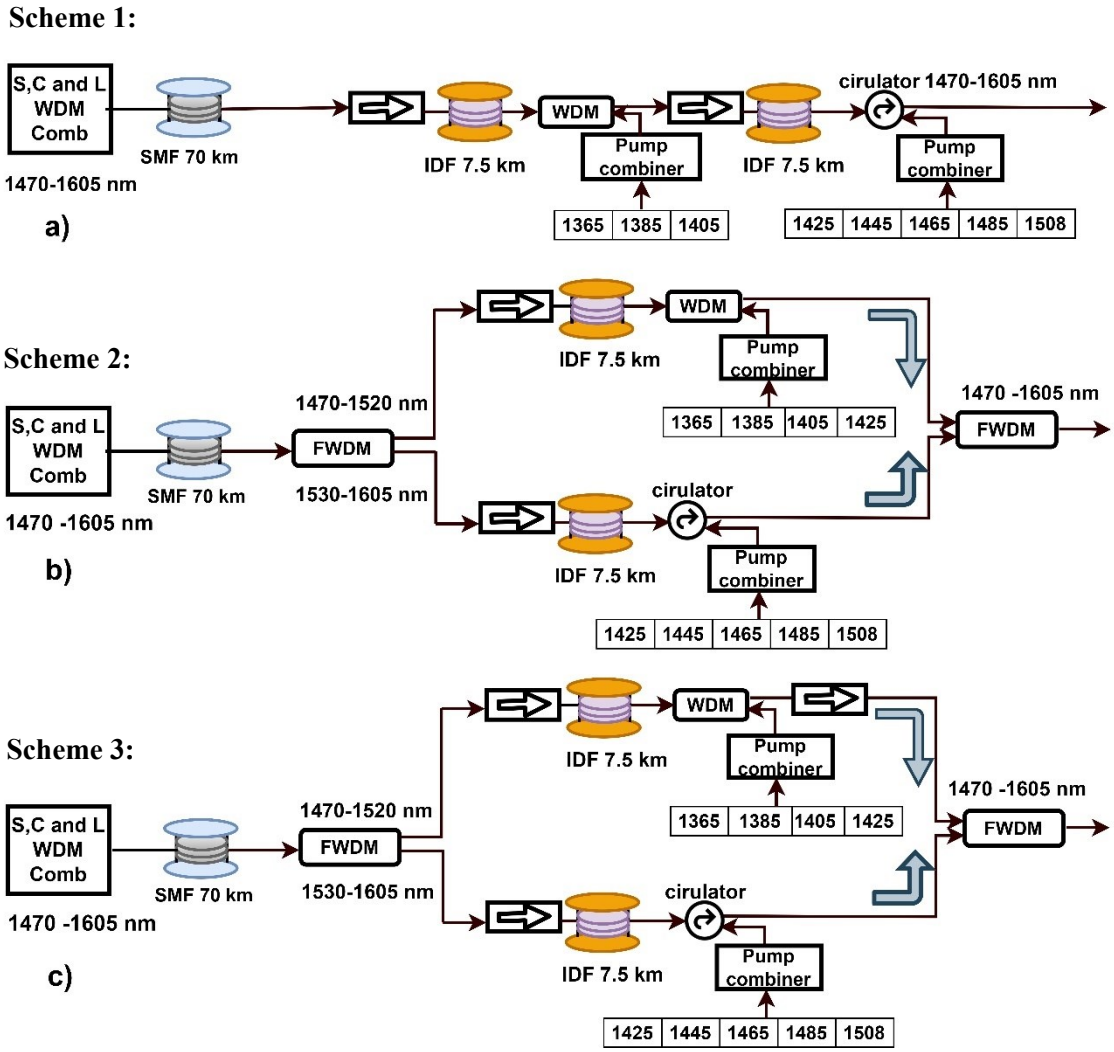

Figure 6.2 Experimental setup for amplifier characterization a) cascaded dual-stage DRA b) in-parallel dual band DRA with reflection c) in-parallel dual band DRA without reflection

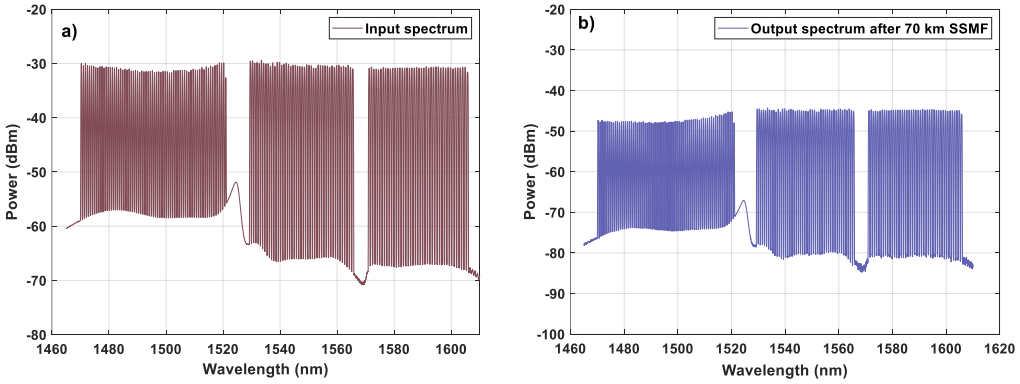

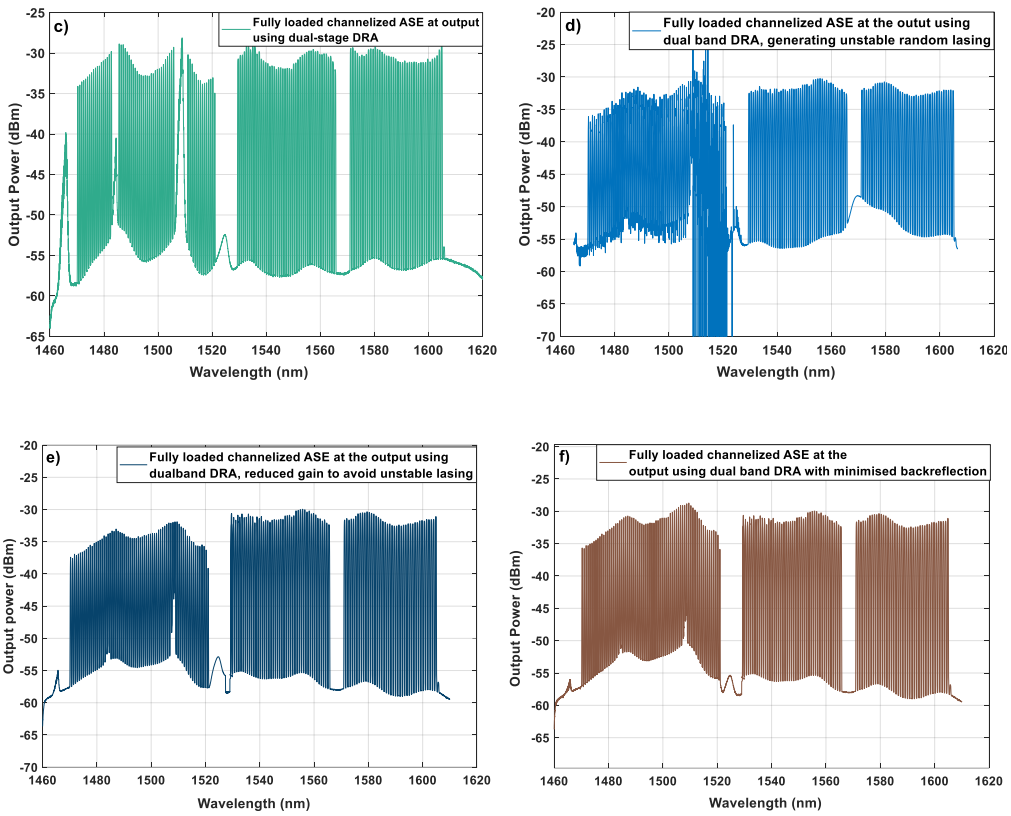

Figure 6.3 Optical spectrum a) input spectrum to 70 km SSMF; b) output spectrum after 70 km transmission; c) output spectra after dual-stage DRA; d) output spectrum after the dual-band DRA with unstable random lasing; e) output spectrum after dual-band DRA, reducing the pump power to avoid unstable lasing; f) out spectrum after dual-band DRA without back-reflection and unstable lasing

The optical spectrums at different stages of the link are illustrated in Figure 6.3 (a-f). The input spectrum is the same as that of the one shown in Figure 6.1 (b). The output spectrum after 70 km of signal propagation is seen to have lower power towards S-band (Figure 6.3 (b)). This is due to the larger attenuation and ISRS power transfer from the S-band to C- and L-band signals. The output spectrum after amplification using a cascaded dual-stage amplifier (Scheme 1) is shown in Figure 6.3 (c). The peaks seen near the wavelengths of ~1485 and ~1508 nm are the Rayleigh backscattered (RBS) spectrum of the 1485 and 1508 nm pumps. When the amplification bandwidth exceeds the Raman stoke shift of 13 THz. (~100 nm), then the pumps co-exist with the signals. In such a scenario the nonlinear crosstalk due to RBS and the Kerr penalties due to the high pump powers degrades the performance of the neighbouring channels [236,265]. However, previous literature has shown that this penalty can be minimized either by the insertion of an appropriate guard band between the overlapping pumps and the signals or by using a narrow rejection filter [266,267]. For scheme 1, a guard band of +/- 2 nm and +/- 3 nm in the vicinity of 1485 and 1508 nm was kept to prevent the overlapping of pumps and the corresponding signals [268]. Figure 6.3 (d-e) are the spectrums of in-parallel dual band DRA (Scheme 2) with unstable lasing due to a half-open random fibre laser cavity. The first spectrum Figure 6.3 (a) shows the

unstable lasing in the S-band when the pump power was increased over a certain value. To prevent the lasing effect the pump powers were reduced, which in turn decreased the overall output power of the S-band signals. The amplified output spectrum without unstable lasing (Scheme 3) with a fully open cavity is illustrated in Figure 6.3 (f). This isolation of the pumps benefited in providing sufficient gain to the S-band signals, by increasing the pump powers as the threshold for unstable lasing in a fully open cavity is very large [262]. In addition to this, the dual-band requires no guard band between the pump and the signals as the amplified bandwidth in each stage is < 13 THz providing a larger number of channel transmission in comparison to cascaded dual-stage DRA. However, this advantage of dual-band design comes at the cost of an additional pump requirement at 1425 nm.

The pump powers required for the three different ultrawideband DRAs are shown below in Table 6.1. A total of 8 pumps was required for the cascaded dual-stage DRA with a total Raman pump power of ~1.9 W for the S-, C-, and L-band amplification. In the case of parallel dual-band, DRA a total pump power of ~2 W and 2.4 W was required for schemes 2 and 3. This requirement of higher pump powers for the dual-band design is due to the addition of the extra 1425 nm pump along with the 8 pumps used in the cascaded dual-stage DRA.

Table 6.1 Pump power and wavelengths for scheme 1, scheme 2 and scheme 3 DRAs

Wavelength (nm)	Pump powers (mW), Scheme1	Pump powers (mW), Scheme2	Pump powers (mW), Scheme3
1365	432	275	366
1385	297	215	309
1405	103	165	224
1425	N/A	234	326
1425 S-band	289	450	450
1445 C-band	304	349	347
1465	269	216	216
1485	67	86	86
1508	112	72	72
Total	1,872	2,062	2,398

The NF for all the below experiments were measured using the 'optical source subtraction method'[269]. This is one of the simplest ways of NF measurement in the optical domain by taking the subtraction between the ASE and the spontaneous spectral emission (SSE) using a calibrated optical spectrum analyser (OSA). Using this technique, the NF of an amplifier can be represented as:

$$Noise\ Figure = \frac{P_{ASE}}{GhvB_{res}} + \frac{1}{G} - \frac{P_{SSE}}{hvB_{res}} \tag{6.1}$$

Here, P_{ASE}, is the ASE power at the amplifier output, G is the amplifier gain, v is the signal frequency, h is the Planck's constant, B_{res} is the resolution bandwidth of the OSA and P_{SSE} is the spectral density of the signal wavelength.

Figure 6.4 (a-b) shows the gain and the NF for scheme 1, scheme 2, and scheme 3 DRAs. For the cascaded dual-stage DRA (Scheme1) an average gain of 13.9 dB was obtained whereas, for the S-band an average gain of 14.7 dB was achieved. Note the achieved net gain was a generic gain of the amplifier but rather the gain required to approximately compensate the loss of the 70 km SSMF. In such a scenario the gain required for S-band was higher in comparison to C- and L-band signals as the S-band signals undergo higher power loss due to their large attenuation coefficient and ISRS power transfer. Similarly for the C- and L-band signals the required gain was lower due to its lower attenuation coefficient and ISRS power gain from the S-band signals.

For scheme 2 the overall gain was 13.5 dB, and for the S-band signals, this was 13.6 dB, a ~1 dB lower than Scheme 1. This is due to the unwanted lasing, which resulted in lowering the pump powers for stability. Correspondingly, for Scheme 3 (dual-band without any back-reflection) the S-band average gain was 15.5 dB, ~1dB higher than Scheme 1 and ~2 dB higher than scheme 2. This higher gain of scheme 3 over schemes 1 and 2 can be attributed to the absence of ISRS power transfer in the amplification stage and also due to the proper isolation of the amplifier section.

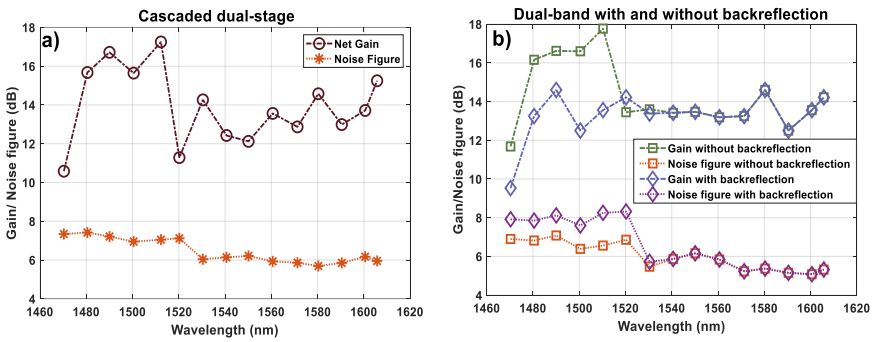

Figure 6.4 Net gain and noise figure for a) cascaded dual-stage DRA (Scheme 1); b) dual-band DRA with back-reflection (Scheme 2); c) dual-band DRA without back-reflection (Scheme 3)

A higher NF was obtained for the S-band signals in comparison to the C- and L-band signals with an average value being 7.5 dB for scheme 1, 8 dB for scheme 2, and 6.8 dB for scheme 3. In the case of C- and L-band signals the average NF was 6 dB for scheme 1 and 5.8 dB for schemes 2 and 3. The overall NF of performance shows that scheme 3 is the best choice of design with a low-value NF in all the bands.

6.1.2 Coherent transmission setup

To evaluate the performance of the above-mentioned schemes, the coherent transmission was performed over a 70 km SSMF with the proposed DRAs in the inline stage. The input spectrum shown in Figure 6.3 (a) was used as a WDM grid. A 30 GBaud PM-16 QAM signal was generated using a 128 GSa/s digital-to-analog converter (DAC) and standard C-band $LiNbO_3$ DP-IQ modulator. A tunable laser source extending from 1450-1620 nm was fetched to the modulator to emulate the WDM carrier from 1470-1605 nm. The modulated signal was then amplified with the corresponding booster amplifiers, which include TDFA for signals from 1470-1520 nm, and C- and L-band EDFA for signals from 1530-1605 nm. The amplified signal was then equalized using a variable optical attenuator (VOA) and was then coupled with the WDM grid using a 50/50 coupler. The total input power to the SSMF was ~16.2 dBm with a power per channel of ~ -5.2 dBm. The average span loss for the 70 km SSMF was 14.8 dB which was then compensated by the proposed DRAs. The amplified spectrums were then passed through a 99/1 tap whose 1% was used for monitoring purposes and the 99% of the power was transferred to the receiver (Rx) chain.

In the Rx chain, the modulated signal was demultiplexed using a wideband optical bandpass filter (OBPF). The modulated signal was then passed through a pre-amp stage with different amplifiers (TDFA for S-band, EDFAs for C- and L-band) for optimal operation of the coherent Rx. The modulated signal was then mixed with a local oscillator using a 90^0 hybrid for balanced detection. The signals were detected using four high-speed photodetectors and the corresponding traces were captured using an 80 GSa/s, 36 GHz bandwidth real-time oscilloscope. The detection procedure was followed by a standard offline DSP for data recovery [270,271]. The recorded symbols together with the transmitted symbols were then used to estimate the Q^2 factor from the hard-decision bit error rate (BER) [17].

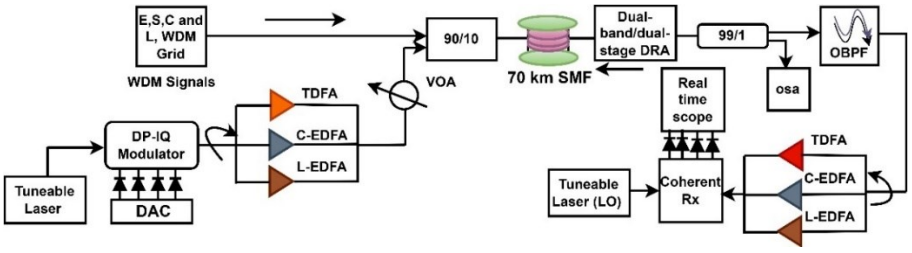

Figure 6.5 Experimental setup for S-, C- and L-band coherent transmission with dual-band and dual-stage DRA as an inline amplifier

6.1.3 Transmission results and discussions

The performance of the DRAs was evaluated by calculating the Q^2 factor for the S-, C-, and L-bands. Figure 6.6 (a-b) shows the B2B and 70 km transmission performance with the three DRAs as an inline amplifier. The B2B performance of both the test case was very similar due to the absence of DRAs and the transmission fibre. The S-band signals were seen to have a lower value of Q^2 factor with an average value of ~16.5 dB whereas, for the C- and L-band this was ~17.2 dB. This degradation in the performance can be attributed to the high NF of the TDFAs in the booster and Rx stages and the low received OSNR of the S-band signals.

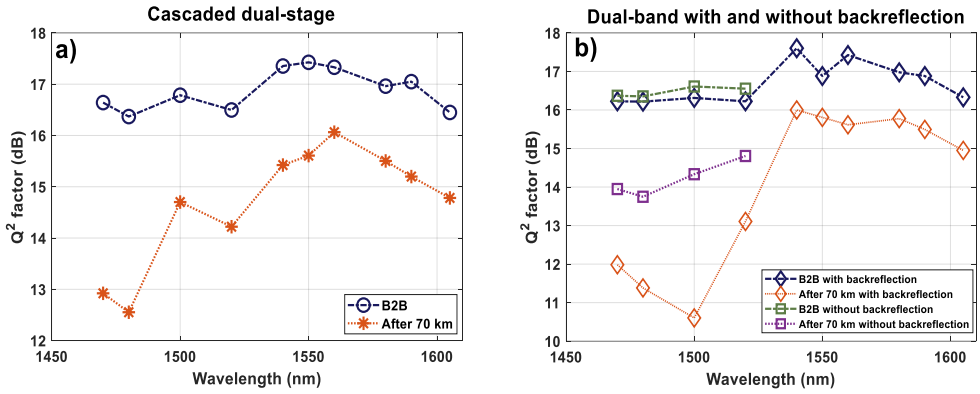

Figure 6.6 Q^2 factor vs wavelength for B2B and 70 km transmission with 30 GBaud PM-16QAM signals a) cascaded dual-stage (scheme 1); b) in-parallel dual band with (scheme 2) and without (scheme 3) back-reflection

The Q^2 factor after 70 km transmission through an SSMF, has a performance variation with different DRAs. For the cascaded dual-stage design an average Q^2 factor of 14.7 dB was obtained across the entire bandwidth. The measured Q^2 factor shows a degrading performance for the S-band signals in contrast to that of the C- and L-band signals with a total performance variation (difference in the best and worst Q^2 factor) of 3.8 dB and an average Q^2 factor of 13.6 dB. In the case of dual-band with back-reflection (Scheme 2), the Raman gain was reduced due to the random lasing, worsening further the transmission performance of the S-band signals. The average Q^2 factor for the whole band was 14.1 dB, and an average Q^2 factor of only 11.8 dB for the S-band. This in contrast is 1.8 dB lower than scheme 1. Once the back-reflection from the end connector was minimized to avoid random lasing (scheme 3), improved performance of the S-band was observed in comparison to both scheme 1 and scheme 2 (Figure 6.6 (b)), because of the reduced pump-to-pump interaction in a dual-band DRA configuration. The average Q^2 factor in S-band was ~14.2 dB, which is 0.6 larger than dual-stage DRA and 2.4 dB larger than dual-band with reflections.

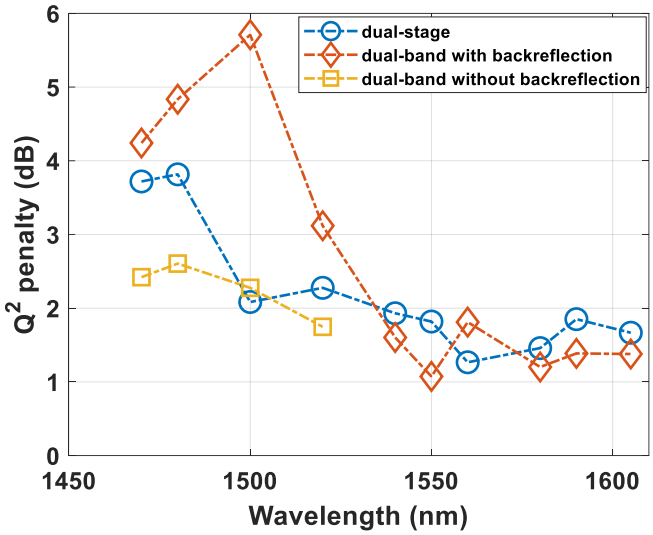

Figure 6.7 Q^2 penalty vs wavelength for 30 GBaud PM-16QAM signals

Similarly, the Q^2 penalty shown in Figure 6.7 has the worst performance for S-band signals with a maximum penalty of 3.8 dB for dual-stage DRA, 5.7 dB for dual-band with back-reflection and 2.6 dB for dual-band without back-reflection. This variation of the Q^2 penalty shows that dual-band architecture without back-reflection is the best design for ultrawideband S-, C- and L-band systems. These experimental results show, that with minimized back reflections, dual-band DRA has better performance than dual-stage DRA. This analysis is particularly important as the proper design of the amplifier is the key to optimized system performance. Moreover, dual-band DRAs have an additional advantage over cascaded dual-stage DRA, as there is no requirement for guard bands between the pumps and signals. This will lead to an increased number of WDM channels incrementing the net throughput of the link. However, the only disadvantage of dual-band is the necessity of an additional 1425 nm pump, which will increase the overall cost and power consumption of the DRA.

6.2 Multistage discrete Raman amplifier for ultrawideband signal amplification

In this section, a multistage discrete Raman amplifier based on a split-combine approach of spectral bands is proposed and its performance penalty was validated over a coherent MBT system. Previous results with S-, C- and L-band DRAs showed that dual-band design is a better suitable design for overall system performance, however, it does come at the cost of an extra pump and additional power consumption. In this section, a combined design of both the dual-band and dual-stage was developed to form a multistage architecture where the E-band and S-, C-, and L-bands were separated and amplified in two different paths, which were then combined for detection and processing. The initial design was performed over a bandwidth of 210 nm which was then reduced to 195 nm due to the limited availability of extended L-band EDFAs. The first step included the characterization of the proposed amplifier which was then proceeded by 10 G

non-return to zero (NRZ) transmission over a 70 km SSMF. In the later stages, the amplifier was validated over a coherent transmission with 30 GBaud PM-16QAM signals.

6.2.1 Multistage discrete Raman amplifier setup

The developed multistage DRA was characterized using the experimental setup shown below in Figure 6.8. The WDM dummy channels included 143x100 GHz channelized ASE from 1470-1520 nm, coupled together with 3 laser diodes at 1411, 1431, and 1451 nm and a 1457 nm PM-16QAM modulating signal to encapsulate a target bandwidth of ~195 nm (25.83 THz). The total input spectrum to the 70 SSMF comprises 147 WDM slots extending from (1410-1605 nm) covering the E-, S-, C-, and L-band of the optical window.

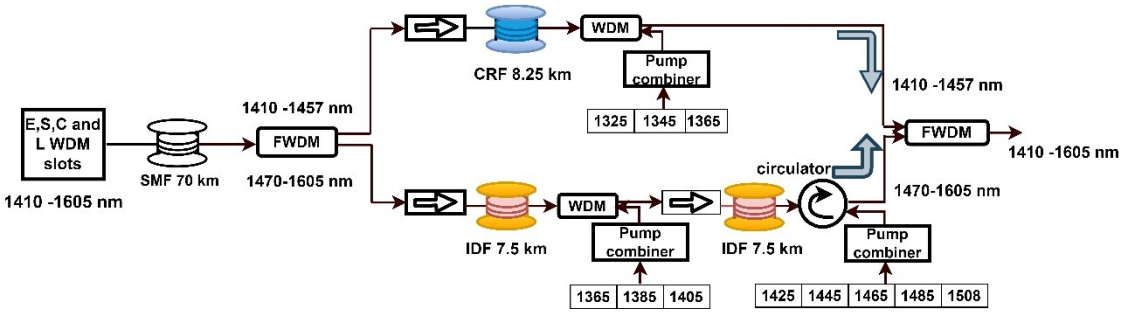

Figure 6.8 Schematic for characterization of the multistage discrete Raman amplifier

Due to the absence of any commercial ASE source and waveshaper that can create a WDM grid in the E-band, 3 laser diodes and a modulating signal were used to cover the partial E-band for the amplifier testing. Nevertheless, the signals were inserted at the extreme ends of the target bandwidths for testing the amplifiers. The S-, C-, and L-bands were generated using the methods explained above in section 6.1.1. The channelized ASE grid was then coupled with the four E-bands signals using a filtered WDM (FWDM) and a 90/10 coupler as shown below in Figure 6.9 forming the E-, S-, C, and L-band WDM comb. The generated signals were then passed through a 70 km SSMF followed by amplification with the multistage DRA.

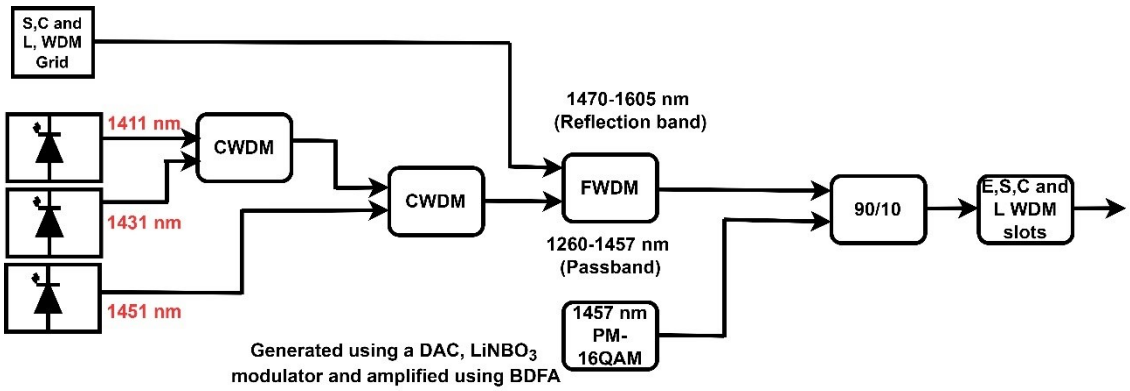

Figure 6.9 E-, S-, C- and L-band WDM generation

The attenuated WDM signals after 70 km transmission were then separated into two bands using a high-power FWDM. Band 1 comprised signals from 1410-1457 nm (E-band) and band 2 signals from 1470-1605 nm (S-, C- and L-band). Signals from 1410-1457 nm were then amplified using a CRF of 8.25 km, pumped in a backward fashion using 1325, 1345, and 1365 nm pumps with pump power values of 435, 276, and 168 mW. Correspondingly, the signals from 1470-1605 nm were amplified using a cascaded dual-stage DRA shown previously in section 6.1.1, with two IDF of 7.5 km as the gain medium. A total of 8 pumps were used to provide amplification of the S-, C- and L-band in two-stage, with the first stage comprising 1365, 1385, and 1405 nm pumps (432, 297, and 103 mW) and the second stage comprising of 1425, 1445, 1465, 1485 and 1508 nm pumps (289, 304, 269, 67 and 172 mW). The dual-stage architecture was chosen despite the dual-band having superior performance, due to the unavailability of passive FWDM that can separate the S-and E-band from the C- and L-band in two stages. This will be part of a future study where the signals will be separated into two bands of 100 nm each, and then will be amplified in a single-stage amplification for each band, minimizing the pump-to-signals overlapping and ISRS power transfer.

6.2.2 Multistage Raman amplifier characterization

Figure 6.10 (a-c) shows the spectra at the input of SSMF, output after 70 km of SSMF, and the amplified spectrum after the multistage DRA. It can be observed that the signals from 1470-1520 nm (S-band) have a higher noise floor, this is due to the high NF of the TDFA used in the grid generation. In addition, a slight tilt of +/-1 dB was also observed for the S-band input spectrum. This tilt arises due to the combining of the S-band with multiple passives resulting in a wavelength-dependent insertion loss before propagation through the fibre. The peaks observed in the vicinity of the S-band (Figure 6.10 (c)) are the Rayleigh backscattered spectrum of 1465, 1485, and 1508 nm pumps, whose zoomed-in spectra are shown in Figure 6.10 (d-e). Appropriate guard bands, as mentioned above in section 6.1.1, were inserted to prevent overlapping between the pumps and the signals. The output spectrum has an average power ripple of +/- 1.5 dB across the entire bandwidth, which in particular is larger towards the lower wavelength of the S-band. This tilt is due to pump power and wavelength limitation of commercially available pumps which are available at only specific wavelengths and power. These shortcomings can be recovered with the availability of customized high-power pumps, fabricated at specific wavelengths. In addition to this amplifier modelling using machine learning and genetic algorithm for amplifier pump and wavelengths optimization can also improve the overall power profile of the UWB signals [272–274].

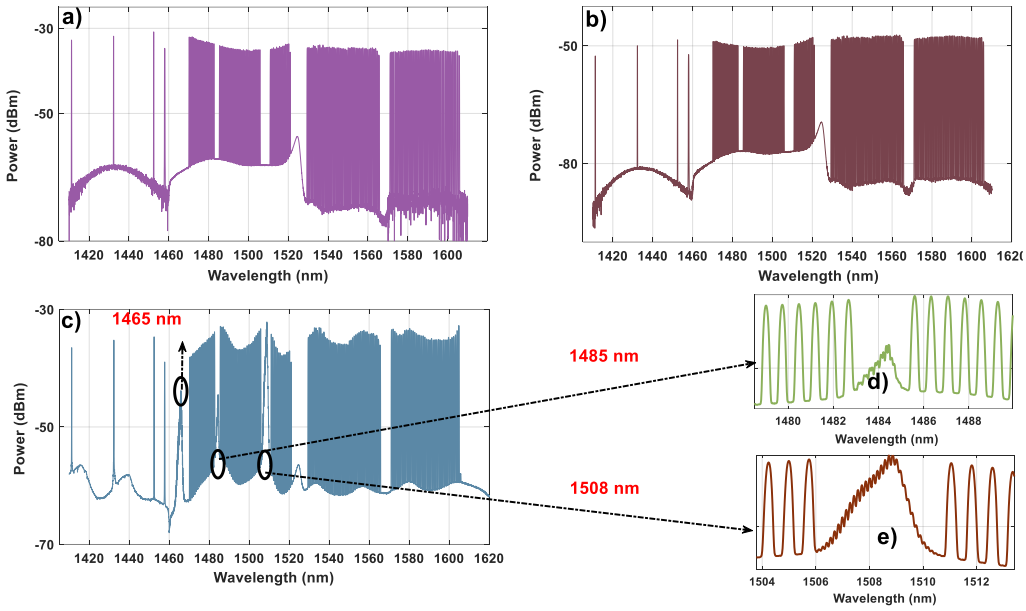

Figure 6.10 Optical spectrum of the E-, S- C- and L-band WDM grid a) input spectrum to 70 km SSMF; b) output spectrum from 70 km SSMF; c) amplified output spectrum after the multistage DRA; zoomed Rayleigh backscattered spectrum of the; d) 1485; e) 1508 nm pumps.

Figure 6.11 (a) shows the Gain and NF of the UWB signals after the multistage Raman amplifier. The net gain for the E-band signals varied from 16 to 13.8 dB. In the S-band regime from 1470-1520 nm, an average gain of 14 dB was obtained across the entire bandwidth, with a minimum gain of 10.2 dB at 1470 nm. Just like the previous characterization for S-, C- and L-band, the emphasis was to compensate the SSMF + FWDM loss, rather than to obtain a flat gain across the bandwidth. Due to the higher attenuation and ISRS power transfer of the S-band signals an average gain of ~16 dB was required to compensate for the loss, to have an approximate power per channel equivalent to C- and L-band. Correspondingly, an average gain of only ~13 dB was required to compensate for the total SSMF+ FWDM loss, as the C- and L-band signals undergo lower power loss and benefits from the ISRS power transfer from S-band in the SSMF and DRA stage 1 of the cascaded dual-stage. The overall NF for the multistage Raman was ~7 dB, with a maximum value of 7.5 dB across the entire bandwidth. In the E-band regime, the average NF was obtained to be ~7 dB, which in the presence of a fully loaded spectrum is expected to have a slight increase in the NF due to an increase in the total power. A slightly lower value of NF was obtained for the C- and L-band signals, with an average value of ~ 6 dB in the range of signals from 1530-1605 nm. The overall shape of the NF in the S-, C-, and L-bands is due to the dual-stage architecture adopted here. Although the gain and NF were measured at an interval of 10 nm for the 1470-1605 nm signals, the values obtained are due to the fully loaded channels in the S-, C- and L-bands as shown in the spectrum of Figure 6.10 (a). Note, the NF in the E- and S-band could be reduced by replacing CRF and IDF with high Raman gain coefficient (g_r) fibres, ideally with

lower E-, and S-band loss, and by employing higher order pumping with two-stage amplification for E- and S-band signals [259,275].

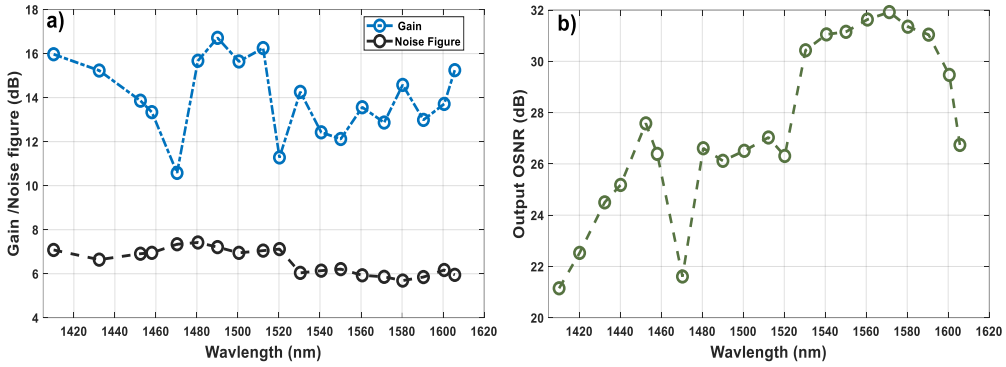

Figure 6.11 E-, S-, C- and L-band multistage discrete Raman amplifier characterization, wavelength vs a) Gain /Noise figure; b) Output OSNR

Figure 6.11 (b) illustrates the OSNR measured at the output stage of the multistage DRA. The measurements were performed by loading a 30 GBaud PM-16QAM signal as a channel under test (CUT), measured at an interval of 10 nm. In the wavelength region from 1470-1605 nm the two side channels adjacent to the CUT were turned off, and the corresponding OSNR was measured using the 3–point method of curve fitting [26]. In the E-band region, no side channels were turned off as there was sufficient channel spacing between the CUT and the neighbouring signals. The OSNR measured at a noise bandwidth of 0.1 nm, or an equivalent frequency bandwidth of 12.5 GHz is (strictly speaking) applicable only at a wavelength of 1548.5 nm (193.6 THz). This bandwidth requires correction in a UWB scenario, where the noise spectral density varies as $B = \frac{c}{\lambda^2} * \Delta\lambda$, here c is the speed of light, $\Delta\lambda$ is the optical spectrum analyzer (OSA) resolution bandwidth which is 0.1 nm and λ is the wavelength of CUT. The measured OSNR shows a degradation towards the E- and S-band with an approximate ~ 4 dB roll-off. The minimum OSNR in the E- and S-band region (1410-1520 nm) was ~21 dB at 1410 and 1470 nm. This degrading OSNR can be attributed to the high NF of the E- and S-band amplifiers and the high input noise floor of the signals whereas, for the 1530-1605 nm signals (C- and L-band), the OSNR variation was from 27-31 dB, an improvement attributable to the low NF of the DRA and the low noise floor of the input ASE grid (Figure 6.10 (a)).

6.2.3 10G NRZ transmission with the multistage discrete Raman amplifier

The ultrawideband multistage DRA was initially tested over a 10 G transmission system over a transmission bandwidth of 210 nm. The transmitter section included a 10 G NRZ PRBS generator with a PRBS length of 10^{31}- 1, a tunable laser source, and a 10 G modulator to generate an optically modulated 10 Gb/s NRZ modulated signal.

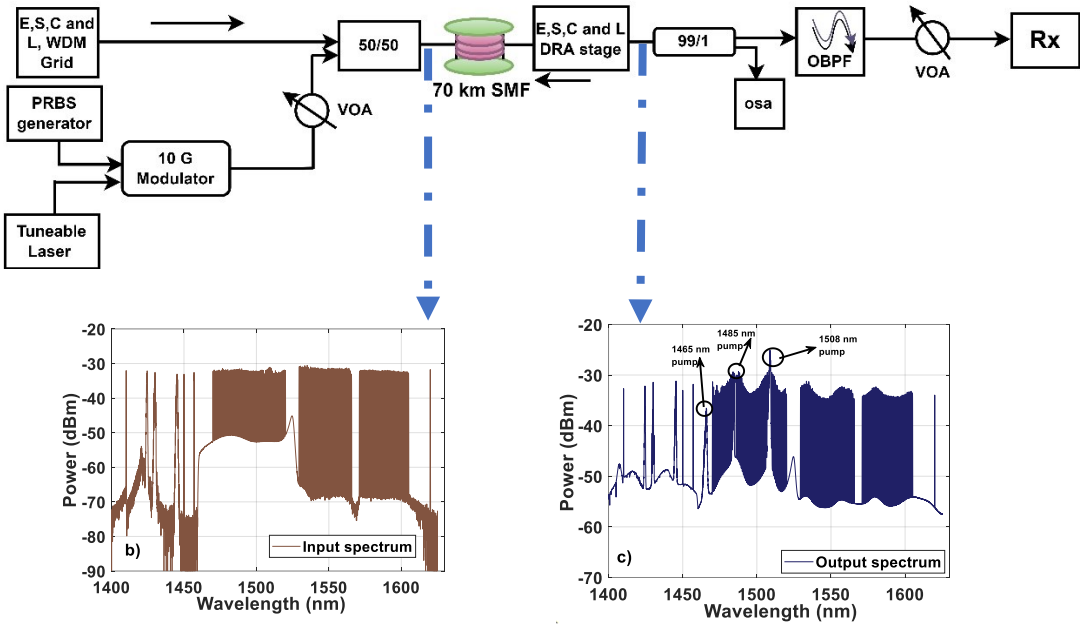

Figure 6.12 10 Gb/s NRZ transmission a) experimental setup b) SSMF input spectrum c) amplified output spectrum

The modulated signal was then coupled with channelized ASE WDM signals extending from 1410 to 1620 nm using a 50/50 coupler. The channelized ASE in the S-, C-, and L-band were generated using the technique as explained in section 6.1.1. The WDM channels were then coupled with 6 independent laser sources in the E-band of which 3 signals in 1410, 1450, and 1457 nm were generated using three tunable laser sources, and the remaining three channels at 1425, 1430, and 1445 nm were generated using diode lasers of ~2 nm in linewidth. Altogether the WDM spectrum comprised 156 channels without guard bands near 1485 and 1508 nm pumps. Due to the limitation in the amplification bandwidth of the L-band EDFA in our facility which extends out to 1605 nm, a laser source at 1620 nm was added to encapsulate an amplification bandwidth of 210 nm. The total input power to the SSMF was 16.2 dBm with a power per channel of -5.8 dBm. The average span loss for the SSMF was ~14.8 dB which was compensated using the multistage DRA shown in Figure 6.8. The input spectrum to SSMF and the amplified output spectrum from the DRA are illustrated in Figure 6.12 (b-c). The peaks seen in the vicinity of the S-band spectrum (circular marker with arrow lines) are the three Rayleigh backscattered spectrum of 1465, 1485, and 1508 nm pumps. The amplified spectrum was then passed through a 99/1 tap whose 1% was used for monitoring the output spectrum and the remaining 99% was then passed to a wideband OBPF for filtering the modulated signals. The filtered signal was then passed through a VOA for the received power sweep and the corresponding BER was calculated from the 10 G commercial receiver.

6.2.3.1 Results and discussion

Figure 6.13 (a-d) shows the received power sweep performance of the multistage DRA after 70 km of SSMF transmission. The 10 Gb/s NRZ performance was measured at an interval of 10 nm and the corresponding BER was measured by sweeping the Rx power by varying the VOA. The four figures shown below correspond to the performance of the signals at four different bands (E-, S-, C-, and L-bands). A degradation in the B2B (dotted silver line with diamond markers) was seen for the 1430 and 1500 nm signals in contrast to the 1550 and 1600 nm signals, showing the performance limitation of the shorter wavelength signals due to the use of commercial C-band components. As for the transmission of the 1430 nm and 1500 nm signals with the DRA a larger penalty was observed which can be largely attributed to the high NF and low OSNR of the E- and S-band signals in comparison to the C- and L-band signals. To explicitly see the performance penalty to the DRA, the power penalty was measured (difference in the received power value at a BER of 10^{-4}) at an assumed BER FEC threshold of 10^{-4}.

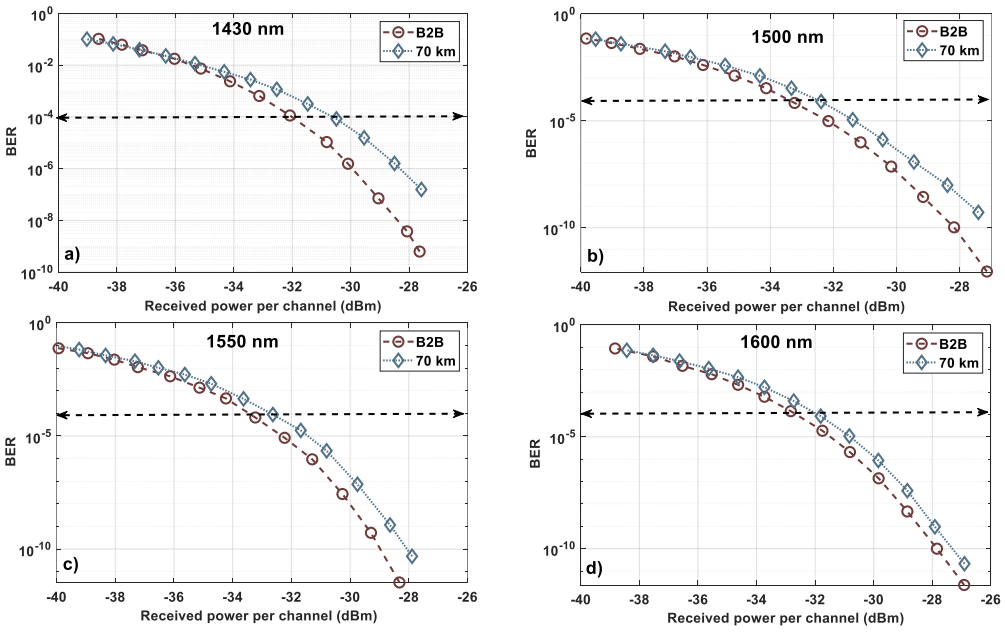

Figure 6.13 BER vs received power per channel for B2B and after 70 km transmission with channels at; a) 1430 nm; b) 1500 nm; c) 1550 nm and d) 1600 nm.

The power penalty was seen to be the highest for the E- and S-band signals with a maximum value of 1.7 dB at 1410 and 1480 nm. This increased power penalty can be attributed to the low received OSNR of the S- and E-band signals, high signal power loss, and the ISRS power transfer from the S- and E-band signals to the C- and L-band signals in the SSMF and the DRA stage. The average power penalty was ~ 1.2 for the E- and S-band signals whereas for the C- and L-band this penalty was ~0.7 dB at a BER of 10^{-4}. The enhanced performance of the C- and L-band can be related to the low NF and high received OSNR of the signals. The performance of the S- and E-

band signals, however, can be improved by implementing a two-stage amplification with appropriate pump powers and wavelengths [213,259]

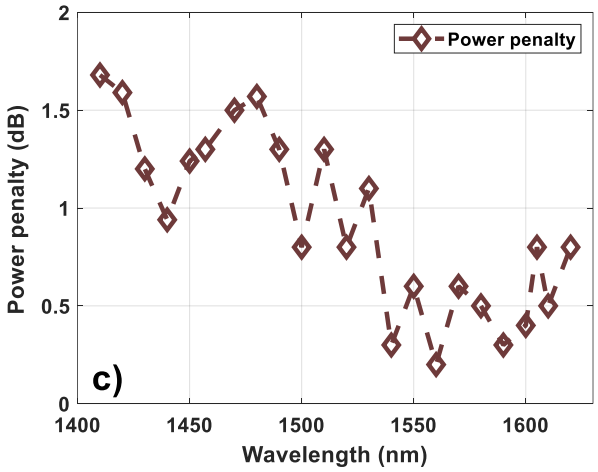

Figure 6.14 Power penalty at BER of 10^{-4} between B2B and 70 km transmission.

6.2.4 E-, S-, C- and L-band coherent transmission with multistage discrete Raman amplifier

The coherent transmission setup is similar to the one explained in section 6.1.2 except for the additional transmission in E-band with the booster and pre-amp BDFA as illustrated in. A 30 GBaud PM-16QAM modulated signal was generated using a 120 GSa/s DAC and standard C-band $LiNbO_3$ DP-IQ modulator. The optical carrier was emulated using two external cavity laser (ECL) sources extending from (1410-1480 nm) and (1480-1620 nm). The modulated signal was then amplified using a booster amplifier for the corresponding wavelengths. Signals from 1410-1457 nm were amplified using in-house BDFA, 1470-1520 nm signals were amplified using TDFA and the remaining 1530-1605 nm signals were amplified using C- and L-band EDFAs. The modulated signal was then coupled with the 146 WDM channels shown in Figure 6.10 (a) using a 90/10 coupler and a VOA for power equalization. The total power to the fibre input section was ~19.6 dBm with a power per channel of ~-2 dBm. The WDM signals were then passed through the 70 SSMF followed by the proposed multistage DRA for signal amplification. The amplified signals were then passed through a 99/1 tap whose 1 % arm was used for measuring the amplified OSNR and the remaining 99% was passed through the OBPF for filtration of the modulated signals.

The Rx chain comprises booster amplifiers targeting specific wavelengths for amplification of the filtered modulated signals followed by an Rx detection segment. The amplified signals were then mixed with a local oscillator (narrow linewidth tunable laser sources) using a 90^0 hybrid for balanced detection and the corresponding traces were captured using four photodetectors and a 36 GHz bandwidth, 80 GSa/s real-time oscilloscope. The captured traces were then processed

using a standard offline DSP for data recovery, and the recorded symbols together with the transmitted symbols were then used to calculate the Q^2 factor from the BER [17,271].

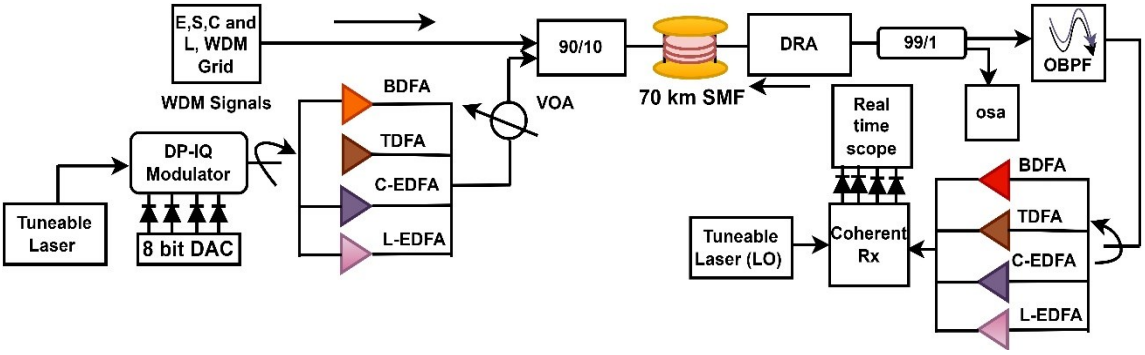

Figure 6.15 30 GBaud PM-16QAM transmission over 70 km SSMF experimental setup

6.2.4.1 Results and discussions

The constellation diagrams of a back-to-back (B2B) and received signals after 70 km transmission at 1430, 1500, 1550, and 1605 nm are illustrated in Figure 6.16. The constellations for B2B and 70 km transmission have the best footprint at 1550 nm with a minimum deviation, whereas these distortions were seen to be larger for other bands with a maximum at 1430 nm followed by 1500 nm and 1605 nm. The larger distortions in the B2B constellation plots for 1430, 1500, and 1605 nm signals in comparison to the 1550 nm signals, indicate the penalties of the standard C-band components in particular the optical hybrid when operated outside the C-band. In addition to this, the noise added by amplifiers such as BDFA, TDFA, and L-band EDFA is higher in comparison to that of C-band EDFA adding additional penalties for the E-, S-, and L-band signals. As for the constellation after 70 km the higher distortion in E- and S-bands can be attributed due to the low received OSNR, and high NF of the DRA.

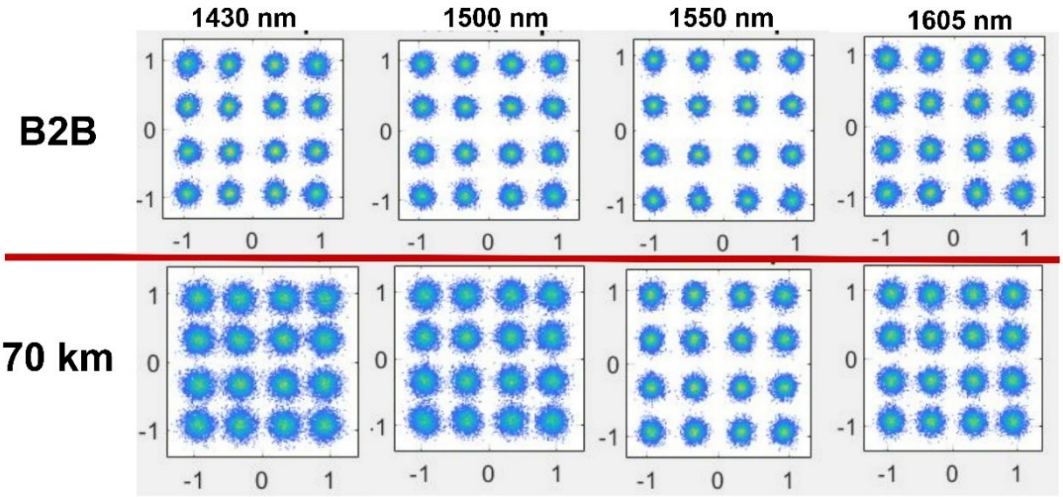

Figure 6.16 Constellation diagrams for B2B and 70 km transmission performance for 1430, 1500, 1550, and 1605 nm 30 GBaud PM-16 QAM signals

The UWB transmission with the B2B system and 70 km SSMF with DRA in the inline stage can be seen below in Figure 6.17. The transmission results (Q^2 Factor) show a detrimental B2B performance (dashed red line circle marker) for E-band (1410-1457 nm) signals, with a roll-off of ~2.5 dB. The minimum Q^2 factor was 15.4 dB at 1410 nm with an average value being ~16.5 dB in the E-band. This performance degradation is primarily because of the use of the standard C-band transceiver components where the degradation is particularly due to, the I/Q imbalance of the transmitter, and the polarization imbalance of the C-band optical hybrid in the receiver stage [276]. As for the S-band (1470-1520 nm), a variation of ~ 2 dB was observed with a minimum value of 16 dB at 1470 nm. This performance degradation towards the shorter wavelength regime of the S-band is due to the high NF of the Tx/Rx TDFA, in addition to the I/Q and polarization imbalance. In the region of the C-band (1530-1570 nm) a steady performance of ~18 dB was observed with its minimum value being 17.5 dB at 1530 nm, which then eventually degrades down to 16.5 dB at 1605 nm in the L-band. The improved performance of the C- and L-band signals is due to the good compatibility of the transceiver components in these regions of operation and also due to the low NF of the C- and L-band EDFAs.

The Q^2 factor after 70 km transmission illustrated in Figure 6.17 (a) (black line with diamond marker) follows the same trend as the B2B curve for the entire bandwidth. The Q^2 penalty shown in Figure 6.17(b) shows a higher penalty towards the E- and S-band region where an average penalty of 3 dB was observed with a maximum penalty of 4 dB at 1410 and 1470 nm. Whereas, for C- and L-band the average penalty was ~1.5 dB with a maximum penalty of 2 dB at 1600 nm. The trend in the Q^2 penalty can be largely related to the DRA NF and output OSNR of the spectral bands shown in Figure 6.11 (a-b), where the maximum NF of the DRA was observed for the E- and S-band signals, with an output OSNR of <28 dB. Similarly, for the C- and L-band the lower Q^2 penalty is due to the low average NF of ~6 dB and an output OSNR > 30 dB.

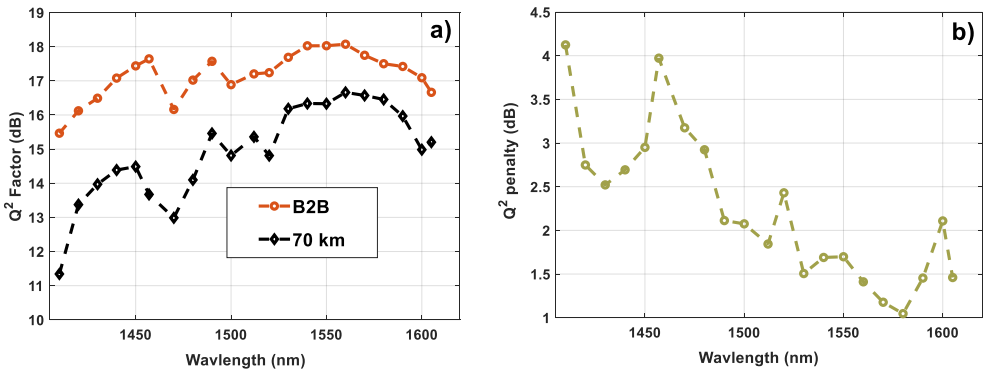

Figure 6.17 30 GBaud PM-16QAM WDM transmission wavelength vs a) Q^2 factor b) Q^2 penalty

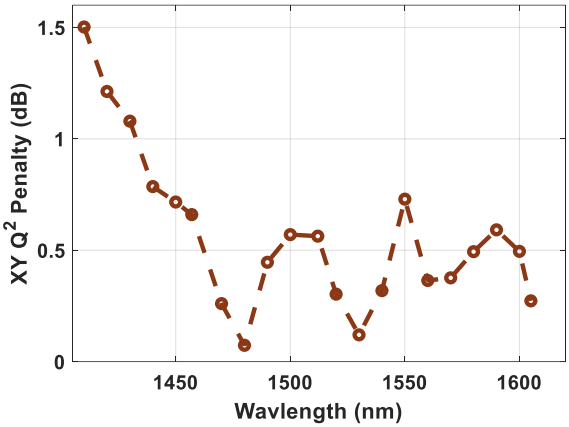

Figure 6.18 Performance penalty (Q^2 Penalty) of X and Y polarization with B2B transmission

As mentioned above, an extension of the UWB system towards the E- and S-band leads to performance degradation due to I/Q and polarization imbalance, when operated using standard C-band transceivers. Hence, to study the detrimental effects of polarization imbalance in the optical hybrid when operated over different bands, the XY Q^2 penalties were measured for a B2B setup (Figure 6.18). This penalty is the difference in the Q^2 factor for X and Y polarization and it varies w.r.t to different wavelengths. Experimental results show a lower polarization penalty for wavelength > 1480 nm with an average value of ~0.5 dB across S-, C-, and L-bands. However, a linear increase in this penalty was observed for wavelength < 1470 nm with a maximum value of ~1.5 dB at 1410. The results of Figure 6.18 indicates that the operation of the system beyond the S-band is subjugated to penalties due to the polarization imbalance and this increases linearly towards the shorter wavelength region of the E-band. In addition to the high NF and low OSNR in the E-band regime, the large polarization imbalance due to the limitation of the optical hybrid is also an important factor in degrading the overall performance of the channels in the E-band. This can somewhat be improved by replacing the standard C-band components with the low-loss components suitable for operations in these bands.

6.3 Hybrid Bismuth Raman amplifier for ultrawideband signal amplification

In this section, we will discuss the performance penalty in a coherent ultrawideband transmission system due to a hybrid combination of Bismuth (Bi) doped fibre amplifier (BDFA) and DRA as an inline amplifier. The primary goal was to amplify E-band signals with a Bi-doped fibre amplifier and the remaining S-, C- and L-band with a dual-stage discrete Raman amplifier.

6.3.1 Hybrid Bi-DRA amplifier setup and characterization

The hybrid Bi-DRA architecture based on the split-combine approach of spectral band is illustrated in Figure 6.19. The schematic resembles that of multistage DRA as explained previously in section 6.2 except for the replacement of DRA in the E-band with a Bi-doped fibre amplifier.

The setup includes an E-, S-, C-, and L-band WDM grid generated using the technique mentioned in sections 6.1 and 6.2, the 147 WDM dummy channels were then passed through a 70 SSMF subjugated to fibre loss and ISRS power transfer. After the SSMF transmission, the optical bands were separated into two paths for the independent amplification stage using a wideband FWDM with a passband from 1260-1457 nm and a reflection band from 1464-1620 nm. The two paths included signals from 1410-1457 nm of the E-band and 1470-1605 nm of the S-, C-, and L-band.

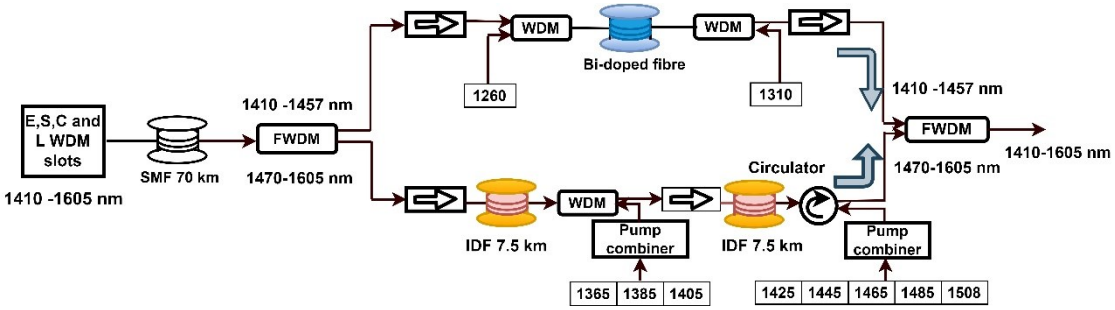

Figure 6.19 Schematic of hybrid Bi-Raman amplifier for E-, S-, C- and L-band signal amplifier

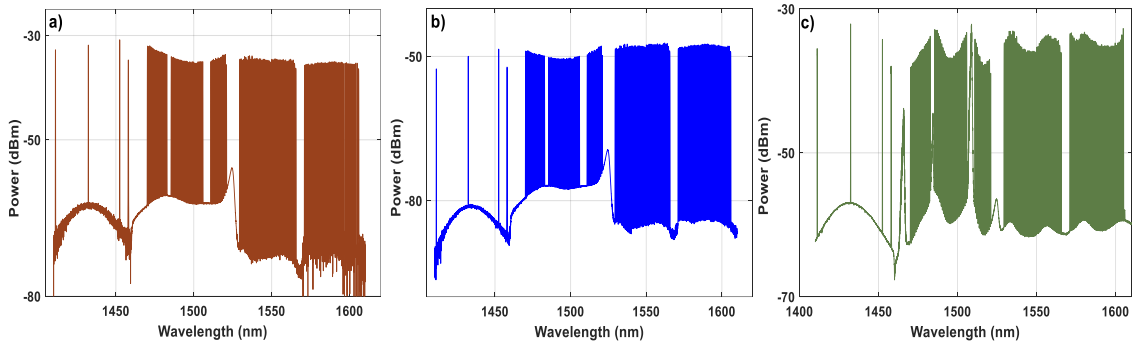

Figure 6.20 E-, S-, C- and L-band (1410-1605) nm spectrums a) input spectrum to SSMF; b) spectrum after 70 km SSMF; c) amplified spectrum after hybrid bi-DRA amplifier

The 1410-1457 nm (E-band) signals were amplified in a bidirectional fashion with two pump diodes at 1260 nm (forward) and 1310 nm (backward) direction with a pump power of 200 mW in each direction. The amplifying medium was 300 m of Bi-doped fibre with the detailed design and development reported in [277,278]. To prevent back-reflection of the forward and backward pump two isolators were added between the FWDMs enabling only the amplified signals to pass through.

The remaining signals from 1470-1605 nm (S-, C- and L-bands) were amplified using a dual-stage DRA replica of the amplifier illustrated in Figure 6.2 (a) of section 6.1.1. The amplifying medium included two 7.5 km of IDF fibre with stage 1 amplification for the S-band and stage 2 for the C- and L-band. Overall, 8 pump lasers at wavelengths of 1365, 1385, 1405, 1425, 1445, 1465, and 1508 nm with pump powers of 432, 297, 103, 289, 304, 269, 67, and 172 mW were used to provide amplification of signals from 1470-1605 nm.

Figure 6.20 (a-c) illustrates the input spectrum to SSMF, the output spectrum after 70 km SSMF, and the amplified spectrum after the hybrid Bi-DRA amplifier. The entire optical spectrum comprises 147 WDM channels with 143x100 GHz channelized ASE in the S-, C- and L-band, 3 laser diodes at 1411, 1431, and 1451 nm, and a PM-16QAM modulating signal at 1457 nm. Similar to the previous case with multistage DRA a higher noise floor was seen for the S-band signal due to the high NF of the TDFA and the higher insertion loss of the waveshaper used in generating the channelized ASE. Whereas in comparison a lower noise floor for the C- and L-band was seen due to the low NF of the C- and L-band EDFAs. Similarly, a lower NF for the E-band signals was observed due to the absence of any amplifier and WSSs.

The measured net gain and NF of the hybrid amplifier are shown below in Figure 6.21. The gain of the BDFA in the E-band was limited to enable matching power to that of DRA. A maximum gain of 18 dB was obtained at 1430 nm and a minimum gain of 12 dB was at 1457 nm.

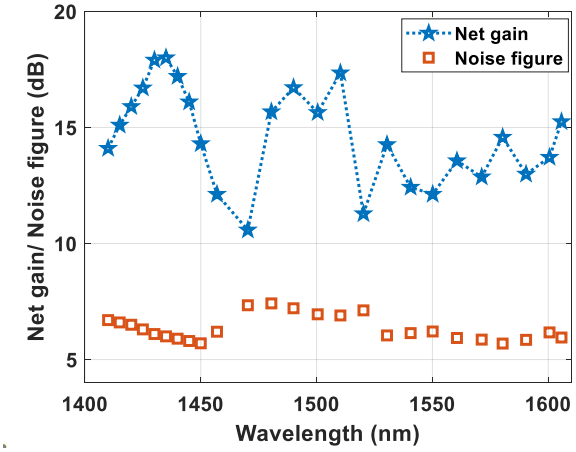

Figure 6.21 Hybrid Bi-Raman amplifier net gain and noise figure

The lower gain at 1457 nm is due to the low efficiency of BDFA at this region due to the relatively lower value of pump power used for matching with the S-, C-, and L-band gain. The gain of BDFA can be increased to > 30 dB in this region with a higher value of pump power. In the DRA section, a higher gain was obtained in the S-band with a maximum gain of 17 dB at 1510 nm and a minimum gain of 11 dB at 1470 nm. To note just like the previous test case of multistage DRA the gain of the BDFA and DRA were optimized to compensate for the loss of the 70 km SSMF and the FWDM splitter. Hence, a tilt in the gain profile was observed with a higher gain requirement of the S-band in comparison to the C- and L-band.

The minimum NF for E-band was 5.7 dB at 1450 and a maximum NF of 6.7 dB was obtained at 1410 nm a behaviour reported previously in [277]. In the dual-stage DRA, the NF has a similar value as reported previously in section 6.2.2, with a maximum NF of 7.4 dB at 1480 nm and a minimum NF of 5.6 dB at 1580. The improved NF of the C- and L-band in comparison to S-band in a dual-stage DRA structure is broadly explained in sections 6.1.2 and 6.2.2 of this chapter.

6.3.2 Coherent transmission with hybrid Bi-DRA

Coherent transmission with the proposed hybrid Bi-DRA as an inline amplifier is shown below in Figure 6.22. The experimental setup is similar to the one shown above in Figure 6.15 of section 6.2.4. The only difference in the setup is the use of the hybrid Bi-DRA in the line stage where the signals from 1410-1457 nm are amplified using a BDFA. Likewise, the input power to the SSMF section was ~19.6 dBm with a power per channel of ~-2 dBm the channels after transmission through the 70 km SSMF with an average loss of ~14.8 dB were compensated using the proposed Bi-DRA and were filtered using an OBPF for separation of the modulating signal. Like previous cases, the reception of the signal was performed by operating the corresponding amplifier for different wavelengths at typical output power. The reception stage was then followed by detection using an 80 GSa/S, 36 GHz real-time oscilloscope, and the corresponding Q^2 factor was calculated from the BER after a standard offline DSP procedure.

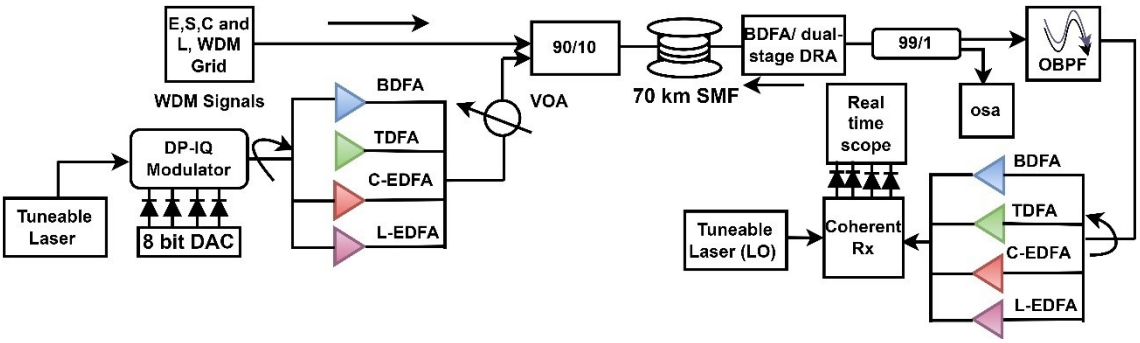

Figure 6.22 Schematic of E-, S-, C- and L-band 30 GBaud PM-16QAM transmission with BDFA and DRA as an inline amplifier.

6.3.2.1 Transmission results and discussion

The transmission performance of the inline Bi-DRA over a 70 km SSMF is shown below in Figure 6.23 (a-b). The wavelength dependency on the system performance was performed by tuning the tunable laser (signal laser and local oscillator) across a bandwidth of 195 nm over 21 different wavelengths from 1410-1605 nm. As shown below in Figure 6.23 (a) the B2B performance (dotted blue line with diamond markers) a decrement in the Q^2 factor was observed towards the shorter wavelength region with a minimum Q^2 factor of 14.3 dB at 1410 nm. A steep roll-off of 2 dB was observed with wavelength variation from 1420 to 1410 nm. This decrement is primarily due to the transceiver and the optical hybrid limitation in the E-band. An average Q^2 factor of 16.5 dB was observed in the E-band with a maximum value of 18 dB at 1457 nm. Moving towards the S-band, a minimum Q^2 factor of 16 dB for B2B transmission was obtained a 1470 nm, due to the high NF of the TDFA in this region of operation. The average value of the Q^2 factor for the S-band was ~17 dB with a maximum of 17.8 dB at 1490 nm.

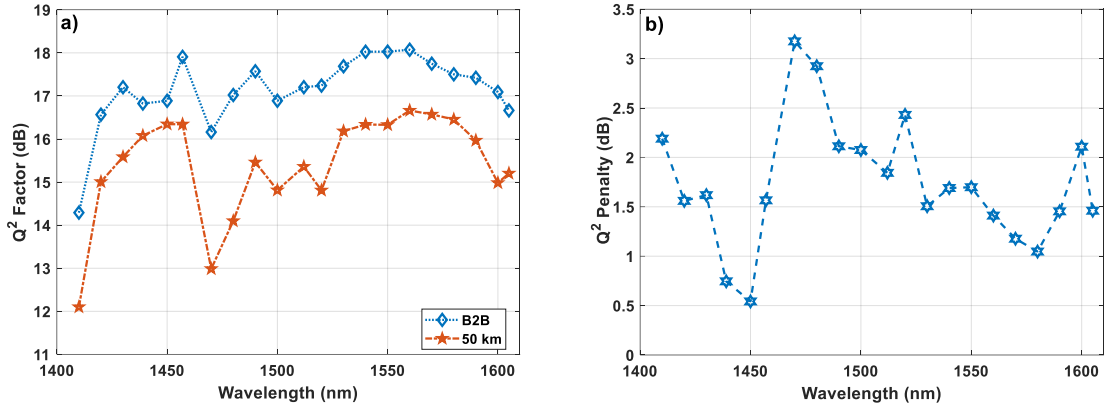

Figure 6.23 30 GBaud PM-16 QAM transmission with Hybrid Bi-DRA as an inline amplifier; wavelength a) Q^2 factor for B2B and 70 km transmission b) Q^2penalty

Towards the C- and L-band a similar performance to that of multistage DRA was observed with an average value of 17.5 dB across the wavelength region from 1530 to 1605 nm. The improved performance of the C- and L-band can be attributed to the improved performance of the C-band transceivers and low NF of the Tx and Rx EDFAs.

The transmission performance after 70 km follows a similar trend to that of B2B performance, where the worst performance was seen at 1410 and 1470 nm with a Q^2 factor of 12 and 13 dB. The performance penalty (Q^2 penalty) was observed to be highest in S-band at 1470 nm with a Q^2 penalty of 3.3 dB. This decrement is due to the high NF and low gain to the dual-stage DRA in this wavelength region and low received OSNR due to the overall noise addition of the TDFA in the Tx and Rx section. The E-band performance penalty was comparable to that of the C- and L-band with a minimum penalty of 0.5 dB at 1450 nm and a maximum penalty of 2.1 dB at 1410 nm. This lower penalty in E-band signals is due to the low NF of the BDFA in this region of operation, as can be seen from the spectrum of Figure 6.21. However, this penalty is likely to increase in the presence of a fully loaded E-band where the crosstalk between the neighbouring channels and ISRS power transfer would be significant, consequently degrading the system performance. Nevertheless, the performance of BDFA in the E-band shows BDFA to be a promising candidate, for future ultrawideband systems encapsulating the E-band.

The Q^2 penalty for the C- and L-band systems shows a similar performance to that of a multistage DRA with a minimum penalty of 1 dB at 1580 nm and a maximum penalty of 2 dB at 1600 nm. This improved performance of the C- and L-band can be attributed to the low NF of the DRA in this region of operation and partial benefit due to the ISRS power gain from the S-band signals in the SSMF and dual stage DRA stage 1 section, improving the overall received OSNR in the reception stage.

6.4 Hybrid distributed-discrete Raman amplifier for ultrawideband signal amplification

In this section, a new design of a Raman amplifier based on a hybrid combination of discrete and distributed Raman amplification (DDRA) has been studied. Previous studies with multistage DRA have shown higher performance penalty (Q^2 penalty) in the E-band due to the larger NF of the E-band DRA. To improve the performance of the E-band signals a novel design of distributed amplification with the E-band followed by a dual-stage DRA in the S-, C-, and L-band has been proposed. This design is of particular interest in ultrawideband systems, as the shorter wavelength channels show a higher performance penalty due to the high nonlinearity, high loss window of the SSMF, and unavailability of suitable transceivers in this region of operation. Additionally, penalties due to the amplifier NF can significantly deteriorate the overall system performance. Hence, it's crucial to design and develop amplifiers with minimal penalties for error-free transmission in the lower bands. Distributed Raman amplifier can be a suitable candidate for such ultrawideband systems due low level of NF and the absence of any nonlinear fibre as a gain medium.

6.4.1 Hybrid distributed-discrete Raman amplifier setup and characterization

The proposed architecture of hybrid DDRA for signal amplification from 1410-1605 nm (195 nm bandwidth) is illustrated in Figure 6.24. Similar, to the multistage DRA the design is based on a split-combine approach of spectral bands to minimize pump-to-pump and pump-to-signal overlapping.

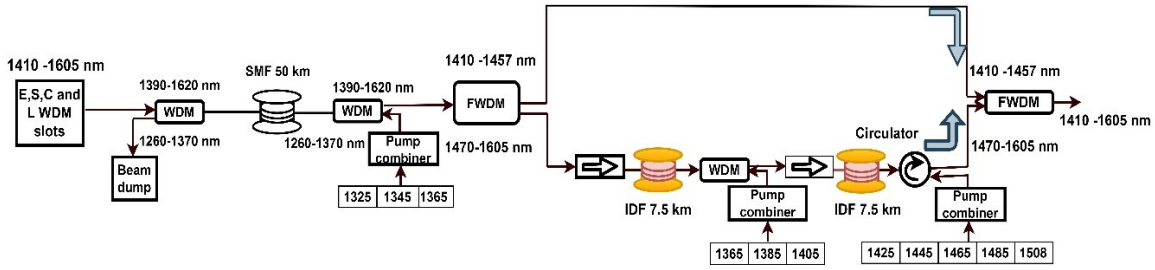

Figure 6.24 Schematic of hybrid distributed discrete Raman amplifier for E-, S-, C- and L-band signal amplification

The WDM spectrum comprises 143x100 GHz channels in the S-, C- and L-band generated using the technique explained in section 6.1.1 coupled with 4 E-band signals of which three are laser diodes at 1411, 1431, and 1451 nm and a PM-16QAM modulated signal at 1457 nm. The amplified spectrum was then passed through a WDM with a passband from 1390-1605nm and a reflection band from 1260-1370 nm. The WDM coupler was chosen due to the unavailability of high-power ultrawideband isolators that can terminate the backwards (BW) propagating pumps in the O-band region and enable the E-, S-, C- and L-band signals to propagate through. Instead,

the WDM coupler was used to dump the BW propagating pump after the amplification stage. The WDM channels were then passed through a 50 km SSMF where the signals from 1410-1457 nm undergo distributed amplification in a BW fashion using three pumps at 1325, 1345, and 1365 nm with pump powers of 439, 153, and 318 mW. We had to reduce the transmission length from 70 km to 50 km as the pump powers were insufficient to compensate for 70 km of SSMF loss due to the low Raman gain coefficient of SSMF. This distance can probably be increased to 60 km but due to the absence of low OH-peak 60 km spools in our facility, the experiments were continued with 50 km of SSMF. In the SSMF stage the S-, C- and L-band signals are devoid of any amplification due to the absence of any suitable pumps but rather undergo attenuation and ISRS power transfer from the shorter wavelengths to the longer wavelengths. The shorter S-band signals in the vicinity of 1470 nm will receive some amplification due to the 1465 nm pump, however parallelly these channels would also transfer the power towards the L-band channels due to ISRS in the SSMF section.

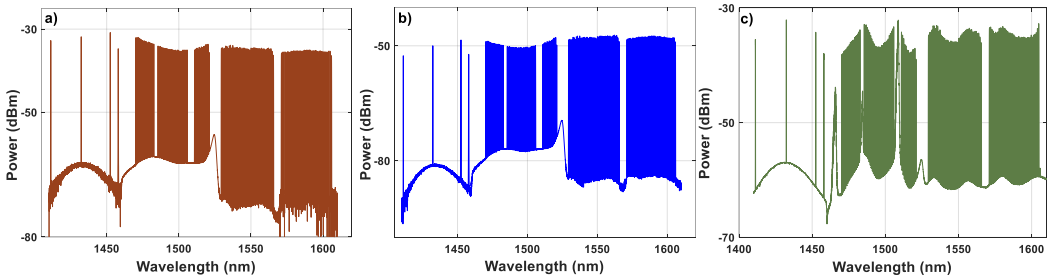

Figure 6.25 Optical WDM spectrum, wavelength vs output power; at a) SSMF input b) output from SSMF c) amplified output spectrum.

The spectral characteristics of the optical WDM signals at different positions of the amplifier are illustrated in Figure 6.25 (a-c). The input spectrum to SSMF whose relative power is shown in Figure 6.25 (a) has a total power of 18.6 dBm with a power per channel of ~-4 dBm. The attenuated signal with no amplification after the 50 km SSMF is shown in Figure 6.25 (a) the average loss of the SSMF and the two WDMs used has a total loss of ~14.2 dB. The spectrum illustrated in Figure 6.25 (c) represents the amplified output spectrum after the hybrid Raman amplification stage.

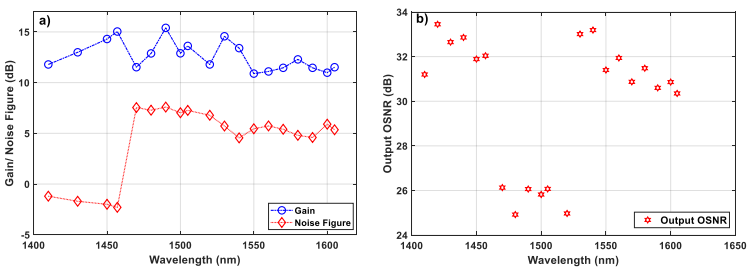

Figure 6.26 Ultrawideband hybrid distribute-discrete Raman amplifier a) net gain and noise figure b) amplified output OSNR

An overall average gain of 14 dB was obtained across the entire bandwidth. A higher gain was required towards the E- and S-band signals due to the higher power loss and ISRS from the E- and S-band signals to the C- and L-band signals. The localized effective NF in the E-band was below 0 dB due to distributed amplification, whereas the highest NF was 7.5 dB at 1470 and 1480 nm. An average NF of 5.5 dB was obtained for the C- and L-band signals (1530-1605 nm). The output OSNR measured after the amplifier using a 30 GBaud PM-16QAM signal, swept at an interval of 10 nm has a value > 30 dB for all the E-, C- and L-band signals whereas for the S-band the value was ~25 dB for all the channels. The low output OSNR for the S-band is because of the low input OSNR, generated due to the high NF of the TDFA and high insertion loss of the waveshaper used in creating the ASE grid. Similarly, the high output OSNR for E-band is due to the use of independent laser sources and for the C- and L-band is due to the low NF of C- and L-band EDFAs used in generating the channelized ASE.

6.4.2 Coherent transmission with hybrid Raman amplifier

The transmission setup for validation of the hybrid DDRA is similar to that of the multistage DRA except for the use of a different inline Raman amplifier and the length of SSMF. Similar to previous test cases, a 30 GBaud PM-16QAM signal was generated using a 120 GSa/s DAC and a C-band $LiNbO_3$ DP-IQ modulator. Two tunable laser sources extending from 1385-1480 and 1480-1620 nm were used to emulate the WDM carrier from 1410-1605 nm. The modulated signals were then amplified using the corresponding booster amplifier and were power levelled using a VOA. The signals were then passed through the 50 km SSMF with parallel distributed amplified amplification from E-band signals followed by discrete amplification from S-, C- and L-band signals. The amplified signals were then passed through a 99/1 tap whose 1% arm was used to calculate OSNR and the remaining 99% power was transmitted. The modulated signal was then filtered using a wideband OBPF followed by a standard detection procedure as mentioned in section 6.2.4 to calculate the Q^2 factor from BER.

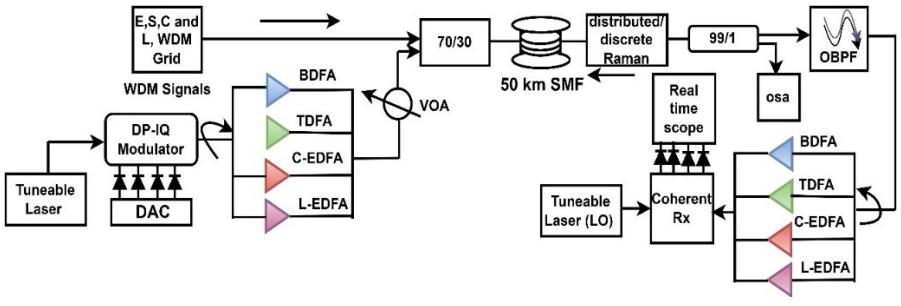

Figure 6.27 Experimental setup for 30 GBaud PM-16QAM transmission with hybrid Bi-DRA as an inline amplifier.

6.4.2.1 Transmission results and discussions

The transmission performance with hybrid DDRA is illustrated in Figure 6.28 (a-c) where a degradation performance towards the E- and S-band (1410-1520 nm) was observed. The B2B Q^2 factor was minimum at 1410 nm for E-band signals with a value of 14 dB and as for the signals from 1470-1520 nm, the minimum value is 15 dB at 1470 nm. A steady performance of ~17 dB was seen for C- and L-band signals with a minimum value of 16.5 dB at 1600 nm. The 2 dB roll-off from C- to S-band, is due to the high NF of the Tx and Rx TDFA. Similarly, for the E-band signals, the degradation is due to the IQ and polarization imbalance of the transceivers in addition to the BDFA NF. Whereas, for the C- and L-band the optimal performance can be attributed to the low NF of the EDFAs and the commercial transceiver's low IQ and polarization imbalance. A similar trend in the transmission performance was seen with 50 km SSMF and the hybrid DDRA where the performance degradation was maximum towards the E- and S-band followed by C- and L-band. The Q^2 penalty (Q^2 factor difference B2B and 50 km transmission) can be well explained by the amplifier NF and output OSNR where the S-band signals have the highest penalty with an average value of 1.9 dB, followed by C- and L-band with an average penalty of 0.9 dB and minimum for E-band with an average penalty of 0.7 dB. The lower penalty in E-band signals can be well attributed to distributed amplification resulting in improved OSNR and low effective NF. In the case of the S-band, the penalty is largely due to the high NF and low output OSNR of the signals < 27 dB for all the signals. As mentioned previously the shorter wavelength channels suffer due to IQ and polarization imbalance with the use of standard C-band components. To study the effects of polarization imbalance due to the optical hybrid the XY polarization penalty was measured i.e., a difference in the Q^2 factor between X and Y polarization with a B2B setup. Figure 6.28 (c) shows a linear increment in the penalty with a maximum value of 1.5 dB at 1410 nm signal (E-band) which decreases linearly and normalizes down to 0.4 dB for C- and L-band signals. This polarization penalty indicates the limitation of the system towards the shorter wavelength channels in a UWB transmission with standard C-band components.

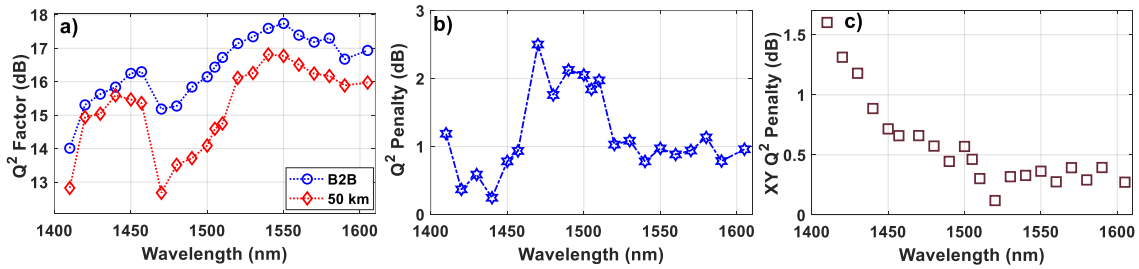

Figure 6.28 30 GBaud PM-16QAM transmission performance wavelength vs a) Q^2 penalty for B2B and 70 km transmission b) Q^2 penalty c) XY Q^2 penalty.

These experimental results show that in UWB systems shorter wavelength channels undergo higher performance degradation due to system limitation, and additional penalties due to inline

amplifiers can significantly degrade the overall performance. Hence, distributed amplification for the shorter wavelength channel followed by discrete amplification for the longer wavelength channels can be a smart approach to minimize the net performance penalty of an MBT system.

6.5 Conclusion

In this chapter, various designs of ultrawideband Raman amplifiers and their performance penalties in a coherent transmission system are discussed. An initial study with three different designs of UWB Raman amplifier (dual-stage, dual-band with back-reflection, and dual-band with no back-reflection) over S-, C-and L-band show that dual-stage benefits from dual-band in terms of overall power consumption. However, the dual-stage design requires inclusion of a guard band of 10 nm between the 1485 and 1508 nm region. This reduced the number of launched channels to 143x100 GHz, reducing the overall transmission bandwidth. Similarly, for the in-parallel dual-band design, there was no requirement for guard-band and hence, the total number of channels that we managed to launch was 156x100 GHz. However, this performance advantage comes at the cost of the additional requirement of the 1425 nm pump, increasing the total amplifier power consumption.

In the next section, S-, C-, and L-band DRA was extended to a multistage E-, S-, C-, and L-band. Three different architectures were presented 1) multistage DRA 2) Hybrid Bi-DRA and 3) Hybrid DDRA. In all these three designs the S, C and L-band were amplified using a cascaded dual-stage DRA, while the E- band (1410-1457) nm were amplified by three different technique that includes single stage DRA, bidirectionally pumped BDFA and a backwards pumped DiRA. Among all the three designs DRA has the worst performance in the E-band with a maximum Q^2 penalty of ~4 dB at 1410 nm. While in the case of hybrid Bi-DRA in the E-band region, the maximum Q^2 penalty was ~2.2 dB at 1410 nm, a 1.8 dB improvement in comparison to the use of DRA in the E-band. The hybrid DDRA has the best performance in this region of operation with a Q^2 penalty similar to that of the C- and L-band. The maximum Q^2 penalty was ~1.1 dB at 1410 nm which is ~ 2.9 dB and ~1.1 dB improvement in comparison to multistage DRA and hybrid Bi-DRA. Towards the S-, C- and L-band (1470-1520) the performance of all three amplifiers are quite identical due to the use of the same amplifier type (cascaded dual-stage DRA) with a maximum Q^2 penalty of ~2 dB.

In addition to this, penalties between X and Y polarization were calculated for the B2B setup to study the transceiver limitation in an MBT system. Experimental results show that shorter wavelength channels suffer from the transceiver IQ and polarization imbalance. This penalty was dominant in the E- and the shorter S-band channels from 1410 to 1480 nm where a linear increment in the Q^2 penalty was observed between the X and Y polarization values extending out to 1.5 dB penalty at 1410 nm.

Chapter 7: Conclusion and future works

7.1 Conclusion

In this thesis, we evaluated the performance of distributed, discrete, and hybrid Raman amplifiers in different bands of the optical communication window for high-capacity coherent systems. Our initial study included nonlinear penalties in discrete Raman amplifiers (DRAs) with different Raman gain fibres. This study was conducted to study the variation of accumulated nonlinear noise with Raman gain fibre type of opposite value of fibre chromatic dispersion (CD). The results obtained from the analytical GN model and long-haul recirculation loop experiments showed that a Raman gain fibre type with a positive value of CD is a better choice for discrete amplification in the inline stage of a long-haul transmission link. In addition to this, it was seen that choosing a Raman fibre type with an optimized value of the nonlinear coefficient is also necessary for the design of DRAs, in long-haul links. If the value of the nonlinear coefficient is too large then the overall accumulated nonlinear noise will also be high and similarly, a lower value of the nonlinear coefficient can result in an insufficient overall amplifier gain.

The next study included distributed Raman amplifiers (DiRA) for short and long-haul coherent systems. In this study, relative intensity noise (RIN) induced penalties were primarily evaluated in two standard single-mode fibres (SSMFs) G.652.D and 6.654.E. The measured RIN was observed to be lower for G.654.E in comparison to its counterpart G.652.D despite the Raman pump operating below the cable cut-off value of G.654.E. To compare the performance of both the test fibre for short and long-haul applications. A Single-span transmission was initially performed under FW pumping configuration. The experimental results showed improved performance of G.654.E over G.652.D. Similarly, a long-haul transmission was conducted with both the test fibres using Bi and BW pumping configuration with experimental results showing transmission reach exceeding >1000 km for G.654.E in comparison to G.652.D. The results in this chapter show that G.654.E is a suitable fibre type for distributed amplification. In addition to this, the lower attenuation and nonlinear coefficient of G.654.E makes it a very suitable choice for long-haul transmission applications where the OSNR is crucial in achieving target distances.

Finally, with the studies of DiRAs and DRAs made previously an investigation was conducted to evaluate the performance of Raman amplifiers in coherent systems enabling multiband transmission (MBT). The first study included performance optimization of two different architectures of DRAs in S-, C- and L- band (1420-1605 nm) WDM transmission systems. The two architectures used for this study cascaded dual-stage DRA and in-parallel dual-band DRA. While cascaded dual-stage DRA has a reduced power consumption the overall estimated net throughput that can be achieved with 200G signals is 28.6 Tb/s. However, in the dual-band DRA the estimated throughput exceeds 2.6 Tb/s with a maximum value of 31.2 Tb/s over a transmission

bandwidth of 17.1THz (135 nm). However, this benefit of dual-band over dual-stage comes at the cost of additional pump requirements increasing the overall power consumption. In terms of bandwidth, the commercially available EDFA over the C- and L-band (1530-1625 nm) can support a total bandwidth of 10.5 THz. Hence, a capacity enhancement of ~ 6.6 THz can be achieved with the two proposed S-, C- and L-band DRAs.

In the next part, the bandwidth was extended further by including the E- band. Three different design of multistage amplification was presented in which the 1470-1605 nm signals were amplified using a cascaded-dual stage architecture and the signals from 1410-1457 nm were amplified using either a DRA, BDFA or a DiRA. Amongst all the three setups the hybrid-DDRA (E-band amplified using DiRA) has the best performance towards the E-band with a minimal Q^2 penalty. Towards the S-, C- and L-band a similar performance was observed due to the use of the same cascaded dual-stage DRA for all three setups. The achieved amplification bandwidth was 25.6 THz (210 nm) initially and was later reduced to 25.2 THz (195 nm) during coherent transmission due to the limitations as explained in Chapter 6. This amplification bandwidth is 14.1 THz larger than the existing EDFA capacity. In terms of net throughput, the estimated capacity with 147x100 GHz, PM-16QAM signal is ~ 29.4 Tb/s. Considering that the supported E-band from 1410-1457 nm is loaded with a 100 GHz spacing WDM grid the number of channels that can be accommodated is 54 WDM channels. In such a scenario the expected throughput with 30 GBaud PM-16QAM signals can be estimated to be around 39.4 Tb/s.

It should also be noted that all the above-mentioned UWB transmissions were performed using SSMF that has no OH absorption peak in the region of the E-band ~1370-1410 nm [35]. However, most of the field-deployed fibres have OH peak present in the region of the E-band, hence there will be performance degradation in the E-band signals in comparison to that of transmission over fibre without OH peak. The multistage and the Bi-DRA illustrated in sections 6.2 and 6.3 might require high pump powers to amplify the signals in the range of 1410-1430 nm as these signals would undergo larger power loss in the SSMF transmission section. In the case of hybrid-DDRA, it would be even more complicated as the Raman gain coefficient for SSMF is smaller. The net gain required for the lower wavelength channels would be significantly large and this might put a limitation on the maximum achievable gain due to the limited pump power availability.

The study throughout the thesis suggests that Raman amplifiers are a potential candidate for future MBT systems. The proposed amplifiers discussed in this thesis emphasize the design challenges, advantages, and limitations of Raman amplifiers in MBT systems. In addition to MBT systems, a separate study on RIN and nonlinear penalties was conducted using DiRA and DRAs. This study showed all the essential parameters that are needed to be taken into consideration before implementing Raman amplifiers in the inline stage of transmission links.

7.2 Future Works

The successful transmission of E-, S-, C- and L-band with different Ramana amplifiers, opens up new opportunities for further exploration of MBT systems. Transmission in the O- and E- and U-band has not been yet widely explored due to the limited commercial-grade equipment to perform a full-scale transmission in these bands. Hence, investigation of different amplifiers such as distributed Raman, discrete Raman, SOAs, BDFA etc, in these bands is crucial before choosing a particular amplifier type for future transmission systems. In addition to this, our UWB experiments lack a fully loaded E- band system due to the absence of commercial-grade WSSs and ASE sources. Hence, it is essential to conduct UWB transmission with fully loaded E- band signals where the ISRS power transfer from E-band to a higher band will degrade the system performance. In the presence of a fully-loaded UWB system, the variation in the power spectral density and the spectral tilt will also impact the performance of the amplifiers in particular the inline ones. These amplifiers are likely to introduce more noise degrading the channel performances. With the advances in spectral efficiency, modern-day coherent technology has reached new heights in terms of the cardinality of data transmission with tailored probabilistic-shaped constellations. Modulation formats such as 256 QAM, and 1024 QAM have been well demonstrated in the C- and L-bands, pushing this limit toward the lower bands such as S- and E-bands is highly challenging due to SNR limitations, and the performance of commercial grade transceivers in these bands. Hence, UWB transmission using high modulation format data with the proposed architecture of Raman amplifiers will be an interesting study to understand the feasibility of future optical networks with MBT systems.

The gain bandwidth of the Raman amplifier can be further extended to the lower E- band and the O-band covering the entire communication window of an SSMF. However, the design of such a UWB amplifier is quite challenging due to the multiple probabilities of pump-to-pump and pump-to-signal overlapping. Extending the amplification window towards these bands also requires the development of commercial-grade pumps at appropriate wavelength and power which can be very crucial as the channels in these bands undergo higher power losses. Further exploration of Raman gain fibres is essential in these bands as the power penalties will be larger in comparison to the commercial C-band. Hence, numerical and analytical modelling can be performed to understand the fibre type that is best suitable for Raman amplification in these bands, which can later be developed for experimental validations. The pump wavelengths and powers used in the experiments of this thesis are not optimized due to the limitations in their power and commercial availability. These pump wavelengths and power can also be further optimized using tools such as machine learning and genetic algorithms for optimal system performance.

The above-mentioned possibilities are beyond the scope of this thesis but at the same time also open up new opportunities to further explore the feasibility of Raman amplifiers in future MBT systems for long-haul and metro networks.

References

1. K. C. Kao and G. A. Hockham, "Dielectric-fibre surface waveguides for optical frequencies," Proc. Iee **113**(7), 1151–1158 (1966).
2. G. P. Agrawal, *Optical Communication: Its History and Recent Progress* (Springer open, 2016).
3. F. P. Kapron, D. B. Keck, and R. D. Maurer, "Radiation losses in Glass Optical Waveguides," Appllied Phys. Lett. **423**(17), (1970).
4. T. Miya, Y. Terunuma, T. Hosaka, and T. Miyashita, "Ultimate low-loss single-mode fibre at 1.55 μm," Electron. Lett. **15**(4), 106–108 (1979).
5. "First Generation Optical Transmission Windows Tutorials," https://www.tutorials.fomsn.com/fiber/optical-communication/first-generation-optical-transmission-windows/.
6. E. Desurvire, C. R. Giles, and J. L. Zyskind, "Erbium doped fibre amplifiers," (1991).
7. D. N. Payne, P. R. Morkel, R. I. Laming, and M. Tachibana, "Erbium doped fibre amplifier with shaped spectral gain," (1996).
8. P. J. Winzer, D. T. Neilson, and A. R. Chraplyvy, "Fiber-optic transmission and networking: the previous 20 and the next 20 years [Invited]," Opt. Express **26**(18), 24190 (2018).
9. A. R. Chraplyvy, A. H. Gnauck, R. W. Tkach, and R. M. Derosier, "8*10 Gb/s transmission through 280 km of dispersion-managed fiber," 1233–1235 (1993).
10. M. M. El Said, S. Member, J. Sitch, and M. I. Elmasry, "An Electrically Pre-Equalized 10-Gb / s Duobinary Transmission System," J. Light. Technol. **23**(1), 388–400 (2005).
11. S. J. Savory, G. Gavioli, R. I. Killey, and P. Bayvel, "Electronic compensation of chromatic dispersion using a digital coherent receiver," Opt. Express **15**(5), 2120–2126 (2007).
12. "Colt 8OOG," https://www.capacitymedia.com/article/29tgv135tpvr6afgf2n0g/colt-deploys-industry-first-800g-technology-in-the-l-band.
13. S. Perrin, *Coherent Optics at 400G , 800G , and Beyond A 2021 Heavy Reading Survey* (2021).
14. Y. Koizumi, K. Toyoda, M. Yoshida, and M. Nakazawa, "1024 QAM (60 Gbit / s) single-carrier coherent optical transmission over 150 km," Opt. Express **20**(11), 12508–12514 (2012).

15. S. L. I. Olsson, J. Cho, S. Chandrasekhar, X. Chen, P. J. Winzer, and S. Makovejs, "Probabilistically shaped PDM 4096-QAM transmission over up to 200 km of fiber using standard intradyne detection," Opt. Express **26**(4), 4522–4530 (2018).

16. X. Chen, J. Cho, A. Adamiecki, and P. Winzer, "16384-QAM transmission at 10 GBD over 25-km SSMF using ploarization-multiplexed probalilistic constellation shaping," in *European Conference and Exhibition on Optical Communication* (2019), pp. 1–4.

17. A. D. Ellis, M. E. McCarthy, M. A. Z. Al Khateeb, M. Sorokina, and N. J. Doran, "Performance limits in optical communications due to fiber nonlinearity," Adv. Opt. Photonics **9**(3), 429 (2017).

18. Infinera, "ICE6 Optical Engine," (2020).

19. "Acacia CIM 8," https://acacia-inc.com/product/coherent-interconnect-module-8/.

20. "Acacia AC1200," https://www.lightwaveonline.com/optical-tech/transmission/article/14039809/acacia-communications-unveils-ac1200sc2-12tbps-singlechip-singlechannel-coherent-optical-module.

21. "WaveLogic™5 Extreme Ciena," https://www.ciena.com/products/wavelogic/wavelogic-5/extreme.

22. E. Narimanov and P. Mitra, "The Channel Capacity of a Fiber Optics Communication System," J. Light. Technol. **20**(3), 530–537 (2002).

23. "Moore and Shannon," https://www.infinera.com/blog/moore-and-shannon-a-tale-of-two-laws/tag/optical/.

24. S. Kumar, "Fundamental Limits to Moore's Law," arXiv 1–3 (2015).

25. A. D. Ellis, N. Mac Suibhne, D. Saad, and D. N. Payne, "Communication networks beyond the capacity crunch," Philos. Trans. R. Soc. A Math. Phys. Eng. Sci. **374**(2062), (2016).

26. "Cisco Annual Internet Report - (2018–2023) White Paper - Cisco," https://www.cisco.com/c/en/us/solutions/collateral/executive-perspectives/annual-internet-report/white-paper-c11-741490.html.

27. P. Martelli, "Impact of the crosstalk in space-division multiplexing," in *International Conference on Transparent Optical Networks* (2017), pp. 24–27.

28. C. Presider, Y. Nishimura, and F. Elec-, "Multicore optical fiber," in *Optical Fiber Communication Conference (OFC)* (1979), pp. 46–48.

29. K. Saitoh and S. Matsuo, "Multicore fibers for large capacity transmission," Nanophotonics **2**(5–6), 441–454 (2013).

30. Y. Sasaki, K. Takenaga, S. Matsuo, K. Aikawa, and K. Saitoh, "Few-mode multicore fibers for long-haul transmission line," Opt. Fiber Technol. **35**, 19–27 (2017).

31. H. Takara, A. Sano, T. Kobayashi, H. Kubota, H. Kawakami, A. Matsuura, and Y. Miyamoto, "1.01-Pb/s (12 SDM/222 WDM/456 Gb/s) Crosstalk-managed Transmission with 91.4-b/s/Hz Aggregate Spectral Efficiency," in *ECOC - European Conference and Exhibition on Optical Communication* (2012), (1), pp. 4–6.

32. G. Rademacher, B. J. Puttnam, R. S. Lu, W. Klaus, T. A. Eriksson, Y. Awaji, and T. Hayashi, "10 . 66 Peta-Bit / s Transmission over a 38-Core-Three-Mode Fiber," (1), 2020–2022 (2020).

33. R. S. Luis, B. J. Puttnam, G. Rademacher, Y. Awaji, and H. Furukawa, "372 Tb/s Unrepeatered 213 km Transmission Over a 125 μm Cladding Diameter, 4-Core MCF," in *Optical Fiber Communication Conference (OFC)* (2022), pp. 3–5.

34. B. J. Puttnam, R. S. Luis, G. Rademacher, Y. Awaji, and H. Furukawa, "High-Throughput and Long-Distance Transmission with >120 nm S-, C- and L-Band Signal in a 125μm 4-Core Fiber," J. Light. Technol. **40**(6), 1633–1639 (2022).

35. A. Ferrari, A. Napoli, J. K. Fischer, N. Costa, A. D'Amico, J. Pedro, W. Forysiak, E. Pincemin, A. Lord, A. Stavdas, J. P. F. P. Gimenez, G. Roelkens, N. Calabretta, S. Abrate, B. Sommerkorn-Krombholz, and V. Curri, "Assessment on the Achievable Throughput of Multi-Band ITU-T G.652.D Fiber Transmission Systems," J. Light. Technol. **38**(16), 4279–4291 (2020).

36. B. J. Puttnam, R. S. Luís, G. Rademacher, M. Mendez-Astudillio, Y. Awaji, and H. Furukawa, "S-, C- and L-band transmission over a 157 nm bandwidth using doped fiber and distributed Raman amplification," Opt. Express **30**(6), 10011 (2022).

37. L. Galdino, A. Edwards, W. Yi, E. Sillekens, Y. Wakayama, T. Gerard, W. S. Pelouch, S. Barnes, T. Tsuritani, R. I. Killey, D. Lavery, and P. Bayvel, "Optical Fibre Capacity Optimisation via Continuous Bandwidth Amplification and Geometric Shaping," IEEE Photonics Technol. Lett. **32**(17), 1021–1024 (2020).

38. M. Asif Iqbal, L. Krzczanowicz, I. Phillips, P. Harper, and W. Forysiak, "150nm SCL-band transmission through 70km SMF using ultra-wideband dual-stage discrete raman amplifier," in *Optical Fiber Communication Conference (OFC)* (2020), pp. 1–3.

39. M. A. Z. Al-Khateeb, M. Tan, M. A. Iqbal, M. McCarthy, P. Harper, and A. D. Ellis, "Four wave mixing in distributed Raman amplified optical transmission systems," 2016 IEEE Photonics Conf. IPC 2016 795–796 (2017).

40. L. Krzczanowicz, M. A. Z. Al-Khateeb, M. Asif Iqbal, I. Phillips, P. Harper, and W. Forysiak, "Performance estimation of discrete Raman amplification within broadband optical networks," in *Optical Fiber Communication Conference (OFC) 2019* (OSA, 2019), pp. 1–3.

41. P. J. Winzer and R. J. Essiambre, "Advanced modulation formats for high-capacity optical transport networks," J. Light. Technol. **24**(12), 4711–4728 (2006).

42. R. J. Essiambre, G. J. Foschini, P. J. Winzer, G. Kramer, and B. Goebel, "Capacity Limits of Optical Fiber Networks," J. Light. Technol. **28**(4), 662–701 (2010).

43. "What is a Mach-Zehnder Modulator and How Does it Work?|Synopsys," https://www.synopsys.com/glossary/what-is-a-mach-zehnder-modulator.html.

44. S. Shimotsu, S. Oikawa, T. Saitou, N. Mitsugi, K. Kubodera, T. Kawanishi, and M. Izutsu, "Single side-band modulation performance of a LiNbO3 integrated modulator consisting of four-phase modulator waveguides," IEEE Photonics Technol. Lett. **13**(4), 364–366 (2001).

45. Y. I. Hammadi and T. S. Mansour, "Relationship between the voltage applied to MZM arms and the generation of optical frequency comb," Int. J. Eng. Technol. **7**(4.15), 405 (2018).

46. "The principle and transfer function of the phase modulator, intensity modulator, and IQ modulator - Advanced Optoelectronic Devices Supplier - Rofe," http://www.rof-oc.com/info-20-43-135.html.

47. M. A. Iqbal, "Advanced Raman Amplification Techniques for High Capacity and Broadband Coherent Optical Transmission Systems Doctor of Philosophy," Aston university (2018).

48. S. Addanki, I. S. Amiri, and P. Yupapin, "Review of optical fibers-introduction and applications in fiber lasers," Results Phys. **10**(June), 743–750 (2018).

49. G. P. Agrawal, *Nonlinear Fiber Optics*, 3rd ed. (2019).

50. G. Saavedra Mondaca, "Optical Fibre Communication Systems in the Nonlinear Regime," University college London (2018).

51. C. R. Menyuk, "Nonlinear pulse propagation in birefringent optical fibers," IEEE J. Quantum Electron. **23**(2), 174–176 (1987).

52. P. K. A. Wai, C. R. Menyuk, and H. H. Chen, "Stability of solitons in randomly varying birefringent fibers," Opt. Lett. **16**(16), 1231 (1991).

53. D. Marcuse, C. R. Menyuk, and P. K. . Wai, "Application of the Manakov-PMD equation to studies of signal propagation in optical fibres with randomly varying birefringence," J. Light. Technol. **15**(9), 1722–1746 (1997).

54. J. Stone, "Reduction of OH Absorption in Optical Fibers by OH → OD Isotope Exchange," Ind. Eng. Chem. Prod. Res. Dev. **25**(4), 609–621 (1986).

55. G. P. Agrawal, *Fiber-Optic Communications Systems, Third Edition.* (Wiley Interscience, 2002), **6**.

56. M. Ohashi, K. Shiraki, and K. Tajima, "Optical Loss Property of Silica-Based Single-Mode Fibers," J. Light. Technol. **10**(5), 539–543 (1992).

57. M. C. Fugihara and A. N. Pinto, "Attenuation fitting functions," Microw. Opt. Technol. Lett. **51**(10), 2294–2296 (2009).

58. K. Tsujikawa, K. Tajima, K. Shiraki, and I. Sankawa, "Method for predicting Rayleigh scattering loss of silica-based optical fibers," J. Light. Technol. **25**(8), 2122–2128 (2007).

59. Marie Wandel, "Attenuation in silica-based optical fibers," Technical University of Denmark (2006).

60. L. N. Binh, *Optical Fiber Communications Systems: Theory and Practice with Matlab® and Simulink® Models* (2011).

61. H. Ghafoori Fard, A. Dehesht, A. Rostami, and S. Nejati, "A novel dispersion-shifted single mode optical fiber design with ultra-high-bit-rate and very low loss for long-haul communications," Opt. Commun. **281**(23), 5779–5787 (2008).

62. L. Grüner-nielsen, M. Wandel, P. Kristensen, C. Jørgensen, L. V. Jørgensen, B. Edvold, B. Pálsdóttir, and D. Jakobsen, "Dispersion-Compensating Fibers," J. Light. Technol. **23**(11), 3566–3579 (2005).

63. S. J. Savory, "Digital coherent optical receivers: Algorithms and subsystems," IEEE J. Sel. Top. Quantum Electron. **16**(5), 1164–1179 (2010).

64. T. R. Woliński, "Polarization in optical fibers," Acta Phys. Pol. A **95**(5), 749–760 (1999).

65. Corning Incorporated, *Polarization-Mode Dispersion* (2017).

66. S. Ten and M. Edwards, *An Introduction to the Fundamentals of PMD in Fibers* (2006), (July).

67. R. W. Boyd, *Nonlinear Optics*, 3rd ed. (Elsevier Academic Press, 1992).

68. A. R. Ghraplyvy and J. Stone, "Measurement of cross-phase modulation In coherent wavelength-division multiplexing using Injection lasers," in *Optical Fiber*

Communication Conference (OFC) (1985), **8**(1984), pp. 56–57.

69. M. S. Abood, M. M. Hamdi, B. A. Taha, M. A.S., and E. M. Alssaedi, "Performance of Effect for XPM and FWM in Fiber Optics," in *Proceedings of International Conference on Emerging Technologies and Intelligent Systems. ICETIS 2021.* (2021), **322**, p. 85990.

70. E. F. Mateo, F. Yaman, T. Wang, and G. Li, "Nonlinearity compensation using digital backward propagation," Opt. InfoBase Conf. Pap. **20**(13), 14362–14370 (2011).

71. M. A. Z. Al-Khateeb, M. E. McCarthy, C. Sánchez, and A. D. Ellis, "Nonlinearity compensation using optical phase conjugation deployed in discretely amplified transmission systems," Opt. Express **26**(18), 23945 (2018).

72. Mohammad Ahmad Zaki Al-Khateeb, "Experimental Demonstration of Performance Enhancement in Non-Linearity Limited Optical Fibre Systems," Aston University (2018).

73. R. L. Lynch, R. L. Maybach, and P. F. Walch, "Design and Deployment of Optically Amplified Undersea Systems," AT&T Tech. J. **74**(1), 83–92 (1995).

74. A. D. Ellis, J. Zhao, and D. Cotter, "Approaching the Non-Linear Shannon Limit," J. Light. Technol. **28**(4), 423–433 (2010).

75. D. J. Richardson, J. M. Fini, and L. E. Nelson, "Space-division multiplexing in optical fibres," Nat. Photonics **7**(5), 354–362 (2013).

76. L. Rapp and M. Eiselt, "Optical Amplifiers for Multi – Band Optical," J. Light. Technol. **40**(6), 1579–1589 (2022).

77. Y. Sun, A. K. Srivastava, J. Zhou, and J. W. Sulhoff, "Optical fiber amplifiers for WDM optical networks," Bell Labs Tech. J. **4**(1), 187–206 (1999).

78. R. I. Laming, J. E. Townsend, D. N. Payne, F. Meli, G. Grasso, and E. J. Tarbox, "Operating in the Saturated Regime," IEEE Photonics Technol. Lett. **3**(3), 253–255 (1991).

79. P. Myslinski, C. Szubert, A. J. Bruce, D. J. Digiovanni, and B. Palsdottir, "Performance of High-Concentration Erbium-Doped Fiber Amplifiers," IEEE Photonics Technol. Lett. **11**(8), 973–975 (1999).

80. P. Myslinski and D. Nguyen, "Effects of Concentration on the Performance of Erbium-Doped Fiber Amplifiers," J. Light. Technol. **15**(1), 112–120 (1997).

81. I. Nusinsky and A. A. Hardy, "Analysis of the Effect of Upconversion on Signal Amplification in Erbium-Doped Fiber," IEEE J. Quantum Electron. **39**(4), 548–554 (2003).

82. "Fiber Optical Networking," https://www.fiber-optical-networking.com/the-application-of-edfa.html.

83. A. Bjarklev, *Optical Fiber Amplifiers: Design and System Applications* (1993).

84. P. F. Wysocki, J. Judkins, R. Espindola, M. Andrejco, A. Vengsarkar, and K. Walker, "Erbium-Doped Fiber Amplifier Flattened Beyond 40 nm Using Long-Period Grating," IEEE Photonics Technol. Lett. **9**(10), 375–378 (1997).

85. J. M. P. Delavaux and J. A. Nagel, "Multi-Stage Erbium-Doped Fiber Amplifier Designs," J. Light. Technol. **13**(5), 703–720 (1995).

86. H. Ono, M. Yamada, T. Kanamori, S. Sudo, and Y. Ohishi, "Amplifiers for WDM Transmission Systems," J. Light. Technol. **17**(3), 490–496 (1999).

87. C. Lei, H. Feng, Y. Messaddeq, and S. LaRochelle, "Investigation of C-band pumping for extended L-band EDFAs," J. Opt. Soc. Am. B **37**(8), 2345 (2020).

88. T. C. Liang, Y. K. Chen, J. H. Su, W. H. Tzeng, C. Hu, Y. T. Lin, and Y. C. Lai, "Optimum configuration and design of 1480-nm pumped L-band gain-flattened EDFA using conventional erbium-doped fiber," Opt. Commun. **183**(1–4), 51–63 (2000).

89. N. Park, J.-H. Lee, and U.-C. Ryu, "Parallel optical fiber amplifier with high power conversion," U.S. patent US 6,317,254 B1 (2001).

90. A. A. Al-Azzawi, A. A. Almukhtar, A. Dhar, M. C. Paul, H. Ahmad, A. Altuncu, R. Apsari, and S. W. Harun, "Gain-flattened hybrid EDFA operating in C + L band with parallel pumping distribution technique," IET Optoelectron. **14**(6), 447–451 (2020).

91. M. Yamada, A. Mori, K. Kobayashi, H. Ono, T. Kanamori, K. Oikawa, Y. Nishida, and Y. Ohishi, "Gain-flattened tellurite-based EDFA with a flat amplification bandwidth of 76 nm," IEEE Photonics Technol. Lett. **10**(9), 452–455 (1998).

92. Y. M. Zakaryia, M. H. Aly, and O. M. and Ahmed E. El-Samahy, "Erbium Doped Fiber Amplifier Performance using Different Host Materials in the Band 1450-1650 Nm: A Comparative Study," IIUM Eng. J. **5**(2), (1970).

93. V. V. Dvoyrin, A. V. Kir'Yanov, V. M. Mashinsky, O. I. Medvedkov, A. A. Umnikov, A. N. Guryanov, and E. M. Dianov, "Absorption, gain, and laser action in bismuth-doped aluminosilicate optical fibers," IEEE J. Quantum Electron. **46**(2), 182–190 (2010).

94. I. A. Bufetov, M. A. Melkumov, S. V. Firstov, K. E. Riumkin, A. V. Shubin, V. F. Khopin, A. N. Guryanov, and E. M. Dianov, "Bi-Doped Optical Fibers and Fiber Lasers," IEEE J. Sel. Top. Quantum Electron. **20**(5), 1–12 (2014).

95. Y. Wang, N. K. Thipparapu, D. J. Richardson, and J. K. Sahu, "Ultra-Broadband Bismuth-Doped Fiber Amplifier Covering a 115-nm Bandwidth in the O and e Bands," J. Light. Technol. **39**(3), 795–800 (2021).

96. A. Donodin, M. Tan, P. Hazarika, V. Dvoyrin, I. Phillips, P. Harper, S. K. Turitsyn, and W. Forysiak, "30-GBaud DP 16-QAM transmission in the E-band enabled by bismuth-doped fiber amplifiers," Opt. Lett. **47**(19), 5152 (2022).

97. J. K. Sahu, N. K. Thipparapu, A. A. Umnikov, P. Barua, and M. Nunez Velazquez, "Amplifier and laser demonstrations in bi-doped silica optical fibers," Opt. InfoBase Conf. Pap. **1**, 1–3 (2014).

98. E. M. Dianov, "Bismuth-doped optical fibers: A challenging active medium for near-IR lasers and optical amplifiers," Light Sci. Appl. **1**(MAY), 1–7 (2012).

99. C. D. Boley, J. W. Dawson, L. S. Kiani, and P. H. Pax, "E-band neodymium-doped fiber amplifier: model and application," Appl. Opt. **58**(9), 2320 (2019).

100. J. W. Dawson, L. S. Kiani, P. H. Pax, G. S. Allen, D. R. Drachenberg, V. V. Khitrov, D. Chen, N. Schenkel, M. J. Cook, R. P. Crist, and M. J. Messerly, "E-band Nd^3+ amplifier based on wavelength selection in an all-solid micro-structured fiber," Opt. Express **25**(6), 6524 (2017).

101. P. H. Pax, V. V. Khitrov, D. R. Drachenberg, G. S. Allen, B. Ward, M. Dubinskii, M. J. Messerly, and J. W. Dawson, "Scalable waveguide design for three-level operation in Neodymium doped fiber laser," Opt. Express **24**(25), 28633 (2016).

102. M. M. Kozak, R. Caspary, and W. Kowalsky, "Thulium-doped fiber amplifier for the S-band," Proc. 2004 6th Int. Conf. Transparent Opt. Networks **2**, 51–54 (2004).

103. F. Roy, F. Leplingard, L. Lorcy, A. Sauze, P. Baniel, and D. Bayart, "48% Power Conversion Efficiency in a Single-Pump Gain-Shifted Thulium-Doped Fiber Amplifier," Opt. InfoBase Conf. Pap. **33**(0), 5–7 (2001).

104. M. H.Aly, M. Nasr, and H. E. Seleem, "Thulium doped fiber amplifier in the S/S + band Employing Different Concentration profiles B," in *Fifth Workshop on Photonics and Its Applications* (2005), pp. 39–49.

105. J. Mirza, S. Ghafoor, N. Habib, F. Kanwal, and K. K. Qureshi, "Performance evaluation of praseodymium doped fiber amplifiers," Opt. Rev. **28**(6), 611–618 (2021).

106. Y. L. P. Reddy, M. Waaiz, S. N. Ahmed, and C. V. K. Reddy, "Optical Properties of Dysprosium (Dy 3 +) doped Fluoroborate Glasses," Int. J. Innov. Sci. Eng. Technol. **4**(7), 4–8 (2017).

107. T. Ivaniga and P. Ivaniga, "Comparison of the optical amplifiers EDFA and SOA based on the BER and Q-factor in C-band," Adv. Opt. Technol. **2017**, (2017).

108. A. Sobhanan, A. Anthur, S. O'Duill, M. Pelusi, S. Namiki, L. Barry, D. Venkitesh, and G. P. Agrawal, "Semiconductor optical amplifiers: recent advances and applications," Adv. Opt. Photonics **14**(3), 571 (2022).

109. "Semiconductor optical amplifiers, explained by RP Photonics Encyclopedia; SOA," https://www.rp-photonics.com/semiconductor_optical_amplifiers.html.

110. M. J. Connelly, "Wideband semiconductor optical amplifier steady-state numerical model," IEEE J. Quantum Electron. **37**(3), 439–447 (2001).

111. A. Elrefaie and C. Lin, "Performance degradations of multigigabit-per-second NRZ/RZ lightwave systems due to gain saturation in traveling-wave semiconductor optical amplifiers," IEEE Photonics Technol. Lett. **1**(10), 330–303 (1989).

112. R. J. Manning, A. D. Ellis, A. J. Poustie, and K. J. Blow, "Semiconductor laser amplifiers for ultrafast all-optical signal processing," J. Opt. Soc. Am. B **14**(11), 3204 (1997).

113. Z. V. Rizou, K. E. Zoiros, and M. J. Connelly, "Semiconductor Optical Amplifier Pattern Effect Suppression Using Optical Notch Filtering," J. Eng. Sci. Technol. Rev. **9**(4), 198–201 (2016).

114. R. Brenot, F. Pommereau, O. Le Gouezigou, J. Landreau, F. Poingt, L. Le Gouezigou, B. Rousseau, F. Lelarge, F. Martin, and G. H. Duan, "Experimental study of the impact of optical confinement on saturation effects in SOA," in *Optical Fiber Communication Conference (OFC)* (2005), pp. 1–3.

115. E. S. Björlin and J. E. Bowers, "Noise Figure of Vertical-Cavity Semiconductor Optical Amplifiers," IEEE J. Quantum Electron. **38**(1), 61–66 (2002).

116. K. Carney, R. Lennox, R. Maldonado-Basilio, S. Philippe, L. Bradley, and P. Landais, "Noise controlled semiconductor optical amplifier based on lateral cavity laser," Electron. Lett. **46**(18), 1288–1289 (2010).

117. K. Carney, R. Lennox, R. Maldonado-Basilio, S. Philippe, F. Surre, L. Bradley, and P. Landais, "Method to improve the noise figure and saturation power in multi-contact semiconductor optical amplifiers: simulation and experiment," Opt. Express **21**(6), 7180 (2013).

118. C. H. Henry, R. Skillman, F. Kazarinov, N. A. Martinsville, and O. Gillete, "Polarization indpendent semiconductor optical amplifier," (1990).

119. M. Itoh, Y. Shibata, T. Kakitsuka, Y. Kadota, and Y. Tohmori, "Polarization-insensitive

SOA with a strained bulk active layer for network device application," IEEE Photonics Technol. Lett. **14**(6), 765–767 (2002).

120. E. Udvary and T. Berceli, "Multifunctional SOAs in optical communication systems," in *ICTON 2009: 11th International Conference on Transparent Optical Networks* (IEEE, 2009), pp. 1–4.

121. J. Renaudier, "Recent advances in ultra-wideband WDM transmission based on semiconductor optical amplifiers," in *Optical Fiber Communication Conference (OFC)* (2019), **Tu3F.5**, pp. 19–21.

122. M. Ionescu, A. Arnould, D. Le Gac, S. Etienne, A. Ghazisaeidi, M. Duval, C. Bastide, H. Bissessur, and J. Renaudier, "20.6 Pb/s·km Unrepeatered Transmission without ROPA: UWB SOA Booster and Backward Raman Amplification," 2020 Eur. Conf. Opt. Commun. ECOC 2020 (1), 2020–2023 (2020).

123. A. Ghazisaeidi, A. Arnould, M. Ionescu, V. Aref, H. Mardoyan, S. Etienne, M. Duval, C. Bastide, H. Bissessur, and J. Renaudier, "99.35 Tb/s Ultra-wideband Unrepeated Transmission over 257 km using Semiconductor Optical Amplifiers and Distributed Raman Amplification," J. Light. Technol. 6–11 (2022).

124. M. E. Marhic, P. A. Andrekson, P. Petropoulos, S. Radic, C. Peucheret, and M. Jazayerifar, "Fiber optical parametric amplifiers in optical communication systems," Laser Photonics Rev. **9**(1), 50–74 (2015).

125. M. E. Marhic, N. Kagi, T.-K. Chiang, and L. G. Kazovsky, "Broadband fiber optical parametric amplifiers," Opt. Lett. **21**(8), 573 (1996).

126. Z. Tong, C. Lundström, P. A. Andrekson, C. J. McKinstrie, M. Karlsson, D. J. Blessing, E. Tipsuwannakul, B. J. Puttnam, H. Toda, and L. Grüner-Nielsen, "Towards ultrasensitive optical links enabled by low-noise phase-sensitive amplifiers," Nat. Photonics **5**(7), 430–436 (2011).

127. V. Gordienko, F. Ferreira, J. R. Lamb, A. Szabo, and N. Doran, "Phase-sensitive amplification of 11 WDM channels across bandwidth of 8 nm in a fibre optic parametric amplifier," in *2020 European Conference on Optical Communications, ECOC 2020* (2020), (1), pp. 1–4.

128. A. Legrand, S. Lanne, C. Simonneau, D. Bayart, A. Mussot, T. Sylvestre, E. Lantz, and H. Maillotte, "impact of pump phase modulation for fiber optical parametric amplifiers," IEEE Photonics Technol. Lett. **16**(5), 1289–1291 (2004).

129. B. P.-P. Kuo, J. M. Fini, L. Grüner-Nielsen, and S. Radic, "Dispersion-stabilized highly-

nonlinear fiber for wideband parametric mixer synthesis," Opt. Express **20**(17), 18611 (2012).

130. V. Gordienko, F. M. Ferreira, C. B. Gaur, and N. J. Doran, "Looped Polarization-Insensitive Fiber Optical Parametric Amplifiers for Broadband High Gain Applications," J. Light. Technol. **39**(19), 6045–6053 (2021).

131. C. B. Gaur, V. Gordienko, P. Hazarika, and N. J. Doran, "Polarization Insensitive Fiber Optic Parametric Amplifier with a Gain Bandwidth of 22 nm in S-Band," in *Optical Fiber Communication Conference (OFC)* (OSA, 2022), pp. 43–45.

132. C. B. Gaur, V. Gordienko, P. Hazarika, and N. J. Doran, "Polarization Insensitive Fiber Optic Parametric Amplifier with a Gain Bandwidth of 22 nm in S-Band," in *European Conference on Optical Communication* (IEEE, 2021), (1), pp. 978–981.

133. C. B. Gaur, V. Gordienko, F. Ferreira, V. Ribeiro, and N. J. Doran, "Fibre optic parametric amplifier for high capacity burst-mode access networks," Opt. Express **29**(14), 21190 (2021).

134. J. D. Marconi, J. M. Chavez Boggio, H. L. Fragnito, and S. R. Bickham, "Nearly 100 nm bandwidth of flat gain with a double-pumped fiber optic parametric amplifier," in *Optical Fiber Communication Conference (OFC)* (2007), pp. 7–9.

135. G. P. (Govind P. . Agrawal, *Lightwave Technology : Components and Devices* (Wiley, 2004).

136. D. Lavery, "Digital Coherent Receivers for Passive Optical Networks," University college London (2013).

137. M. Tan, "Raman fibre laser based amplification in coherent transmission systems," Aston University (2016).

138. E. Ip, A. P. Lau, D. J. Barros, and J. M. Kahn, "Coherent detection in optical fiber systems: erratum," Opt. Express **16**(26), 21943 (2008).

139. S. Makovejs, "High-speed optical fibre transmission using advanced modulation formats," PhD thesis (July), University College London (2011).

140. M. S. Faruk and S. J. Savory, "Digital Signal Processing for Coherent Transceivers Employing Multilevel Formats," J. Light. Technol. **35**(5), 1125–1141 (2017).

141. S. J. Savory, "Digital filters for coherent optical receivers," Opt. Express **16**(2), 804 (2008).

142. A. D. Ellis, M. E. McCarthy, M. A. Z. Al-Khateeb, and S. Sygletos, "Capacity limits of

systems employing multiple optical phase conjugators," Opt. Express **23**(16), 20381 (2015).

143. R. A. Shafik, M. S. Rahman, and A. H. M. R. Islam, "On the extended relationships among EVM, BER and SNR as performance metrics," in *Proceedings of 4th International Conference on Electrical and Computer Engineering, ICECE 2006* (2006), (December), pp. 408–411.

144. "How Error Vector Magnitude (EVM) Measurement Improves Your System-Level Performance | Analog Devices," https://www.analog.com/en/technical-articles/how-evm-measurement-improves-system-level-performance.html.

145. A. Alvarado, T. Fehenberger, B. Chen, and F. M. J. Willems, "Achievable Information Rates for Fiber Optics: Applications and Computations," J. Light. Technol. **36**(2), 424–439 (2018).

146. J. Cho, L. Schmalen, and P. J. Winzer, "Normalized Generalized Mutual Information as a Forward Error Correction Threshold for Probabilistically Shaped QAM," in *European Conference on Optical Communication, ECOC* (2017), pp. 1–3.

147. J. Cho and P. J. Winzer, "Probabilistic Constellation Shaping for Optical Fiber Communications," J. Light. Technol. **37**(6), 1590–1607 (2019).

148. N. S. Bergano and C. R. Davidson, "Circulating loop transmission experiments for the study of long-haul transmission systems using erbium-doped fiber amplifiers," J. Light. Technol. **13**(5), 879–888 (1995).

149. P. Harper, "Long distance dispersion managed soliton transmission experiments," Aston University (1997).

150. R. Hui and M. . Sullivan, *Fiber Optic Measurement Techniques*, 1st ed. (Academic press, 2009).

151. M. G. Taylor and L. Road, "Observation of new polarisation dependence effect in long haul optically amplified system," in *Optical Fiber Communication Conference (OFC)* (1993), pp. 291–294.

152. D. S. Millar, "Digital Signal Processing for Coherent Optical Fibre Communications," University College London (2011).

153. G. P. Agrawal and Headley Clifford, "Raman amplification in fiber optical communication systems," in *Raman Amplification in Fiber Optical Communication Systems* (Elsevier Academic Press, 2005).

154. J. Bromage, "Raman Amplification for Fiber Communications Systems," J. Light.

Technol. **22**(1), 79–93 (2004).

155. K. Rottwitt and J. H. Povlsen, "Analyzing the fundamental properties of Raman amplification in optical fibers," J. Light. Technol. **23**(11), 3597–3605 (2005).

156. B. Bouzid, "Analysis and review of Erbium doped fiber amplifier," in *2013 Saudi International Electronics, Communications and Photonics Conference, SIECPC 2013* (IEEE, 2013), pp. 1–5.

157. S. D. Alaruri, "Single Stage C-Band Erbium-Doped Fiber Amplifier (EDFA) Development and Performance Evaluation," Int. J. Meas. Technol. Instrum. Eng. **7**(2), 41–49 (2018).

158. F. A. Flood, "L-Band Erbium-Doped Fiber Amplifiers," in *Optical Fiber Communication Conference (OFC)* (1994), pp. 102–104.

159. L. F. Mollenauer, R. H. Stolen, and M. N. Islam, "Experimental Demonstration of Soliton Propagation in Long Fibers: Loss Compensated By Raman Gain.," Opt. Lett. **10**(5), 229–231 (1985).

160. P. Hansen, L. Eskildsen, S. Grubb, A. Vengsarkar, S. Korotky, and T. Strasser, "442 km repeaterless transmission in a 10 Gbit/s system experiment," Electron. Lett. **32**, 1018–1019 (1996).

161. B. Zhu, L. Leng, L. E. Nelson, Y. Qian, J. Bromage, S. Stulz, and S. Kado, "non-zero dispersion fiber with simultaneous C + L-band dispersion compensation," 4–6 (2002).

162. T. N. Nielsen, A. J. Stentz, K. Rottwitt, D. S. Vengsarkar, Z. J. Chen, P. B. Hansen, J. H. Park, K. S. Feder, S. Cabot, S. Stulz, D. W. Peckham, L. Hsu, C. K. Kan, A. F. Judy, S. Y. Park, L. E. Nelson, and L. Grüner-Nielsen, "3.28-Tb/s transmission over 3 × 100 km of nonzero-dispersion fiber using dual C- and L-band distributed Raman amplification," IEEE Photonics Technol. Lett. **12**(8), 1079–1081 (2000).

163. B. Mikkelsen, G. Raybon, R. . Essiambre, A. . Stenz, T. . Nielson, D. . Peckham, L. Nielsen-Gruner, K. Dreyer, and J. . Johnson, "320-Gb / s Single-Channel Pseudolinear Transmission over 200 km of," IEEE Photonics Technol. Lett. **12**(10), 1400–1402 (2000).

164. Neilsen T.N, "1.6 Tb/s (40x40 Gb/s) transmission over 4x100km nonzero-dispersion fiber using hybrid Raman/erbium-doped inline amplifiers," in *European Conference on Optical Communication* (1999), pp. PD2-2.

165. M. Nissov, C. R. Davidson, K. Rottwitt, R. Menges, P. C. Corbett, D. Innis, and N. S. Bergano, "100 Gb/s (10×10 Gb/s) WDM transmission over 7200 km using distributed Raman amplification," in *IEE Conference Publication* (1997), (448 /5), pp. 9–12.

166. K. Rottwitt and H. D. Kidorf, "A 92 nm Bandwidth Raman Amplifier," in *Optical Fiber Communication Conference (OFC)* (1998), (PD6-1), pp. 448–451.

167. A. K. Srivastava, D. L. Tzeng, A. J. Stentz, J. E. Johnson, M. L. Pearsall, O. Mizuhara, T. A. Strasser, K. F. Dreyer, J. W. Sulhoff, L. Zhang, P. D. Yeates, J. R. Pedrazzani, A. M. Sergent, R. E. Tench, J. M. Freund, T. V. Nguyen, H. Manar, Y. Sun, C. Wolf, M. M. Choy, R. B. Kummer, D. Kalish, and A. R. Chraplyvy, "High-speed WDM Transmission in AllWave™ Fiber in Both the 1.4-μm and 1.55-μm Bands," in *Optical Amplifiers and Their Applications* (1998), **25**, pp. 246–249.

168. N. A. F. Sena, *A Brief Introduction to Using Ode45 in MATLAB* (n.d.), **1**(5).

169. L. F. Shampine and M. W. Reichelt, *Solving Boundary Value Problems for Ordinary Differential Equations in M Atlab with Bvp4c* (2000), **75275**.

170. A. Iqbal, L. Krzczanowicz, I. D. Philips, P. Harper, and W. Forysiak, "Performance characterisation of ultra-wideband Raman amplifiers," in *45th European Conference on Optical Communication (ECOC)* (2019), pp. 1–4.

171. P. B. Hansen, G. Veselka-jacobovitz, G. Neilsen , L, and A. J. Stentz, "Raman amplification for loss compensation in dispersion compensating fibre modules," Electron. Lett. **34**(11), 1136–1137 (1998).

172. G. Neilsen , L, Y. Qian, and P. . Gaarde, "Raman Amplifiers for Telecommunications," in (Springer New yok, 2007), **1**(1–2), pp. 161–189.

173. X. Zhou and M. Birk, "100 nm broadband Raman amplification in NZ-DSF fiber with zero-dispersion wavelength around 1500 nm," in *Optics InfoBase Conference Papers* (2004), **1**, pp. 3–5.

174. N. Takachio and H. Suzuki, "Application of Raman-distributed amplification to WDM transmission systems using 1.55-μm dispersion-shifted fiber," J. Light. Technol. **19**(1), 60–69 (2001).

175. T. Miyamoto, M. Tanaka, J. Kobayashi, T. Tsuzaki, M. Hirano, T. Okuno, M. Kakui, and M. Shigematsu, "Highly nonlinear fiber-based lumped fiber Raman amplifier for CWDM transmission systems," J. Light. Technol. **23**(11), 3475–3483 (2005).

176. M. J. Li, S. Li, and D. A. Nolan, "Nonlinear fibers for signal processing using optical Kerr effects," J. Light. Technol. **23**(11), 3606–3614 (2005).

177. S. Namiki and Y. Emori, "Broadband Raman amplifiers design and practice," in *OSA Trends in Optics and Photonics* (2000), pp. 10–13.

178. S. Namiki and Y. Emori, "Ultrabroad-band Raman amplifiers pumped and gain-equalized

by wavelength-division-multiplexed high-power laser diodes," IEEE J. Sel. Top. Quantum Electron. **7**(1), 3–16 (2001).

179. B. Zhu, L. Leng, L. E. Nelson, Y. Qian, J. Bromage, S. Stulz, and S. Kado, "non-zero dispersion fiber with simultaneous C + L-band dispersion compensation," in *Optical Fiber Communication Conference (OFC)* (2002), pp. 4–6.

180. K. Mochizuki, N. Edagawa, and Y. Iwamoto, "Amplified Spontaneous Raman Scattering in Fiber Raman Amplifiers," J. Light. Technol. **4**(9), 1333 (1986).

181. N. Anders Olsson and J. Hegarty, "Noise Properties of a Raman Amplifier," J. Light. Technol. **4**(4), 396–399 (1986).

182. E. Desurvire, *Erbium-Doped Fiber Amplifiers: Principles and Applications* (2002), **48**(2).

183. E. Desurvire, *Erbium-Doped Fiber Amplifiers: Principles and Applications* (1994).

184. M. D. Mermelstein, K. Brar, and C. Headley, "RIN transfer measurement and modeling in dual-order Raman fiber amplifiers," J. Light. Technol. **21**(6), 1518–1523 (2003).

185. D. T. Cassidy, N. April, J. O. Soc, and D. T. Cassidy, "Spontaneous-emission factor of semiconductor diode lasers Daniel," J. Opt. Soc. Am. B **8**(4), 747–752 (1991).

186. C. R. S. Fludger, V. Handerek, and R. J. Mears, "Pump to Signal RIN Transfer in Raman Fiber Amplifiers," J. Light. Technol. **19**(8), 1140–1148 (2001).

187. M. Tan, P. Rosa, M. A. Iqbal, I. D. Phillips, J. Nuño, J. D. Ania-Castañón, and P. Harper, "RIN mitigation in second-order pumped raman fibre laser based amplification," in *Asia Communications and Photonics Conference, ACPC 2015* (2015), **1**(c), pp. 6–8.

188. M. A. Iqbal, M. Tan, A. El-Taher, and P. Harper, "RIN and transmission performance improvement using second order and broadband first order forward Raman pumping," in *2017 Opto-Electronics and Communications Conference, OECC 2017 and Photonics Global Conference, PGC 2017* (2017), (c), pp. 1–4.

189. P. Hazarika, M. Tan, M. A. Iqbal, L. Krzczanowicz, A. A. i. Ali, I. Phillips, P. Harper, and W. Forysiak, "RIN induced penalties in G.654.E and G.652.D based distributed Raman amplifiers for coherent transmission systems," Opt. Express **29**(20), 32081 (2021).

190. P. B. Hansen, L. Eskildsen, A. J. Stentz, T. A. Strasser, J. Judkins, J. J. DeMarco, R. Pedrazzani, and D. J. DiGiovanni, "Rayleigh scattering limitations in distributed Raman pre-amplifiers," IEEE Photonics Technol. Lett. **10**(1), 159–161 (1998).

191. J. Mei, D. Liu, and D. Huang, "Impact of multipath interference on noise figure of fiber Raman amplifiers," in *Asia-Pacific Optical and Wireless Communications* (2002), **4905**,

pp. 588–595.

192. E. Brinkmeyer, "Analysis of the backscattering method for single-mode optical fibers," J. Opt. Soc. Am. **70**(8), 1010 (1980).

193. J. D. Ania-Castañón and S. K. Turitsyn, "Noise and gain optimisation in bi-directionally pumped dispersion compensating amplifier modules," Opt. Commun. **224**(1–3), 107–111 (2003).

194. J. D. Ania-Castañón, "Quasi-lossless transmission using second-order Raman amplification and fibre Bragg gratings," Opt. Express **12**(19), 4372 (2004).

195. R. W. Hellwarth, "Third-order optical susceptibilities of liquids and solids," Prog. Quantum Electron. **5**(79), 90002 (1977).

196. K. M. Muguro, "EFFECTS OF POLARIZATION IN A DISTRIBUTED RAMAN FIBRE AMPLIFIER By," Nelson Mandela Metropolitan University December (2011).

197. J. P. Gordon and H. Kogelnik, "PMD fundamentals: Polarization mode dispersion in optical fibers," Proc. Natl. Acad. Sci. U. S. A. **97**(9), 4541–4550 (2000).

198. S. Popov, E. Vanin, and G. Jacobsen, "Influence of polarization mode dispersion value in dispersion-compensating fibers on the polarization dependence of Raman gain," Opt. Lett. **27**(10), 848–850 (2002).

199. Q. Lin and G. P. Agrawal, "Polarization mode dispersion–induced fluctuations during Raman amplifications in optical fibers," Opt. Lett. **27**(24), 2194 (2002).

200. Q. Lin and G. P. Agrawal, "Vector theory of stimulated Raman scattering and fiber-based Raman amplifiers," J. Opt. Soc. Am. **20**(8), 1616–1631 (2003).

201. D. K. Boiyo, S. Kuja, D. Waswa, G. Amolo, R. R. G. Gamatham, E. K. R. Kipnoo, T. B. Gibbon, and A. W. R. Leitch, "Effects of polarization mode dispersion (PMD) on Raman gain and PMD measurement using an optical fibre Raman amplifier," in *IEEE AFRICON Conference* (2013), pp. 1–5.

202. S. Cui and J. Liu, "Gain variations in bi-directionally pumped fiber Raman amplifier due to," in *Asia-Pacific Optical and Wireless Communications, 2003, Wuhan, China Downloaded* (2023), (May 2004), pp. 725–730.

203. P. K. A. Wai and C. R. Menyuk, "Polarization mode dispersion, decorrelation, and diffusion in optical fibers with randomly varying birefringence," J. Light. Technol. **14**(2), 148–157 (1996).

204. S. Sergeyev, S. Popov, and A. T. Friberg, "Modeling polarization-dependent gain in fiber

Raman amplifiers with randomly varying birefringence," Opt. Commun. **262**, 114–119 (2006).

205. J. C. Bouteiller, L. Leng, and C. Headley, "Pump-pump four-wave mixing in distributed raman amplified systems," J. Light. Technol. **22**(3), 723–732 (2004).

206. R. E. Neuhauser, P. M. Krummrich, H. Bock, and C. Glingener, "Impact of nonlinear pump interactions on broadband distributed Raman amplification," in *Optical Fiber Communication Conference (OFC)* (2001), **MA4-1**, pp. 6–8.

207. T. Te Kung, C. Ten Chang, J. C. Dung, and S. Chi, "Four-wave mixing between pump and signal in a distributed Raman amplifier," J. Light. Technol. **21**(5), 1164–1170 (2003).

208. N. Shibata, R. P. Braun, and R. G. Waarts, "Phase-Mismatch Dependence of Efficiency of Wave Generation Through Four-Wave Mixing in a Single-Mode Optical Fiber," IEEE J. Quantum Electron. **23**(7), 1205–1210 (1987).

209. P. Hazarika, M. Abu-Romoh, M. Tan, L. Krzczanowicz, T. T. Nguyen, M. A. Iqbal, I. Phillips, P. Harper, M. J. Li, and W. Forysiak, "Impact of chromatic dispersion in discrete Raman amplifiers on coherent transmission systems," Opt. Fiber Commun. Conf. 1–3 (2021).

210. M. A. Z. Al-Khateeb, M. A. Iqbal, M. Tan, A. Ali, M. McCarthy, P. Harper, and A. D. Ellis, "Analysis of the nonlinear Kerr effects in optical transmission systems that deploy optical phase conjugation," Opt. Express **26**(3), 3145 (2018).

211. J. F. Hayes, "Paths Beneath the Seas: Transatlantic Telephone Cable Systems," IEEE Can. Rev. 18–22 (2006).

212. K. Kikuchi, "History of coherent optical communication and challenges for the future," in *EEE/LEOS Summer Topical Meetings* (2008), **TuC1.1**, pp. 107–108.

213. S. Liang, S. Jain, L. Xu, K. R. H. Bottrill, N. Taengnoi, M. Guasoni, P. Zhang, M. Xiao, Q. Kang, Y. Jung, P. Petropoulos, and D. J. Richardson, "High Gain , Low Noise , Spectral-Gain-Controlled ," J. Light. Technol. **39**(5), 1458–1463 (2021).

214. D. Qian, M. F. Huang, E. Ip, Y. K. Huang, Y. Shao, J. Hu, and T. Wang, "101.7-Tb/s (370×294-Gb/s) PDM-128QAM-OFDM transmission over 3×55-km SSMF using pilot-based phase noise mitigation," in *Optical Fiber Communication Conference (OFC)* (2011), (PDPB5), pp. 7–9.

215. A. Sano, T. Kobayashi, S. Yamanaka, A. Matsuura, H. Kawakami, Y. Miyamoto, K. Ishihara, and H. Masuda, "102.3-Tb/s (224 x 548-Gb/s) C- and extended L-band all-raman transmission over 240 km using PDM-64QAM single carrier FDM with digital pilot tone,"

in *Optical Fiber Communication Conference (OFC)* (2012), pp. 8–10.

216. F. Hamaoka, M. Nakamura, S. Okamoto, K. Minoguchi, T. Sasai, A. Matsushita, E. Yamazaki, and Y. Kisaka, "Ultra-wideband WDM transmission in S-C- A nd L-bands using signal power optimization scheme," J. Light. Technol. **37**(8), 1764–1771 (2019).

217. P. Poggiolini, G. Bosco, A. Carena, V. Curri, Y. Jiang, and F. Forghieri, "A Detailed Analytical Derivation of the GN Model of Non-Linear Interference in Coherent Optical Transmission Systems," arXiv (128), 1–25 (2012).

218. P. Poggiolini, A. Carena, V. Curri, G. Bosco, and F. Forghieri, "Analytical modeling of nonlinear propagation in uncompensated optical transmission links," IEEE Photonics Technol. Lett. **23**(11), 742–744 (2011).

219. A. El-Taher, M. Tan, M. A. Iqbal, L. Krzczanowicz, I. D. Phillips, W. Forysiak, and P. Harper, "High gain, flattened, discrete raman fiber amplifier and its transmission performance," Opt. InfoBase Conf. Pap. (c), 45 (2017).

220. S. P. Neves Cani, M. Freitas, R. T. R. Almeida, and L. C. Calmon, "Raman Amplifier Performance of Dispersion Compensating Fibers," SBMO/IEEE MTT-S Int. Microw. Optoelectron. Conf. Proc. **2**, 553–558 (2003).

221. P. Hazarika, M. Abu-romoh, M. Tan, L. Krzczanowicz, T. T. Nguyen, M. A. Iqbal, I. Phillips, P. Harper, Ming-Jun Li, and W. Forysiak, "Impact of Chromatic Dispersion in Discrete Raman Amplifiers on Coherent Transmission Systems," in *2021 Optical Fiber Communications Conference and Exhibition (OFC)* (OSA, 2021), pp. 1–3.

222. P. Poggiolini, G. Bosco, A. Carena, V. Curri, Y. Jiang, and F. Forghieri, "The GN-model of fiber non-linear propagation and its applications," J. Light. Technol. **32**(4), 694–721 (2014).

223. A. Carena, V. Curri, G. Bosco, P. Poggiolini, and F. Forghieri, "Modeling of the impact of nonlinear propagation effects in uncompensated optical coherent transmission links," J. Light. Technol. **30**(10), 1524–1539 (2012).

224. J. M. Senior, *Optical Fiber Communications Principles and Practice*, 3rd ed. (2009), (3).

225. X. Liu and B. Lee, "A fast method for nonlinear Schrödinger equation," IEEE Photonics Technol. Lett. **15**(11), 1549–1551 (2003).

226. D. Semrau, R. I. Killey, and P. Bayvel, "The Gaussian Noise Model in the Presence of Inter-Channel Stimulated Raman Scattering," J. Light. Technol. **36**(14), 3046–3055 (2018).

227. D. Semrau, R. I. Killey, and P. Bayvel, "A Closed-Form Approximation of the Gaussian

Noise Model in the Presence of Inter-Channel Stimulated Raman Scattering," J. Light. Technol. **37**(9), 1924–1936 (2019).

228. P. W. Wisk, M. F. Yan, and B. Zhu, "(12) United States Patent," (2016).

229. L. E. Nelson, X. Zhou, B. Zhu, M. F. Yan, P. W. Wisk, and P. D. Magill, "All-Raman-amplified, 73 nm seamless band transmission of 9 Tb/s over 6000 km of fiber," IEEE Photonics Technol. Lett. **26**(3), 242–245 (2014).

230. K. O. Hill, D. C. Johnson, B. S. Kawasaki, and R. I. MacDonald, "Cw three-wave mixing in single-mode optical fibers," J. Appl. Phys. **49**(10), 5098–5106 (1978).

231. K. Inoue, "Phase-mismatching characteristic of four-wave mixing in fiber lines with multistage optical amplifiers K.," Opt. Lett. **17**(11), 801–803 (1992).

232. C. Kurtzke, "Suppression of Fiber Nonlinearities by Appropriate Dispersion Management," IEEE Photonics Technol. Lett. **5**(10), 1250–1253 (1993).

233. M. Eiselt, "Impact of non-linear fiber effects on fiber choice for ultimate transmission capacity," in *Conference on Optical Fiber Communication, Technical Digest Series* (2000), **1**, pp. 58–60.

234. M. A. Iqbal, M. A. Z. Al-Khateeb, L. Krzczanowicz, I. D. Phillips, P. Harper, and W. Forysiak, "Linear and Nonlinear Noise Characterisation of Dual Stage Broadband Discrete Raman Amplifiers," J. Light. Technol. **37**(14), 3679–3688 (2019).

235. M. A. Iqbal, G. Di Rosa, L. Krzczanowicz, I. Phillips, P. Harper, A. Richter, and W. Forysiak, "Impact of pump-signal overlap in S+C+L band discrete Raman amplifiers," Opt. Express **28**(12), 18440 (2020).

236. A. H. Gnauck, R. M. Jopson, and P. J. Winzer, "Demonstration of Counter-Propagating Raman Pump Placed Near Signal-Channel Wavelengths," IEEE Photonics Technol. Lett. **29**(1), 154–157 (2017).

237. T. Xu, N. A. Shevchenko, D. Lavery, D. Semrau, G. Liga, A. Alvarado, R. I. Killey, and P. Bayvel, "Modulation format dependence of digital nonlinearity compensation performance in optical fibre communication systems," Opt. Express **25**(4), 3311 (2017).

238. "Optical Preamplifier an overview ScienceDirect Topics," https://www.sciencedirect.com/topics/engineering/optical-preamplifier.

239. T. T. Nguyen, T. Zhang, E. Giacoumidis, A. A. I. Ali, M. Tan, P. Harper, L. P. Barry, and A. D. Ellis, "Coupled Transceiver-Fiber Nonlinearity Compensation Based on Machine Learning for Probabilistic Shaping System," J. Light. Technol. **39**(2), 388–399 (2021).

240. J. Cheng, M. Tang, A. P. T. Lau, C. Lu, L. Wang, Z. Dong, S. M. Bilal, S. Fu, P. P. Shum, and D. Liu, "Pump RIN-induced impairments in unrepeatered transmission systems using distributed Raman amplifier," Opt. Express **23**(9), 11838 (2015).

241. ITU-T, "Characteristics of a cut-off shifted single-mode optical fibre and cable Recommendation," (2016).

242. Y. Yamamoto, "Practical Aspects of G . 654 . E Fibers for Terrestrial Long Haul Transmission," in (OFC 2019 © OSA 2019, 2019), pp. 9–11.

243. N. Guo, Y. Li, M. Gao, Y. Shen, Z. Liu, X. Jiang, S. Cao, Y. Qian, and G. Shen, "Spectrum Efficiency and Cost Evaluation for G . 654 . E Fiber Based Optical Transmission Systems," in *Asia Communications and Photonics Conference 2020 © OSA 2020* (Optical Society of America, 2020, 2020), p. paper M4A.274.

244. J. D. Downie, S. Makovejs, J. E. Hurley, M. Mlejnek, and H. De Pedro, "G.654.E optical fibers for high-data-rate terrestrial transmission systems with long reach," in *Proceedings of SPIE* (2018), (January), p. 23.

245. J. D. Downie, J. Hurley, H. DePedro, S. Garner, J. Blaker, A. Zakharian, S. Ten, and G. Mills, "Measurements and modeling of multipath interference at wavelengths below cable cut-off in a G654 optical fiber span," Opt. Express **25**(8), 9305 (2017).

246. J. Cheng, M. Tang, S. Fu, P. P. Shum, D. Yu, L. Wang, and D. Liu, "Relative Phase Noise-Induced Phase Error and System Impairment in Pump Depletion / Nondepletion Regime," J. Light. Technol. **32**(12), 2277–2286 (2014).

247. M. Mlejnek, J. D. Downie, and M. O'Sullivan, "Examination of Potential Terrestrial System Effects From Raman Pumps Below Cable Cutoff in G.654.E Fibers," J. Light. Technol. **37**(17), 4282–4294 (2019).

248. M. Tan, P. Rosa, S. T. Le, V. V. Dvoyrin, M. A. Iqbal, S. Sugavanam, S. K. Turitsyn, and P. Harper, "RIN mitigation and transmission performance enhancement with forward broadband pump," IEEE Photonics Technol. Lett. **30**(3), 254–257 (2018).

249. K. Keita, P. Delaye, R. Frey, and G. Roosen, "ы ы," J. Opt. Soc. Am. B **23**(12), 2479–2485 (2006).

250. Y. Ohki, N. Hayamizu, and S. Irino, *Pump Laser Module for Co-Propagating Raman Amplifier* (2003), (24), pp. 6–12.

251. W. S. Pelouch, "Raman Amplification : An Enabling Technology for Long-Haul Coherent Transmission Systems," J. Light. Technol. **34**(1), 6–19 (2016).

252. M. N. Islam, "Raman amplifiers for telecommunications," IEEE J. Sel. Top. Quantum

Electron. **8**(3), 548–559 (2002).

253. A. Iqbal, M. Tan, and P. Harper, "On the Mitigation of RIN Transfer and Transmission Performance Improvement in Bidirectional Distributed Raman Amplifiers," J. Light. Technol. **36**(13), 2611–2618 (2018).

254. G. Rizzelli, M. A. Iqbal, F. Gallazzi, P. Rosa, M. Tan, P. Corredera, J. D. Ania-Castañón, and P. Harper, "FBG reflectivity impact on RIN in ultralong laser amplifiers," Eur. Conf. Opt. Commun. ECOC **24**(25), 625–627 (2016).

255. C. R. . Fludger and V. Handerek, "Pump to signal RIN transfer in silicon Raman amplifiers," J. Light. Technol. **19**(8), 1140–1148 (2001).

256. J. Cheng, M. Tang, S. Fu, P. P. Shum, D. Liu, M. Xiang, Z. Feng, and D. Yu, "Relative phase noise estimation and mitigation in Raman amplified coherent optical communication system," Opt. Express **22**(2), 1257 (2014).

257. S. Faralli, S. Sugliani, G. Sacchi, F. Di Pasquale, and S. B. Papernyi, "Bidirectional Higher Order Cascaded Raman Amplification Benefits for 10-Gb/s WDM Unrepeated Transmission Systems," J. Light. Technol. **4**(8), 179–181 (2005).

258. M. S. Faruk and S. J. Savory, "Digital Signal Processing for Coherent Transceivers Employing Multilevel Formats," J. Light. Technol. **35**(5), 1125–1141 (2017).

259. M. A. Iqbal, L. Krzczanowicz, I. D. Philips, P. Harper, and W. Forysiak, "Noise Performance Improvement of Broadband Discrete Raman Amplifiers Using Dual Stage Distributed Pumping Architecture," J. Light. Technol. **37**(14), 3665–3671 (2019).

260. A. E. El-Taher, V. Karalekas, P. Harper, and J. D. Ania-Castañón, "High efficiency supercontinuum generation using ultra-long Raman fibre cavities," Eur. Conf. Opt. Commun. ECOC **17**(20), 17909–17915 (2008).

261. W. L. Zhang, Y. J. Rao, J. M. Zhu, Z. X. Y. Z. N. Wang, and X. H. Jia, "Low threshold 2^nd-order random lasing of a fiber laser with a half-opened cavity," Opt. Express **20**(13), 14400 (2012).

262. Z. Wang, H. Wu, M. Fan, L. Zhang, Y. Rao, W. Zhang, and X. Jia, "High power random fiber laser with short cavity length: Theoretical and experimental investigations," IEEE J. Sel. Top. Quantum Electron. **21**(1), 10–15 (2015).

263. M. Tan, P. Rosa, S. T. Le, M. A. Iqbal, I. D. Phillips, and P. Harper, "Transmission performance improvement using random DFB laser based Raman amplification and bidirectional second-order pumping," Opt. Express **24**(3), 2215 (2016).

264. R. A. Perez-Herrera, P. Roldan-Varona, M. Galarza, S. Sañudo-Lasagabaster, L.

Rodriguez-Cobo, J. M. Lopez-Higuera, and M. Lopez-Amo, "Hybrid Raman-erbium random fiber laser with a half open cavity assisted by artificially controlled backscattering fiber reflectors," Sci. Rep. **11**(1), 1–8 (2021).

265. T. Tanaka, K. Torii, M. Yuki, H. N. Naito, T. Naito, and I. Yokota, "200-nm Bandwidth WDM Transmission around 1.55 ,um using Distributed Raman Amplifier," in *28th European Conference on Optical Communication, ECOC* (2002), (1), pp. 530–533.

266. T. Naito, T. Tanaka, K. Torii, Shimojoh Naomasa, and H. Nakamoto, "A Broadband Distributed Raman Amplifier for Bandwidths Beyond 100 nm Takao," in *Optical Fiber Communication Conference (OFC)* (2002), pp. 116–117.

267. T. Tanaka, H. Nakamoto, K. Torii, T. Naito, and I. Yokota, "Suppression of optical SNR degradation due to Rayleigh scattered pump light in broadband Raman amplifier," in *European Conference on Optical Communication* (IEEE, 2002), **2**(1), pp. 4–5.

268. M. A. Iqbal, G. Di Rosa, L. Krzczanowicz, I. Phillips, P. Harper, A. Richter, and W. Forysiak, "Impact of pump-signal overlap in S+C+L band discrete Raman amplifiers," Opt. Express **28**(12), 18440 (2020).

269. D. Derickson, *Fiber Optic Test and Measurement*, 3rd ed. (Prentice Hall PTR, 1998).

270. P. Skvortcov, I. Phillips, W. Forysiak, T. Koike-Akino, K. Kojima, K. Parsons, and D. S. Millar, "Nonlinearity Tolerant LUT-Based Probabilistic Shaping for Extended-Reach Single-Span Links," IEEE Photonics Technol. Lett. **32**(16), 967–970 (2020).

271. P. Skvortcov, C. Sanchez-Costa, I. Phillips, and W. Forysiak, "Receiver DSP highly tolerant to transmitter IQ impairments," in *Optical Fiber Communication Conference (OFC)* (OSA, 2019), **TH1D.2**, pp. 10–12.

272. G. C. M. Ferreira, S. P. N. Cani, M. J. Pontes, and M. E. V. Segatto, "Optimization of distributed Raman amplifiers using a hybrid genetic algorithm with geometric compensation technique," IEEE Photonics J. **3**(3), 390–399 (2011).

273. D. Zibar, A. M. Rosa Brusin, U. C. De Moura, F. Da Ros, V. Curri, and A. Carena, "Inverse System Design Using Machine Learning: The Raman Amplifier Case," J. Light. Technol. **38**(4), 736–753 (2020).

274. U. C. De Moura, M. A. Iqbal, M. Kamalian, L. Krzczanowicz, F. Da Ros, A. M. R. Brusin, A. Carena, W. Forysiak, S. Turitsyn, and D. Zibar, "Multi-Band Programmable Gain Raman Amplifier," J. Light. Technol. **39**(2), 429–438 (2021).

275. Y. Hadjar, N. J. Traynor, and S. Gray, "Noise figure tilt reduction in ultrawide-band WDM through second-order Raman amplification," IEEE Photonics Technol. Lett. **16**(4), 1200–

1202 (2004).

276. R. Emmerich, M. Sena, R. Elschner, C. Schmidt-Langhorst, I. Sackey, C. Schubert, and R. Freund, "Enabling S-C-L-band systems with standard C-band modulator and coherent receiver using nonlinear predistortion," Opt. InfoBase Conf. Pap. **40**(5), 1360–1368 (2021).

277. A. Donodin, V. Dvoyrin, E. Manuylovich, L. Krzczanowicz, W. Forysiak, M. Melkumov, V. Mashinsky, and S. Turitsyn, "Bismuth doped fibre amplifier operating in E- and S-optical bands," Opt. Mater. Express **11**(1), 127 (2021).

278. A. Donodin, M. Tan, P. Hazarika, V. Dvoyrin, I. Phillips, P. Harper, S. Turitsyn, and W. Forysiak, "30 GBaud DP 16-QAM Transmission in E-band Enabled by Bismuth-doped Fiber Amplifiers," Opt. Lett. **47**(19), 5152–5155 (2022).